ISTANBUL TECHNICAL UNIVERSITY ★ GRADUATE SCHOOL OF SCIENCE ENGINEERING AND TECHNOLOGY

IDENTIFICATION, MODELLING AND OPTIMISATION OF STRUCTURES WITH PASSIVE DAMPING TREATMENTS

Ph.D. THESIS

Hasan KÖRÜK

Department of Mechanical Engineering

Mechanical Engineering Programme

JUNE 2013

ISTANBUL TECHNICAL UNIVERSITY ★ GRADUATE SCHOOL OF SCIENCE ENGINEERING AND TECHNOLOGY

IDENTIFICATION, MODELLING AND OPTIMISATION OF STRUCTURES WITH PASSIVE DAMPING TREATMENTS

Ph.D. THESIS

Hasan KÖRÜK
(503082009)

Department of Mechanical Engineering

Mechanical Engineering Programme

Thesis Advisor: Prof. Dr. Kenan Y. ŞANLITÜRK

JUNE 2013

İSTANBUL TEKNİK ÜNİVERSİTESİ ★ FEN BİLİMLERİ ENSTİTÜSÜ

PASİF SÖNÜMLÜ YAPILARIN KARAKTERİZASYONU, MODELLENMESİ VE OPTİMİZASYONU

DOKTORA TEZİ

Hasan KÖRÜK
(503082009)

Makine Mühendisliği Anabilim Dalı

Makine Mühendisliği Programı

Tez Danışmanı: Prof. Dr. Kenan Y. ŞANLITÜRK

HAZİRAN 2013

Hasan Körük, a **Ph.D.** student of ITU **Graduate School of Science Engineering and Technology** student ID **503082009**, successfully defended the **dissertation** entitled "**IDENTIFICATION, MODELLING AND OPTIMISATION OF STRUCTURES WITH PASSIVE DAMPING TREATMENTS**", which he prepared after fulfilling the requirements specified in the associated legislations, before the jury whose signatures are below.

Thesis Advisor :	**Prof. Dr. Kenan Y. ŞANLITÜRK** İstanbul Technical University	.....
Jury Members :	**Prof. Dr. H. Temel BELEK** İstanbul Technical University	.....
	Prof. Dr. A. Rüstem ASLAN İstanbul Technical University	.....
	Prof. Dr. Yavuz YAMAN Middle East Technical University	.....
	Associate Prof. Dr. İpek BAŞDOĞAN Koç University	.....

Date of Submission : 24 April 2013
Date of Defense : 10 June 2013

To my wife and mother,

FOREWORD

I would like to thank and express my deepest gratitude to my supervisor, Prof. Kenan Y. Şanlıtürk, for his invaluable guidance and suggestions, and intimate support. His scientific knowledge and creative thinking always strike me with admiration.

I would like to thank to the thesis jury members, Prof. H. Temel Belek and Prof. A. Rüstem Aslan for their supports and encouragements. Also, I would like to thank to all the members of the Machine Theory Group of the Mechanical Engineering Department at ITU.

I would like to specially thank to Prof. Rajendra Singh from The Ohio State University for providing me the opportunity to do research in the Acoustics and Dynamic Laboratory at the Department of Mechanical and Aerospace Engineering and his continual guidance during my research there. I want also thank to Dr. Jason T. Dreyer, Dr. O. Taha Şen and all the people from the Acoustics and Dynamic Laboratory for their help and encouragement.

I also would like to thank to ITU Rectorship and Tinçel Kültür Vakfı for their financial supports to do research at The Ohio State University.

Lastly, I would like to thank to my wife and my family for their love.

June 2013

Hasan KÖRÜK
(Mechanical Engineer)

TABLE OF CONTENTS

Page

FOREWORD ..... **ix**
TABLE OF CONTENTS ..... **xi**
ABBREVIATIONS ..... **xv**
LIST OF TABLES ..... **xvii**
LIST OF FIGURES ..... **xix**
SUMMARY ..... **xxiii**
ÖZET ..... **xxvii**
1. INTRODUCTION **1**
1.1 Problem 1
1.2 Literature Review 3
1.2.1 Material testing 3
1.2.1.1 Material testing methods 3
1.2.1.2 Oberst beam method 4
1.2.2 Experimental identification of damping levels of structures 5
1.2.3 Damping prediction 7
1.2.4 Quantification of non-proportional damping 9
1.2.5 Optimisation 10
1.2.5.1 Optimisation techniques 10
1.2.5.2 Damping optimisation 11
1.3 Objectives of The Thesis 12
1.4. Outline of The Thesis 13
2. IDENTIFICATION OF DAMPING MATERIALS **15**
2.1 Introduction 15
2.2 Damping Materials 16
2.2.1 Viscoelasticity 16
2.2.2 Vibration damping 17
2.2.2.1 Hysteresis loop 17
2.2.2.2 Complex modulus 19
2.2.3 Effects of environmental factors 20
2.2.4 Passive damping treatments 21
2.2.5 Material testing methods 22
2.3 Oberst Beam Method (OBM) 22
2.3.1 Determination of mechanical properties of materials 25
2.3.1.1 Bending vibration of an Oberst beam: Theory 25
2.3.1.2 Extraction of material properties 28
2.4 Preparation of The Test Rig: Assessment of Oberst Rig Parameters 29
2.5 Electromagnetic Effect 34
2.5.1 Introduction 34
2.5.2 Experimental study 36
2.5.3 Theoretical modelling of electromagnetic effect 42

2.5.4 Results 48
2.5.5 Removing the adverse effects of electromagnetic excitations 53
2.6 Determination of Mechanical Properties of Sample Materials 59
2.7 Concluding Remarks 61
3. IDENTIFICATION OF DAMPING UNCERTAINTY 63
3.1 Introduction 63
3.2 Theoretical Background 64
3.2.1 Frequency response function estimations 64
3.2.2 Signal to noise ratio 67
3.2.3 System identification 67
3.2.3.1 Half-power method 67
3.2.3.2 Circle-fit method 68
3.2.3.3 Line-fit method 70
3.3 Damping Uncertainty Due to Noise: Numerical Simulation 72
3.4 Damping Uncertainty Due to Exponential Windowing: Experimental Study . 80
3.4.1 Numerical damping due to exponential windowing and its removal 80
3.4.2 FRF measurements 82
3.4.3 Results 85
3.5 Concluding Remarks 89
4. MODELLING DAMPED STRUCTURES 91
4.1 Introduction 91
4.2 A Damping Prediction Approach Based on The MSE Method 92
4.3 Formulation of A Composite FE with Damping Capability 94
4.4 Comparisons and Experimental Validation 99
4.4.1 Test case I: Undamped shell 99
4.4.2 Test case II: Completely damped beams 102
4.4.3 Test case III: Partially damped beam 104
4.4.4 Test case IV: Damped U-plate 105
4.5 Assessment of The Damping Prediction Procedure Based on MSE Method. 108
4.6 Concluding Remarks 117
5. QUANTIFICATION OF MODE SHAPE COMPLEXITY 119
5.1 Introduction 119
5.2 Existing Parameters: State-of-The-Art 120
5.3 A Novel Parameter for Quantification of Mode Shape Complexity 122
5.4 Comparisons and Validation 126
5.4.1 Proportionally damped system 128
5.4.2 Non-proportionally lightly damped system 129
5.4.3 Non-proportionally highly damped system 131
5.5 Concluding Remarks 135
6. PASSIVE DAMPING OPTIMISATION 137
6.1 Introduction 137
6.2 Optimisation Procedure 138
6.2.1 Statement of the optimisation problem 138
6.2.2 Selection of the optimisation method 139
6.2.3 The Big Bang-Big Crunch (BB-BC) method 140
6.3 Results 142
6.3.1 Damping optimisation for a single mode 143
6.3.2 Damping optimisation for multiple modes 146
6.4 Concluding Remarks 148
7. CONCLUSIONS AND SUGGESTIONS FOR FUTURE WORK 149

7.1 Conclusions 149
7.2 Suggestions for Future Work 153
REFERENCES 155
CURRICULUM VITAE 169

ABBREVIATIONS

BB-BC	**:** Big Bang-Big Crunch
BC	**:** Boundary Condition
CE	**:** Complex Eigenvalue
DFR	**:** Direct Frequency Response
DFT	**:** Discrete Fourier Transform
DM	**:** Damping Material
DOF	**:** Degree of Freedom
FE	**:** Finite Element
FT	**:** Fourier Transform
FRF	**:** Frequency Response Function
GA	**:** Genetic Algorithm
MCC	**:** Modal Correlation Coefficient
MCF	**:** Mode Complexity Factor
MDOF	**:** Multi Degree of Freedom
MIMO	**:** Multi Input Multi Output
MP	**:** Mean Phase
MPC	**:** Modal Phase Collinearity
MPD	**:** Mean Phase Deviation
MSC	**:** Mode Shape Complexity
MSE	**:** Modal Strain Energy
OBM	**:** Oberst Beam Method
RDT	**:** Random Decrement Technique
SDOF	**:** Single Degree of Freedom
SE	**:** Strain Energy
SIMO	**:** Single Input Multi Output
SNR	**:** Signal to Noise Ratio
STFT	**:** Short-Time Fourier Transform
WT	**:** Wavelet Transform

LIST OF TABLES

Page

Table 2.1 : The $\beta_n L$ values. 27
Table 2.2 : The C_n values. 28
Table 2.3 : The expressions for material identification based on ASTM E 756. 29
Table 2.4 : Natural frequencies and loss factors for various excitation force levels. 32
Table 2.5 : Identified natural frequencies using repeated mounting cases. 34
Table 2.6 : Natural frequencies and estimated Young's modulus of a steel beam of L= 220 mm exposed to different levels of magnetic field. 39
Table 2.7 : Correct values of the natural frequencies of a steel bare beam of L= 220 mm with fixed-free BCs. 41
Table 2.8 : The errors in natural frequencies and Young's modulus of a steel bare beam of L= 220 mm exposed to different levels of magnetic field. 41
Table 2.9 : Estimated natural frequencies and corresponding loss factor values using the measured FRFs on two different Oberst beams. 44
Table 2.10 : Spring stiffness k and the corresponding β values used in the analyses. 45
Table 2.11 : Natural frequencies, estimated Young's modulus and corresponding errors for a steel beam (L= 220 mm) for various values of k (N/m). 46
Table 2.12 : Results of the proposed approach based on linear extrapolation for a steel bare beam (L= 220 mm). 59
Table 2.13 : Results of the proposed approach based on non-linear extrapolation for a steel bare beam (L= 220 mm). 59
Table 2.14 : Identified Young's moduli (E and E^m) and loss factors (η and η^m) for steel and damping (viscoelastic) materials using OBM. 60
Table 3.1 : Numerical values of parameters used in the model. 74
Table 3.2 : Natural frequencies and loss factors: Exact values and values determined using the noise-free FRF. 75
Table 3.3 : Estimated loss factor (minimum and maximum) values using noisy FRFs for a range of SNR. 79
Table 3.4 : Uncertainty values in estimated loss factors for a range of SNR. 79
Table 3.5 : Data acquisition parameters. 84
Table 3.6 : Actual modal damping values (obtained without applying windowing). 86
Table 4.1 : Material properties of the plate structure. 100
Table 4.2 : Predicted natural frequencies of the plate for very fine mesh. 100
Table 4.3 : Predicted natural frequencies of the plate for various mesh sizes. 101
Table 4.4 : Measured and predicted natural frequencies of a steel beam (L= 220 mm). 103
Table 4.5 : Measured and predicted results of a fully damped beam with DM-1… 104
Table 4.6 : Measured and predicted results of a fully damped beam with DM-2… 104
Table 4.7 : Measured and predicted results of a fully damped beam with DM-3… 104
Table 4.8 : Measured and predicted results of a partially damped beam. 105

Table 4.9 : Materials and dimensions of the damping patches used in the U-plate. 106
Table 4.10 : Material properties used in the FE models of the damped U-plate. 107
Table 4.11 : Measured and predicted natural frequencies and loss factors of the damped U-plate. 107
Table 4.12 : Geometric and material properties of the each layer of the non-proportionally damped structure. 109
Table 4.13 : Natural frequencies (ω) of the non-proportionally damped structure predicted via MSE method and the corresponding errors in natural frequencies for various damping levels of damping material (η_m). 110
Table 4.14 : Loss factors of the non-proportionally damped structure (η_s) predicted via the MSE method and the corresponding errors (ε) in damping levels for various damping levels of damping material (η_m). 110
Table 4.15 : Loss factors of the proportionally damped structure (η_s) predicted via the MSE method and the corresponding errors (ε) for various values of η_m. 111
Table 4.16 : The MPDs for various damping levels of damping material (η_m) for both the proportionally and non-proportionally damped structures. ... 112
Table 4.17 : Predicted natural frequencies and loss factors of the plates damped one side and both sides using the composite FE-based CE method (FINES) and the FE-based MSE method and the MPDs. 115
Table 4.18 : The MPDs of the damped beams. 116
Table 5.1 : Material properties of the regions of the beam analysed for various damping cases. 127
Table 5.2 : Predicted natural frequencies and associated modal damping levels for various damping cases. 128
Table 5.3 : Calculated MSC, MP, MPD, MPC and MCC values for non-proportionally lightly damped system. 130
Table 5.4 : Calculated MSC, MP, MPD, MPC and MCC values for the non-proportional highly damped system. 133

LIST OF FIGURES

Page

Figure 2.1 : Cyclic stress-strain curve vs. time for elastic (left), viscous (middle) and viscoelastic (right) materials (Key: --- $\varepsilon(t)$ and ─ $\sigma(t)$). 17
Figure 2.2 : Hysteresis loop for a viscoelastic material under harmonic loading. 18
Figure 2.3 : Hysteretic model or complex modulus approach. 20
Figure 2.4 : Variation of complex modulus with temperature (constant frequency) for a typical viscoelastic material. 21
Figure 2.5 : Free and constrained layer damping treatments. 22
Figure 2.6 : Configurations of uniform, single-sided and double-sided damped and sandwiched cantilever beams used in Oberst beam method. 23
Figure 2.7 : Experimental test setup including Oberst test rig for identification of damping materials. 24
Figure 2.8 : Illustration of a typical FRF measurement using an Oberst test rig. 24
Figure 2.9 : FRFs for various numbers of averages (5, 10 and 50 averages). 31
Figure 2.10 : Comparison of FRFs for random and sine sweep excitations. 31
Figure 2.11 : FRFs measured for various forcing levels (low, medium and high). .. 32
Figure 2.12 : A stopper for assuring repeatability. 33
Figure 2.13 : FRF measurements for various mounting changes. 34
Figure 2.14 : Non-contact excitation system in OBM. 36
Figure 2.15 : Positioning of the test sample in an Oberst test rig. 38
Figure 2.16 : Estimated Young's moduli for all the modes except the first one against the gap parameter, δ. 40
Figure 2.17 : Estimated Young's moduli against the gap parameter, δ for 1st (a), 2nd (b), 3rd (c), and 4th (d) modes. 40
Figure 2.18 : Electromagnetic field around the free end of the beam (left) and two parallel springs at the free end of the beam (right). 44
Figure 2.19 : Errors in natural frequencies against spring stiffness, k for 1st (a), 2nd (b), 3rd (c), and 4th (d) modes. 47
Figure 2.20 : Young's modulus for various levels of magnetic field (δ values)..... 48
Figure 2.21 : Errors in natural frequencies (left) and Young's moduli (right) for various levels of magnetic field (for various δ values). 49
Figure 2.22 : Errors in natural frequencies (left) and Young's moduli (right) for various level of magnetic field (δ values) excluding the first mode. .. 49
Figure 2.23 : Sensitivities of natural frequencies to stiffness modification at the tip of the beam. 49
Figure 2.24 : Errors in natural frequencies (left) and Young's modulus (right) against the levels of magnetic field (for various δ values). 50
Figure 2.25 : Corresponding k values for δ values for each mode. 51
Figure 2.26 : Error in Young's modulus with respect to gap parameter for various beam lengths (L) calculated using the second mode of the beam. 52

Figure 2.27 : Error in Young's modulus with respect to spring stiffness for various beam lengths calculated using the second mode of the beam. 53
Figure 2.28 : Natural frequencies against the gap parameter, δ for 1st (a), 2nd (b), 3rd (c) and 4th (d) modes. 54
Figure 2.29 : Determined natural frequencies against the squared gap parameter, δ^2 for 1st (a), 2nd (b), 3rd (c), and 4th (d) modes. 55
Figure 2.30 : Determination of the "correct" natural frequencies via linear extrapolation (left) and non-linear extrapolation (right). 58
Figure 3.1 : Frequency and angle definitions in circle-fit procedure. 70
Figure 3.2 : Damping estimation using line-fit algorithm. 72
Figure 3.3 : A mass-spring system. 73
Figure 3.4 : A typical FRF. 75
Figure 3.5 : Sample generated FRFs with additive noise. 75
Figure 3.6 : Typical analyses for damping estimation using the noise-free FRF for 1st (a), 2nd (b) and 3rd (c) modes. 76
Figure 3.7 : Typical analyses for damping estimation using the noisy FRF for 1st (a), 2nd (b) and 3rd (c) modes. 77
Figure 3.8 : Estimated damping values using noisy FRFs with SNR_{dB}= 10 (a), 15 (b), 20 (c), 25 (d), 30 (e) and 40 (f). 78
Figure 3.9 : Damping uncertainty versus SNR value. 79
Figure 3.10 : An example of original signal (left), exponential window function (middle) and windowed signal (right). 80
Figure 3.11 : Exponential windowing with different levels of numerical damping applied to SDOF (left) and MDOF (right) systems. 81
Figure 3.12 : Experimental set-up for the case study. 83
Figure 3.13 : Time domain signals with and without windowing. 84
Figure 3.14 : Typical measured FRFs: with and without exponential windowing. .. 84
Figure 3.15 : A typical FRF and coherence function. 86
Figure 3.16 : Uncertainty values for two different methods. 87
Figure 3.17 : Uncertainties in modal damping values with respect to decay rate: (a) 1st–4.4 Hz, (b) 2nd–12.5 Hz, (c) 3rd–24.2 Hz, (d) 4th–40 Hz modes. 87
Figure 3.18 : Damping uncertainty versus decay rate. 88
Figure 3.19 : Damping uncertainty versus added numerical damping. 88
Figure 4.1 : Quadrilateral flat shell element with 6 DOFs per node. 95
Figure 4.2 : Connectivity and geometry definition of the 4-node composite FE. 96
Figure 4.3 : Geometric definition of the layers. 97
Figure 4.4 : Undamped plate structure (thickness = 1 mm) used in the analyses. 99
Figure 4.5 : Errors in natural frequencies of the plate for fine-5 mm (left), medium-10 mm (centre) and coarse-20 mm (right) mesh sizes. 101
Figure 4.6 : Comparisons of the actual natural frequencies of the plate with the predicted results for 2nd (left), 4th (centre) and 7th (right) modes. 101
Figure 4.7 : Completely damped (Oberst) beam. 103
Figure 4.8 : Partially damped beam. 105
Figure 4.9 : FE model of the damped U-plate prepared using FINES program. 105
Figure 4.10 : Experimental setup for measurement of FRFs on the damped U-plate. 106
Figure 4.11 : Measured and predicted natural frequencies (up) and loss factors (below) of the damped U-plate. 108
Figure 4.12 : Non-proportionally damped structure. 109

Figure 4.13 : 2nd (a), 4th (b), 6th (c) and 8th (d) mode shapes of proportionally (up) and non-proportionally (bottom) damped structures (Re-Im plane). 112
Figure 4.14 : The average values of MPD (a) and the errors in the predicted damping levels (b) as a function of the average damping levels of structures. 113
Figure 4.15 : The average values of the errors in the predicted damping levels as a function of the average MPD values. 114
Figure 4.16 : Plates damped one side (left) and both sides (right)..... 115
Figure 4.17 : Natural frequencies (left) and modal loss factors (right) of the plate damped one side. 115
Figure 4.18 : Natural frequencies (left) and modal loss factors (right) of the plate damped both sides. 116
Figure 5.1 : A completely real mode shape: standing wave. 123
Figure 5.2 : A completely complex mode shape: travelling wave..... 124
Figure 5.3 : Strain energy as a function of time: completely real (left), completely complex (middle) and typical complex (right) modes. 125
Figure 5.4 : Damped structure used in simulations (L=2.0 m, b=5 mm, h=4 mm). 127
Figure 5.5 : Non-proportionally damped beam..... 127
Figure 5.6 : Normalised strain energy (SE) of 8th (left), 14th (middle) and 16th (right) modes for the proportionally damped case (η_{beam} =0.4)..... 129
Figure 5.7 : 4th (left), 7th (middle) and 11th (right) modes for the proportionally damped case (η_{beam}=0.4)..... 129
Figure 5.8 : 4th (left), 7th (middle) and 11th (right) modes for the non-proportionally lightly damped system. 131
Figure 5.9 : Normalised strain energy (SE) of 8th (left), 14th (middle) and 16th (right) modes for the non-proportionally highly damped system..... 133
Figure 5.10 : 4th (left), 11th (middle) and 17th (right) modes of the non-proportionally highly damped system..... 133
Figure 5.11 : MSC with respect to MPD and MPC for non-proportionally highly damped structure. 134
Figure 5.12 : Comparison of MSC and normalised MPC and MPD for non-proportionally lightly (left) and highly (right) damped structures (○ MSC, ▷ MPC and □ MPD)..... 134
Figure 6.1 : Flowchart of damping optimisation algorithm based on BB-BC..... 142
Figure 6.2 : Damping optimisation for the first mode of the beam: Distribution of the damping material between damping patches at some iteration steps. 144
Figure 6.3 : Strain energy distributions of the structure for the first mode. 144
Figure 6.4 : The results for maximisation of the loss factors of the 1st mode..... 145
Figure 6.5 : Damping optimisation for the 2nd mode of the beam: Distribution of the damping material between damping patches at some iteration steps. 145
Figure 6.6 : Strain energy distributions of the structure for the second mode..... 146
Figure 6.7 : The results for maximisation of the loss factors of the 2nd mode..... 146
Figure 6.8 : Damping optimisation for the average loss factor of the first two modes of the beam: Distribution of the damping material between damping patches at some iteration steps..... 147
Figure 6.9 : Results for maximisation of the average loss factors of the first two modes of the structure (Key: ○ Mode 1, □ Mode 2 and Δ Average). 148

IDENTIFICATION, MODELLING AND OPTIMISATION OF STRUCTURES WITH PASSIVE DAMPING TREATMENTS

SUMMARY

Damping materials are used in many fields of engineering including automotive, aeronautics, aerospace, acoustics and domestic appliances in order to minimise undesirable vibrations and radiated noise as well as for eliminating the risk of high cycle fatigue failures of critical components. This is usually done by coating various parts of a structure using the so-called viscoelastic materials so as to provide additional damping. However, as the use of damping materials brings additional cost and additional weight to a structure, there is a strong need for designing and optimising those treatments for maximum benefit using minimum amount of material. This is still a difficult optimisation problem, mainly due to the difficulties associated with damping predictions of general structures and solving the optimisation problems. Furthermore, this process requires establishing reliable methods for the determination of the properties of damping materials and for the prediction of damping in structures. However, damping materials generally exhibit non-linear behaviour and the accurate predictions of the dynamic properties of composite structures, especially the damping levels, are quite difficult because of inherent coupling between nonlinear material behaviour. This thesis aims to improve and propose methods for the identification, modelling and optimisation of structures with passive damping treatments and presents new analytical, numerical and experimental studies on these topics.

Although the Oberst beam method is widely used for the measurement of the mechanical properties of viscoelastic or damping materials, the effects of measurement parameters including the adverse effects of non-contact excitation system used in this method, its modelling and minimisation are not explored elsewhere. Therefore, the effects of various parameters, such as the amplitude of the excitation, mounting conditions, input excitation type and the length of the test sample on measured data using an Oberst test rig are examined in an attempt to improve the accuracy of the estimated material properties. After that, the adverse electromagnetic effects due to non-contact exciters are investigated. For this purpose, extensive tests are carried out so as to determine the undesirable effects of electromagnetic excitation experimentally. Based on experimental evidence, electromagnetic field around the free end of the Oberst beam is modelled by some stiffness elements. Furthermore, a method is proposed for removing the adverse effects of the electromagnetic excitation in order to obtain more accurate material properties for uniform as well as composite beams. After this improvement, damping and elastic properties of the materials to be used in the theoretical models of structures with passive damping treatments are determined using the Oberst beam method.

In some circumstances, the approach used for the determination of damping levels of structures using measured data may not yield reliable answers in the sense that the identified damping levels may exhibit high level of uncertainty in practice. A systematic study on damping uncertainty is performed in this thesis. Damping uncertainty in the frequency domain estimation is explored when the data are contaminated by noise and when numerical damping via exponential windowing is introduced during the signal processing phase of the spectrum estimation. Some numerical simulations are performed first in order to assess the adverse effects of noise on damping estimations and resulting damping uncertainty is examined as a function of noise level in the data. Then, damping uncertainty due to the use of exponential windowing is investigated using experimental data. A relationship between damping uncertainty and the level of added numerical damping is presented when the so-called line-fit method is used for damping estimation from measured Frequency Response Functions (FRFs).

A Finite Element (FE) procedure based on the Modal Strain Energy (MSE) is presented for the purpose of modelling damped structures. Also, the theoretical background of a composite FE with damping capability is summarised and it is validated in this thesis. The damping capability validated here is based on a composite shell element with physical drilling degrees of freedom, where the structural damping is represented by means of complex element stiffness matrix of the individual layers. Such formulation allows modelling damped structures and performing modal analysis of the resulting complex eigenvalue problem. Then, some test cases are prepared and FRFs are measured in order to validate the procedure based on the MSE method and the composite FE. The material properties used in the models of the sample structures are identified experimentally using the Oberst beam method. The results obtained from the MSE method and the composite FE are compared with experimental results and the accuracy of both methods is assessed. Furthermore, the accuracy of the MSE method is examined as a function of damping level and mode shape complexity arising from non-proportional distribution of damping in structures. It is noted during this process that there is no universally accepted parameter for the quantification of mode shape complexity in the literature. A novel approach is proposed in this thesis in order to quantify mode shape complexity for general structures to overcome this void. The proposed new parameter is based on conservation of energy principle when a structure is vibrating at a specific mode during a period of vibration. The levels of complexity of the individual mode shapes of a sample structure are quantified using the proposed new parameter and the validity and the generality of the new parameter are demonstrated by comparing the results with those obtained by using other parameters available in the literature.

Finally, in order to meet the need for a cost-effective optimisation methodology, an efficient approach based on the Big Bang- Big Crunch (BB-BC) optimisation method is proposed. First, the BB-BC method is summarised and an optimisation methodology based on the BB-BC technique coupled with the damping prediction approach using the MSE method is introduced. After that, for the purpose of validating, the proposed optimisation methodology is used to maximise modal damping of a single mode of a structure whose optimised configurations are known for the individual modes. Then, the performance of the proposed optimisation procedure is demonstrated for the maximisation of damping levels for multiple modes at the same time. The optimisation methodology given in this thesis is a

heuristic population-based evolutionary (global) optimisation method and the convergence speed of this method is quite high. Overall, it is shown that the BB-BC technique coupled with the damping prediction approach based on the MSE method can be used effectively for optimisation of passive damping treatments applied to general structures in practice.

PASİF SÖNÜMLÜ YAPILARIN KARAKTERİZASYONU, MODELLENMESİ VE OPTİMİZASYONU

ÖZET

Sönüm malzemeleri, yapıların istenmeyen titreşimlerini ve yapılardan yayılan gürültüyü azaltmak ve kritik parçaların yorulmalarını önlemek için otomotiv, havacılık, uzay, akustik ve ev eşyaları gibi pek çok alanda kullanılırlar. Bu durum, yapıların çeşitli kısımlarına uygulanan ve genelde viskoelastik malzeme diye bilinen malzemelerin sağladığı ek sönüm ile sağlanmaktadır. Ancak, sönüm malzemelerinin kullanımı yapıya ek ağırlık ve maliyet getirdiğinden, bu uygulamaların minimum malzeme miktarı ile maksimum fayda sağlayacak şekilde optimize edilmesi gerekmektedir. Öte yandan, (genel) yapıların sönüm değerlerinin tahmini ve optimizasyonu ile ilgili zorluklardan dolayı söz konusu optimizasyon halen oldukça zor bir problemdir. Dahası, yapıların sönüm seviyelerinin optimizasyonu işlemi, sönüm malzemelerinin özelliklerinin belirlenmesi ve genel olarak yapıların sönüm değerlerinin tahmin edilmesi için güvenilir metodların kullanılmasını gerektirir. Ancak, kompozit yapıların dinamik özelliklerinin, özellikle de sönüm değerlerinin, doğru şekilde tahmini, sönüm malzemelerinin doğasından kaynaklanan lineer olmayan davranışlardan dolayı oldukça zordur. Tüm bu problem ve gereksinimleri dikkate alarak, bu tez pasif sönüm uygulamalı yapıların karakterizasyonu, modellenmesi ve optimizasyonu ile ilgili metodların geliştirilmesini ve önerilmesini ve bu konular üzerinde analitik, sayısal ve deneysel yeni çalışmalar sunmayı amaçlamaktadır.

Viskoelastik veya sönüm malzemelerinin mekanik özelliklerinin deneysel yoldan belirlenmesi için Oberst kiriş metodu yaygın olarak kullanılmasına rağmen, bu metodda kullanılan temassız tahrik sisteminin istenmeyen etkilerinin ortaya konulması, modellenmesi ve azaltılması dahil olmak üzere ölçüm parametrelerinin etkileri literatürdeki mevcut çalışmalarda incelenmemiştir. Bu yüzden, tahmin edilen malzeme özelliklerinin doğruluğunun seviyesini artırmak amacıyla bir Oberst test düzeneği kullanılmış, ölçülen veriler üzerinde tahrik genliği, bağlantı şartları, tahrik türü ve test numunelerinin uzunluğu gibi parametrelerin etkileri incelenmiştir. Daha sonra, Oberst test düzeneğindeki temassız sarsıcının istenmeyen elektromagnetik etkileri literatürde ilk defa bu tez kapsamında deneysel ve teorik olarak araştırılmıştır. Bu amaçla, çok sayıda test gerçekleştirilerek elektromagnetik tahrik sisteminin istenmeyen etkileri ortaya konulmuştur. Deneysel bulgular sonucunda, Oberst kirişinin serbest ucu etrafındaki istenmeyen elektromagnetik etki yay elemanlar kullanılarak modellenmiştir. Elektromagnetik etkiden kaynaklanan hatalar ortaya konulmuş, bu etkinin frekansa ve test numunelerinin uzunluğuna bağlı olarak değişimi de tezde sunulmuştur. Sonuçta, Oberst test düzeneğindeki ölçüm parametrelerinin optimize edilmesi gerektiği, Oberst kirişinin serbest ucu etrafındaki elektromagnetik etkinin sisteme ek bir kısıt getirdiği ve bu kısıtın yay elemanlarla modellenebileceği ortaya konulmuştur. Oberst çubuğunun ilk titreşim modunun elektromagnetik etkiden en fazla etkilendiği ve frekans (mod numarası) artıkça

elektromagnetik etkinin (dolayısıyla malzeme özelliklerindeki hatanın) azaldığı deneysel ve teorik olarak tespit edilmiştir. Ayrıca, kısa test numunelerinin kullanılması durumunda malzeme özelliklerindeki hataların azalacağı ortaya konulmuştur. Elektromagnetik sarsıcının istenmeyen etkisini (dolayısıyla malzeme özelliklerindeki hatayı) azaltmak için, test numunesinin elektromagnetik etki altındaki kısmının kısa olması gerekmektedir. Test numunesinin elektromagnetik etki altındaki kısmının kısa tutulamaması durumunda, daha doğru malzeme özellikleri elde etmek için elektromagnetik tahrikin istenmeyen etkilerini kaldırmaya yönelik hem homojen hem de kompozit kirişler için kullanılabilecek bir metod önerilmiştir. Tüm iyileştirmelerden sonra, pasif sönüm uygulamalı yapıların teorik modellerinde kullanılacak malzemelerin sönüm ve elastik özellikleri Oberst kiriş metodu kullanılarak belirlenmiştir.

Yapıların teorik modellerinin doğrulanmasında kullanılması başta olmak üzere, yapıların sönüm seviyelerinin deneysel yoldan tespit edilmesi sıkça gerekmektedir. Öte yandan, bazı durumlarda, yapıların sönüm değerlerinin belirlenmesi için kullanılan yöntemler tespit edilen sönüm değerlerinin yüksek düzeyde belirsizlik içermesi açısından güvenli olmayan cevaplar verebilirler. Bu tez kapsamında, yapıların sönüm belirsizliği üzerine sistematik bir çalışma gerçekleştirilmiştir. Daha açık olarak, analizi yapılan verilerdeki gürültünün ve spektrum hesaplamasında sinyallere uygulanan üstel pencereleme fonksiyonunun sayısal sönümünün tespit edilen sönüm değerleri üzerindeki etkisi literatürde ilk defa bu tez kapsamında incelenmiştir. Öncelikle, gürültünün sönüm tahmini üzerindeki istenmeyen etkilerini değerlendirmek için çok serbestlik dereceli (sönümlü) bir sistem ele alınmış ve bu sayısal sistem için çeşitli gürültü seviyelerinde frekans tepki fonksiyonları üretilmiştir. Gürültü içeren frekans tepki fonksiyonları analiz edilerek ilgili modların sönüm değerleri tespit edilmiştir. Neticede, sönüm belirsizliği verideki gürültü düzeyinin fonksiyonu olarak ortaya konmuştur. Daha sonra, üstel pencereleme fonksiyonundan kaynaklanan sönüm belirsizliğini incelemek için örnek bir yapı üzerinden çeşitli düzeylerde sayısal sönüm içeren çok sayıda frekans tepki fonksiyonu ölçülmüştür. Ölçülen frekans tepki fonksiyonları analiz edilerek yapının toplam modal sönüm değerleri belirlenmiş ve pencereleme fonksiyonundan kaynaklanan sayısal sönümün çıkartılmasıyla gerçek modal sönüm değerleri hesaplanmıştır. Tahmin edilen sönüm değerleri gerçek sönüm değerleriyle karşılaştırılarak, sönüm belirsizliği ile üstel pencereleme fonksiyonu dolayısıyla eklenen sayısal sönüm arasında bir ilişki sunulmuştur. Sonuçta, üstel pencereleme fonksiyonu dolayısıyla eklenen sayısal sönüm değerinin sistemin gerçek sönümüne eşit ve daha fazla olması durumunda, sönümdeki belirsizliğin önemli seviyelere ulaştığı görülmüştür. Burada frekans tepki fonksiyonları üzerinden sönüm tespiti doğrusal çizgi ve eğri uydurma yöntemleri kullanılarak yapılmış ve doğrusal çizgi uydurma yönteminin daha düşük belirsizlik değerleri verdiği görülmüştür.

Bu tezde sönümlü yapıların modellenmesi ile ilgili olarak iki farklı yöntem önerilmiştir. Öncelikle, modal (gerinim) enerji metoduna dayalı genel yapıları modellemeye uygun ve oldukça verimli bir prosedür sunulmuştur. Daha sonra, sönüm kabiliyetine sahip bir kompozit sonlu elemanın teorisi verilerek, bu elemanın formülasyonu sistematik bir yolla bu tez kapsamında doğrulanmıştır. Kompozit kabuk eleman, fiziksel anlamda yüzeyine dik yönde dönme serbestlik derecesine sahip homojen kabuk elemanların üst üste yığılmasıyla oluşturulmuştur. Sönüm kabiliyeti de kompleks direngenlik matrisi vasıtasıyla sağlanmıştır. Böyle bir formülasyon, sönümlü yapıların modellenmesini ve kompleks özdeğer probleminin

çözülmesiyle yapıların doğal frekanslarının, sönüm değerlerinin ve kompleks titreşim biçimlerinin elde edilmesini sağlamaktadır. Modal enerji metoduna dayalı prosedürü ve kompozit eleman formülasyonunu doğrulamak için bazı test numuneleri hazırlanmış ve test numuneleri üzerinde frekans tepki fonksiyonları ölçülmüştür. Test numunelerinin hazırlanmasında kullanılan sönüm malzemelerinin özellikleri Oberst kiriş metodu kullanılarak belirlenmiş, modal enerji metoduna dayalı sönüm tahmini yönteminden ve kompozit eleman formülasyonundan elde edilen sonuçlar deneysel verilerle karşılaştırılarak, iki yöntemin kabiliyetleri değerlendirilmiştir. Sonuçta, hem modal enerji metodunun hem de kompozit eleman formülasyonunun pasif sönümlü yapıların sönüm değerlerini yüksek hassasiyetle tahmin ettiği görülmüştür. Dahası, modal enerji metodunun doğruluğu, sönüm seviyesinin ve yapıya uygulanan orantısal olmayan sönüm uygulamasından kaynaklanan mod şekli komplekslik düzeyinin fonksiyonu olarak ilk defa bu tez kapsamında incelenmiştir.

Modal enerji metodu mod şekli komplekslik düzeyinin fonksiyonu olarak incelenirken, literatürde henüz mod şekli komplekslik düzeyini güvenilir bir şekilde ölçebilen ve literatürde genel olarak kabul görmüş tatmin edici bir yöntemin veya parametrenin olmadığı görülmüştür. Literatürdeki bu boşluğu doldurmak maksadıyla bu tez kapsamında mod şekli komplekslik düzeyini ölçmek için yeni ve özgün bir yaklaşım önerilmiştir. Önerilen yeni parametre, enerjinin korunumu ilkesine dayanmakta olup, sistemin direngenlik ve modal özelliklerini dikkate alarak hesaplanmaktadır. Örnek bir yapının mod şekillerinin komplekslik değerleri çeşitli modlar için hesaplanmış, sonuçlar literatürdeki diğer parametrelerin ürettiği sonuçlarla karşılaştırılmış ve yeni parametrenin geçerliliği ve üstünlüğü ortaya konulmuştur.

Son olarak, etkin ve verimli bir optimizasyon metodolojisi ihtiyacını karşılamak üzere Big Bang-Big Crunch (BB-BC) optimizasyon metoduna dayalı bir optimizasyon yöntemi sunulmuştur. Önce, BB-BC optimizasyon metodunun teorik alt yapısı verilmiş, BB-BC optimizasyon metodu ve modal enerji sönüm tahmini yöntemine dayalı bir optimizasyon yöntemi bu tez kapsamında ortaya konulmuştur. Daha sonra, önerilen optimizasyon yöntemi doğrulanmıştır. Bunun için, belli modlar da optimum konfigürasyonları belli olan bir yapı ele alınarak, o modlar için teker teker optimizasyon işlemi gerçekleştirilmiştir. Takibinde, önerilen optimizasyon yöntemi birden fazla modun sönümünün aynı anda maksimize edilmesi için kullanılmıştır. Optimize edilen konfigürasyonların sönüm değerlerinin, sönüm malzemesinin yapıya uniform kaplanması durumundaki sönüm değerlerinden oldukça yüksek olduğu görülmüştür. Burada önerilen optimizasyon prosedürü global bir metod olup, yakınsama hızı oldukça yüksektir. Sonuç olarak, modal enerji metoduna dayalı BB-BC optimizasyon tekniğinin pratikte pasif sönüm uygulamalarının optimizasyonunda etkin bir şekilde kullanılabileceği gösterilmiştir.

1. INTRODUCTION

Vibration and acoustic behaviour of machines are becoming increasingly more important as these properties are usually linked with the quality and customer satisfaction of many commercial products. Furthermore, the current trend in the design of machines is to provide more functionality, comfort and higher efficiency while reducing the cost. As a result, optimisation during the design stage is becoming increasingly more important in order to produce competitive products.

Passive damping materials such as viscoelastic materials are widely used in many industries including automotive, aerospace, aeronautics and domestic appliances as a means of reducing excessive vibration and structure borne noise. This is usually done by coating various parts of a structure using such materials so as to provide additional damping. However, using damping materials also brings their drawbacks as added weight and additional cost. Additional weight may also mean higher fuel consumption and more pollution in some applications. Therefore, there is a strong need for designing and optimising passive damping treatments for maximum benefit using minimum amount of material. It should be noted that this process also requires establishing reliable methods for determination of the properties of damping materials as well as for damping prediction of structures treated with damping materials.

1.1 Problem

Design parameters such as the locations, the amount of damping treatments and the material type determine the effectiveness of the passive damping application. Trial and error approaches are widely used as a traditional way of optimising these design parameters, usually using experimental prototypes for general structures. However, optimisation via trial and error fashion can easily become cumbersome, very time consuming and prohibitively expensive as this approach requires building many prototypes due to there being so many alternative combinations of damping materials, damping treatment locations and the amount of material that can be used.

As an alternative to trial and error approaches, engineering structures are sometimes treated with damping materials using the information obtained from modal properties of the untreated or undamped structures in practice. However, this does not usually provide the optimised condition since the dynamic properties of the damped structure usually differ from those of the undamped structure. Therefore, a cost-effective theoretical or numerical methodology is required in order to be able to model and optimise damping treatments of structures in an efficient way. In practice, the emphasis is usually on optimising the locations and sizes of damping treatments.

Although mass and stiffness optimisations of undamped or lightly damped structures are quite common, studies on modelling structures with passive damping treatments and optimisation of passive damping treatments in the literature are relatively rare. Furthermore, the studies on modelling and optimisation of damping treatments in the literature are mainly related to systems with special geometries. One of the reasons for this is due to the difficulty in modelling the highly nonlinear damping materials in damping predictions and optimisations. One other difficulty in using known global optimisation methods is related to unacceptable computational time required to optimise damping treatments applied to structures with large number of degrees of freedom. Another difficulty is related to systems with non-proportional damping treatments which result in complex mode shapes, a situation that leads to further difficulties in modelling, analysis and optimisation of such systems.

Accurate damping and elastic properties of viscoelastic materials are required to develop theoretical models of structures with passive damping treatments for the purposes of damping prediction and optimisation. As damping materials generally exhibit non-linear behaviour and their mechanical properties (Young's modulus, loss factor) also depend on both frequency and temperature, special experimental procedures are needed to determine the mechanical properties of such materials. Although there are some standard methods including Oberst beam method for identification of damping materials, it is still difficult to determine material properties with high accuracy due to the adverse effects of sensors and measurement parameters. Experimental identification of the damping levels of structures is often required for many purposes including validation of damping models in structural analysis. It is worth stating here that there is also some difficulty in identification of damping levels of structures using experimental data in the sense that the identified

damping levels may exhibit high level of uncertainty due to noise and signal processing parameters.

1.2 Literature Review

In this section, a literature survey is performed on the methods for the determination of the dynamic properties of damping/viscoelastic materials (Section 1.2.1); experimental identification of damping levels of structures including damping uncertainty (Section 1.2.2); damping prediction methods for structures with passive damping (Section 1.2.3); quantification of mode shape complexity due to non-proportional damping treatments (Section 1.2.4); and optimisation methods/methodologies including damping optimisation (Section 1.2.5).

1.2.1 Material testing

1.2.1.1 Material testing methods

Materials used for passive damping treatments generally exhibit non-linear behaviour and their mechanical properties (Young's modulus, loss factor) also depend on frequency and temperature. Therefore, special experimental procedures are needed to determine the mechanical properties of these materials. There are standard methods for characterisation of both thin-layered damping materials and viscoelastic supports in practice.

The Oberst Beam Method (OBM) described in ASTM E 756 [1] and SAE J 1637 [2] standards and the Geiger plate test defined in SAE J 671 standard [3] are the main standard methods that can be used to measure dynamic properties of thin-layered damping materials. OBM is accepted as the classical method for the characterisation of damping materials based on Frequency Response Function (FRF) measurements on some typical beams described in ASTM E 756 standard [1]. This method is often used for testing various materials including metals, enamels, ceramics, rubbers, plastics, reinforced epoxy matrices and woods. On the other hand, a steel plate is used and damping of the structure is determined by measuring the system's decay rate in the Geiger plate test [3].

The so-called direct, indirect and driving point methods defined in ISO 10846-2 [4], -3 [5] and -5 [6] standards, respectively, are used to determine the dynamic properties of viscoelastic supports. Also, ISO 4664-2 standard [7] specifies methods for the determination of dynamic properties of vulcanized or thermoplastic rubbers in shear over a wide temperature range at low frequencies and at comparatively low strains while ASTM D 945 standard [8] covers the use of the so-called Yerzley mechanical oscillograph for measuring mechanical properties, such as resilience, dynamic modulus, static modulus, kinetic energy and creep of rubber vulcanizates when the deformations are considered small.

1.2.1.2 Oberst beam method

The first important work on measurements and identification of damping levels (loss factors) of composite structures is published by Oberst in 1952 [9]. He derived a set of equations for free-layer damping treatment. Although some other associated works are done by Gross [10], Ross et al. [11], Kerwin [12] and DiTaranto [13], mainly the procedure suggested by Oberst are used in OBM.

The use of contacting transducers and shakers is not recommended in OBM as they introduce artificial mass loading and damping, significantly reducing the quality of the results in OBM [14]. Therefore, it is strongly recommended in the literature that non-contact response transducers and non-contact electromagnetic excitation should be used in OBM [1-2, 14]. If a non-ferromagnetic material is used as the material of the base beam, it is necessary to glue a small piece of ferromagnetic material for providing magnetic excitation. Although the OBM is referenced in some standards [1-2] and it is widely used in many scientific studies [15-33], detailed information in the literature on how to perform a successful Oberst beam experiment is very limited.

The drawbacks of the classical Oberst beam technique are discussed in some studies [14, 34] and some new modified Oberst methods are also suggested. Wojtowicki et al. [14] proposed a method to increase the precision of the measurement. Mainly, they replaced the classical cantilever Oberst beam by a double sized free-free beam of twice the length excited at its midpoint thereby allowing half of the beam to be modelled with clamped-free boundary conditions. The analysis is based on an FRF measured between the imposed velocity at the centre (measured with an accelerometer) and an arbitrary point on the beam (measured with a laser

vibrometer). Liao and Wells [34] proposed a modified Oberst beam technique (for non-stiff materials) with some advantages over the conventional Oberst beam technique: the layer properties can be evaluated at any frequency; the base beam can be partially covered; and it does not require the complex modulus of the base beam to be fairly constant around the resonance frequencies analysed to yield accurate results.

1.2.2 Experimental identification of damping levels of structures

There are various methods for the determination of damping levels of structures using experimental data [16, 35-43]. These methods can be broadly divided in three main groups: (i) time-domain decay-rate methods, (ii) frequency-domain modal analysis curve-fitting methods and (iii) other methods based on energy and wave propagation [42, 44]. Logarithmic decrement and step-response methods are two examples from group (i), magnification factor, the half-power bandwidth, the circle-fit and the line-fit methods are some of the well-known frequency-domain methods from group (ii) whereas power input method is an example from group (iii).

Not surprisingly, the amount of published work on damping identification in the literature is huge. In frequency domain, for example, there are methods based on Single Degree of Freedom (SDOF) modal analysis methods such as circle-fit [36] and line-fit [37] and Multi Degree of Freedom (MDOF) modal analysis methods [35, 38, 45]. These methods can estimate modal damping levels using a single FRF. Single Input Multi Output (SIMO) methods [46] and Multi Input Multi Output (MIMO) methods [35] that are based on multi FRFs are also developed, studied and widely used in the literature for damping identification. The frequency domain methods mentioned above are also called Frequency Response Methods as they are utilising spectrums or FRFs obtained by transforming the time-domain data via Discrete Fourier Transform-DFT [16, 35, 47]. It is known that the DFT is commonly suitable and has good accuracy for analysing stationary signals. However, the frequency domain methods based on DFT have some drawbacks [48-52] for non-stationary signals. Short-Time Fourier Transform (STFT), on the other hand, is used to eliminate some of the limitations of DFT related to non-stationary signals by dividing the signal into blocks and computing the spectrum of those blocks with the help of a sliding window [50-53]. More advanced approach, Wavelet Transform

(WT), is used in an attempt to overcome the weaknesses of the methods based on Fourier Transform [52, 54-57]. WT is an approach based on decomposing a time signal into its constituent parts. The shape and magnitude of these components depends on the selected wavelet [52, 58]. Damping identification methods based on WT are also proposed in the literature [55, 57]. For determination of modal parameters of a structure subjected to the ambient loading, WT method is generally applied in conjunction with the so-called Random Decrement Technique (RDT) to identify the modal parameters [44, 59]. As far as the WT is concerned, the time and frequency resolutions of the WT may have huge effects on the identification accuracy [48]. Also, there are some modified WT methods to reduce the so-called end-effect [60-61] and some WT methods are very resistant to noise [62-63].

Time-domain identification approaches are also used in the literature, especially for those cases where no input but only response measurements are available. However, it is known that the noise levels of the response data may have significant adverse effects on the accuracy of the identified damping levels. Also, the time domain approaches are generally accepted to be computationally expensive compared to the alternative [48]. On the other hand, time-domain decay-rate methods, such as logarithmic decrement method, are known to be effective if a single mode of vibration can be isolated from others. Similarly, the power input method is quite effective for obtaining frequency-averaged damping levels of structures under steady state vibration [42].

The frequency response based methods, including circle-fit [36] and line-fit [37] methods, are widely used in practice for damping identification from measured FRFs. These methods have high accuracy in identification of damping levels of structures when measurements are made properly. However, when the FRFs are to be measured under impact excitation, the oscillations created by an impact may not decay to negligible level within the measurement period, especially for the lightly damped structures. In such cases, an exponential window often needs to be applied so as to minimise the leakage effects [64]. However, applying an exponential window to transient signals inevitably introduces the so-called numerical damping. Although, this numerical damping can be removed later, it can introduce high level of damping uncertainty especially when the numerical damping is significantly higher than that of the actual damping level.

Available literature on damping uncertainty associated with damping identification is very limited and the majority of the available work on damping uncertainty is mainly concerned with the effect of damping uncertainty on system response so as to establish more realistic prediction bounds [65-68]. It should be noted, however, that quantifying the damping uncertainty itself is a topic which has not attracted the required attention in spite of the fact that there is a real need for such information in practice. Uncertainties associated with damping estimation is especially important for lightly damped structures as the error introduced by various sources can be very significant compared to the actual level of damping. A few existing approaches on damping uncertainty broadly deal with estimation of damping uncertainty based on deviation of the raw data used in the analyses from the expected trend [38]. Although it is not directly related to damping uncertainty, Jokinen et al. [69] dealt with the problems associated with windowing and uncertainty in computing the power spectral density estimates of a signal. Also, Yan et al. [48] proposed an identification method based on wavelet transform to consider the uncertainty effect on modal parameters. Associated with uncertainty, De Troyer et al. [70] proposed an approach to determine the variances on the resonance frequencies and damping ratios. They calculated uncertainties of the resonance frequencies and damping ratios for some noise levels. Pintelon et al. [71] presented a numerical method for determination of the uncertainty on the modal parameters in operational modal analysis.

1.2.3 Damping prediction

Accurate predictions of the dynamic properties of composite structures, especially the damping levels, are quite difficult because of inherent coupling between nonlinear material behaviour and other nonlinear effects [47, 72-75]. Although there are some rheological models such as Maxwell, Kelvin-Voigt and the standard linear solid models for viscoelastic materials where springs and dampers are arranged in series and/or parallel in order to determine their stress or strain interactions [76-78], computational methods [74, 79-81] are widely used for modelling damped structures. On the other hand, although Statistical Energy Analysis-SEA [80-81] can be used for creating structural models for the purpose of vibration and acoustic analyses of structures, Finite Element (FE) methods [74, 79] are widely used to predict damping levels of structures in practice.

There are basically three approaches for damping modelling in finite element applications [79], namely; Direct Frequency Response (DFR), Modal Strain Energy (MSE) and Complex Eigenvalue (CE) methods. In the DFR method [82], FRF matrix is obtained by inversion of the dynamic stiffness matrix. Then, damping values can be determined by analysing the FRFs. The DFR method is very costly in terms of computation time as it requires computation of the FRF matrix at individual frequencies. Rastogi [82] in his paper evaluated the capabilities and limitations of the DFR method and modal frequency response analysis using a FE program. In the MSE method [79], the eigenvalue problem of the actual (damped) system is not solved. Instead, the so-called Normal Modal Analysis [79] of the undamped system is performed to compute the strain energy ratios for individual modes in order to estimate the modal damping levels. During this process, it is assumed that the mode shapes of the damped system are the same as those of the undamped system. In the CE method [83-84], on the other hand, the complex eigenvalue problem is needed to be solved without simplifying assumption. Although the CE method is a known approach for the predictions of damping levels of structures, it is computationally more expensive the MSE method.

In the literature, it is seen that damping levels of structures in general are either determined by the MSE method [79, 85-86] or other formulations that are specifically designed for special structures such as beams and plates. For example, Rao et al. [85] in their paper used the MSE method together with the FE approach and estimated the modal parameters of simply supported damped beams. Zhang and Chen [86] used a FE procedure based on the MSE method for predicting the modal loss factor of composite beams. Cortés and Elejabarrieta [87] formulated a homogenised model for the flexural stiffness to investigate structural vibration of flexural beams. Moreira and Rodrigues [88] developed a model to simulate the dynamic response of composite plates. Plagianakos and Saravanos [89] presented a FE based formulation for predicting modal damping and natural frequencies of curvilinear composite shell structures while modal loss factors are calculated using the energy (dissipation) method.

1.2.4 Quantification of non-proportional damping

Non-proportional damping distribution within a structure causing non-uniform energy dissipation results in complex mode shapes [90-98]. It is known that complex modes can also arise from gyroscopic effects, aerodynamic effects, wave propagation and non-linear structural behaviour [96, 99-102]. There are many situations where the level of mode shape complexity is to be quantified. For example, there are various methods in structural dynamics that are based on the assumption that the mode shapes are normal (real) or close to being normal. These methods are mainly those dealing with applications of modal analysis such as the transformation of complex modes into real ones, response computation and damping estimation [35, 103-108]. These methods are being used in practice even though the actual mode shapes are not normal or may not be close to being normal. It is known that the reliability and the accuracy of these methods are adversely affected as the mode shapes become more and more complex. Therefore, there is a need for the quantification of mode shape complexity in order to establish the reliability and the accuracy of such methods as a function of the level of mode shape complexity. Quantification of mode shape complexity is also needed in other applications, for example, correlation and comparison studies where the similarity of mode shapes from different models are to be determined.

Several parameters have been proposed in the literature to quantify the level of mode shape complexity although they are not derived from the fundamental definition of a mode shape being complex. The main parameters utilised to measure the mode shape complexity in the literature are: Mean Phase Deviation (MPD), Modal Correlation Coefficient (MCC), Modal Phase Collinearity (MPC), Mode Complexity Factor 1, 2 and 3 (MCF1, MCF2 and MCF3). MPD [105-106, 109] is actually an indicator of phase scatter of a mode shape rather than being a direct parameter to quantify the level of complexity of a mode shape. Similarly, MCC [99] is only a correlation function between two vectors (the real and imaginary parts of the eigenvector) while MPC [49, 98, 105, 109-112] is associated with the correlation of phase angles. Also, as stated by Ewins [35], MCF1, MCF2 and MCF3 [35, 38, 101] are not established as the universally-accepted indicators.

There are also some other parameters suggested in the literature for quantifying the non-proportional damping in a structure [113-120], noting that mode shape

complexity is attributed to the non-proportional damping. Those parameters are based on relative magnitudes of coupling terms in the modal damping matrix and system response, the difference between the optimal complex modes and their corresponding normal modes, the minimum and the maximum of the eigenvalues of the modal damping matrix, etc. [96, 97, 102, 108, 113-120]. These parameters are mainly used to determine the validity of a proportional damping assumption. In general, the parameters suggested in the literature for quantifying the level of non-proportional damping yield different values for the same mode of a system.

1.2.5 Optimisation

1.2.5.1 Optimisation techniques

Optimisation can be defined as the process of obtaining the best result under given constraints [121]. There is no unique optimisation method applicable to all problems. Depending on the problem, appropriate optimisation technique is selected and the problem is adapted to the optimisation method selected. Optimisation problem can be classified in various ways [121-125]. Depending on whether constraints exist or not, any optimisation problem can be classified as constrained or unconstrained. One other classification of optimisation problems is based on the nature of expressions for objective function and constrains. If the objective function and constraints are linear functions of design variables, in this case the optimisation problem is called linear optimisation or linear programming. If any of the functions among the objective and constraints is nonlinear then the optimisation problem is known as nonlinear optimisation problem. Also, optimisation can be local or global. In the case of global optimisation problems [125], global extremes are searched. That is, global optimisation requires the arrival to the best possible decision in any given set of circumstances [126].

In the literature, there are many unconstrained and constrained optimisation methods [121-125]. The unconstrained minimization methods are iterative in nature, i.e., they start from an initial trial solution and proceed toward the minimum point in a sequential manner. The unconstrained optimisation methods can be divided into two broad categories according to whether the derivatives of the function are required: direct search and descent methods [121, 122]. The direct search methods such as

random and grid search methods require only the objective function values but not the partial derivatives of the function in order to find the minimum; hence they are often called the non-gradient methods. On the other hand, the descent techniques such as steepest descent and Newton's methods require, in addition to the function values, the first and in some cases the second derivatives of the objective function. The constrained optimisation problem can be classified into two broad categories as direct methods and indirect methods [122]. In the direct methods, the constraints are handled in an explicit manner; on the other hand, in most of the indirect methods, the constrained problem is solved as a sequence of unconstrained minimisation problems. It should be noted that most of the constrained and unconstrained optimisation methods in the literature are suitable for finding local minimums.

Nature is usually considered as the main source of ideas for proposing global optimisation methods. Genetic algorithms, simulated annealing, particle swarm optimisation method, ant colony optimisation method, TABU search optimisation method, brunch and bound, clustering methods, Big Bang–Big Crunch search and stochastic global optimisation methods (Kushner’s and Stuckman’s methods and controlled random search) are the main global optimisation methods in the literature [121-127]. Among these methods, genetic algorithms are widely used to tackle hard search and optimisation problems. These methods are random search techniques that basically model the basic principles and mechanisms of Mendelian genetics and mechanisms of natural evolution theory along with population genetics. On the other hand, Kushner’s method is only for one-dimensional problems while Stuckman’s method is an extension of Kushner’s method and it is for multi-dimensional problems.

1.2.5.2 Damping optimisation

As stated before, passive damping materials such as viscoelastic materials are widely used in many industries as a means of reducing excessive noise and vibrations [16, 72, 128-130]. Although mass and stiffness optimisations of structures are quite common, damping optimisation studies in the literature are relatively rare. Furthermore, the studies on optimisation of damping treatments in the literature are mainly related to systems with special geometries. For example, Hajela and Lin [131] and Trindade [132] studied optimisation of damping treatments on beams using

genetic algorithms. Ro and Baz [133] studied optimisation of the position of active constrained damping layers on a plate using steepest descend method. On the other hand, Subramanian et al. in their study [134] applied damping treatments to different regions of vehicle panels by simply considering the modal strain energy of untreated structure to determine the optimal parameters. Recently, Chia et al. [135] used the so-called cellular automata method to obtain an optimal coverage of constrained layer treatments on structures. It is seen that although some methodologies seem to be applicable for relatively simple structures, it is still difficult to utilise them for damping optimisation of general structures. One of the reasons for this is due to the difficulty in modelling the highly nonlinear damping materials in damping predictions and optimisations. One other difficulty in using conventional global optimisation methods such as genetic algorithms is related to unacceptable computational time required to optimise damping treatments applied to structures with large number of degrees of freedom.

Although the genetic algorithm [127] appears to be one of the widely used global optimisation approaches to solve various optimisation problems, they may suffer from premature convergence, convergence speed and execution time problems. On the other hand, recently introduced Big Bang-Big Crunch (BB-BC) method [126] for global optimisation seems to be effective and faster than others. Like genetic algorithm, this method is a random search method and its superiority has been demonstrated over other heuristic population-based search techniques when employed to perform global optimisation tasks [For example, 126, 136-138].

1.3 Objectives of The Thesis

The main objectives of this thesis are to improve, develop and propose methods/approaches in order to identify, model and finally optimise structures with passive damping treatments. The specific objectives of this thesis can be summarised as:

i) Assessment of the available methods for the estimation of dynamic properties of damping materials,

ii) Improve the method or methods so as to obtain dynamic properties of materials (damping and elasticity modulus) with better accuracy,

iii) Identify and quantify the levels of uncertainty due to noise and signal processing parameters in measured damping levels of structures,

iv) Present damping prediction methods for modelling structures with passive damping treatments in an effective way and validate the methods using experimental data,

v) Propose an approach for quantification of mode shape complexity due to non-proportional damping of passive damping treatments, and

vi) Propose an effective methodology to optimise passive damping treatments for general structures.

1.4. Outline of The Thesis

After a brief introduction of the subject, the problem is stated, a literature survey is presented and the objectives of the thesis are outlined in Chapter 1. Chapter 2 is devoted to the identification of the dynamic properties of damping materials. The effects of various parameters, such as the mounting conditions and the length of the test sample on measured data using an Oberst test rig are examined. The electromagnetic effects created by non-contact exciters are studied experimentally and the electromagnetic field around the free end of the Oberst beam is modelled. A method is proposed to remove the adverse effects of the electromagnetic excitation. The material properties of some commercially available materials are determined using the improved test rig.

The difficulties in the identification of the damping levels of structures in the frequency domain estimation methods are examined in Chapter 3. Some numerical simulations are performed in order to assess the adverse effects of noise on damping estimations and the resulting damping uncertainty is examined as a function of noise level in the data. Then, damping uncertainty due to the use of exponential windowing is investigated using experimental data. A relationship between damping uncertainty and the level of added numerical damping is presented.

Chapter 4 is devoted to damping prediction. A FE procedure based on the MSE method is presented for the purpose of modelling damped structures. Also, the theoretical background of a composite FE with damping capability is summarised. The method based on the MSE method and the composite FE formulation are

validated by comparing the theoretical predictions with experimentally identified natural frequencies and the associated damping levels using a few test structures. Also, the accuracy of the MSE method is examined as a function of damping level and mode shape complexity arising from non-proportional distribution of damping in structures. Furthermore, a novel approach is proposed in order to quantify mode shape complexity due to passive damping treatments after reviewing the existing methods for quantification of mode shape complexity in Chapter 5.

An approach for optimisation of passive damping treatments that can be applied to general structures is presented in Chapter 6. For this purpose, an optimisation methodology based on the BB-BC technique coupled with the damping prediction approach using the MSE method is introduced. The performance of the proposed optimisation procedure is demonstrated for the maximisation of damping levels for single and multiple modes and its effectiveness for damping optimisation is assessed. After all, some concluding remarks and suggestions for future work are given in Chapter 7.

2. IDENTIFICATION OF DAMPING MATERIALS

2.1 Introduction

Designing and optimisation of passive damping treatments require establishing reliable methods for the determination of the properties (damping level and elasticity modulus) of damping materials to be used for the prediction of damping levels of structures. However, damping materials generally exhibit non-linear behaviour [16] and the accurate predictions of the dynamic properties of composite structures, especially the damping levels, are quite difficult because of inherent coupling between nonlinear material behaviour. Therefore, special experimental procedures are needed to determine the mechanical properties of these materials. The Oberst Beam Method (OBM) is widely used for this purpose in practice [1]. However, detailed information about how to perform a successful Oberst beam experiment is quite limited in the literature. In this chapter, it is aimed to suggest a methodology to improve OBM for the identification of damping materials with good accuracy. Then, the damping and the elastic properties of materials to be used in the theoretical models of the test structures with passive damping treatments are determined using OBM.

This chapter is organized as follows. After a brief theoretical background for damping materials and the damping mechanism is presented, OBM is described. Then, the effects of various parameters, such as the amplitude of the excitation, mounting conditions, input excitation type and the length of the test sample on measured data using an Oberst test rig are examined in an attempt to improve the accuracy of the estimated material properties. Then, electromagnetic effects created by non-contact exciters are studied. For this purpose, extensive tests are carried out so as to determine the adverse effects of electromagnetic excitation experimentally. Based on experimental evidence, electromagnetic field around the free end of the Oberst beam is modelled by some stiffness elements. Furthermore, a method is proposed for removing the adverse effects of the electromagnetic excitation in order

to obtain more accurate material properties for uniform as well as composite beams. After this improvement, damping and elastic properties of materials to be used in the theoretical models of structures with passive damping treatments are determined using OBM.

2.2 Damping Materials

Damping can be described as the conversion of mechanical energy of a structure into thermal energy, i.e., the amount of energy dissipation is a measure of the damping level of a structure [16, 139-140]. There are many forms of damping such as Coulomb friction, joint damping, fluid viscosity, air damping, particle damping, magnetic hysteresis and piezoelectric damping. The most common form of damping utilised to solve noise and vibration related problems is material or viscoelastic damping, usually applied as passive damping treatments to structures [1, 16, 139-140].

Damping or viscoelastic materials are used in many applications including domestic appliances and vehicles in order to reduce structureborne vibrations [72, 75]. Amorphous polymers, semi crystalline polymers, biopolymers, metals at very high temperatures and bitumen materials are some examples of viscoelastic materials. Polymeric materials have long molecular chains and carbon atoms join strongly together. Long chains can be linked strongly or weakly according to composition and processing of the polymer. Damping arises from relaxion and recovery of the polymer network after it has been deformed. It is noted that temperature and frequency have strong effects on the properties of viscoelastic materials [16, 76-77, 139, 141].

2.2.1 Viscoelasticity

Most materials used in engineering are assumed to behave according to Hooke's linear elasticity theory under small deformations, i.e., there is a linear relationship between stress and strain as $\sigma = E\varepsilon$ where σ, ε and E are stress, strain and modulus of elasticity, respectively. Such materials are called elastic materials, and these materials strain instantaneously when stretched and just as quickly return to their original state once the stress is removed. Overall, a purely elastic material can be defined as the material in which all the energy stored in the sample during loading

is returned when the load is removed. On the other hand, in contrast to an elastic material, a purely viscous material (no stiffness component) does not store energy. All the energy is dissipated as pure damping once the load is removed. In this case, the stress is proportional to the rate of the strain as $\sigma = \mu\left(d\varepsilon/dt\right)$ where μ is the viscosity. Viscoelastic materials have both elastic and viscous properties and, as such, exhibit time dependent strain. Some of the energy stored in a viscoelastic system is recovered upon removal of the load, and the remaining energy is dissipated in the form of heat [76-77, 139, 141].

Cyclic stress-strain curves vs. time for typical elastic, viscous and viscoelastic materials are given in Figure 2.1. The stress and strain curves for elastic materials move completely in phase while there is $\pi/2$ radian phase difference between stress and strain in the case of viscous material. On the other hand, with cyclic stress at frequency ω, there is a phase ϕ between stress and strain in the case of the viscoelastic material where ϕ is between 0 and $\pi/2$ [139-140]. This phase angle is also a measure of damping in the material [72] as explained in the next section.

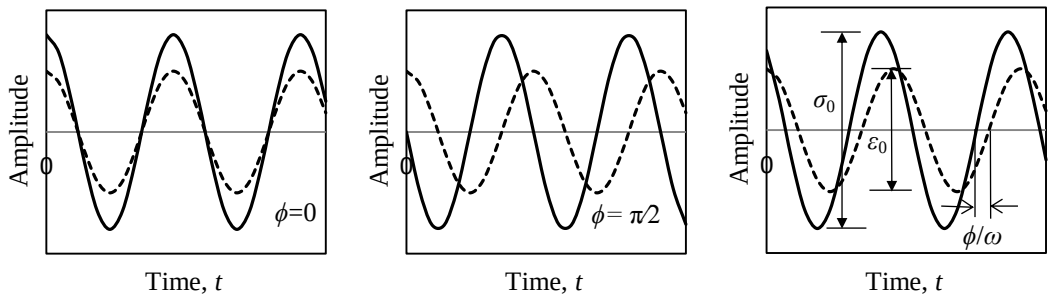

Figure 2.1 : Cyclic stress-strain curve vs. time for elastic (left), viscous (middle) and viscoelastic (right) materials (Key: --- $\varepsilon(t)$ and — $\sigma(t)$).

2.2.2 Vibration damping

2.2.2.1 Hysteresis loop

Under cyclic loading at constant frequency ω and amplitude σ_0 (referring to Figure 2.1), the stress for a viscoelastic material can be expressed as follow.

$$\sigma\left(t\right) = \sigma_0 e^{j\omega t} \tag{2.1}$$

The resulting strain for the viscoelastic material will be

$$\varepsilon(t) = \varepsilon_0 e^{j(\omega t - \phi)} \tag{2.2}$$

where σ_0 and ε_0 are the amplitudes of the stress and strain and $j = \sqrt{-1}$. The hysteresis of the material can be defined by plotting the input stress $\sigma(t)$ versus responding resulting strain $\varepsilon(t)$ for one cycle of motion as in Figure 2.2. The elliptical shape shown in Figure 2.2 is defined as the hysteresis loop. The area captured within the hysteresis loop, ΔU is equal to the dissipated energy per cycle of harmonic motion by the material while U here represents the maximum stored energy [139]. It should be noted that the stress-strain curve of a purely elastic material (or spring) is a line where ΔU=0.

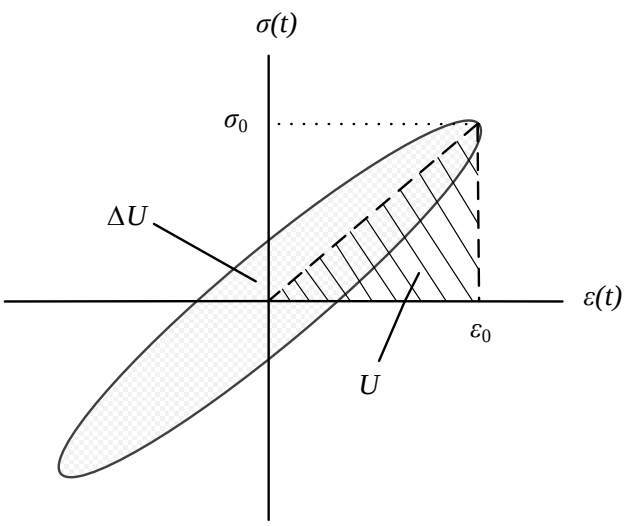

Figure 2.2 : Hysteresis loop for a viscoelastic material under harmonic loading.

For reasonable levels of damping, the relationship between the structural damping ratio (or material damping) and associated energy terms in Figure 2.2 is given as [74]

$$\eta = \frac{1}{2\pi}\frac{\Delta U}{U} \tag{2.3}$$

where η is also known as loss factor. This relation can also be written as follow.

$$\eta = \frac{\oint \sigma d\varepsilon}{\pi \sigma_0 \varepsilon_0} \tag{2.4}$$

2.2.2.2 Complex modulus

Modulus of a viscoelastic material can be represented by a complex (or dynamic) quantity, possessing both the stored and dissipative energy components. Complex stress and strain can be written as follows

$$\sigma(t) = \sigma_0 e^{j\omega t} = \sigma_0 \left(cos(\omega t) + j\, sin(\omega t) \right) \tag{2.5}$$

$$\varepsilon(t) = \varepsilon_0 e^{j(\omega t - \phi)} = \varepsilon_0 \left(cos(\omega t - \phi) + j\, sin(\omega t - \phi) \right) \tag{2.6}$$

Complex modulus of the material can be written as follows

$$E^* = \frac{\sigma_0 e^{j\omega t}}{\varepsilon_0 e^{j(\omega t - \phi)}} = \frac{\sigma_0}{\varepsilon_0} cos(\phi) + j \frac{\sigma_0}{\varepsilon_0} sin(\phi) = E' + jE'' \tag{2.7}$$

where E^* is the complex modulus, E' and E'' are known as the storage and the loss modulus, respectively [16, 142]. The real part of this complex term, storage modulus, relates to the elastic behaviour of the material. The imaginary component (loss modulus) relates to the viscous behaviour of the material, and it is related to the energy dissipation ability of the material. Complex modulus also can be written as

$$E^* = E' \left(1 + j \frac{E''}{E'} \right) = E' (1 + j\eta) \tag{2.8}$$

where η is the loss factor as defined before. The loss factor is also related to the phase angle, ϕ via $\eta = \tan(\phi)$ as can be seen from Equations 2.7 and 2.8. The complex modulus indicates that the stiffness and damping properties of a material can be represented by single degree of freedom hysteretic model as in Figure 2.3 where k^* and m are complex stiffness and mass, respectively, and $f(t)$ and $x(t)$ represent time varying force and displacement. Also, the complex modulus can be defined as a function of temperature and frequency. Provided that the motion is harmonic, the hysteretic model is preferred when modelling structures with passive damping treatments as the hysteretic model has a better representation of the actual behaviour of viscoelastic materials in which damping is proportional to strain and is independent of rate [74, 139-140].

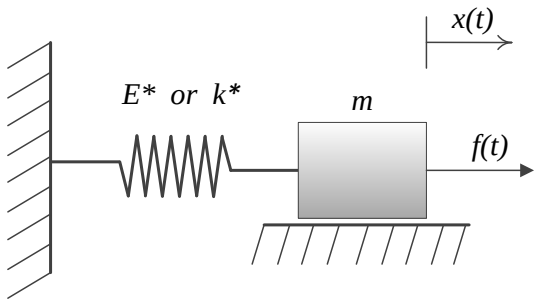

Figure 2.3 : Hysteretic model or complex modulus approach.

2.2.3 Effects of environmental factors

Effective noise and vibration control requires good understanding of the variation of damping properties with environment [16]. Properties of viscoelastic materials are influenced by many parameters, such as temperature, frequency, dynamic strain rate, static preload, time effects (creep and relaxion), aging, oil exposure, high temperature exposure, vacuum and pressure. The viscoelastic damping arises from the polymer network after it has been deformed as stated before. Both temperature and frequency effects have a large bearing on the molecular motion and hence on the damping characteristics [47]. As a result, a viscoelastic material can be in various phases over the broad temperature and frequency ranges in which it is used.

Changes in storage modulus, loss modulus and loss factor a typical viscoelastic material at constant frequency are given in Figure 2.4. In the glassy region, the polymer chains are rigidly ordered and crystalline in nature, hence possessing glass-like behaviour. Storage modulus is at its highest level for the material in this region, and damping levels are typically low. In the transition region, the viscoelastic material goes through its most rapid rate of change in stiffness and possesses its highest level of damping performance. In this region, the long molecular chains of the polymer are in a semi-rigid and semi-flow state, and are able to rub against adjacent chains. These frictional effects result in the mechanical damping characteristic of viscoelastic materials. In the rubbery region, the material reaches a lower level in stiffness. Damping is at a lower level. A material selected to exist in this region is ideally suited for such devices as isolators or tuned mass dampers because the modulus varies only slightly with changes in temperature and frequency [16, 47, 139, 142]. In the flow region, the material is like a fluid.

An important property of viscoelastic materials is that frequency and temperature have opposite effects. For example, while increasing temperature results in decreasing storage modulus of the viscoelastic material, increasing frequency results in increasing storage modulus.

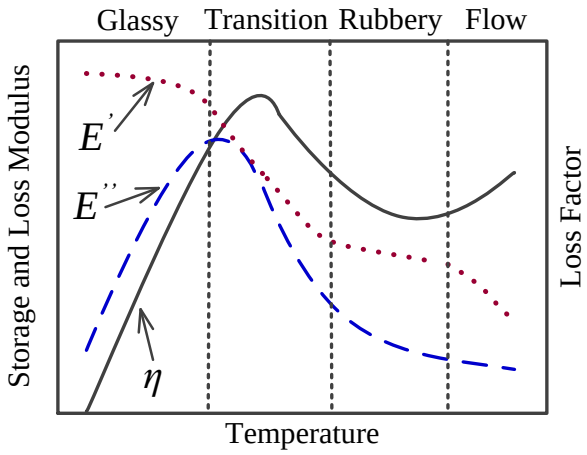

Figure 2.4 : Variation of complex modulus with temperature (constant frequency) for a typical viscoelastic material.

2.2.4 Passive damping treatments

Amount of the energy dissipated by damped structures depends to a high degree on the mechanism of deformation that is induced in a viscoelastic material. Thus, arrangement of layers plays an important role. The most common configuration is the one in which damping material is glued on the base layer. This is known as free layer damping or unconstrained layer treatment (Figure 2.5). This approach provides vibration control of the base layer through extensional damping. One of the other most common configurations comprises viscoelastic core covered with usually metallic sheet and bonded to vibrating layer or constrained layer (Figure 2.5). In this configuration (known as constrained layer treatment), shear deformations are very important in the core when face sheets undergo extension. Constrained layer treatment is more costly than that of the free layer. Although these aforementioned viscoelastically damped layers [16] are widely used to provide damping to various types of structures in practice, there are also some other damping applications such as high temperature laminates, damping treatment with air gap, smart damping materials (i.e., piezoelectric materials) and frictional materials such as fiberglass [75, 129, 142] to improve vibration and acoustic characteristics of machines for special purposes.

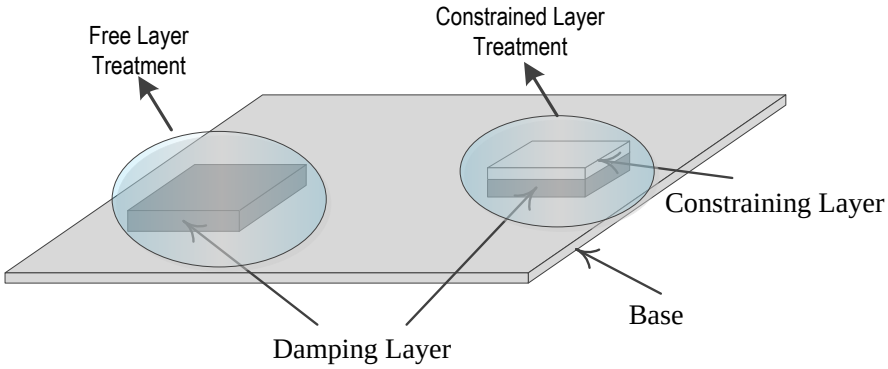

Figure 2.5 : Free and constrained layer damping treatments.

2.2.5 Material testing methods

There are various standard methods for characterisation of damping materials as summarised in Section 1.2.1. The so-called direct, indirect and driving point methods defined in ISO 10846-2, -3 and -5 standards [4-6], respectively, are used to determine the dynamic properties of viscoelastic supports. The Oberst Beam Method (OBM) described in ASTM E 756 [1] and SAE J 1637 [2] standards and the Geiger plate test defined in SAE J 671 standard [3] are the main methods used to measure dynamic properties of thin-layered damping materials.

OBM [1] - a resonance based method - is very appropriate for the measurement of the dynamic properties of damping materials used in many fields including domestic appliances and automotive industry. The main reasons for this are that; (a) damping materials are most effective at resonances, and (b) as in OBM, damping material is coated on sheet metals in domestic appliances, automotive applications, etc. Overall, OBM is selected for the characterisation of damping materials in this thesis.

2.3 Oberst Beam Method (OBM)

OBM is accepted as the classical method for the characterisation of damping materials based on Frequency Response Function (FRF) measurements on some typical beams as described in ASTM E 756 standard [1]. Uniform, free-layer damped and sandwiched beams are used in this method. The configuration of the test specimen is selected based on the type of damping material to be tested and the mechanical properties to be determined. Three types of specimen configurations used in OBM [1] are described as follow: (i) Self-supporting materials are evaluated by preparing a single (homogeneous) test beam from the material itself. In this case,

Young's modulus and damping level of the material are identified at natural frequencies using the modal properties of the beam identified from measured FRF. (ii) The elastic and damping properties of non-self-supporting materials are evaluated in a two-step process. First, the FRF measured on the bare (base) beam is analysed to determine the natural frequencies within a frequency range of interest. The base beam is almost always made of a lightly damped material such as steel or aluminium. Then, the measured FRF on the damped beam is analysed in order to determine the natural frequencies and corresponding modal loss factors of the composite beam. Using the identified modal properties of the bare and the damped (composite) beams, Young's modulus and loss factor of the damping material are identified at natural frequencies of the damped (composite) beam. (iii) Shear modulus and damping levels of non-self-supporting materials are determined similar to the two-step process described above. However, in this case, two identical base beams are to be used and the composite beam is to be prepared using the sandwich specimen configuration. Figure 2.6 shows typical examples of uniform and multilayer cantilever beams, the roots of which are clamped into heavy and stiff blocks. It should be noted that the bending modes of a beam are measured for the determination of material properties at individual natural frequencies in OBM.

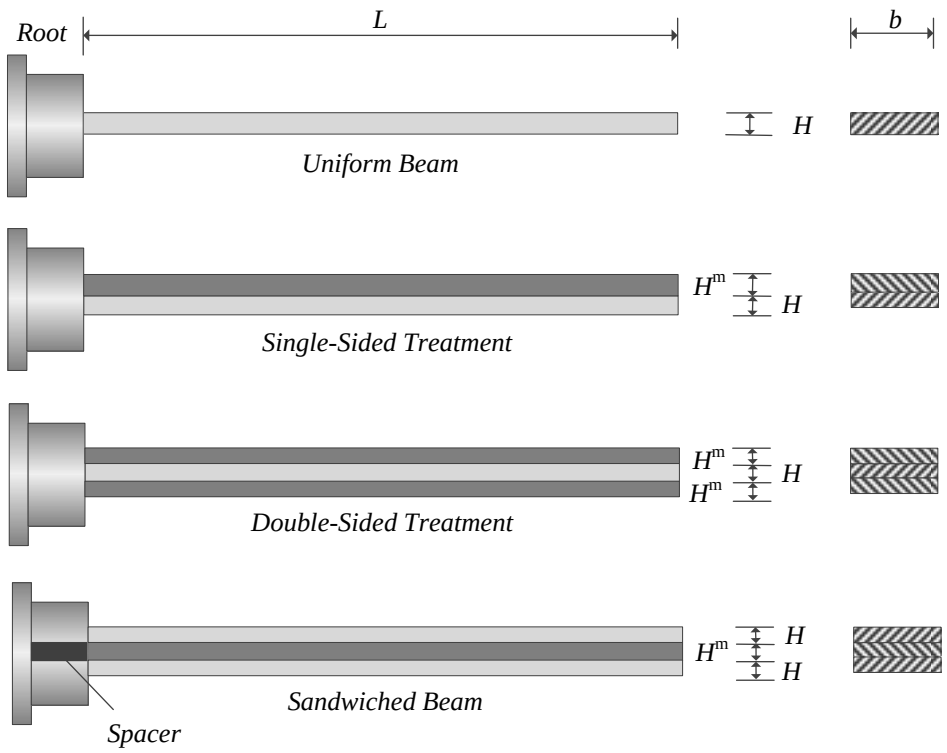

Figure 2.6 : Configurations of uniform, single-sided and double-sided damped and sandwiched cantilever beams used in Oberst beam method.

The Oberst test rig used in this study consists of a cantilever beam mounted on a test stand, an exciter, a response sensor and associated data acquisition and signal processing system. The experimental test set-up is shown in Figure 2.7. Both the response sensor and the exciter used in this test rig are of non-contact type. The response sensor is a velocity-sensitive magnetic transducer. The exciter, on the other hand, is an electromagnetic type located at the free end of the beam. Measurement procedure for acquiring an FRF using the Oberst test rig is illustrated in Figure 2.8.

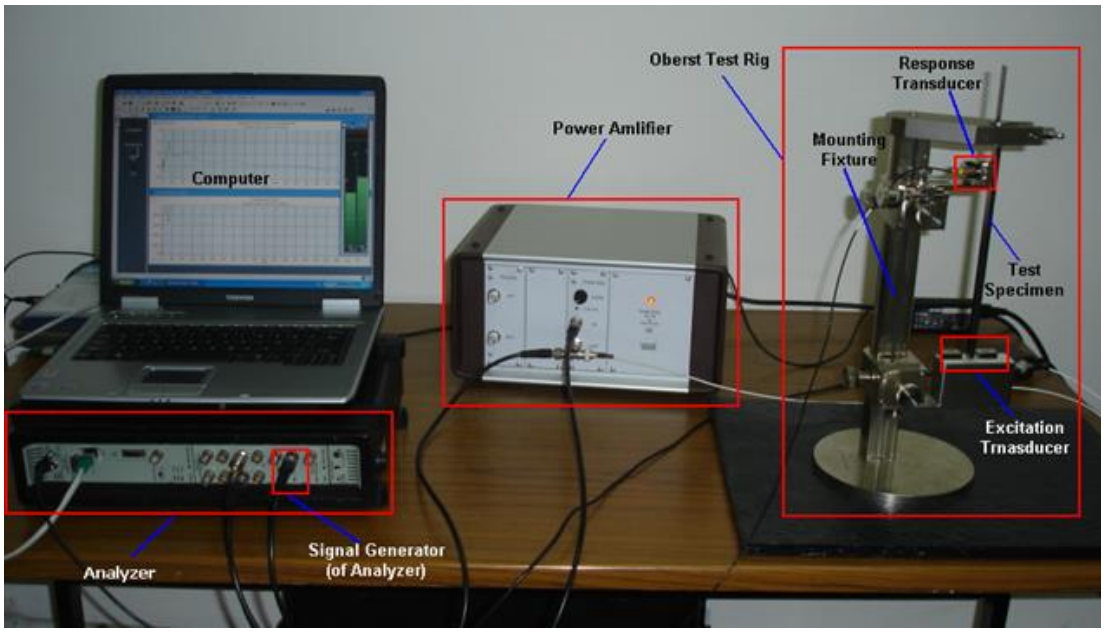

Figure 2.7 : Experimental test set-up including Oberst test rig for identification of damping materials.

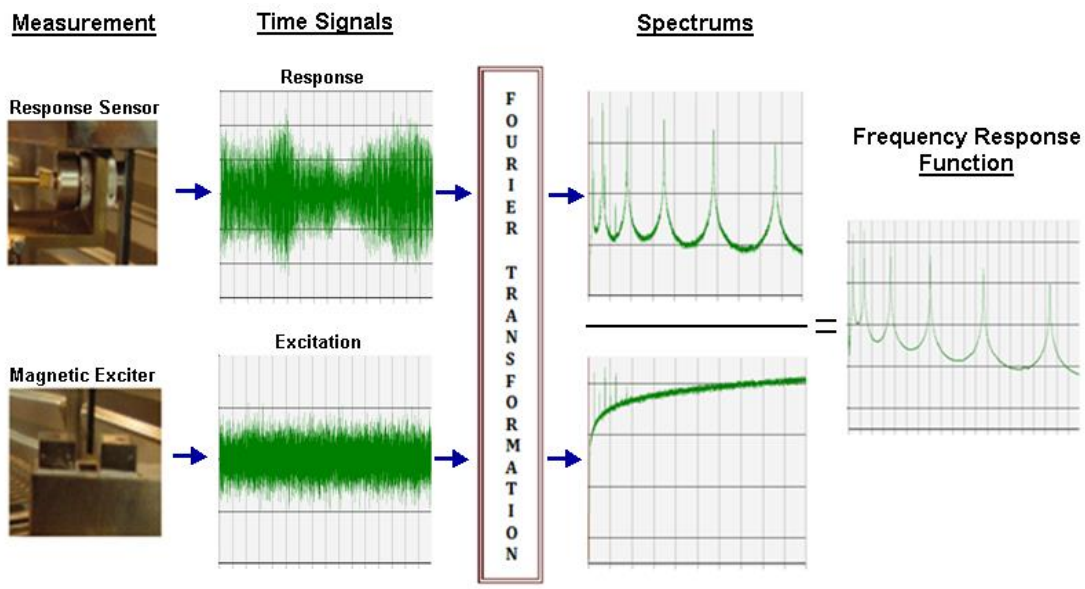

Figure 2.8 : Illustration of a typical FRF measurement using an Oberst test rig.

2.3.1 Determination of mechanical properties of materials

2.3.1.1 Bending vibration of an Oberst beam: Theory

Ignoring the rotational inertia effects and shear deformations [143], the equation of motion for the flexural (bending) vibrations of a beam can be written as

$$\rho A(x)\frac{\partial^2 w(x,t)}{\partial t^2}+\frac{\partial^2}{\partial x^2}\left[EI(x)\frac{\partial^2 w(x,t)}{\partial x^2}\right]=f(x,t) \qquad \textbf{(2.9)}$$

where x is the beam axial direction, $w(x,t)$ is the transverse deflection (in y direction), ρ is mass density of the beam material, $A(x)$ is the cross sectional area, $EI(x)$ is the bending (flexural) stiffness, E is the Young's modulus of the beam material, $I(x)$ is the cross sectional area moment of inertia with respect to z axis, and $f(x,t)$ is the total external force applied to the element per unit length. Assuming I and A are constant as in the case of the test samples used in OBM [1], the free vibration equation of the beam can be written as

$$c^2\frac{\partial^4 w(x,t)}{\partial x^4}+\frac{\partial^2 w(x,t)}{\partial t^2}=0 \qquad \textbf{(2.10)}$$

where $c=\sqrt{EI/\rho A}$. The Boundary Conditions (BCs) for the clamped (x=0) and free (x=L) ends of the beam are given as

$$w\big|_{x=0}=0 \qquad \left.\frac{\partial w}{\partial x}\right|_{x=0}=0 \qquad \textbf{(2.11)}$$

$$EI\left.\frac{\partial^2 w}{\partial x^2}\right|_{x=L}=0 \qquad \left.\frac{\partial}{\partial x}\left[EI\frac{\partial^2 w}{\partial x^2}\right]\right|_{x=L}=0 \qquad \textbf{(2.12)}$$

Assuming a harmonic solution of the form $w(x,t)=X(x)T(t)$ allows expressing Equation 2.10 as

$$\ddot{T}(t)+\omega^2 T(t)=0 \qquad \textbf{(2.13)}$$

$$X^{\mathrm{IV}}(x)-\left(\omega/c\right)^2 X(x)=0 \tag{2.14}$$

where $X^{\mathrm{IV}}(x)=\mathrm{d}X^4(x)/\mathrm{d}x^4$ and $\ddot{T}(t)=\mathrm{d}T^2(t)/\mathrm{d}t^2$. Solution of Equation 2.13 can be written as

$$T(t)=A\sin\omega t+B\cos\omega t \tag{2.15}$$

Assuming a solution $X(x)=Ae^{\sigma x}$ for Equation 2.14, the general solution of this equation can be written as

$$X(x)=a_1\sin\beta x+a_2\cos\beta x+a_3\sinh\beta x+a_4\cosh\beta x \tag{2.16}$$

where

$$\beta^4=\left(\frac{\omega}{c}\right)^2=\frac{\rho A\omega^2}{EI} \tag{2.17}$$

Applying the BCs given in Equations 2.11 and 2.12 to Equation 2.16 yields a set of equations which can be expressed in matrix form as

$$\begin{bmatrix} 0 & 1 & 0 & 1 \\ 1 & 0 & 1 & 0 \\ -\sin\beta\ell & -\cos\beta\ell & \sinh\beta\ell & \cosh\beta\ell \\ -\cos\beta\ell & \sin\beta\ell & \cosh\beta\ell & \sinh\beta\ell \end{bmatrix}\begin{bmatrix} a_1 \\ a_2 \\ a_3 \\ a_4 \end{bmatrix}=\begin{bmatrix} 0 \\ 0 \\ 0 \\ 0 \end{bmatrix} \tag{2.18}$$

Setting the determinant of the matrix above to zero, the characteristic equation is obtained as

$$\cosh\left(\beta L\right)\cdot\cos\left(\beta L\right)+1=0 \tag{2.19}$$

Only graphical or numerical solution of this characteristic equation is possible. To obtain the solution graphically, the characteristic equation can be written as

$$\cosh\left(\beta L\right)=-\sec\left(\beta L\right) \tag{2.20}$$

where the βL values satisfying the characteristic equation are the eigenvalues which yields the natural frequencies. By plotting Equation 2.20, the $\beta_n L$ values are determined as given in Table 2.1.

Table 2.1 : The $\beta_n L$ values.

$\beta_1 L$	$\beta_2 L$	$\beta_3 L$	$\beta_n L$ (for n>3)
1.875	4.694	7.855	$(\pi/2)(2n-1)$

So, the corresponding natural frequencies can be determined using Equation 2.17 as expressed below

$$\omega^2 = \beta^4 \frac{EI}{\rho A} = (\beta L)^4 \frac{EI}{\rho A L^4} \tag{2.21}$$

For beams with rectangular cross sections (as for the Oberst beam [1]), that is, $A=bH$ and $I = bH^3/12$ **,** the natural frequencies are obtained as

$$\omega_n = (\beta_n L)^2 \sqrt{\frac{EH^2}{12\rho L^4}} \tag{2.22}$$

Using $\omega_n = 2\pi f_n$, Young's modulus is determined as

$$E = \frac{4\pi^2 f_n^2 12\rho L^4}{H^2 (\beta_n L)^4} \tag{2.23}$$

Defining a new parameter C_n (to resemble to ASTM E 756 standard [1]) E can be given as

$$E = \frac{12\rho L^4 f_n^2}{H^2 C_n^2} \tag{2.24}$$

where

$$C_n^2 = \frac{(\beta_n L)^4}{4\pi^2} \tag{2.25}$$

The C_n values are given in Table 2.2. It is clear that knowing $\beta_n L$ thus C_n values is sufficient to calculate the Young's modulus of the beam based on the measured natural frequencies of the beam as it is described further in the next section.

Table 2.2 : The C_n values.

C_1	C_2	C_3	C_n (for n>3)
0.55959	3.5069	9.8194	$(\pi/2)(n-0.5)^2$

2.3.1.2 Extraction of material properties

As stated, uniform, free-layer damped and sandwiched beams can be used in OBM. The natural frequencies and damping values (loss factors) of the test samples are determined by analysing the measured FRFs using some resonance-based system identification methods such as half-power [1], circle-fit [36] and line-fit [37] methods and the material properties are then identified according to the theoretical background presented in the previous section and the procedure described in ASTM E 756 standard [1].

For uniform or bare beams, the elasticity moduli of the material corresponding to individual modes are directly extracted using Equation 2.24 while the material loss factors corresponding to individual modes are identified directly by analysing the measured FRF. For the extraction of the material properties for composite structures given in Figure 2.6, the equivalent bending stiffness *EI* of the composite beams can be determined. Then, the Young's moduli and loss factors corresponding to individual modes of the damping material are extracted using Equation 2.21 once the natural frequencies and loss factors of the bare and composite beams are determined using the measured FRFs. The expressions for material identification for all the configurations given in Figure 2.6 according to ASTM E 756 [1] standard are summarised in Table 2.3 [1, 16]. Referring to Table 2.3, H and H^m are the thicknesses of base beam and damping layer (m), respectively; ρ and ρ^m are the mass densities of base beam and damping material (kg/m^3), respectively; f_n and f_n^c are the resonance frequencies for mode n of base and composite beams (Hz), respectively; Δf_n and Δf_n^c are the half-power bandwidths for mode n of base and composite beams (Hz), respectively; E_n, E_n^m and G_n^m are the Young's moduli of base beam and damping material and shear modulus of damping material (Pa) for mode n,

respectively and η_n, η_n^c, η_n^m and $\eta_n^{m,s}$ are the loss factor of base beam material, the loss factor of composite beam, the loss factor of damping material and shear loss factor of damping material for mode *n*, respectively.

Table 2.3 : The expressions for material identification based on ASTM E 756.

Elasticity or Shear Modulus	*Extensional or Shear Loss Factor*
Bare Beam	
$E_n = \dfrac{12\rho L^4 f_n^2}{H^2 C_n^2}$	$\eta_n = \dfrac{\Delta f_n}{f_n}^{*}$
Single-Sided Treatment	
$E_n^m = \dfrac{\left[(A_n - B) + \sqrt{(A_n - B)^2 - 4h^2(1 - A_n)}\right] E_n}{2h^3}$	$\eta_n^m = \dfrac{(1+e_n h)(1+4e_n h+6e_n h^2+4e_n h^3+e_n^2 h^4)}{e_n h(3+6h+4h^2+2e_n h^3+e_n^2 h^4)}\eta_n^c$
Double-Sided Treatment	
$E_n^m = \dfrac{\left[(f_n^c/f_n)^2(1+2dh)-1\right]E_n}{8h^3+12h^2+6h}$	$\eta_n^m = \eta_n^c + \dfrac{E_n}{(8h^3+12h^2+6h)E_n^m}\eta_n^c$
Sandwiched Beam	
$G_n^m = \dfrac{\left[(X_n - Y) - 2(X_n - Y)^2 - 2(X_n \eta_n^c)^2\right] 2\pi C_n E_n H H_1}{\left[(1-2X_n+2Y)^2 + 4(X_n \eta_n^c)^2\right] L^2}$	$\eta_n^{m,s} = \dfrac{X_n}{(X_n - Y) - 2(X_n - Y)^2 - 2(X_n \eta_n^c)^2}\eta_n^c$
where	
$A_n = (f_n^c/f_n)^2(1+dh)$ $\quad B = 4+6h+4h^2$	$d = \rho^m/\rho$ $\quad h = H^m/H$
$X_n = (f_n^c/f_n)^2(2+dh)(Y/2)$ $\quad Y = 1\Big/\left[6(1+h)^2\right]$	$e_n = E_n^m/E_n$ $\quad \eta_n^c = \Delta f_n^c/f_n^c$

*Also, line-fit or circle-fit methods can be used to identify modal loss factors from measured FRFs.

2.4 Preparation of The Test Rig: Assessment of Oberst Rig Parameters

The use of contacting transducers and shakers is not recommended in OBM [1] as they introduce artificial mass loading and damping, significantly reducing the quality of the results in OBM [14]. Therefore, it is strongly recommended in the literature that non-contact response transducers and non-contact electromagnetic excitation system should be used [1-2, 14] in OBM. If a non-ferromagnetic material is used as the material of the base beam, it is necessary to glue a small piece of ferromagnetic material for providing magnetic excitation. Although the drawbacks of contacting type of transducers can be eliminated by using non-contact response and excitations transducers, there are still other critical issues, as presented in this thesis, which can adversely affect the measured data when OBM is used in practice. Therefore, all the

parameters affecting the test results need to be optimised in order to obtain the material properties with high accuracy. Although OBM is referenced in some standards [1-2] and it is widely used in many scientific studies [15-33], detailed information in the literature on how to perform a successful Oberst beam experiment is very limited. This chapter is addressing this problem.

Preliminary tests on the Oberst beam revealed that the electromagnetic effect created by a non-contact exciter could be very significant source of error in estimated material properties. Extensive tests are carried out so as to quantify the level of the adverse effects of electromagnetic excitation experimentally as described in Section 2.5. However, in order to ensure that the systematic errors investigated in the next section (Section 2.5) are mostly associated with the adverse effect of the electromagnetic excitation, the errors associated with other parameters and conditions should be eliminated or minimised first. Therefore, many FRFs are measured using various samples under various conditions so as to determine and select the best measurement parameters. Comparisons are made in terms of measured FRFs and sometimes in terms of natural frequencies.

The frequency range of interest is set to 2-2000 Hz, which is also compatible with the frequency range of the sensors used. Also, appropriate frequency resolution is selected and Hanning window is applied to both response and excitation signals. A sufficient number of averages should be used in Oberst beam tests in order to minimise the noise levels in measured FRFs. The FRFs measured on a typical homogeneous steel beam for 5, 10 and 50 averages are given in Figure 2.9. Ten or more averaging seems to be appropriate although this may vary depending on the measurement system. In this work, FRF measurements are made using about 50 averages.

Two different types of excitations, namely sine sweep and random, are applied in turn and corresponding FRFs in the case of a typical damped (composite) beam with a length of L= 220 mm are obtained and presented in Figure 2.10. As can be seen, almost identical results are obtained in both cases when appropriate sine sweep parameter is selected. As a result, it is decided to use random type of excitation for the rest of the results presented in this work.

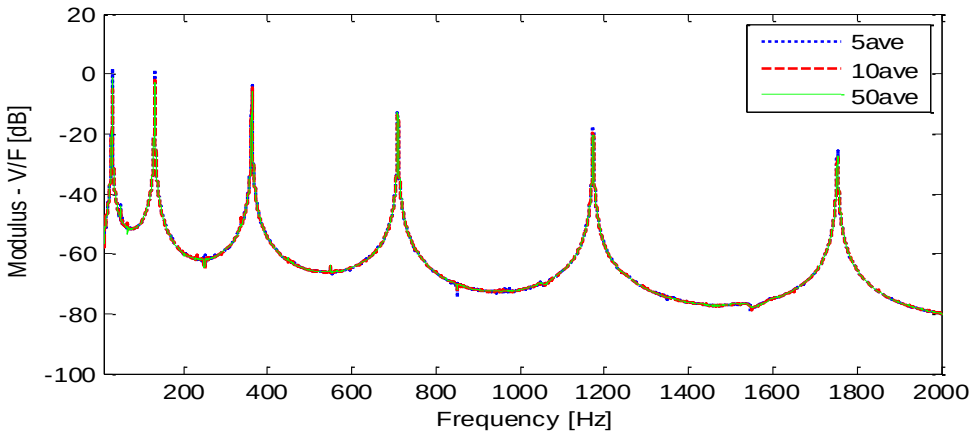

Figure 2.9 : FRFs for various numbers of averages (5, 10 and 50 averages).

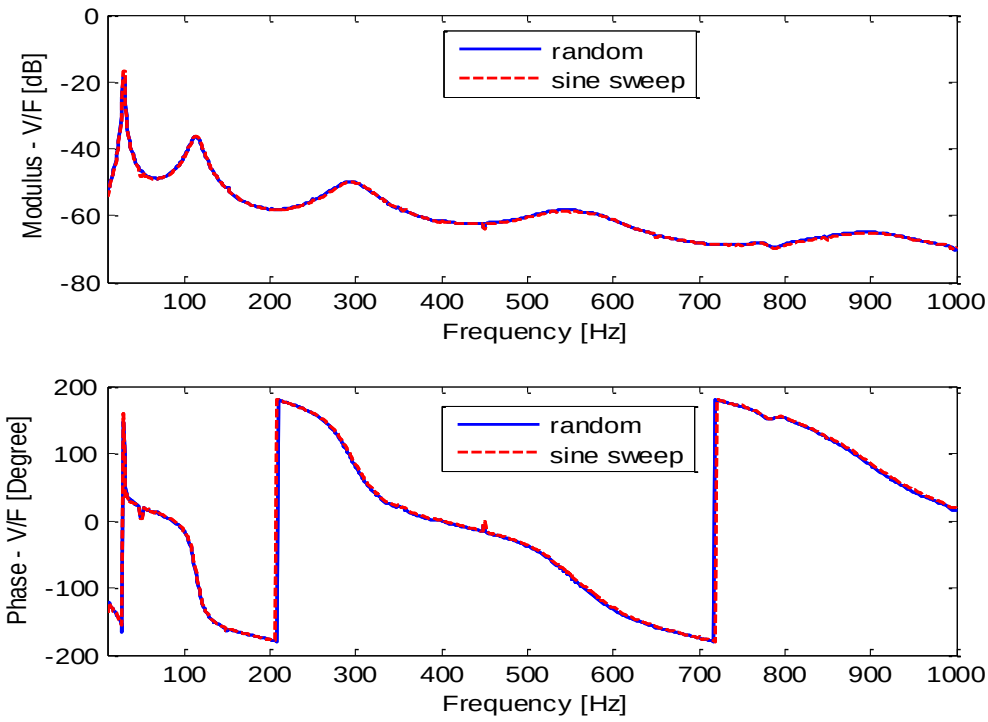

Figure 2.10 : Comparison of FRFs for random and sine sweep excitations.

For a given non-contact exciter, there is a range of excitation levels that can be applied. It is essential that the excitation must be strong enough to obtain high signal to noise ratio. However, unless non-linear material behaviour is of interest, it is also necessary not to exceed certain level of excitation in order to remain within the linear range. This is assured after some trial tests so as to establish a range that is appropriate for reliable measurements. Some FRFs are measured using forcing levels within this linear range, identified here as low, medium and high. The results are compared in Figure 2.11 where it is seen that identical results can be obtained if the

linearity is assured. Identified natural frequencies and damping levels using the FRFs in Figure 2.11 corresponding to three different forcing levels are listed in Table 2.4 for the first three modes. As expected, the differences between the natural frequencies and damping levels identified from 3 FRFs in Figure 2.11 are negligible. It is worth restating that appropriate forcing level should be determined before making the final measurements and this depends on the Oberst testing system used. It is almost certain that this process requires some initial trial tests.

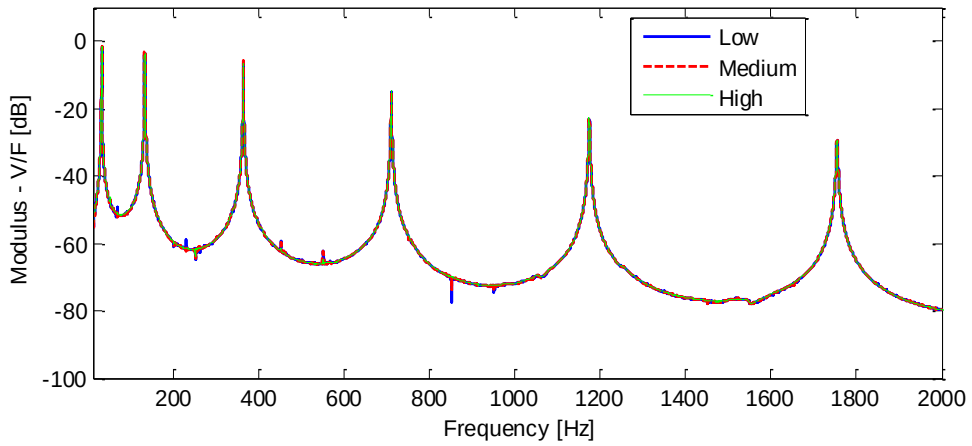

Figure 2.11 : FRFs measured for various forcing levels (low, medium and high).

Table 2.4 : Natural frequencies and loss factors for various excitation force levels.

Bending Mode No	Natural Frequency, f (Hz)			Loss Factor, η		
	High	Medium	Low	High	Medium	Low
2	113.3	113.5	113.5	0.0016	0.0015	0.0016
3	301.0	301.2	301.0	0.0012	0.0012	0.0011
4	586.4	586.4	586.4	0.0012	0.0011	0.0011

As it is not specified in ASTM E 756 standard [1], the length of the test specimen needs to be decided. It is obvious that longer specimens are more flexible than shorter ones. So, if more number of modes within the frequency range of interest are to be investigated, longer specimens should be selected, and vice versa. It is also worth keeping in mind that the length of the beam should be chosen such that the natural frequencies of the beam should not coincide with the frequency of the main electric power (i.e., 50 or 60 Hz). It is shown in Section 2.5 that the error in the estimated material properties due to electromagnetic effect also depends on the length of the Oberst beam.

In the case of a composite beam, at least two FRF measurements (one for a bare beam and the other for a damped beam) need to be made for the determination of material properties as stated before. This requires that mounting conditions for the bare and the damped beams should be as identical as possible. Repeatable mounting conditions are also required for averaging purposes. Some trial measurements are made again in order to check how much this requirement can be satisfied. This is done by reinstalling the same beam to the Oberst stand and making a new FRF measurement and this process is repeated a few times to check the degree of repeatability in terms of clamping conditions and the actual beam length. It is found that the use of a kind of gauge or a "stopper" shown in Figure 2.12 is very useful for assuring that the beam will have almost the same free length every time it is installed. This approach is utilised and very good repeatability is obtained as illustrated in Figure 2.13. In order to quantify the degree of repeatability, the natural frequencies corresponding to the three FRF measurements given in Figure 2.13 are listed in Table 2.5. As it can be seen, the results are almost identical and the error due to repeatability issue can be considered negligible if a stopper is used during clamping. Although not presented here for brevity, many other repeatability tests are also performed, including, for example, the repeatability tests related to nominally identical bare and damped beams.

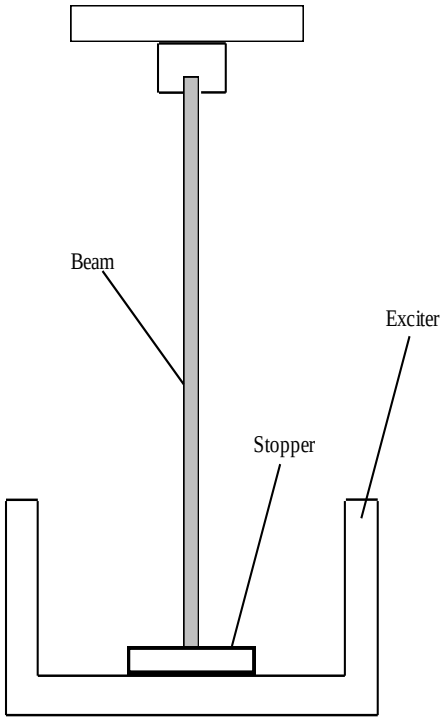

Figure 2.12 : A stopper for assuring repeatability.

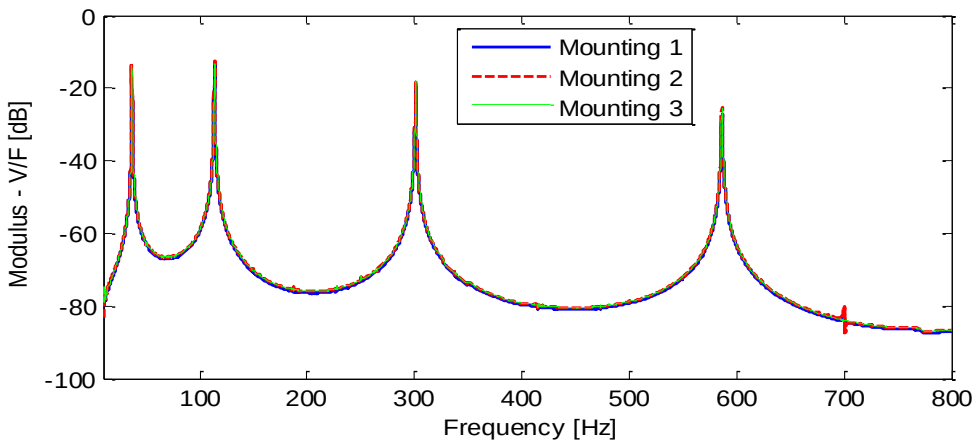

Figure 2.13 : FRF measurements for various mounting changes.

Table 2.5 : Identified natural frequencies using repeated mounting cases.

Bending Mode No	Natural Frequency, *f* (Hz)		
	1st Measurement	2nd Measurement	3rd Measurement
2	113.5	113.5	113.5
3	301.0	300.9	301.0
4	586.4	586.1	586.4

In what follows, the electromagnetic effects created by a non-contact exciter are examined in detail, keeping in mind that the systematic errors in the next section are mostly associated with the electromagnetic field as other errors associated with secondary parameters and conditions are eliminated or minimised as described above.

2.5 Electromagnetic Effect

2.5.1 Introduction

In practical applications, non-contact excitation is widely used in OBM. However, studies on adverse effects of non-contact excitation, its modelling and minimisation in the Oberst beam testing is not available in the literature. Non-contact excitation is generally assumed to have no adverse effects. However, as it is demonstrated in this section, the electromagnetic field around the free-end of the Oberst beam can change the dynamic behaviour of the Oberst beam significantly. Although not directly related to OBM, there are some studies [144-147] associated with mechanical effects of electromagnetic field on structures. Chen and Yeh [144] identified a relationship between the DC current through the coil and the stiffness of a non-contact

electromagnetic device. They specified that as the current flows through the coil, the coil becomes an electromagnet and the mutual acting forces between the electromagnet and the pair of magnets make the electromagnetic device function like a spring applied to the beam. They also showed the relationship between the non-dimensionalised spring stiffness and the DC coil current of the electromagnetic device for a beam specimen. Schmidt et al. [145] described an electromagnetic exciter to achieve a controllable stiffness. Fan and Pan [146] stated that the electromagnetic exciter they used in their study provided additional stiffness on the system. Also, spring stiffness may change as a function of displacement [147].

Although the adverse effects of non-contact magnetic excitation in the Oberst beam test method are not directly addressed before, there are some studies already published in the literature dealing with the variation of the damping and natural frequency of cantilever beams under magnetic field [148-157]. Takagi et al. [149] conducted experiments to measure the change in natural frequency and damping for a thin plate subjected to strong uniform magnetic field. They showed the increase in natural frequency and damping with external magnetic field. Zhou and Miya [151] developed a theoretical model to predict the increase in natural frequency of ferromagnetic plates under uniform magnetic fields and compared the results with existing experimental data. Zhou and Miya [151] neglected the effect of the eddy current in their model. Bonisoli and Vigliani [154], on the other hand, investigated the damping and stiffening effects of passive permanent magnets on Euler-Bernoulli beam by including the interaction between permanent magnets and induced eddy currents. More recent work by Lee and Lin [157] proposed a magnetic force model to predict the natural frequency of a beam plate subjected to an in-plane magnetic field. Lee and Lin [157] included axial and transverse magnetic force as well as the Lorentz force due to induced eddy current.

As mentioned, the electromagnetic exciter used in this study is a non-contact type. The magnetic response transducer used in this study is also non-contact type. The electromagnetic exciter with push-pull excitation capability combined with a power amplifier module is utilised for non-contact excitation of the beam. A schematic view of the excitation unit in the Oberst Beam test rig is given in Figure 2.14. As can be seen, the exciter is located at the free end of the beam, which consists of an iron frame, a coil and a permanent magnet. The tip of the beam is positioned into the

electromagnetic exciter slot. In Figure 2.14, the length of the section of the beam exposed into the exciter slot is represented by a so-called gap parameter δ. When the electric current flows through the coil, the mutually acting forces between the iron frames excite the beam. In the next section, the electromagnetic effect of the non-contact exciter in Oberst beam method is investigated experimentally.

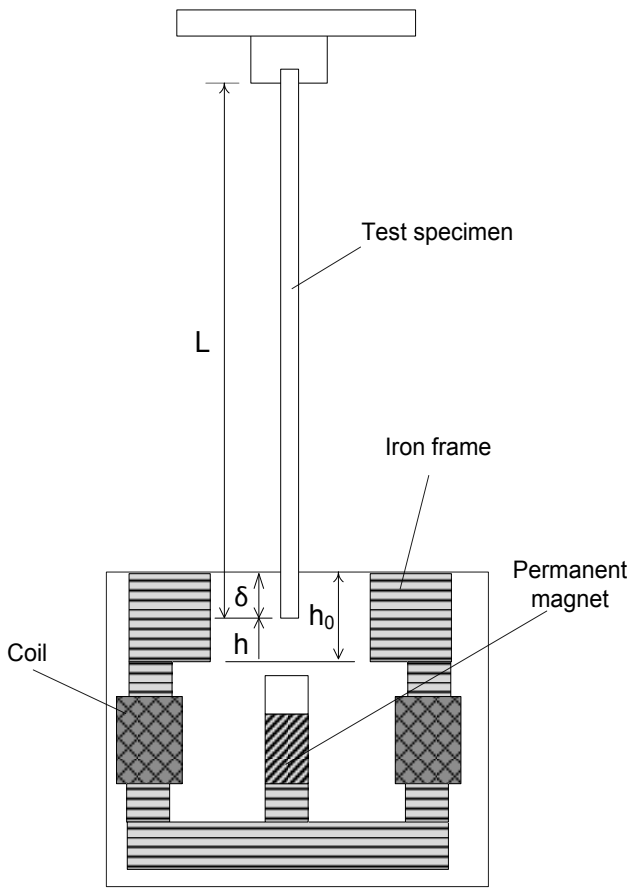

Figure 2.14 : Non-contact excitation system in OBM.

2.5.2 Experimental study

Extensive tests are carried out in order to identify the adverse effects of electromagnetic excitation. The effect of electromagnetic field on the dynamics of the Oberst beam is varied by changing the position of the free end of the beam in the electromagnetic exciter slot (see Figure 2.14). The effect of electromagnetic excitation on the measured results is investigated as a function of the so-called gap parameter δ ($\delta = h_0 - h$) shown in Figure 2.14, the range of which is from 1 mm to 9 mm.

It should be noted that the level of electromagnetic forcing action is maximum when the tip of the test specimen is almost at the bottom of the electromagnetic exciter slot (i.e., δ is very large). However, the electromagnetic forcing action is minimum when the tip of the test specimen is almost at the top of the electromagnetic exciter slot (i.e., δ is very small). It should also be noted that a composite beam comprising a base beam and one or more damping layers requires stronger electromagnetic excitation (i.e., larger value of the gap parameter δ) than a typical steel bare beam in order to identify the natural frequencies and corresponding loss factors. Especially, highly damped homogeneous and composite beams require comparatively stronger excitation (larger value of δ) in order to be able to identify the damping levels using the measured FRFs accurately. Furthermore, in the case of a composite beam, at least two FRF measurements (one for bare beam and the other for damped beam) are needed for the determination of the material properties of the damping layer.

In this study, a homogeneous steel beam is used to investigate the electromagnetic effects in the Oberst beam test method. Many FRFs are measured under different levels of electromagnetic field created by a non-contact exciter. Then, comparisons are made in terms of natural frequencies and material properties. The natural frequencies and loss factors are determined using measured FRFs by utilising the line-fit method [37]. It should be noted that the theories behind the measurements of FRFs and formulations of system identification methods including line-fit method are given in detail in Chapter 3. Then, material properties are determined according to the procedure described in ASTM E 756 standard [1]. Here, when δ<1 mm, the magnetic field around the free end of the steel beam is not sufficiently strong enough to excite the beam in order to be able to identify the natural frequencies and corresponding loss factors using the measured FRF. On the other hand, $\delta\approx$10 mm is physically the maximum possible value for the gap parameter in this study. The current practice is to position the tip of the beam either at about the middle of the exciter slot or to maximise the so-called gap parameter δ (Figure 2.15). In either case, the adverse effect of electromagnetic excitation is also currently ignored in practice.

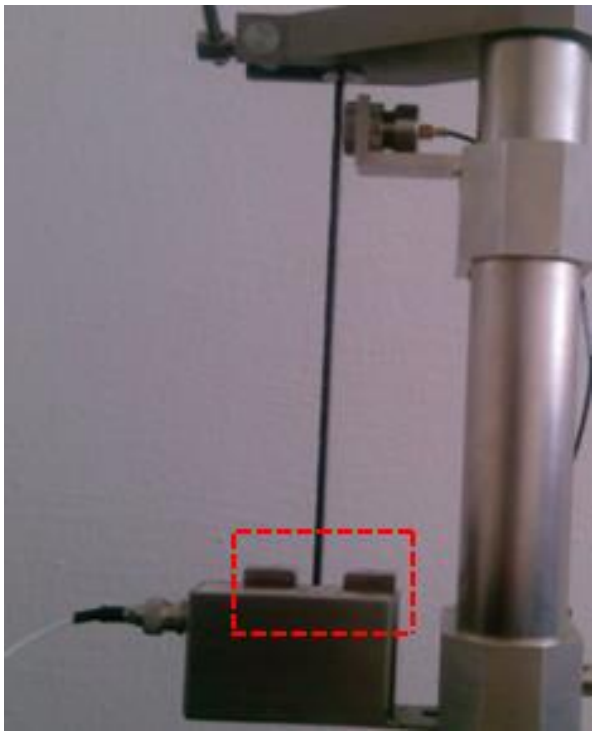

Figure 2.15 : Positioning of the test sample in an Oberst test rig.

Various FRFs are measured on a bare beam of length L= 220 mm that is exposed to different levels of magnetic field (for δ=1 mm to δ=9 mm) and the corresponding natural frequencies are determined. Young's modulus is calculated each time using Equation 2.24, the thickness and the width of the beam being 1 mm and 10 mm, respectively. Also, the density of the steel beam is measured to be 7870 kg/m^3. For the test beam, the natural frequencies (f) and the estimated Young's modulus (E) are listed in Table 2.6. The estimated Young's moduli for all the modes except the first one are plotted against the gap parameter, δ, in Figure 2.16. In order to demonstrate the level of variation of the estimated Young's modulus for individual modes, the results are reproduced in Figure 2.17. It is clearly seen that as the gap parameter increases, the natural frequencies and the associated Young's modulus increase for all the modes. Inspection of the results in Table 2.6 reveals that as the gap parameter is varied from 1 mm to 9 mm, the value of the estimated Young's modulus varies from 232.5 GPa to 1006.8 GPa when the first mode is considered. For the second, third and forth modes, the corresponding ranges of the estimated Young's modulus are 204.8 - 235.0 GPa, 204.0 - 208.6 GPa and 204.0 - 205.5 GPa, respectively.

Table 2.6 : Natural frequencies and estimated Young's moduli of a steel beam of L= 220 mm exposed to different levels of magnetic field.

		δ=1 mm			δ=2 mm
Mode	f (Hz)	E (GPa)	Mode	f (Hz)	E (GPa)
1	18.2	232.50	1	18.8	248.38
2	106.7	204.80	2	106.9	205.57
3	298.2	203.99	3	298.3	204.15
4	584.3	203.99	4	584.4	204.04
		δ=3 mm			δ=4 mm
Mode	f (Hz)	E (GPa)	Mode	f (Hz)	E (GPa)
1	19.4	265.35	1	20.6	300.68
2	107.0	205.95	2	107.3	207.11
3	298.4	204.28	3	298.4	204.28
4	584.4	204.06	4	584.4	204.04
		δ=5 mm			δ=6 mm
Mode	f (Hz)	E (GPa)	Mode	f (Hz)	E (GPa)
1	22.0	341.94	1	24.5	424.07
2	107.6	208.27	2	108.4	211.30
3	298.5	204.42	3	298.8	204.88
4	584.6	204.22	4	584.6	204.22
		δ=7 mm			δ=8mm
Mode	f (Hz)	E (GPa)	Mode	f (Hz)	E (GPa)
1	28.0	553.89	1	31.4	695.69
2	109.5	215.69	2	110.9	221.24
3	299.4	205.65	3	300.0	206.48
4	585.1	204.55	4	585.5	204.83
		δ=9 mm			
Mode	f (Hz)	E (GPa)			
1	37.8	1006.79			
2	114.3	235.01			
3	301.5	208.55			
4	586.5	205.53			

As can be seen in Figures 2.16 and 2.17, the variation of the identified Young's modulus as a function of the gap parameter is huge for the first mode. However, the identified Young's modulus is affected less as the mode number is increased. It should be noted that the Oberst beam used in this study is made of mild steel and, for a given gap parameter, its Young's modulus is not supposed to change as a function of frequency or mode. Accordingly, the variation of the Young's modulus presented in Figure 2.16 or 2.17 is attributed to the adverse effects of the non-contact magnetic excitation which appears to increase as the gap parameter increases. It is therefore inferred that the correct Young's modulus for the mild steel in this study can be identified when the gap parameter is set to the minimum value. Based on this, the

correct value of the Young's modulus for this material is converged to 204 GPa. Then, the correct (reference) natural frequencies of the test beam with fixed-free boundary conditions and length, L=220 mm, corresponding to Elasticity modulus being 204 GPa are calculated using Equation 2.24 and listed in Table 2.7. As expected, the natural frequencies in Table 2.7 are close to those that can be obtained when the gap parameter is 1 mm.

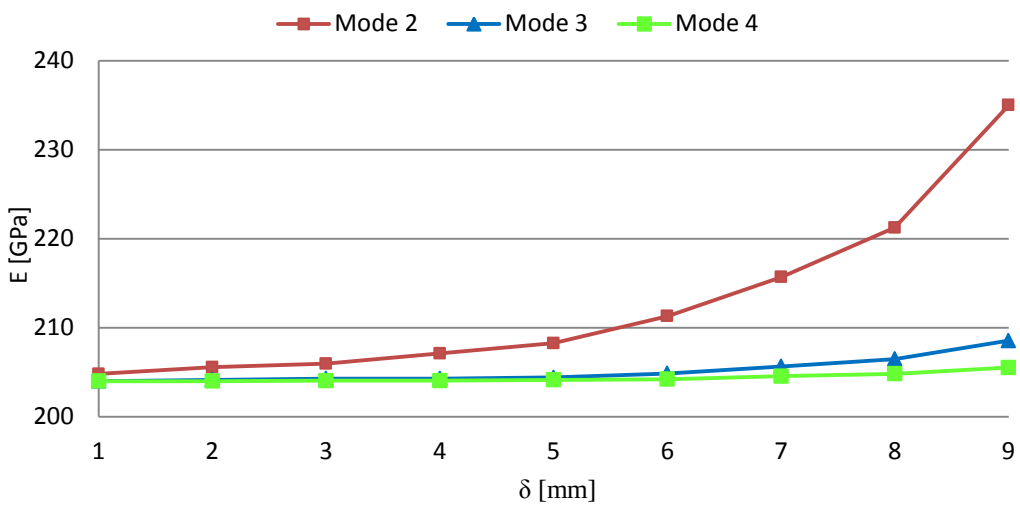

Figure 2.16 : Estimated Young's moduli for all the modes except the first one against the gap parameter, δ.

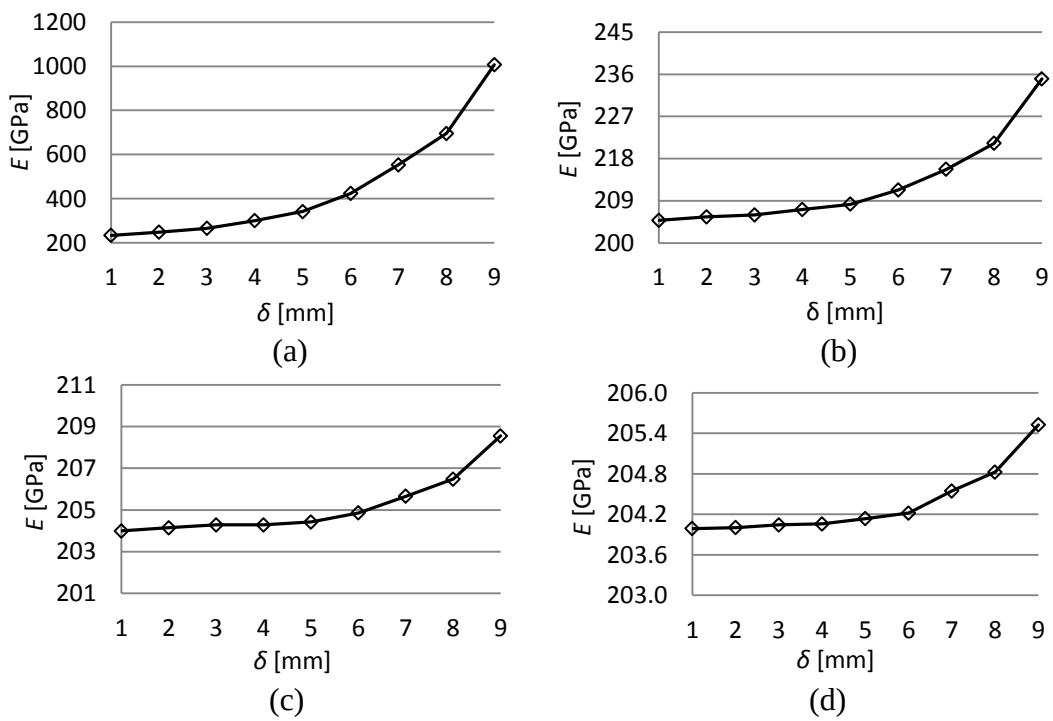

Figure 2.17 : Estimated Young's moduli against the gap parameter, δ for 1st (a), 2nd (b), 3rd (c), and 4th (d) modes.

Table 2.7 : Correct values of the natural frequencies of a steel bare beam of L=220 mm with fixed-free BCs.

Bending Mode No	Natural Frequency, f (Hz)
1	16.99
2	106.46
3	298.12
4	584.22

After identifying the correct values of the natural frequencies and Young's modulus, the corresponding errors in natural frequencies and Young's modulus are calculated and listed in Table 2.8.

Table 2.8 : The errors in natural frequencies and Young's modulus of a steel bare beam of L= 220 mm exposed to different levels of magnetic field.

δ=1 mm			δ=2 mm		
Mode	Error in f (%)	Error in E (%)	Mode	Error in f (%)	Error in E (%)
1	7.0	14.5	1	10.4	21.8
2	0.3	0.4	2	0.4	0.8
3	0.0	0.0	3	0.1	0.1
4	0.0	0.0	4	0.0	0.0
δ=3 mm			δ=4 mm		
Mode	Error in f (%)	Error in E (%)	Mode	Error in f (%)	Error in E (%)
1	14.1	30.1	1	21.4	47.5
2	0.5	1.0	2	0.8	1.6
3	0.1	0.2	3	0.1	0.2
4	0.0	0.1	4	0.0	0.1
δ=5 mm			δ=6 mm		
Mode	Error in f (%)	Error in E (%)	Mode	Error in f (%)	Error in E (%)
1	29.5	67.7	1	44.2	108.0
2	1.1	2.1	2	1.8	3.6
3	0.1	0.3	3	0.2	0.5
4	0.1	0.2	4	0.1	0.2
δ=7 mm			δ=8 mm		
Mode	Error in f (%)	Error in E (%)	Mode	Error in f (%)	Error in E (%)
1	64.8	171.6	1	84.7	241.2
2	2.9	5.8	2	4.2	8.5
3	0.4	0.9	3	0.6	1.3
4	0.2	0.3	4	0.2	0.5
δ=9 mm					
Mode	Error in f (%)	Error in E (%)			
1	122.2	393.8			
2	7.4	15.3			
3	1.1	2.3			
4	0.4	0.8			

The first mode of the beam is also included in Table 2.8 for various values of the gap parameter δ. It is worth stating here that sinusoidal expansion for the mode shapes of vibration is assumed in ASTM E 756 standard [1] and this standard states that "for sandwich composite beams, this approximation is acceptable only at the higher modes, and it has been the practice to ignore the first mode results. For the uniform and free-layer damped beam configurations the first mode results may be used." It is clearly seen here that the first mode is the worst affected by the gap parameter and the use of the data for the first mode does not result in any consistent material properties. Even when δ=3 mm, the value of the error in estimated Young's modulus is about 30% for the first mode. The values of the errors in estimated Young's modulus are 15.3% for the second mode and 2.3% for the third mode when δ=9 mm. More detailed discussion and comparisons of the results are given in Section 2.5.4.

2.5.3 Theoretical modelling of electromagnetic effect

The objective of this section is to model the electromagnetic effect created by non-contact exciters in the Oberst test rig. For this, the mechanical effect of electromagnetic field on the system needs to be investigated.

Although the adverse effects of magnetic excitation in OBM are not specifically addressed, there are many studies published in the literature investigating the magnetic viscous damping and the increase of natural frequency of structural components vibrating under magnetic fields [148-157]. As far as the magnetic damping is concerned, a conductor moving relative to the magnetic source generates eddy currents that are dissipated into heat due to the resistivity of the conductor. This process of the generation and dissipation of eddy current causes the system to function as a viscous damper [155]. It should be noted that in references [148-157], mechanical systems are externally forced to vibrate in a magnetic field, i.e., the magnetic field itself was not the main source of excitation. Under this condition, it is found in these investigations that the magnetic viscous damping ratio increases as a function of the magnetic flux density. For example, Takagi et al. [149], Zhou and Miya [151] and Lee and Lin [157] studied the variation in damping level of a cantilevered beam forced to vibrate in magnetic field and their results show that the increase in the damping level of the structure can be very significant at strong levels of magnetic induction.

In order to examine the actual effect of the electromagnetic exciter on the damping level of the Oberst beam studied here, the estimated second and the third natural frequencies and the corresponding loss factors obtained from measured FRFs on the steel beams whose lengths are L=180 mm and L=220 mm are listed in Table 2.9. It should be noted that the second mode is the second worst affected mode and, as stated before, the use of the data for the first mode does not result in any consistent material properties. As can be seen in Table 2.9, the electromagnetic excitation does not have any remarkable effect on the damping values of the beams. For example, for the second mode of the beam with L=180 mm, at relatively higher electromagnetic field effect (large δ value), the loss factor η is about 0.0013 (corresponding viscous damping ratio =0.00065) while η is 0.0012 at very low electromagnetic field effect (small δ value). In this case, the difference is only 0.0001. In most cases, this level of difference is quite compatible with the repeatability of the damping estimation using the measurement system and the damping estimation methods. Furthermore, it should be noted that the identified modal damping levels listed in Table 2.9 are about η = 0.001 and this level of damping is very compatible with the expected level for mild steel measured in non-vacuum environment [158]. As a result, it can be safely said that the electromagnetic exciter does not introduce any significant level of damping to the system under test. This statement, at first, may not appear to be in accordance with the results in references [149, 151, 157]. However, there is no conflict at all. Possible reasons why the magnetic damping level introduced by the electromagnetic exciter is negligible in the tests here are as follows: (i) The levels of magnetic flux density used in non-contact excitation in OBM are quite small, (ii) Only a small portion of the Oberst beam, i.e., only the tip of the beam, is exposed to the magnetic field, and (iii) Unlike the test structures in cited references, the Oberst beam here is not externally forced to vibrate in a magnetic field. Instead, the dynamic magnetic field itself is used as an excitation.

Considering the results presented above, it seems appropriate to model the electromagnetic effect as a stiffness modification [144, 149, 151, 154, 157] to the specimen. Accordingly, the electromagnetic field around the free end of the clamped beam is modelled by two parallel springs, the spring coefficients of the individual springs being $k/2$ as depicted in Figure 2.18. In what follows, the effect of modifying the Oberst beam with a spring at the free end is modelled and analysed. Then,

predictions are compared with those obtained from Oberst beam tests in order to verify that the electromagnetic excitation has in fact an additional stiffness effect.

Table 2.9 : Estimated natural frequencies and corresponding loss factor values using the measured FRFs on two different Oberst beams.

	L=180 mm				*L*=220 mm			
	Mode 2		Mode 3		Mode 2		Mode 3	
δ (mm)	f (Hz)	η	f (Hz)	η	f (Hz)	η	f (Hz)	η
1	157.83	0.0012	441.48	0.0011	106.7	0.0012	298.2	0.0009
3	158.05	0.0012	441.58	0.0011	107.0	0.0012	298.4	0.0009
5	158.66	0.0012	441.85	0.0011	107.6	0.0013	298.5	0.0010
7	160.11	0.0013	442.50	0.0011	109.5	0.0014	299.4	0.0010
9	163.78	0.0013	444.16	0.0012	114.3	0.0014	301.5	0.0010

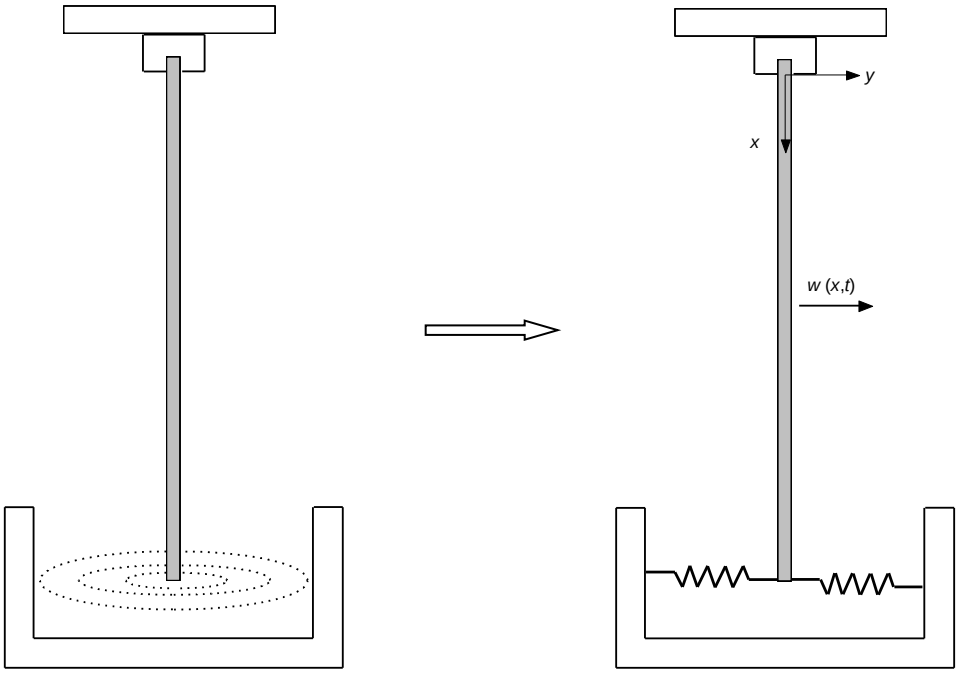

Figure 2.18 : Electromagnetic field around the free end of the beam (left) and two parallel springs at the free end of the beam (right).

The system in Figure 2.18 is a beam with fixed-linear spring BCs. The equation of motion for the free transverse vibration of the beam is already given by Equation 2.10. The eigenvalue problem of a beam with fixed-linear spring BCs is solved in the literature [159]. Here, this problem is utilised for modelling the magnetic effect at the free end of the Oberst beam. The BCs of the clamped end (x=0) of a beam is given by Equation 2.11 and the BCs of the other end (x=L) of the beam supported by spring of the beam are given by

$$EI\left.\frac{\partial^2 w}{\partial x^2}\right|_{x=L}=0 \qquad \left.\frac{\partial}{\partial x}\left[EI\frac{\partial^2 w}{\partial x^2}\right]\right|_{x=L}=-kw\big|_{x=L} \tag{2.26}$$

where L is the length of the beam. Assuming a solution of the form $w(x,t)=X(x)e^{i\omega t}$, the following equation can be written:

$$X(x)=a_1\sin\alpha x+a_2\cos\alpha x+a_3\sinh\alpha x+a_4\cosh\alpha x \tag{2.27}$$

where

$$\alpha^4=\frac{\rho A\omega^2}{EI} \tag{2.28}$$

Applying the BCs, the characteristic equation is obtained as [159]

$$\lambda^{3/4}\left(\cosh\lambda^{3/4}\cos\lambda^{1/4}+1\right)-\beta\left(\cos\lambda^{1/4}\sinh\lambda^{3/4}-\cosh\lambda^{1/4}\sin\lambda^{1/4}\right)=0 \tag{2.29}$$

where

$$\beta=\frac{kL^3}{EI} \tag{2.30}$$

$$\lambda=\frac{\rho AL^4\omega^2}{EI} \tag{2.31}$$

For specific values of β which is proportional to k, the value of the characteristic equation is plotted against λ values and the roots of the characteristic equation are determined graphically. Then, the natural frequencies are calculated using Equation 2.31. The stiffness coefficient of magnetic spring (k) and the corresponding β values used in the analyses here are listed in Table 2.10. This makes it possible to relate the k values to β values and vice-versa.

Table 2.10 : Spring stiffness k and the corresponding β values used in the analyses.

k (N/m)	0	8	16	32	64	96	128	160	192	255
β	0	0.5	1	2	4	6	8	10	12	16

After λ values, thus the natural frequencies for each individual mode, are determined, the Young's modulus of the beam material is calculated using the Equation 2.24. Note that, in reality, the increase in stiffness of the beam is due to the magnetic

spring, but as the electromagnetic effect is not known at the beginning and not considered in the calculation procedure in OBM [1-2], this effect manifests itself as an artificial increase in the Young's modulus of the Oberst beam material. This is precisely the main motivation behind the study here. Natural frequencies, estimated Young's modulus and the corresponding errors in natural frequencies and Young's moduli of the bare beam of L= 220 mm for different spring stiffness k (or β values) are listed in Table 2.11. It should be noted that the correct values of natural frequencies and Young's modulus are those corresponding to the case when k=0. When $k \neq 0$, the expected errors in calculated natural frequencies are plotted against the magnetic spring stiffness k for individual modes in Figure 2.19.

Table 2.11 : Natural frequencies, estimated Young's modulus and corresponding errors for a steel beam (L= 220 mm) for various values of k (N/m).

			k=0					k=8		
Mode	λ	f (Hz)	Error in f (%)	E (GPa)	Error in E (%)	λ	f (Hz)	Error in f (%)	E (GPa)	Error in E (%)
1	12.36	16.99	0.0	203.94	0.0	14.35	18.30	7.7	236.60	16.0
2	485.5	106.46	0.0	203.88	0.0	487.5	106.68	0.2	204.72	0.4
3	3807	298.12	0.0	203.92	0.0	3809	298.20	0.0	204.03	0.1
4	14620	584.22	0.0	203.93	0.0	14620	584.22	0.0	203.93	0.0
			k=16					k=32		
Mode	λ	f (Hz)	Error in f (%)	E (GPa)	Error in E (%)	λ	f (Hz)	Error in f (%)	E (GPa)	Error in E (%)
1	16.32	19.52	14.9	269.19	32.0	20.2	21.72	27.8	333.29	63.4
2	489.5	106.90	0.4	205.57	0.8	493.6	107.35	0.8	207.30	1.7
3	3811	298.28	0.1	204.14	0.1	3815	298.44	0.1	204.36	0.2
4	14620	584.22	0.0	203.93	0.0	14630	584.42	0.0	204.07	0.1
			k=64					k=96		
Mode	λ	f (Hz)	Error in f (%)	E (GPa)	Error in E (%)	λ	f (Hz)	Error in f (%)	E (GPa)	Error in E (%)
1	27.73	25.44	49.8	457.24	124.2	34.95	28.56	68.1	576.27	182.6
2	501.9	108.25	1.7	210.79	3.4	510.5	109.17	2.5	214.39	5.2
3	3823	298.75	0.2	204.78	0.4	3831	299.06	0.3	205.21	0.6
4	14630	584.42	0.0	204.07	0.1	14640	584.62	0.1	204.21	0.1
			k=128					k=160		
Mode	λ	f (Hz)	Error in f (%)	E (GPa)	Error in E (%)	λ	f (Hz)	Error in f (%)	E (GPa)	Error in E (%)
1	41.87	31.26	84.0	690.37	238.5	48.5	33.65	98.1	799.98	292.3
2	519.2	110.10	3.4	218.06	7.0	528.1	111.04	4.3	221.80	8.8
3	3839	299.37	0.4	205.63	0.8	3847	299.69	0.5	206.07	1.1
4	14650	584.82	0.1	204.35	0.2	14660	585.02	0.1	204.49	0.3
			k=192					k=255		
Mode	λ	f (Hz)	Error in f (%)	E (GPa)	Error in E (%)	λ	f (Hz)	Error in f (%)	E (GPa)	Error in E (%)
1	54.84	35.78	110.6	904.46	343.5	66.71	39.46	132.3	1100.07	439.4
2	537.2	111.99	5.2	225.61	10.7	555.9	113.92	7.0	233.45	14.5
3	3856	300.04	0.6	206.55	1.3	3872	300.66	0.9	207.39	1.7
4	14670	585.22	0.2	204.63	0.3	14680	585.42	0.2	204.77	0.4

It is clearly seen here that the first mode is the worst affected by the magnetic spring stiffness and the first obvious result is that the use of the first mode does not result in any consistent material properties. As the spring stiffness increases, the natural frequencies and the Young's modulus increase for all individual modes. When k=8 N/m, the natural frequency of the second mode, the calculated Young's modulus (E) and the error in E are found to be 106.68 Hz, 204.72 GPa and 0.4%, respectively. When k=255 N/m, these values jump to about 113.92 Hz, 233.45 GPa and 14.5%, respectively. Detailed discussion and comparisons of the results with experimental data are given in Section 2.5.4.

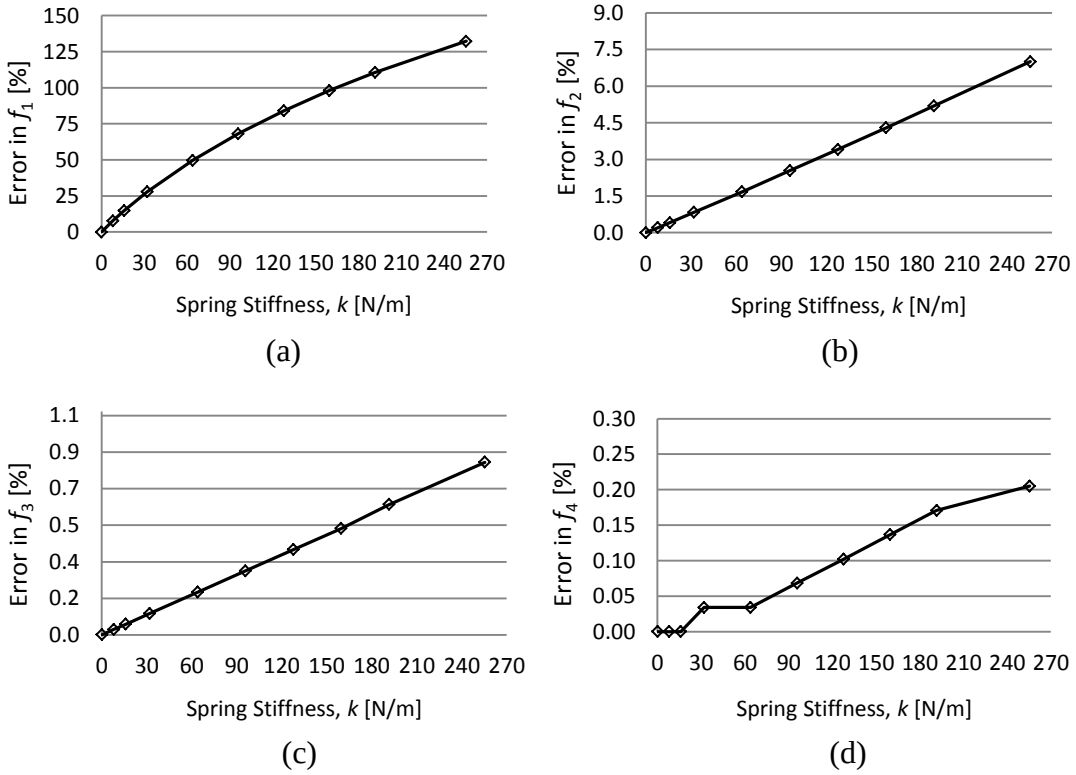

Figure 2.19 : Errors in natural frequencies against spring stiffness, k for 1st (a), 2nd (b), 3rd (c), and 4th (d) modes.

As a final remark of this section, it is worth pointing out that the electromagnetic interaction is actually a distributed effect rather than being concentrated at the tip of the beam. However, results from a FE analysis, not presented here for brevity, showed that modelling the stiffness modification as a distributed effect does not make any significant changes in natural frequencies for the first 4 modes considered here.

2.5.4 Results

Experimental results and those obtained from theoretical modelling of the electromagnetic field created by the non-contact exciter described in Section 2.5.2 and 2.5.3 are evaluated and compared here. Based on experimental data, the estimated Young's moduli are plotted against the mode number for various values of the gap parameter, δ, in Figure 2.20. Also, the errors in natural frequencies and Young's modulus are plotted against the mode number for different values of δ in Figure 2.21. It is clearly seen here again that the first mode is the worst affected by the gap parameter. The experimental results in Figure 2.21 are plotted again in Figure 2.22, but this time the data associated with the first mode are excluded so as to make the effects of δ on other modes more obvious. It is clear that as the mode number increases, the effect of the gap parameter decreases. The reason for this is that the magnetic spring at the tip of the beam affects the lower modes more than the higher ones. The reason for this is that the natural frequencies of the lower modes of a cantilever beam are more sensitive to the stiffness modification at the tip of the beam. Sensitivities of the natural frequencies of the clamped beam to the tip stiffness modification ($\partial f/\partial k$) are calculated and presented in Figure 2.23. The results clearly confirm the statement above. Considering the results presented so far, it is strongly recommend that the first mode should not be used if the adverse effect of the electromagnetic excitation is not removed. In fact, the results here show that the errors introduced in estimated material properties due to adverse effect of the electromagnetic excitation can also be quite large even for higher modes.

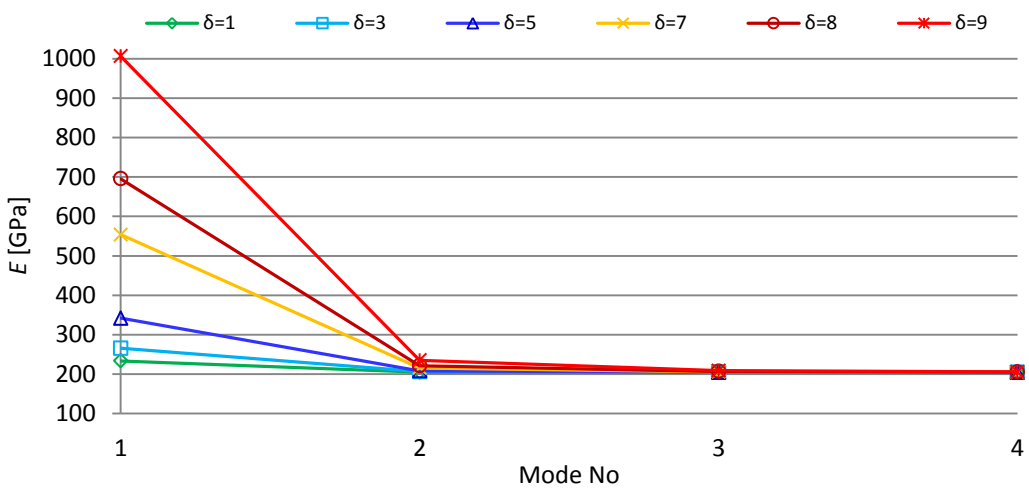

Figure 2.20 : Young's modulus for various levels of magnetic field (δ values).

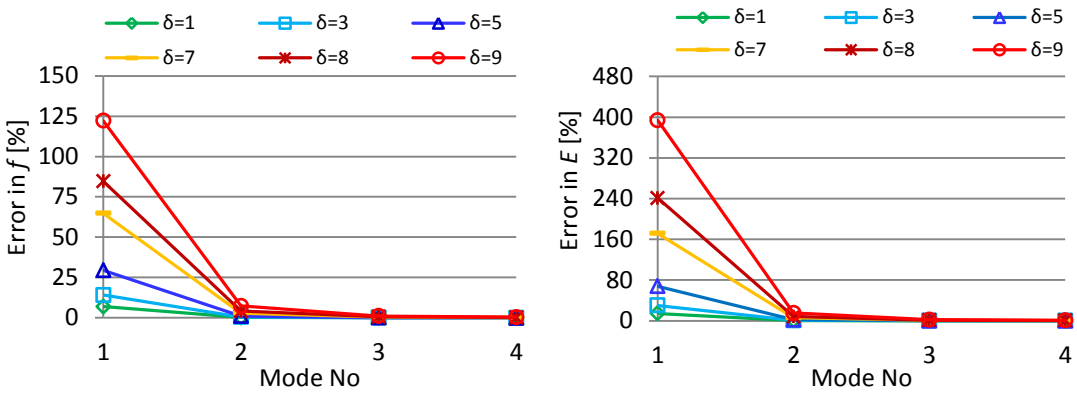

Figure 2.21 : Errors in natural frequencies (left) and Young's moduli (right) for various levels of magnetic field (for various δ values).

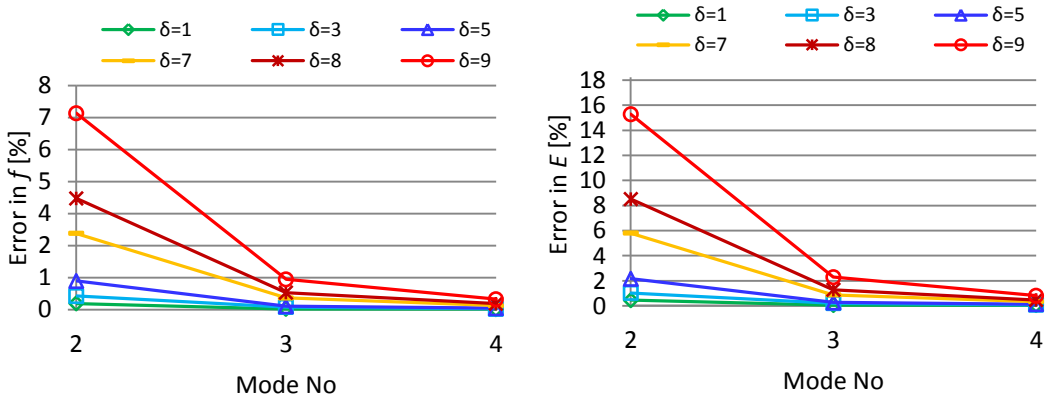

Figure 2.22 : Errors in natural frequencies (left) and Young's moduli (right) for various level of magnetic field (δ values) excluding the first mode.

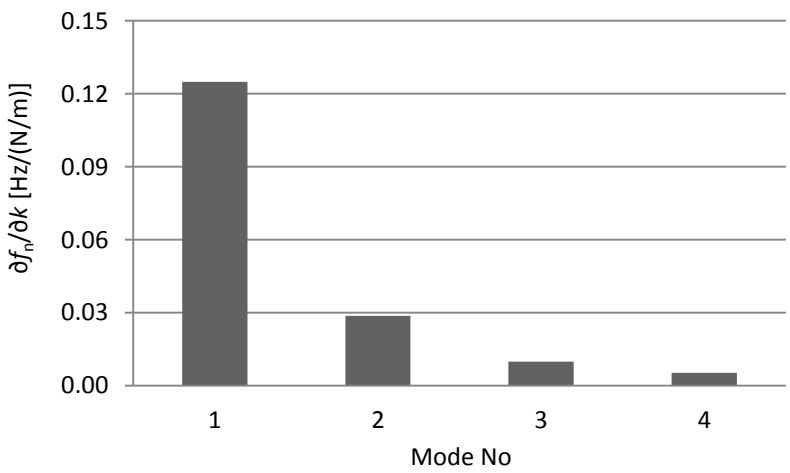

Figure 2.23 : Sensitivities of natural frequencies to stiffness modification at the tip of the beam.

The errors in natural frequencies (f) and Young's modulus (E) are plotted against δ value for individual modes (excluding the first mode) in Figure 2.24. It is obvious

that all the modes are somewhat affected by the gap parameter. As δ increases, the errors in f and E increase for all the modes. It is also seen that the second mode is more affected than other higher modes and electromagnetic effect decreases as the mode number increases. These results suggest that the gap parameter δ should be as small as possible. However, δ should not be less than the minimum level required for adequate excitation of the Oberst beam. For the non-contact exciter used in this thesis, the value of the gap parameter less than about 3 mm may yield relatively less errors in natural frequencies. It should be noted, however, that the errors in Young's modulus are several times greater than the error in natural frequencies. Therefore, it is very important to be able to identify the natural frequencies with higher accuracy than the accuracy required for the material properties.

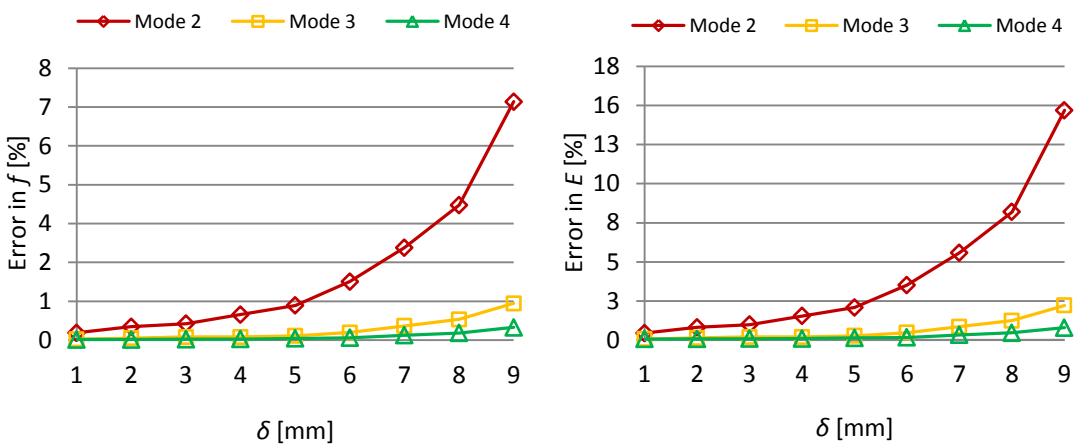

Figure 2.24 : Errors in natural frequencies (left) and Young's modulus (right) against the levels of magnetic field (for various δ values).

As described in Section 2.5.3, non-contact electromagnetic excitation introduces an additional stiffness at the free-end of the Oberst beam. Increase in stiffness coefficient of the magnetic spring makes the Oberst beam stiffer, resulting in higher natural frequencies. Therefore, instead of the gap parameter, the experimental results in Figures 20-22 and Figure 2.24 can also be presented as a function of the corresponding magnetic spring coefficient (k) that yields the same values of natural frequencies and Young's moduli. The values of the magnetic spring coefficient satisfying this requirement are determined for individual modes and presented in Figure 2.25. The first observation in Figure 2.25 is that the magnetic spring coefficient exhibits non-linear behaviour with respect to the gap parameter δ. It is also seen in the same figure that linear spring can represent the electromagnetic

effect successfully up to a certain gap parameter beyond which the estimated *k* values for individual modes start to deviate from each other, exhibiting higher stiffness values at higher modes. This is again possibly due to the non-linear behaviour of the magnetic spring coefficient with respect to the amplitude of vibration for individual modes under white noise type of random excitation.

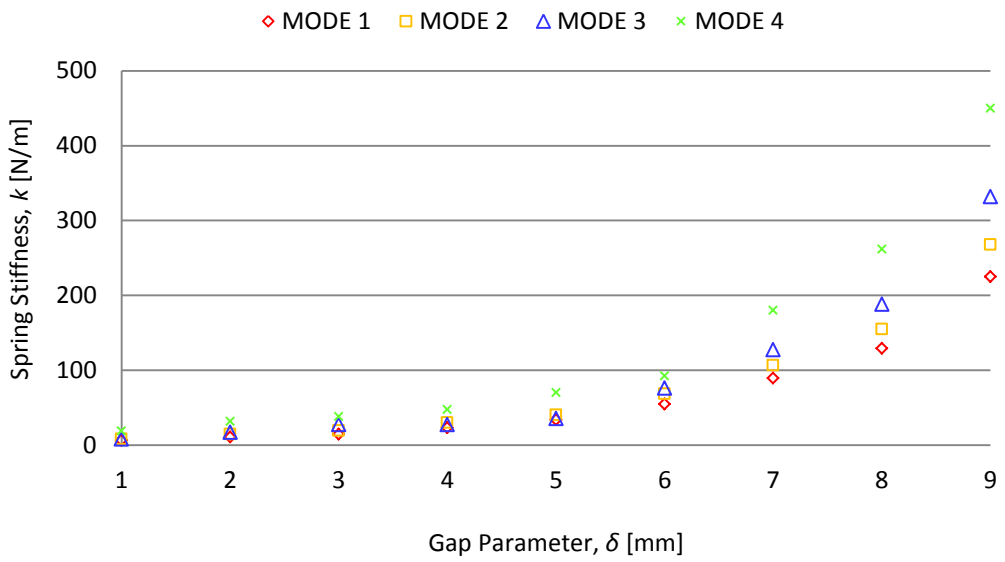

Figure 2.25 : Corresponding *k* values for δ values for each mode.

The results indicate that in the case of the gap parameter δ=9 mm, the error in Young's modulus is about 15% for the second mode. The same level of error in Young's modulus for this mode is obtained if the value of the magnetic spring is set to 270 N/m. This level of error (i.e., 15%) is quite large, noting that the material properties are supposed to be determined with high accuracy using sensitive OBM. Excluding the first mode, the results presented so far also indicate that if the allowable error in estimated Young's modulus is to be less than 2 %, the maximum value of the gap parameter should be 4 mm or less which in turn leads to magnetic spring stiffness value being less than 40 N/m. It is obvious that significant levels of errors can be introduced in the Oberst beam tests if the magnetic exciters are used without taking the electromagnetic spring effect into considerations. However, as shown in the next section, the adverse effect of the magnetic exciter can be removed from the results.

By conducting experiments on beams with various lengths, it is shown here that the level of errors vary with the length of the Oberst beam. In Figure 2.26, the values of the errors in the estimated Young's modulus using the second natural frequencies are

plotted for various beam lengths as a function of the gap parameter (again for δ=1 mm to δ=9 mm). Figure 2.26 shows that the gap parameter, or electromagnetic spring, affects the longer beams more than the short ones. This is not surprising since the long beams are more flexible than the short ones and the same magnetic spring will affect the flexible beams more than relatively stiffer beams in terms of changes in natural frequencies. It is seen that as the δ value decreases, the results converge to the same "correct" value of the Young's modulus. This also implies that the δ value must be kept as low as possible while keeping the non-contact excitation at acceptable levels.

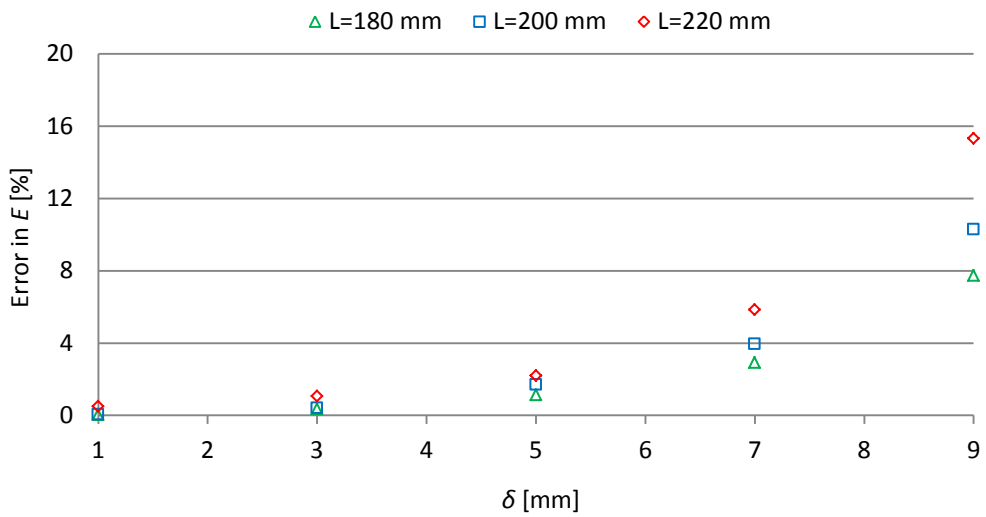

Figure 2.26 : Error in Young's modulus with respect to gap parameter for various beam lengths (L) calculated using the second mode of the beam.

The values of the errors in estimated Young's modulus using the second mode are plotted for various beam lengths as a function of magnetic spring stiffness k in Figure 2.27. It is seen again that as the k value decreases, the results converge to the same "correct" value of the Young's modulus. Here, the experiments and the analyses are performed using beam lengths of L=180 mm, L=200 mm and L=220 mm, noting that ASTM E 756 standard [1] suggests the length of the cantilever beam to be between 180 to 250 mm. As seen in Figures 2.26 and 2.27, using longer beam samples results in higher errors. For example, the errors in E for beams of length, L=180 mm, 200 mm and 220 mm are about %8, %11 and %15, respectively when δ=9 mm (or when k=270 N/m).

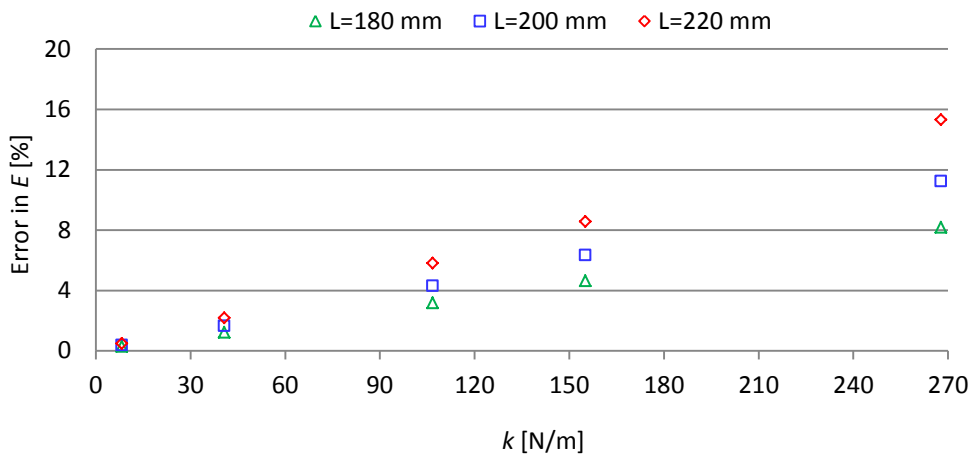

Figure 2.27 : Error in Young's modulus with respect to spring stiffness for various beam lengths calculated using the second mode of the beam.

The results presented so far clearly demonstrates that non-contact magnetic exciter also acts like a spring attached between the tip of the Oberst beam and the ground, and this can introduce very significant levels of errors in estimated material properties. One simple approach to minimise this adverse effect may appear to position the tip of the Oberst beam into the exciter slot such that the gap parameter is as small as possible. However, it is very likely that a very small gap parameter will result in not being able to excite the system properly for adequate FRF measurements. Therefore, the majority of the measurements have to be performed using adequate (not very small) gap parameter and the adverse effects of the electromagnetic field should be removed.

2.5.5 Removing the adverse effects of electromagnetic excitations

As described in this chapter so far, the adverse effect of electromagnetic excitation can be removed for homogeneous materials whose properties are known to be independent of frequency. Removing this adverse effect from test results for homogeneous Oberst beams that are made of materials with frequency dependent properties may appear to be somewhat difficult at first sight. The reason for this is that, in this case, the increase in natural frequencies can be due to both electromagnetic effect and frequency-dependent material properties. However, it is very reasonable to assume that the changes in elastic properties of materials can be considered negligible for a very narrow frequency range defined by the natural frequencies of the Oberst beam with and without the electromagnetic effect for a particular mode of vibration. Therefore, for the narrow frequency range described,

the changes in natural frequencies can be attributed to the effect of electromagnetic excitation only.

The removal of the adverse effects of electromagnetic excitation certainly requires some preliminary tests in order to identify the natural frequencies of a test beam as a function of the gap parameter. The results of the extensive tests performed in this chapter are presented in Figure 2.28 for modes 1 to 4. It is immediately seen that the overall trend for individual modes is very similar. It is also seen in Figure 2.28 that, for the particular electromagnetic exciter used in this thesis, the natural frequency variation with respect to the gap parameter is almost linear up to a certain gap parameter (i.e., δ= 4 mm) beyond which the relationship becomes quite non-linear. Therefore, if an electromagnetic exciter is to be used in the non-linear region, such non-linear behaviour must be taken into account during the removal of the adverse effects. It is noted, however, that this non-linear behaviour can also be described using a linear equation if the natural frequencies are plotted as a function of the square of the gap parameter (δ^2). The effectiveness of such an approximation is illustrated in Figure 2.29 where the natural frequencies in Figure 2.28 are plotted as a function δ^2 for δ=3 to 8 mm.

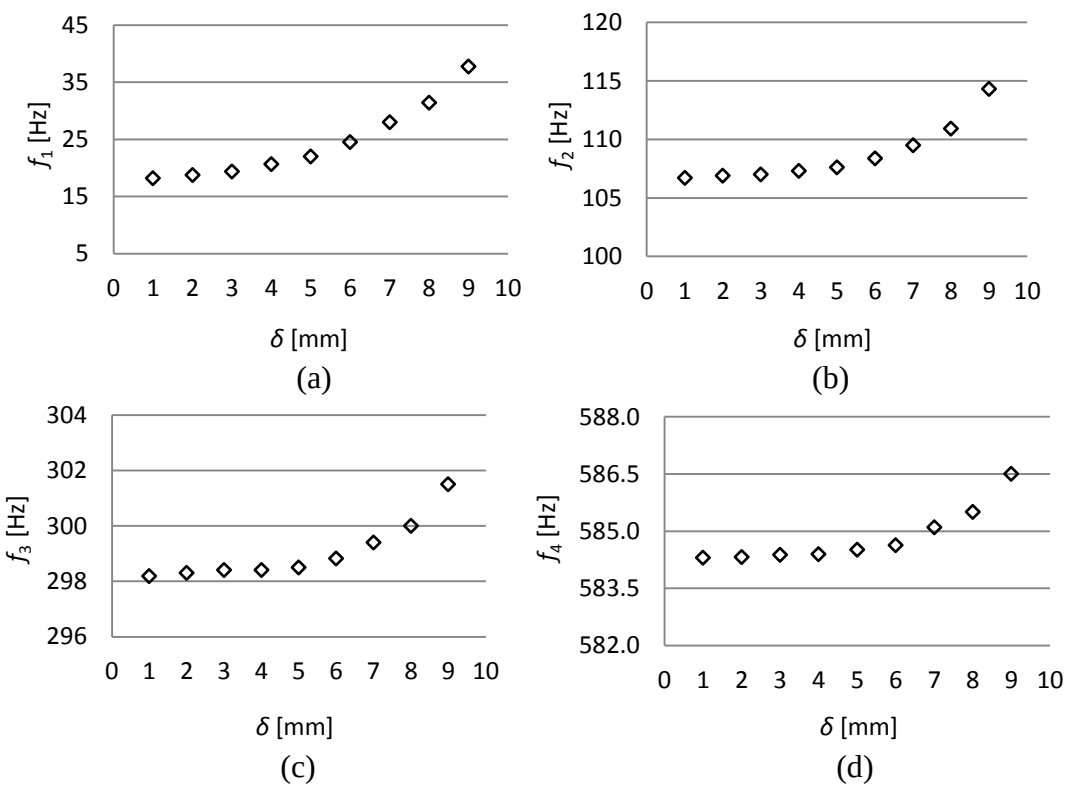

Figure 2.28 : Natural frequencies against the gap parameter, δ for 1st (a), 2nd (b), 3rd (c) and 4th (d) modes.

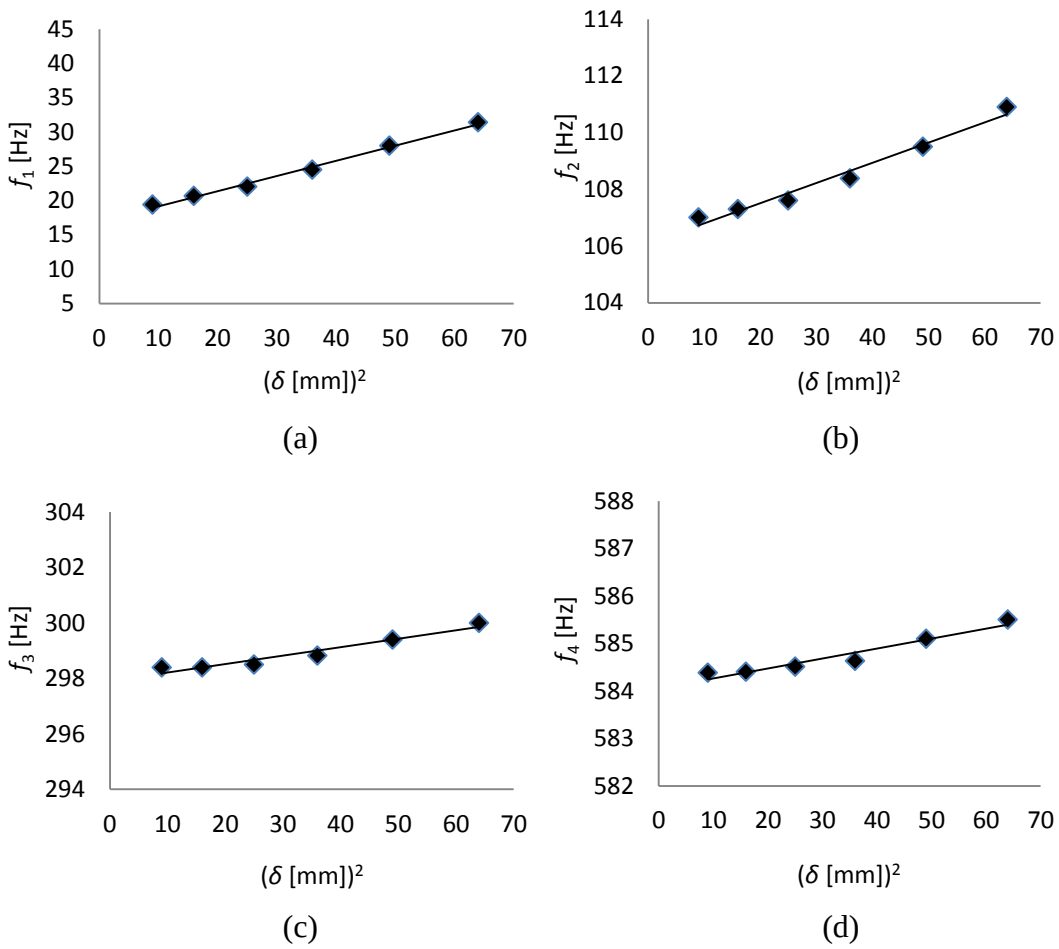

Figure 2.29 : Determined natural frequencies against the squared gap parameter, δ^2 for 1st (a), 2nd (b), 3rd (c), and 4th (d) modes.

The published studies in the literature are revisited so as to determine if there is any established relationship between the natural frequencies of the Oberst beam and the so-called gap parameter. Takagi et al. [149] experimentally demonstrated that natural frequency of a ferromagnetic thin plate (beam), which is set along the uniform magnetic field, increases with external magnetic induction due to magnetic stiffness effect. The results in [149] show that the measured natural frequency increases with the in-plane magnetic field in a convex manner. Zhou and Miya [151] neglected the effect of eddy current on the natural frequency and developed a theoretical magnetic force model based on variational principle. They used this model to predict the natural frequencies of a beam plate under an in-plane magnetic field and compared the predictions with the experimental data in [149]; the predicted natural frequencies concavely increase with the in-plane magnetic field, but the experimental data are convex curves. Bonisoli and Vigliani [154] proposed a complex viscous damping model for describing both damping and dynamic stiffening effects due to eddy

currents induced in the vibrating cantilever beam under passive effects of rare-earth permanent magnets. They demonstrated the validity of the model by comparing the measured and the predicted frequency response functions. Bonisoli and Vigliani [154] also introduced an equivalent single degree of freedom model and derived expressions for the magnetic viscous damping and the magnetic stiffening coefficients. It is very interesting to note that the magnetic stiffening coefficient obtained in Bonisoli and Vigliani [154] is a second order function (when the magnetic induction gradient is assumed to be constant) in terms of the geometric dimension (*b*) of the permanent magnet, which may loosely be interpreted as the gap parameter in the study here. However, if the magnetic induction gradient is not constant, it is expected that the natural frequency variation with respect to the geometric dimension (*b*) of the permanent magnet will be a non-linear function. More recent and probably the most advanced work presented by Lee and Lin [157] proposed several magnetic force models to study the dynamic behaviour of ferromagnetic beam plate under uniform magnetic field. Their model included the contribution of the tangential and normal components of the magnetic field on the boundary and the corresponding natural frequency for the cantilever beam under an in-plane magnetic field is expressed as

$$\omega^2 = \omega_1^2 + \frac{1}{\Delta}\int_0^L N_x(x)\left[\frac{d\hat{w}}{dx}\right]^2 \mathrm{d}x - \frac{1}{\Delta}\int_0^L \hat{q}_y^m(x)\hat{w}(x)\mathrm{d}x - \frac{1}{\Delta}\int_0^L \hat{q}_y^L(x)\hat{w}(x)\mathrm{d}x \qquad \textbf{(2.32)}$$

where

$$\Delta = \rho a\int_0^L \left[\hat{w}(x)\right]^2 dx \qquad \textbf{(2.33)}$$

where ω_1 represents the natural frequency of the beam without any magnetic loading, $N_x(x)$ is the axial force, $\hat{q}_y^m(x)$ is the transverse magnetic force, $\hat{q}_y^L(x)$ is the Lorentz force due to eddy current, $\hat{w}(x)$ is the mode shape of the beam and, a and D are the thickness and the flexural rigidity of the beam, respectively. After various simplifying assumptions, Lee and Lin [157] predicted the natural frequencies and compared these results with experimental data. However, their results still show that the predicted natural frequency curves are concave while the experimental data are

convex curves when the applied magnetic induction increases from 0 Tesla to 0.6 Tesla. It is also shown in [157] that the prediction of the distribution of the transverse magnetic force around the tip of the beam is quite difficult.

It is worth stating here that all the studies summarised above are dealing with the dynamics of beam-like structures which are forced to vibrate under uniform magnetic field. However, the Oberst beam in this thesis is partially excited at the tip by time-varying magnetic field itself, which makes the theoretical modelling of the dynamics of the Oberst beam a very challenging task.

Based on the arguments summarised above, a procedure is proposed in this thesis in order to remove the adverse effects of the electromagnetic excitation from individual modes. This procedure is based on estimating the natural frequencies of the test beam corresponding to zero gap parameter via extrapolation. The steps of the proposed method are as follows:

i) Perform some preliminary tests and identify the minimum acceptable gap parameter δ_1 at which the magnetic exciter provides sufficient levels of excitation.

ii) Determine the natural frequencies (${}_1 f_r$) of the test beam at δ_1.

iii) Increase the gap parameter to a new higher value, δ_2, and determine the natural frequencies (${}_2 f_r$) again.

iv) If it cannot be guaranteed (based on previous experience or data) that the electromagnetic exciter is operating within the linear range in terms of the gap parameter, repeat the tests at least for one more gap parameter (δ_3) and determine the corresponding natural frequencies.

v) Using the identified natural frequencies associated with different values of the gap parameter, estimate the "correct" natural frequencies of the beam for individual modes corresponding to zero gap parameter (${}_0 f_r$) via linear or non-linear extrapolation, whichever is more appropriate.

vi) Estimate material properties of the homogeneous beam using the "correct" natural frequencies of the beam.

The linear and non-linear extrapolation processes that can be used in this procedure are schematically illustrated in Figure 2.30. The measured data will reveal whether the electromagnetic exciter is operating within the linear or non-linear range, hence

which extrapolation technique to use. It is worth stating here that performing tests corresponding to more than 2 or 3 different values of the gap parameter can yield more accurate extrapolation results at the expense of more test time. It should also be stated that the proposed procedure above does not depend on whether the beam is uniform or composite. Therefore, this procedure is equally applicable for composite beams.

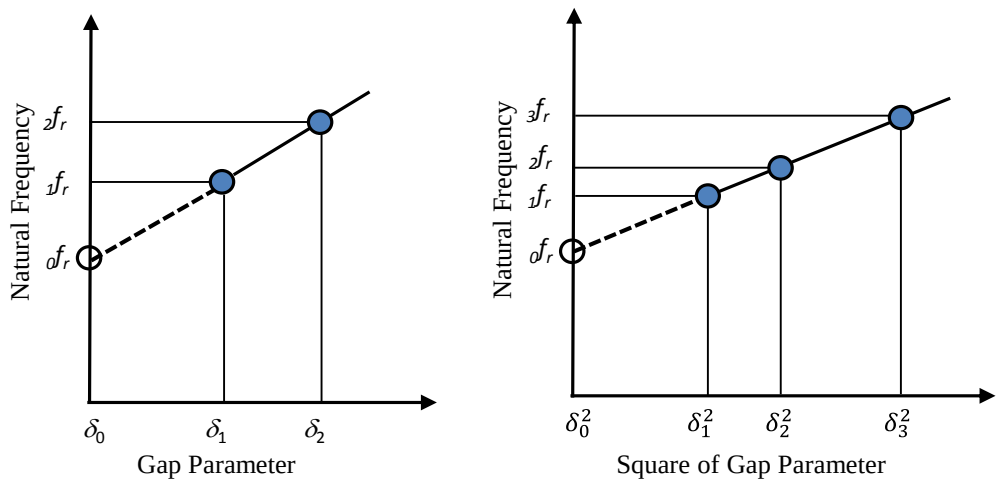

Figure 2.30 : Determination of the "correct" natural frequencies via linear extrapolation (left) and non-linear extrapolation (right).

The proposed procedure described above is applied to the homogeneous beam used in this study for various values of the gap parameter. Some of the results - natural frequencies, estimated Young's Moduli and associated errors - are presented in Table 2.12 when linear extrapolation is used. As can be seen, the errors in the corrected values are significantly smaller than the initial errors. For example, when the first and the second modes are considered, the errors in the calculated Young's modulus before any correction are 21.8% and 0.8%, respectively when δ_1 =2 mm. However, when the corrected natural frequencies are used (with δ_2 =4 mm), these values decrease to -1.4% and 0.1%, respectively.

If the measured data (corresponding to at least 3 different gap parameter values) suggest that the magnetic exciter is operating within the non-linear range, then it is more appropriate to use the non-linear extrapolation process. Some sample results are presented in Table 2.13 so as to assess to performance of the proposed method for the non-linear case. The results in Table 2.13 confirm that the non-linear extrapolation technique is also very effective in reducing the errors caused by the

electromagnetic exciter. For example, if δ_1 =4 mm, the errors in the calculated Young's modulus before any correction are 47.5% and 1.6%, respectively for the first and the second modes. However, when the corrected natural frequencies are used (δ_2 =5 mm and δ_3 =6 mm), these values drop to 4.6% and -0.2%.

Table 2.12 : Results of the proposed approach based on linear extrapolation for a steel bare beam (L= 220 mm).

			δ_1=2 and δ_2=4			
Mode	f_{meas} (Hz)	$f_{corrected}$ (Hz)	E_{meas} (GPa)	$E_{corrected}$ (GPa)	Error in E_{meas} (%)	Error in $E_{corrected}$ (%)
1	18.8	16.9	248.4	201.1	21.8	-1.4
2	106.9	106.5	205.6	204.0	0.8	0.1
3	298.3	298.2	204.1	204.0	0.1	0.1
4	584.3	584.2	204.0	203.9	0.0	0.0
			δ_1=2 and δ_2=5			
Mode	f_{meas} (Hz)	$f_{corrected}$ (Hz)	E_{meas} (GPa)	$E_{corrected}$ (GPa)	Error in E_{meas} (%)	Error in $E_{corrected}$ (%)
1	18.8	16.6	248.4	194.3	21.8	-4.7
2	106.9	106.4	205.6	203.8	0.8	-0.1
3	298.3	298.2	204.1	204.0	0.1	0.0
4	584.3	584.2	204.0	203.9	0.0	0.0

Table 2.13 : Results of the proposed approach based on non-linear extrapolation for a steel bare beam (L= 220 mm).

			δ_1=4 and δ_2=5 and δ_3=6			
Mode	f_{meas} (Hz)	$f_{corrected}$ (Hz)	E_{meas} (GPa)	$E_{corrected}$ (GPa)	Error in E_{meas} (%)	Error in $E_{corrected}$ (%)
1	20.6	17.4	300.7	213.4	47.5	4.6
2	107.3	106.4	207.1	203.5	1.6	-0.2
3	298.4	298.0	204.3	203.8	0.2	-0.1
4	584.4	584.2	204.1	203.9	0.1	0.0
			δ_1=4 and δ_2=6 and δ_3=8			
Mode	f_{meas} (Hz)	$f_{corrected}$ (Hz)	E_{meas} (GPa)	$E_{corrected}$ (GPa)	Error in E_{meas} (%)	Error in $E_{corrected}$ (%)
1	20.6	16.8	300.7	199.2	47.5	-2.3
2	107.3	105.9	207.1	201.8	1.6	-1.0
3	298.4	297.8	204.3	203.4	0.2	-0.2
4	584.4	583.9	204.1	203.7	0.1	-0.1

2.6 Determination of Mechanical Properties of Sample Materials

After all the improvements on the Oberst test rig presented in the previous sections, damping and elastic properties of some commercially available materials to be used in the theoretical models of structures with passive damping treatments in Chapter 4 are determined using OBM in this section. Single-sided treatments are used to

identify five different damping materials named as DM-1, DM-2, DM-3, DM-4 and DM-5. The base beam is made of steel and the width and mounted free length of the samples are b=10 mm and L=220 mm, respectively. Thickness of the base (steel) beam is H=1.0 mm while the thicknesses (H^m) of the damping materials (DM-1, DM-2, DM-3, DM-4 and DM-5 used here) are 2.2 mm. Also, the measured densities of the steel and damping materials DM-1, DM-2, DM-3, DM-4 and DM-5 are ρ=7866.7 kg/m^3 and ρ^m=2372.0, 2218.8, 2312.9, 2312.9 and 2218.8 kg/m^3, respectively.

As described in the previous sections, FRF measurements are performed on both bare and damped composite beams at various (bending) modes of vibration using the Oberst test rig given in Figure 2.7 and the procedure in Figure 2.8, and natural frequencies and modal loss factors of the bare beam (f and η) and composite beams (f^c and η^c) are identified on the measured FRFs using line-fit method [37-38] and the results are given in Table 2.14. After that, Young's moduli and material loss factors of steel (E and η) and damping materials (E^m and η^m) are determined using the formulations in Table 2.3 according to ASTM E 756 standard [1] and the results are given again in Table 2.14. As stated before, the materials whose mechanical properties given in Table 2.14 are used to prepare some test structures in Chapter 4.

Table 2.14 : Identified Young's moduli (E and E^m) and loss factors (η and η^m) for steel and damping (viscoelastic) materials using OBM.

Material	Bending Mode No	f (Hz)	η	E (GPa)	η
Steel	2	107.0	0.0016	205.9	0.0020
	3	299.0	0.0014	205.0	0.0015
	4	584.5	0.0012	204.0	0.0014
	5	966.6	0.0011	204.2	0.0012
Material	Bending Mode No	f^c (Hz)	η^c	E^m (GPa)	η^m
DM-1	2	97.9	0.0919	1.05	0.33
	3	274.6	0.1213	1.07	0.43
	4	537.7	0.1451	1.07	0.51
DM-2	2	102.4	0.1199	1.29	0.37
	3	286.7	0.1537	1.30	0.47
	4	548.8	0.1896	1.13	0.64
DM-3	2	104.0	0.0993	1.52	0.29
	3	307.7	0.1020	2.06	0.25
	4	617.6	0.1031	2.32	0.23
DM-4	2	90.2	0.0585	0.45	0.43
	3	253.0	0.0722	0.47	0.50
DM-5	2	92.4	0.0796	0.54	0.46
	3	260.9	0.0893	0.62	0.47

2.7 Concluding Remarks

Identification of damping materials is studied in this chapter. First, the theoretical background for damping materials including vibration damping is presented. Then, the Oberst Beam Method (OBM) is selected for the characterisation of damping materials in this thesis and the theoretical background of OBM is presented. After that, the effects of various parameters in the Oberst beam test, including the amplitude of the excitation, mounting conditions, input excitation type and the length of the test sample are examined in an attempt to improve the accuracy of the estimated material properties. Then, extensive tests are performed so as to determine adverse effects of electromagnetic excitation. Based on observed evidence, the electromagnetic field around the free end of the Oberst beam is modelled using a spring between the tip of the beam and the ground. Also, a method is proposed for removing the adverse effects of the electromagnetic excitation in order to obtain more accurate material properties for uniform as well as composite beams.

The assessment of the Oberst test rig parameters revealed the following conclusions. (i) A sufficient number of averages should be used in the Oberst beam tests in order to minimise the noise levels in measured FRFs. (ii) Almost identical results are obtained for both sine sweep and random type excitations when appropriate sine sweep parameter is selected. (iii) Appropriate forcing level should be determined before making the final measurements and this depends on the Oberst testing system used. It is almost certain that this process requires some initial trial tests. (iv) If more number of modes within the frequency range of interest are to be investigated, longer specimens should be selected, and vice versa. It is also worth keeping in mind that the length of the beam should be chosen such that the natural frequencies of the beam should not coincide with the frequency of the main electric power (i.e., 50 or 60 Hz). (v) Mounting conditions for the bare and the damped beams should be as identical as possible. It is found that the use of a kind of gauge or a “stopper” is very useful for assuring that the beam will have almost the same free length every time it is installed. (iv) The electromagnetic effect created by non-contact exciter could be very significant source of error in estimated material properties and this topic should be investigated in detail.

The systematic study on the effects of the non-contact electromagnetic excitation system revealed the following conclusions. (i) The electromagnetic field created by a non-contact exciter around the free end of the Oberst beam introduces additional constraints on the system. This adverse effect is modelled as a spring between the tip of the beam and the ground. The stiffening behaviour of the non-contact electromagnetic exciter can significantly reduce the accuracy of the estimated material properties. The errors in identified natural frequencies and, thus, estimated Young's modulus increase as the length of the segment of the beam exposed to the electromagnetic field (the gap parameter) increases. (ii) The first mode is the worst affected by the adverse effect of electromagnetic excitation and the use of the data associated with the first mode does not result in any consistent material properties unless the results are corrected. The errors in estimated material properties due to the stiffening effect of electromagnetic field decreases as the mode number increases. (iii) If relatively longer beams are used in the Oberst beam tests, the stiffening effect of electromagnetic field causes higher levels of errors in natural frequencies and estimated material properties. (iv) One way of reducing the stiffening effect of electromagnetic excitation, hence the error in estimated material properties, is to minimise the length of the segment of the beam exposed to the magnetic field (gap parameter) as much as possible. However, in some cases, it is very likely that this leads to insufficient levels of excitation for accurate measurements of FRFs and results in difficulties in estimating the modal parameters, especially for the Oberst beams made of materials with significant levels of damping or thick materials. Therefore, in practice, some measurements need to be performed using adequate gap parameter. In such cases, it is recommended that the adverse effects of electromagnetic excitation should be removed from test results. A method is proposed to remove the adverse effects of electromagnetic excitation from test results in order to determine the material properties with better accuracy in this thesis.

After all improvement on the Oberst test rig, damping and elastic properties of some materials to be used in the theoretical models of structures with passive damping treatments are determined using OBM.

3. IDENTIFICATION OF DAMPING UNCERTAINTY

3.1 Introduction

Identification of the damping and elastic properties of damping materials is studied in Chapter 2. In addition to the identification of the properties of damping materials, experimental identification of damping levels of structures is also required to validate the theoretical models of damped structures. However, the preliminary tests show that there is still some level of difficulty in identification of damping levels of structures using experimental data in the sense that the identified damping levels may exhibit high level of uncertainty due to noise and signal processing parameters. Therefore, a systematic study on damping uncertainty is performed in this chapter to overcome the void about damping uncertainty in the literature.

There are many sources of uncertainty that may adversely affect the accuracy of the damping estimation using measured data. The study here is concentrating on two of such major sources and aims to estimate (i) damping uncertainty due to inherent noise in the data, and (ii) damping uncertainty due to the use of exponential windowing prior to the spectrum estimation. The first source, noise, is inevitable and always present in the data, the level of which can be identified experimentally using Signal-to-Noise Ratio (SNR) via coherence function. It is not surprising that there are some studies [70-71] already available in the literature on noise as a source of uncertainty. However, the second source of damping uncertainty due to the use of exponential windowing is a topic which has not attracted sufficient attention in the literature. When impact (hammer) testing is used for Frequency Response Function (FRF) measurement, exponential windowing is often utilised before the spectrum estimation in order to avoid leakage. However, applying an exponential window to transient signals inevitably introduces the so-called numerical damping which may well be significantly higher than that of the actual damping level of the structure under test. This situation then raises the question of damping uncertainty due to adding high level of artificial damping, especially when the data are contaminated by noise. It should be stated, however, that damping uncertainty in estimated damping

level also depends on the method used for damping identification. One of the frequency domain methods, namely the line-fit method [37] is predominantly used in this investigation. The circle-fit method [36] is also used for comparison purposes.

The outline of this chapter is as follows. First, a theoretical background is provided for FRF measurements and damping estimation methods. The rest of this chapter is divided into two parts. In the first part, a damped three Degree of Freedom (DOF) system is used for simulation purposes and FRFs for this numerical system are generated with specified levels of SNR. The noisy FRFs are then analysed and individual modal damping levels are estimated. This allowed assessment of the damping uncertainty associated with noisy data characterised by SNR and damping uncertainties are estimated as a function of noise level. In the second part, the theory behind the effects of exponential windowing function is presented. Then, an experimental set-up for the measurement of FRFs with and without using exponential windowing function is described. Many FRFs are measured on a test case for the assessment of the damping uncertainty caused by the use of exponential windowing. These FRFs are then analysed in order to estimate modal damping levels for individual modes and the artificial damping due to windowing function is removed from the total damping levels. Finally, results are processed to evaluate the uncertainty of the damping estimation caused by using exponential windowing. Some results are presented showing a relationship between the uncertainty of the estimated damping level and the level of added numerical damping due to exponential windowing.

3.2 Theoretical Background

3.2.1 Frequency response function estimations

Theoretically, the FRF matrix in receptance format, $\alpha(\omega)$, for a linear system can be obtained by inverting the dynamic stiffness matrix in the following equations of motion

$$(\mathbf{K} - \omega^2\mathbf{M} + i\omega\mathbf{C})\mathbf{X} = \mathbf{F} \tag{3.1}$$

$$\boldsymbol{\alpha}(\omega) = (\mathbf{K} - \omega^2\mathbf{M} + i\omega\mathbf{C})^{-1} \tag{3.2}$$

where **M**, **K** and **C** are mass, stiffness and viscous damping matrices, respectively, **F** and **X** are the excitation and response vectors, respectively, and ω is the excitation frequency. Individual elements of the FRF matrix, more often than not, can also be obtained experimentally as explained below.

Once the input force $f(t)$ and the output vibrations $x(t)$ are measured in time domain, Fourier Transformations (FTs) of the signals are calculated and the FRF, not necessarily in receptance format, can be calculated as

$$H(\omega) = \frac{X(\omega)}{F(\omega)} \tag{3.3}$$

where $X(\omega)$ and $F(\omega)$ are the FTs of the time domain signals $x(t)$ and $f(t)$, respectively. As synchronous averaging is required, uncorrelated components (noise) is difficult to remove and the so-called coherence function is not available in the formulation in Equation 3.3. Better ways of FRF estimation are also available in the literature [35, 160]. For example, multiplication of Equation 3.3 by the complex conjugate of $F(\omega)$ yields

$$H_1(\omega) = \frac{F^*(\omega)X(\omega)}{F^*(\omega)F(\omega)} = \frac{S_{fx}(\omega)}{S_{ff}(\omega)} \tag{3.4}$$

where $S_{ff}(\omega)$ and $S_{fx}(\omega)$ are the auto spectral density function of $f(t)$ and the cross spectral density function of $f(t)$ and $x(t)$, respectively. Here the spectral densities are given as

$$S_{ff}(\omega) = \frac{F^*(\omega)F(\omega)}{\Delta\omega} \tag{3.5}$$

$$S_{fx}(\omega) = \frac{F^*(\omega)X(\omega)}{\Delta\omega} \tag{3.6}$$

where $\Delta\omega = 1/T$ is the frequency resolution and T is the measurement period. When $H_1(\omega)$ is measured, the uncorrelated signal is attenuated in the cross spectrum while the uncorrelated signal remains in the input auto spectrum. As an alternative to the formulation of $H_1(\omega)$, another FRF estimator is obtained by multiplying Equation 3.3 by the complex conjugate of $X(\omega)$ as

$$H_2(\omega) = \frac{X^*(\omega)X(\omega)}{X^*(\omega)F(\omega)} = \frac{S_{xx}(\omega)}{S_{xf}(\omega)} \tag{3.7}$$

where $S_{xx}(\omega)$ and $S_{xf}(\omega)$ are the auto spectral density function of $x(t)$ and the cross spectral density of $x(t)$ and $f(t)$. $S_{xx}(\omega)$ is computed in a way similar to that of $S_{ff}(\omega)$ and $S_{xf}(\omega)$ is the complex conjugate of $S_{fx}(\omega)$. When $H_2(\omega)$ is measured, the uncorrelated signal is attenuated in the cross spectrum while the uncorrelated signal remains in the output auto spectrum. It is worth stating that synchronous averaging is not required for the calculations of $H_1(\omega)$ and $H_2(\omega)$. Although there are some other FRF formulations in the literature, $H_1(\omega)$ and $H_2(\omega)$ are widely used in practical applications. In the context of this thesis, $H_1(\omega)$ is mostly measured and used.

The coherence function, γ^2 - being an indication of the degree of linear relationship between input and output - is always checked during FRF measurements and it is given as [35]

$$\gamma^2(\omega) = \frac{S_{fx}^*(\omega)S_{fx}(\omega)}{S_{ff}(\omega)S_{xx}(\omega)} \tag{3.8}$$

The coherence function can also be expressed in terms of two FRF estimations in Equations 3.4 and 3.7 as

$$\gamma^2(\omega) = \frac{H_1(\omega)}{H_2(\omega)} \tag{3.9}$$

The coherence can be less than unity due to (i) the existence of unmeasured force input to the system, (ii) inadequate frequency resolution leading to bias error, (iii) the presence of uncorrelated noise on the signals $f(t)$ and $x(t)$ and (iv) a non-linear relationship between f and x.

3.2.2 Signal to noise ratio

As the uncertainty in damping estimation caused by noise is examined in the next section, it is appropriate to present the definition of noise in measured FRFs here. The noise level, measured as signal-to-noise ratio in dB ($\mathrm{SNR_{dB}}$), is defined as

$$\mathrm{SNR_{dB}} = 10\log_{10}\left(\frac{P_{\mathrm{signal}}}{P_{\mathrm{noise}}}\right) = 10\log_{10}\left(\frac{A_{\mathrm{signal}}}{A_{\mathrm{noise}}}\right)^2 \qquad \textbf{(3.10)}$$

where P and A above represent the signal power and the root mean square (RMS) amplitude, respectively. SNR is also defined as [161]

$$\mathrm{SNR} = \frac{\gamma^2}{1-\gamma^2} \qquad \textbf{(3.11)}$$

It is obvious that the SNR defined by Equation 3.11 is readily available in FRF measurements when spectrum averaging is used.

3.2.3 System identification

The half-power [35], circle-fit [36] and line-fit [37] methods can be used to obtain natural frequencies, mode shapes and damping values from measured FRFs of structures [35-39]. For completeness, these methods are briefly described below.

3.2.3.1 Half-power method

As the half-power method [35, 39] is the simplest system identification method, the formulation of this method is presented here first. Half-power points are defined as the two frequencies where the response amplitude is $1/\sqrt{2}$ of the maximum response level [39]. Using the definition of the half-power points, the frequencies corresponding to half power points (ω_a, ω_b) are in relation with η_r and ω_r as

$$\eta_r = 2\zeta_r = \frac{\omega_a^2 - \omega_b^2}{2\omega_r^2} \tag{3.12}$$

For small η_r, damping level is approximated as

$$\eta_r \cong \frac{\omega_a - \omega_b}{\omega_r} = \frac{\Delta\omega}{\omega_r} \tag{3.13}$$

Furthermore, by assuming that the overall response around a particular natural frequency is attributed to a single mode [35] as represented in Equation 3.14, the local maximum value of the FRFs, $|\hat{\alpha}|$, hence the modal constant, ${}_rA$, is determined as given in Equations 3.15 and 3.16, respectively.

$$\alpha_{jk}(\omega) = \frac{{}_rA_{jk}}{\omega_r^2 - \omega^2 + i\eta_r\omega_r^2} + \sum_{s=1, s\neq r}^{N} \frac{{}_sA_{jk}}{\omega_s^2 - \omega^2 + i\eta_s\omega_s^2} \tag{3.14}$$

$$|\hat{\alpha}| = \frac{{}_rA}{\eta_r\omega_r^2} \tag{3.15}$$

$${}_rA = |\hat{\alpha}|\eta_r\omega_r^2 \tag{3.16}$$

3.2.3.2 Circle-fit method

The circle-fit method [35-36, 39] is based on fitting a circle to an FRF data around the vicinity of a natural frequency. The response model of a system with structural damping can also be expressed as in Equation 3.17 since the effect of the modal constant, ${}_rA_{jk}$, is to scale the size of the circle by the amplitude $|{}_rA_{jk}|$ and rotate it by the phase angle $\angle{}_rA_{jk}$ [35].

$$\bar{\alpha}(\omega) = \frac{1}{\omega_r^2 - \omega^2 + i\eta_r\omega_r^2} \tag{3.17}$$

Considering the plot of $\bar{\alpha}(\omega)$ with the given parameters in Figure 3.1, the expressions in Equations 3.18 and 3.19 can be written for any frequency ω as

$$\tan\phi = \frac{\eta_r}{1-\left(\omega/\omega_r\right)^2} \tag{3.18}$$

$$\tan\left(\frac{\pi}{2}-\phi\right) = \tan\left(\frac{\theta}{2}\right) = \frac{1-\left(\omega/\omega_r\right)^2}{\eta_r} \tag{3.19}$$

Using the expressions in Equations 3.18 and 3.19, Equation 3.20 can be obtained. The natural frequency can be determined by differentiating Equation 3.20 with respect to θ and then with respect to ω, and then setting the resulting equation to zero.

$$\omega^2 = \omega_r^2\left(1-\eta_r \tan\left(\theta/2\right)\right) \tag{3.20}$$

Referring to Equation 3.19, the following expressions for the specific points in Figure 3.1 can be written as

$$\tan\left(\theta_a/2\right) = \left[\left(\omega_a/\omega_r\right)^2 - 1\right]\Big/\eta_r \tag{3.21}$$

$$\tan\left(\theta_b/2\right) = \left[1-\left(\omega_b/\omega_r\right)^2\right]\Big/\eta_r \tag{3.22}$$

Then, the modal loss factor can be obtained from these two expressions as:

$$\eta_r = \frac{\omega_a^2 - \omega_b^2}{\omega_r^2\left(\tan\left(\theta_a/2\right)+\tan\left(\theta_b/2\right)\right)} \tag{3.23}$$

When Equation 3.17 is plotted in Re-Im plane, it traces a circle, diameter of which is given by

$${}_rD_{jk} = 1\big/\eta_r\omega_r^2 \tag{3.24}$$

By scaling the size of the circle by $\left|{}_rA_{jk}\right|$, the modal constant is determined as [35]

$$\left|{}_rA_{jk}\right| = \eta_r\omega_r^2\,{}_rD_{jk} \tag{3.25}$$

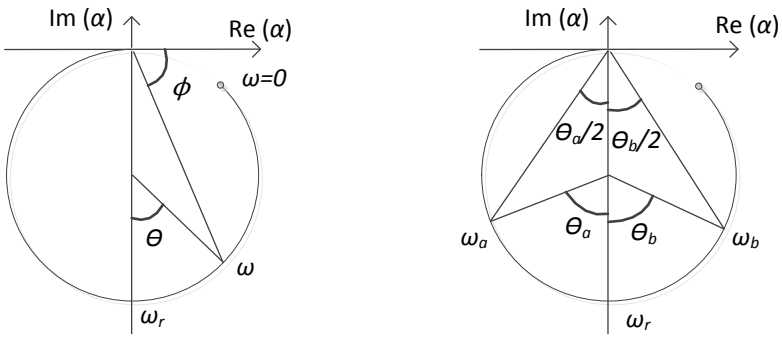

Figure 3.1 : Frequency and angle definitions in circle-fit procedure.

3.2.3.3 Line-fit method

The line-fit analysis procedure for a MDOF system assumes that around a particular natural frequency ω_r, with modal constant ${}_rA$ and damping η_r, the response includes a constant residual term ${}_rR$ which represents the contribution of the modes other than the one of the interest [35, 37, 39, 162] as given in below.

$$\alpha_{jk}(\omega)_{\omega\simeq\omega_r} \cong \frac{{}_rA_{jk}}{\omega_r^2-\omega^2+i\eta_r\omega_r^2} + {}_rR_{jk} \qquad \textbf{(3.26)}$$

A new FRF term, $\alpha'_{jk}(\omega)$, which is the difference between the actual FRF and the value of the FRF at one fixed frequency in the range of interest $\left(\alpha_{jk}(\Omega)\right)$, is defined in line-fit method in order to remove the residual effect [35] as

$$\alpha'_{jk}(\omega) = \alpha_{jk}(\omega) - \alpha_{jk}(\Omega) \qquad \textbf{(3.27)}$$

The inverse FRF defined below is used for the modal analysis.

$$\Delta(\omega) = \frac{\left(\omega^2-\Omega^2\right)}{\alpha'_{jk}(\omega)} \qquad \textbf{(3.28)}$$

This can also be written as [35, 39]:

$$\Delta(\omega) = \frac{\left(\omega_r^2-\omega^2+i\eta_r\omega_r^2\right)\left(\omega_r^2-\Omega^2+i\eta_r\omega_r^2\right)}{{}_rA_{jk}} \qquad \textbf{(3.29)}$$

The $\Delta(\omega)$ is separated into the real and imaginary parts which are mainly related to the variable frequency, ω, as

$$\mathrm{Re}(\Delta) = m_R\omega^2 + C_R \qquad \mathrm{Im}(\Delta) = m_I\omega^2 + C_I \tag{3.30}$$

where

$$m_R = a_r\left(\Omega^2 - \omega_r^2\right) - b_r\left(\eta_r\omega_r^2\right), \quad m_I = -b_r\left(\Omega^2 - \omega_r^2\right) - a_r\left(\eta_r\omega_r^2\right) \tag{3.31}$$

and

$$_rA_{jk} = a_r + ib_r \tag{3.32}$$

By selecting a fixed frequency Ω_j in the vicinity of a natural frequency ω_r and then calculating the possible $\Delta(\omega)$ using the remaining measured data points, real and imaginary values are plotted against ω^2. Least squares fit approach is used to compute the best-fit straight line in each case to determine $m_R\left(\Omega_j\right)$ and $m_I\left(\Omega_j\right)$ for the selected frequency, Ω_j. These m_R and m_I parameters are also linear functions of Ω^2 as given below [35, 38, 39].

$$m_R = n_R\Omega^2 + d_R, \qquad m_I = n_I\Omega^2 + d_I \tag{3.33}$$

where

$$n_R = a_r \qquad n_I = -b_r \tag{3.34}$$

$$d_R = -b_r\left(\eta_r\omega_r^2\right) - a_r\left(\omega_r^2\right) \qquad d_I = -b_r\left(\omega_r^2\right) - a_r\left(\eta_r\omega_r^2\right) \tag{3.35}$$

Defining $p = n_I/n_R$ and $q = d_I/d_R$, the following expressions can be written.

$$\eta_r = \frac{(q-p)}{1+pq}; \quad \omega_r^2 = \frac{d_R}{(p\eta_r - 1)n_R}; \quad a_r = \frac{\omega_r^2(p\eta_r - 1)}{(1+p^2)d_R}; \quad b_r = -a_r p \tag{3.36}$$

The set of plots of the parameters $m_R(\Omega)$ and $m_I(\Omega)$ against Ω^2 will also result in straight lines. By determining the slopes of the best-fit straight lines through these two set of plots, the best values of n_R and n_I, and their intercepts with the vertical axis, d_R and d_I are found and finally modal parameters are determined [35, 38, 39]. A typical graphical output of this algorithm is illustrated in Figure 3.2 [38].

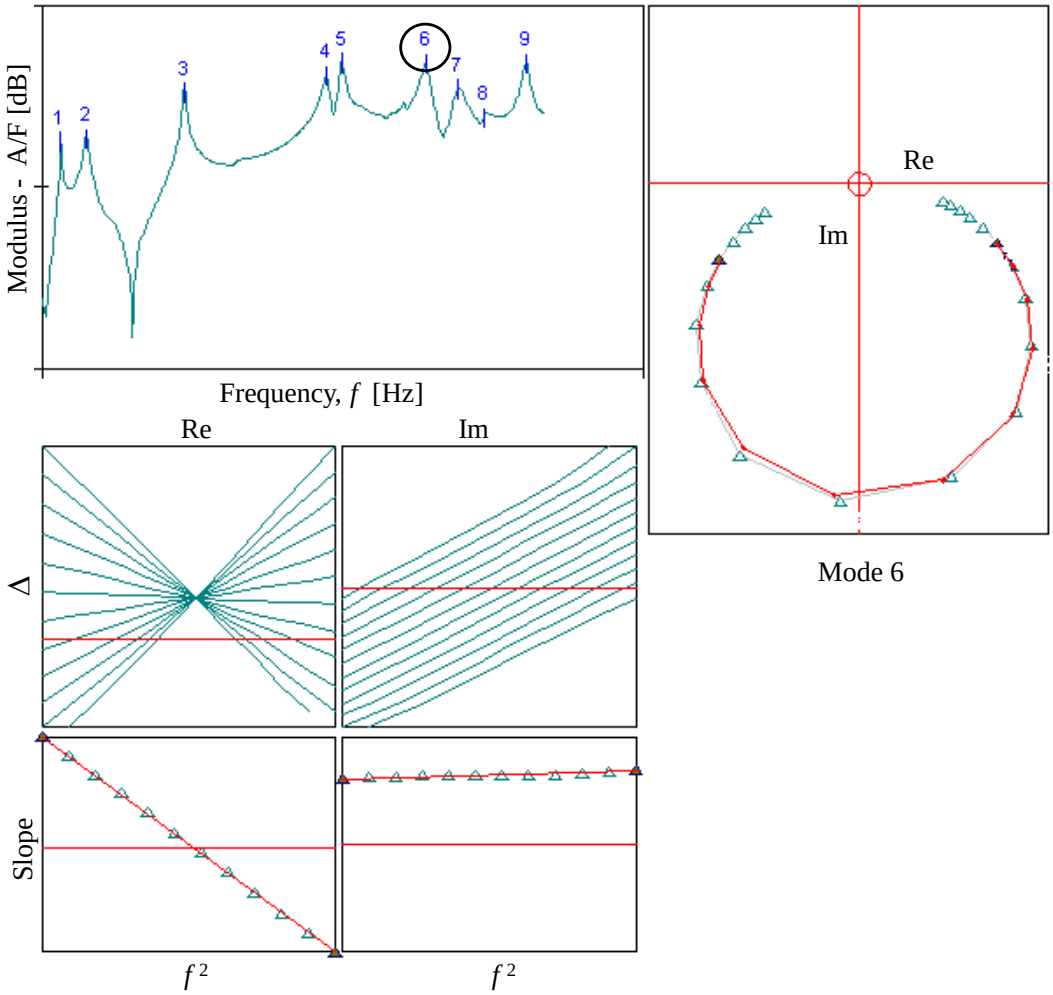

Figure 3.2 : Damping estimation using line-fit algorithm.

3.3 Damping Uncertainty Due to Noise: Numerical Simulation

In this section, it is aimed to assess and estimate the level of uncertainty in the estimated damping levels associated with noisy data alone. Therefore, no windowing function is involved in this section. The next section deals with the use of exponential windowing function with noisy data via an experimental study.

A simple one–dimensional mass-spring system given in Figure 3.3 is used here. This system is assumed to comprise some spring elements with complex stiffness coefficients defined as

$$k_1^* = k_1(1 + i\eta_a) \tag{3.37}$$

$$k_2^* = k_2(1 + i\eta_b) \tag{3.38}$$

$$k_3^* = k_3(1 + i\eta_c) \tag{3.39}$$

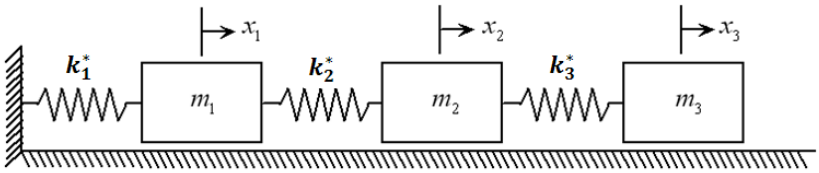

Figure 3.3 : A mass-spring system.

For this system, assuming harmonic free vibration leads to the following equation in the frequency domain

$$(\mathbf{K}^* - \lambda^2\mathbf{M})\boldsymbol{\psi} = \mathbf{0} \tag{3.40}$$

where $\mathbf{K}^*$ indicates complex stiffness matrix here. The solution of the eigenvalue problem above yields

$$\lambda_r^2;\ \boldsymbol{\psi}_r \quad r = 1,2,3 \tag{3.41}$$

where λ_r^2 and $\boldsymbol{\psi}_r$ are complex eigenvalues and eigenvectors (mode shapes), respectively. By defining $\lambda_r^2 = \omega_r^2(1 + i\eta_r)$, natural frequencies and loss factors are determined using Equations 3.42 and 3.43, respectively.

$$\omega_r^2 = \mathrm{Re}\left(\lambda_r^2\right) \tag{3.42}$$

$$\eta_r = \frac{\mathrm{Im}\left(\lambda_r^2\right)}{\mathrm{Re}\left(\lambda_r^2\right)} \tag{3.43}$$

If mass normalised mode shapes, $\boldsymbol{\phi}_r$, are used, an FRF between a response coordinate *j* and an excitation coordinate *k* can be expressed as [35]

$$\alpha_{jk}(\omega) = \sum_{r=1}^{N} \frac{(\phi_{jr})(\phi_{kr})}{\omega_r^2 - \omega^2 + i\eta_r\omega_r^2} \tag{3.44}$$

It is aimed here to demonstrate damping uncertainty associated with using noisy data, i.e., noisy FRF here. For this purpose, using the structural parameters listed in Table 3.1, the eigenvalue problem in Equation 3.40 is solved and mass normalized mode shapes ($\boldsymbol{\phi}_r$) are calculated. Then, a typical FRF shown in Figure 3.4 is generated using Equation 3.44. First of all, the exact loss factor values are calculated for each mode according to Equation 3.43. Using the line-fit method described earlier, the loss factor values are also determined using the noise-free FRF. Then, the loss factors are estimated again using the same line-fit method, but this time using the noisy FRFs. For this purpose, new FRFs contaminated with additive white Gaussian noise are generated. Two typical FRFs with SNR_{dB} values of 10 and 50 are presented in Figure 3.5. As stated, additive type of noise (see Equation 3.10) is considered here, which is the main reason why the data around natural frequencies are less affected. It should also be noted that only the data around natural frequencies are used for damping estimation in this study. Here, the frequency resolution is set to 0.05 Hz and about 40 FRFs are regenerated and analysed for each SNR value.

Exact loss factors (η_{exact}) calculated using Equation 3.43 and loss factors determined by analysing the noise-free FRF using line fit method (η_{lf}) are listed in Table 3.2. As expected, the estimated loss factor values by analysing the noise-free FRF are the same as the exact values. Perfect matching is also seen in Figure 3.6 where the raw and the regenerated FRFs using the estimated modal parameters are compared in complex plane for three modes.

Table 3.1 : Numerical values of parameters used in the model.

k_1, k_2,	9500	4000	1200
m_1, m_2, m_3 (kg)	0.9	0.4	0.1
η_a, η_b, η_c (%)	2.0	1.0	1.0

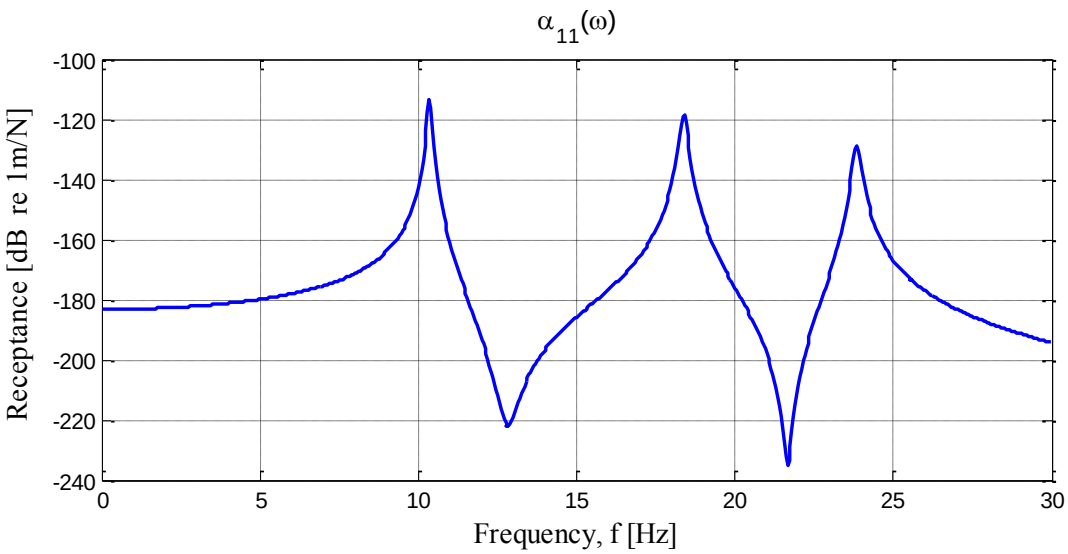

Figure 3.4 : A typical FRF.

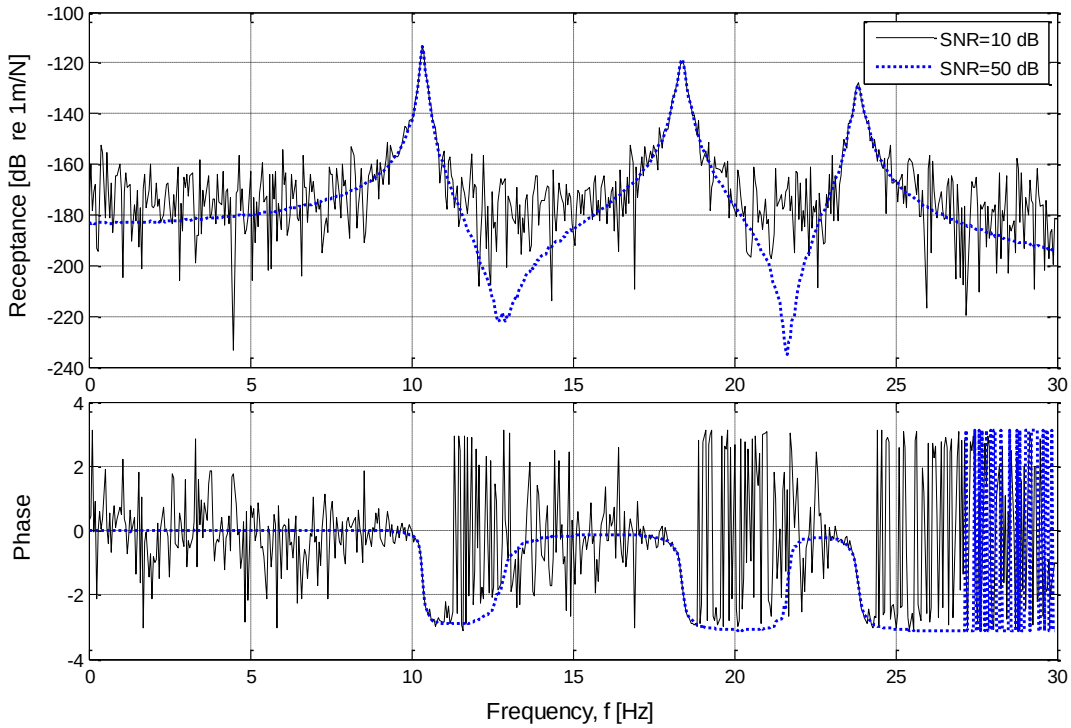

Figure 3.5 : Sample generated FRFs with additive noise.

Table 3.2 : Natural frequencies and loss factors: exact values and values determined using the noise-free FRF.

Mode No	1	2	3
f_{exact} (Hz)	10.358	18.378	23.837
f_{lf} (Hz)	10.358	18.378	23.837
η_{exact} (%)	1.483	1.340	1.177
η_{lf} (%)	1.483	1.340	1.177

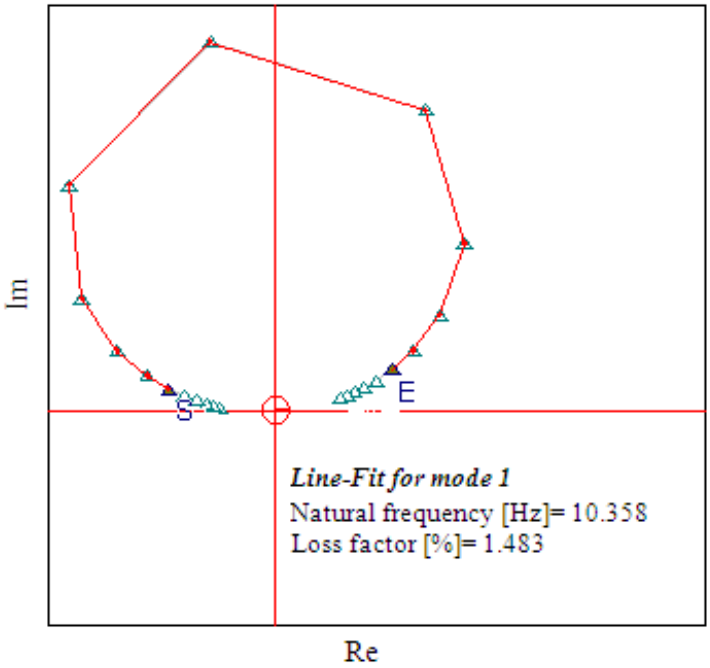

(a)

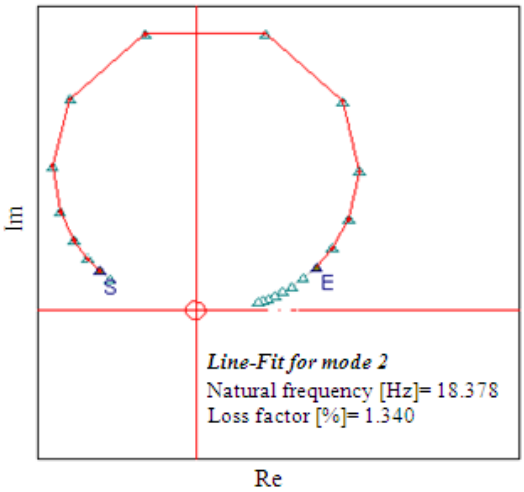

(b)

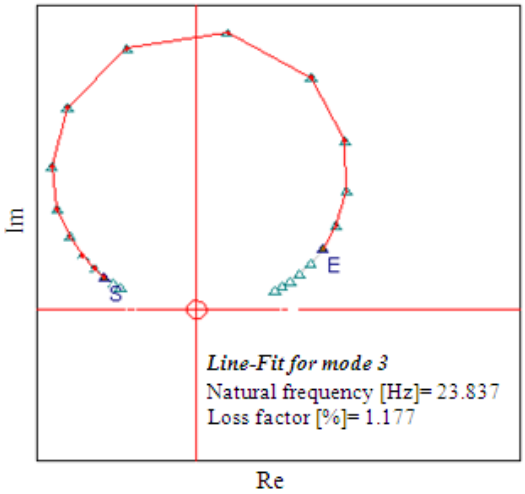

(c)

Figure 3.6 : Typical analyses for damping estimation using the noise-free FRF for 1st (a), 2nd (b) and 3rd (c) modes.

The noisy FRFs are also analysed using the same line-fit method in order to determine the damping levels and the associated uncertainty. The raw and the regenerated FRFs using the estimated modal parameters are compared in complex plane again for three modes in Figure 3.7. It is not surprising that noisy data inevitably introduce some loss of accuracy in estimated damping levels. Even if the SNR is kept constant, different levels of modal damping is estimated each time new noisy FRF is generated and analysed. Modal damping values determined using all

generated noisy FRFs with different SNR values are presented in Figure 3.8 for the three modes of the damped 3 DOF system. As expected, as SNR increases the damping values obtained from FRFs converge to actual damping values for individual modes.

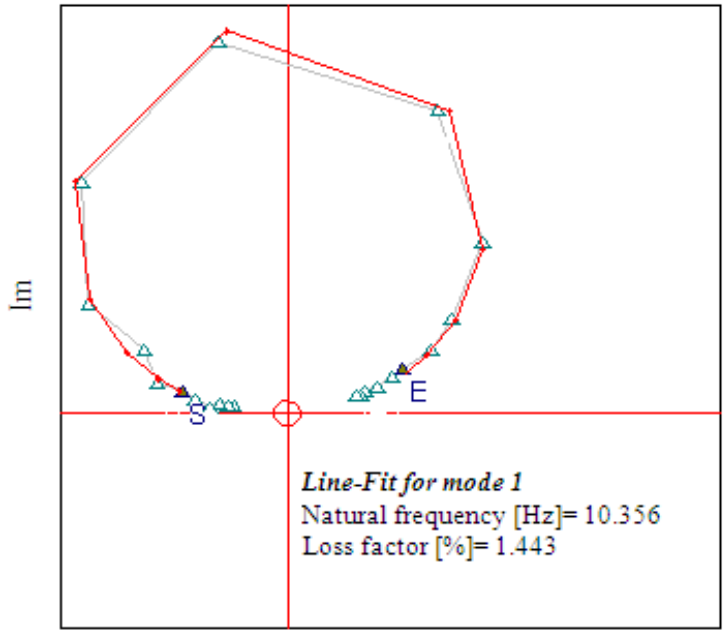

(a)

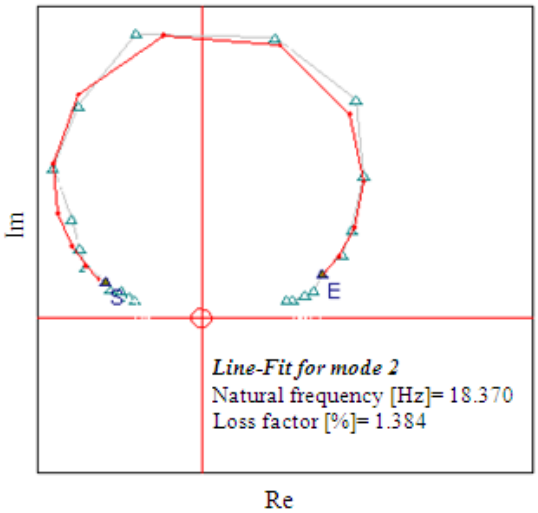

(b)

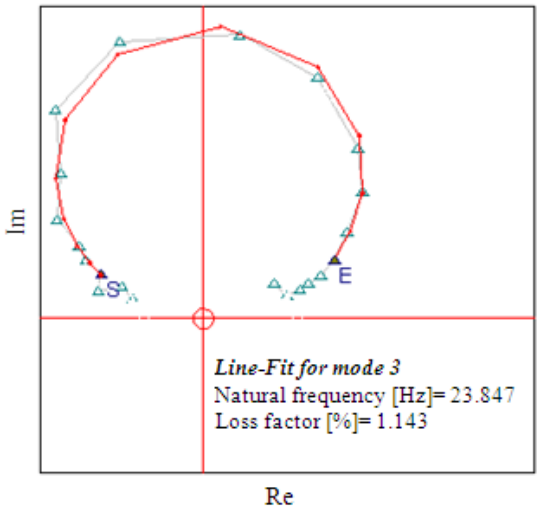

(c)

Figure 3.7 : Typical analyses for damping estimation using the noisy FRF for 1st (a), 2nd (b) and 3rd (c) modes.

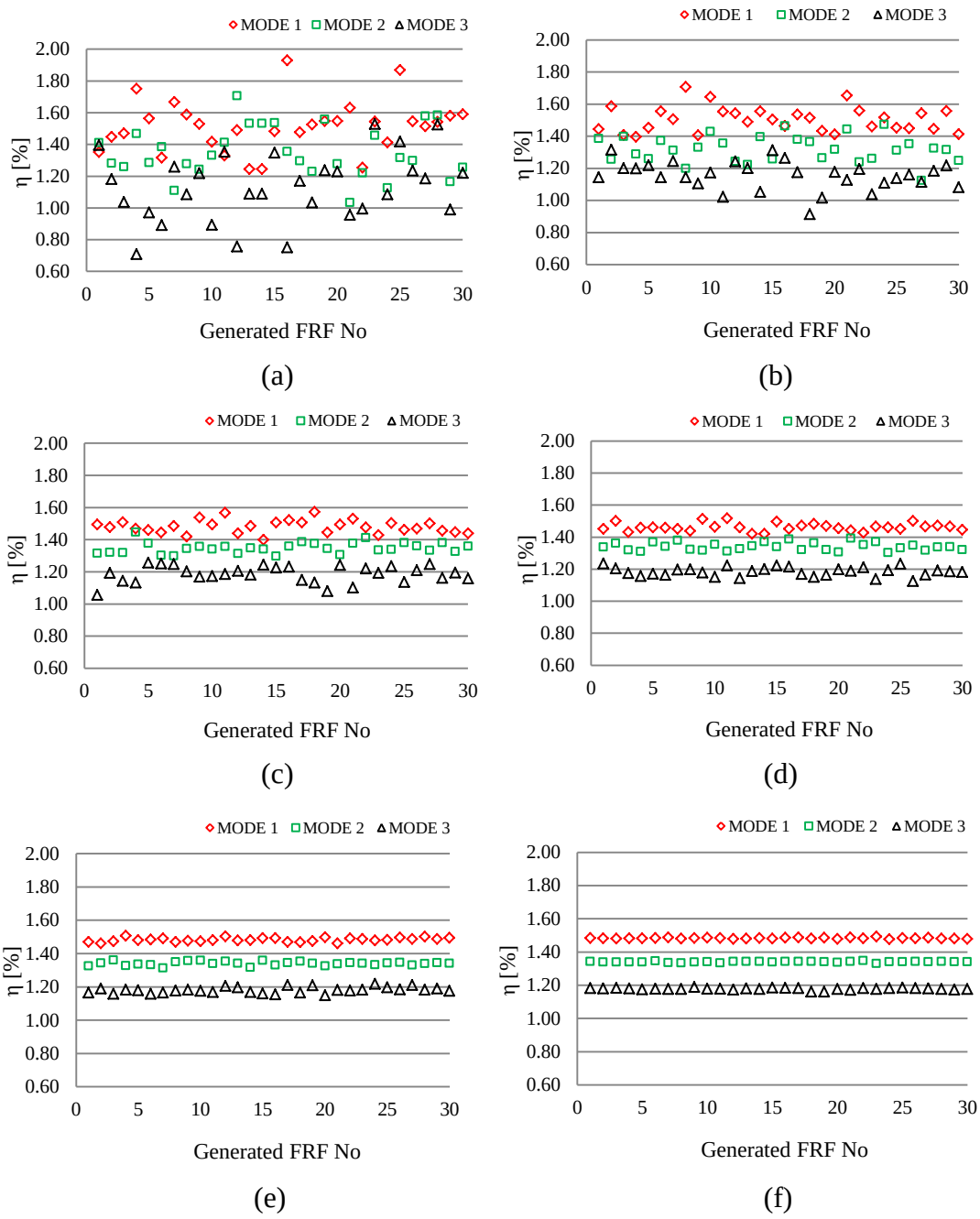

Figure 3.8 : Estimated damping values using noisy FRFs with SNR_{dB}= 10 (a), 15 (b), 20 (c), 25 (d), 30 (e) and 40 (f).

An uncertainty parameter is defined here so as to quantify the variability of the damping estimation as

$$\text{Uncertainty}[\%]= \frac{|\eta_{\max} - \eta_{\min}|}{\eta_{\text{actual}}} \cdot 100 \qquad \textbf{(3.45)}$$

The maximum and the minimum modal damping values for various SNR values are listed in Table 3.3 for individual modes. Then, damping uncertainties are calculated

using Equation 3.45 and the results are presented in Table 3.4. As can be seen, the line-fit method is very successful in dealing with noisy data and yields damping levels with an uncertainty close to zero when SNR_{dB} is greater than 50. However, if the noise level is higher, the uncertainty in estimated damping levels starts to increase and can reach to very high levels, especially if SNR_{dB} is less than 30.

Table 3.3 : Estimated loss factor (minimum and maximum) values using noisy FRFs for a range of SNR.

SNR_{dB}	Mode 1	Mode 2	Mode 3
50	1.480 - 1.484	1.338 - 1.342	1.171 - 1.181
40	1.476 - 1.492	1.330 - 1.348	1.160 - 1.189
30	1.461 - 1.507	1.313 - 1.360	1.149 - 1.218
25	1.421 - 1.518	1.303 - 1.393	1.126 - 1.236
20	1.399 - 1.573	1.298 - 1.447	1.056 - 1.257
15	1.395 - 1.706	1.123 - 1.472	0.913 - 1.316
10	1.244 - 1.929	1.033 - 1.406	0.709 - 1.529
η_{exact} (%)	1.483	1.340	1.177

Table 3.4 : Uncertainty values in estimated loss factors for a range of SNR.

	Uncertainty (%)		
SNR_{dB}	Mode 1	Mode 2	Mode 3
50	<0.3	<0.3	<0.6
40	1.1	1.3	2.5
30	3.1	3.5	5.9
25	6.5	6.7	9.3
20	11.7	11.1	17.1
15	21.0	26.0	34.2
10	46.2	50.2	69.7

Damping uncertainty values for different SNR values in Table 3.4 are also presented in graphical form in Figure 3.9. As can be seen, there is a gradual increase in uncertainty for all the modes as the SNR value decreases.

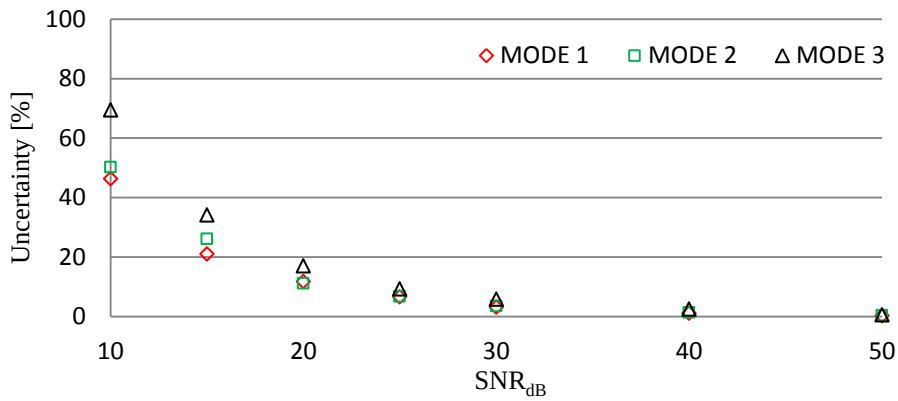

Figure 3.9 : Damping uncertainty versus SNR value.

3.4 Damping Uncertainty Due to Exponential Windowing: Experimental Study

The experimental study presented here aims to establish the levels of damping uncertainty that can be encountered in practice when exponential windowing needs to be used before the FRF calculations and when the data also contain inevitable noise.

3.4.1 Numerical damping due to exponential windowing and its removal

Windowing functions are often applied to signals in order to minimise leakage. If $x(t)$ is the time domain response of a structure, and $w(t)$ is the windowing function, then the windowed signal, $x'(t)$, is obtained as

$$x'(t) = w(t) \cdot x(t) \tag{3.46}$$

This is illustrated in Figure 3.10 when $w(t)$ is an exponential windowing function in the form of $e^{-\tau t}$ where τ is called the decay rate.

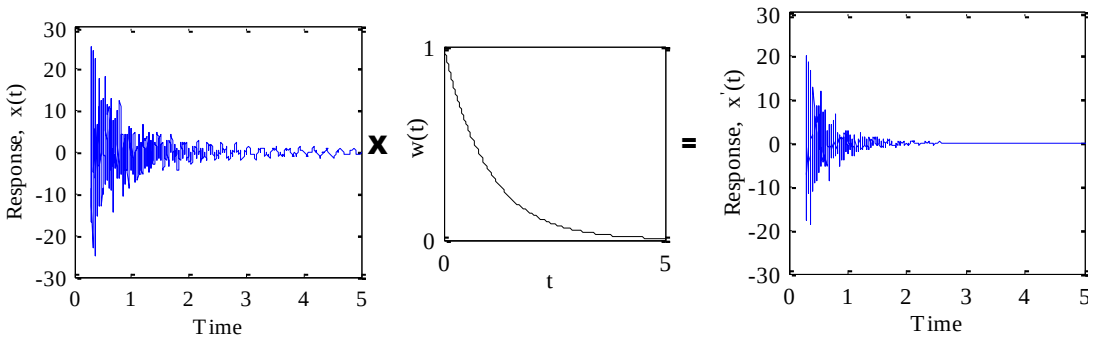

Figure 3.10 : An example of original signal (left), exponential window function (middle) and windowed signal (right).

It is well known that exponential windowing artificially introduces numerical damping, the level of which increases as the decay rate, τ, increases. In Figure 3.11, exponential windowing functions with different levels of numerical damping are shown for SDOF and MDOF systems.

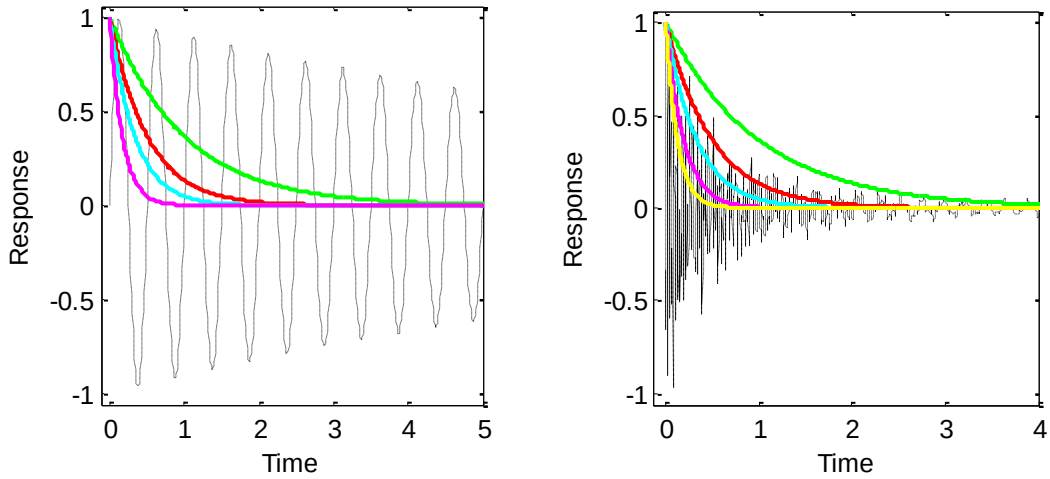

Figure 3.11 : Exponential windowing with different levels of numerical damping applied to SDOF (left) and MDOF (right) systems.

Theoretically, it is possible to remove the artificially added numerical damping due to exponential windowing. This is summarised briefly below for the case of a SDOF system. The free vibration response of a SDOF system is expressed as

$$x(t) = Xe^{-\omega_0 \xi t} e^{j\left(\omega_0 \sqrt{1-\xi^2} t\right)} \tag{3.47}$$

Here, ω_0 is the undamped natural frequency and ξ is the viscous damping ratio. If the signal $x(t)$ is multiplied by an exponential window, the modified response $x'(t)$ becomes

$$x'(t) = Xe^{-\tau t} e^{-\omega_0 \xi t} e^{j\left(\omega_0 \sqrt{1-\xi^2} t\right)} = Xe^{-(\tau + \omega_0 \xi)t} e^{j\left(\omega_0 \sqrt{1-\xi^2} t\right)} \tag{3.48}$$

As can be seen, the total damping for the windowed signal is

$$\bar{\xi} = \frac{\tau + \omega_0 \xi}{\omega_0} = \xi + \frac{\tau}{\omega_0} \tag{3.49}$$

Therefore, the correct (actual) damping level can be determined by removing the artificial damping as

$$\xi = \bar{\xi} - \frac{\tau}{\omega_0} \tag{3.50}$$

If the damping level is to be expressed in terms of loss factor (η), Equation 3.50 becomes

$$\eta = \bar{\eta} - \frac{2\tau}{\omega_0} \tag{3.51}$$

Although the formulation presented above is based on SDOF assumption, the same approach can be extended for MDOF systems; hence the actual damping for the *r*th mode of a MDOF system is given by

$$\eta_r = \bar{\eta}_r - \frac{2\tau}{\omega_r} \tag{3.52}$$

where η_r and $\bar{\eta}_r$ are the correct (actual) and the total loss factors of the *r*th mode respectively, and ω_r is the natural frequency of the *r*th mode.

3.4.2 FRF measurements

The damping uncertainty due to exponential windowing is explored here experimentally by studying a practical test structure. Although FRF measurements are performed on a few structures with passive damping treatments, the results of a passively damped helicopter blade is chosen here noting that similar difficulties are encountered during damping identification for all structures. In the experiments, FRFs are measured using a modal impact hammer, a few accelerometers and an analyser with proper signal conditioning hardware [163]. Repeatability check of the measurements is performed and calibration of all the system is checked both at the beginning and at the end of experiments.

The data for the first set of measurements are acquired without the need for exponential windowing. This is achieved by deliberately setting the measurement period (T) sufficiently long for the transient signal so that the transient vibration signal decays to negligible level at the end of the measurement period. This set of measurement will provide the actual (correct) damping level without the adverse effect of numerical damping. Then, keeping the number of data points (N) constant, measurement period is reduced each time and an appropriate exponential window is applied to transient vibration signal. In other words, during each measurement, N is kept constant while the sampling rate and the measurement period (T) are varied.

During individual measurements, the parameter for exponential window is chosen such that its unit value at the beginning drops to 1% of the unit value at the end of the measurement period. Another point to note is that as the sampling rate increases, the frequency span increases and the frequency resolution decreases. This means that as the measurement period is reduced, more and more numerical damping is applied due to exponential windowing. However, it is not clear how much uncertainty this process may introduce. In this section, it is aimed to investigate and to quantify this uncertainty caused by exponential windowing. The structure on which the FRFs are measured is given in Figure 3.12. The data acquisition parameters used during FRF measurements are listed in Table 3.5. As stated, the exponential decay rate (τ) in Table 3.5 is chosen such that at the end of each measurement period its value is 1% of the initial value.

Figure 3.12 : Experimental set-up for the case study.

Typical time domain signals with and without exponential windowing are given in Figure 3.13. As can be seen, multiplying the signal with an exponential window forces the signal to decay to zero at the end of the measurement period. Also, a measured FRF without using any windowing function and FRFs obtained using windowed signals are presented in Figure 3.14. The effect of the exponential windowing, i.e., numerical damping, is clearly seen in these FRFs.

Table 3.5 : Data acquisition parameters.

Measurement No	Measurement Period, T (s)	Decay Rate, τ (s^{-1})	Frequency Span, FS (Hz)	Frequency Resolution, Δf (Hz)
1	32.0	No Windowing	0.7-200	0.0313
2	32.0	0.14	0.7-200	0.0313
3	16.0	0.29	0.7-400	0.0625
4	8.00	0.58	0.7-800	0.1250
5	6.40	0.72	0.7-1000	0.1563
6	4.00	1.15	0.7-1600	0.2500
7	3.20	1.44	0.7-2000	0.3125
8	2.00	2.30	0.7-3200	0.5000
9	1.28	3.60	0.7-5000	0.7813
10	1.00	4.61	0.7-6400	1.0000

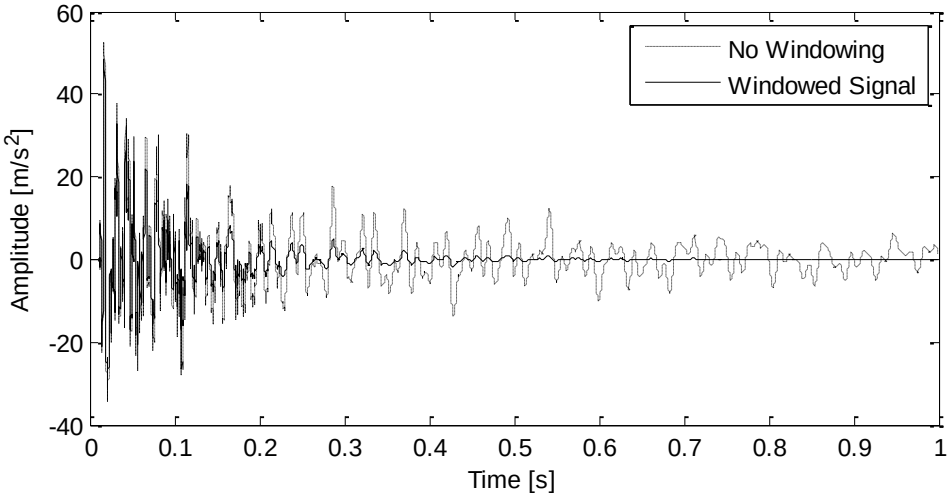

Figure 3.13 : Time domain signals with and without windowing.

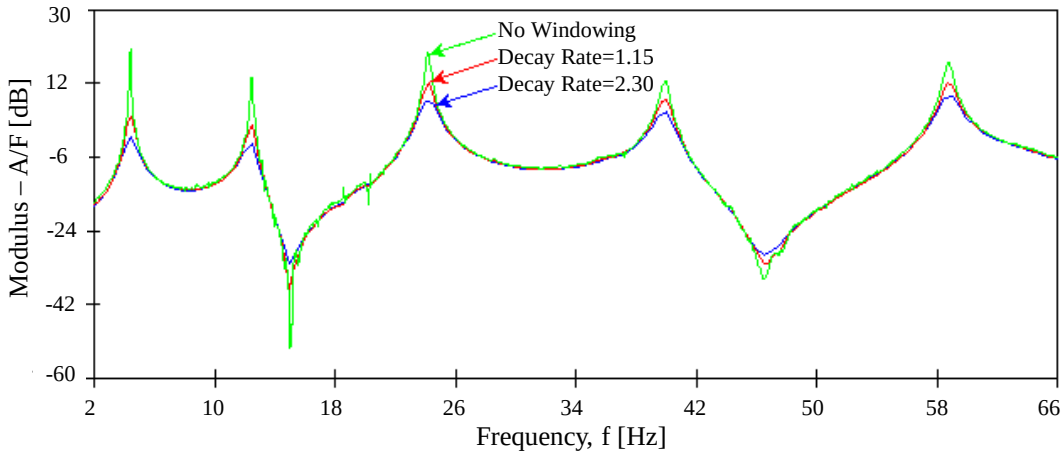

Figure 3.14 : Typical measured FRFs: with and without exponential windowing.

3.4.3 Results

During FRF measurements, spectrum averaging is carried out and the coherence function is also recorded. A typical FRF and the associated coherence function are given in Figure 3.15. It is noted that FRF is nearly noise-free and the coherence value is greater than 0.999 (mostly equal to nearly unity) around natural frequencies. Using Equation 3.11, it is determined that SNR value is greater than 30 dB. As a result, the damping uncertainties due to exponential windowing presented in this section are valid when SNR in FRF data is greater than 30 dB around natural frequencies.

Measured actual (correct) modal damping values for the first five modes of the test structure (Measurement No: 1) are listed in Table 3.6. These values are determined under such conditions that there was no need for applying exponential window function. Therefore, they are free of so-called numerical damping, hence they are considered as the actual damping values. Similarly, using the parameters listed in Table 3.5, measurements labelled as Measurement No 2 to 10 are performed and corresponding modal damping values including the numerical damping are estimated from FRFs using the line-fit method [37-38]. Each set of measurements indicated by "Measurement No" in Table 3.5 actually consists of many repeated measurements, number of repeat measurements being varied from 10 to 15. Using the expression in Equation 3.52, the contribution of the numerical damping is removed from the estimated total damping values. Ideally, the corrected damping level should be identical to the actual damping level. However, as one might expect, this is not so in practice: if the artificial (numerical) damping is relatively high this can introduce significant level of damping uncertainty. This in turn may result in the corrected (numerical damping removed) and the actual damping levels being significantly different from each other. As stated before, SNR values around natural frequencies in the FRFs were higher than 30 dB. Therefore, it can be said that the uncertainty values determined in this section are mainly because of exponential windowing and these results are valid when the noise level in FRFs around natural frequencies is very low.

By comparing the corrected damping levels and the actual damping values in Table 3.6, damping uncertainty with respect to the level of added numerical damping is explored. For each decay rate listed in Table 3.5, the total damping value - the sum of the actual damping and the numerical damping - is determined using the line-fit

approach. Then, the actual damping values are calculated using the expression in Equation 3.52. The maximum and the minimum damping values are determined and the uncertainty values are calculated for individual decay rates using Equation 3.45.

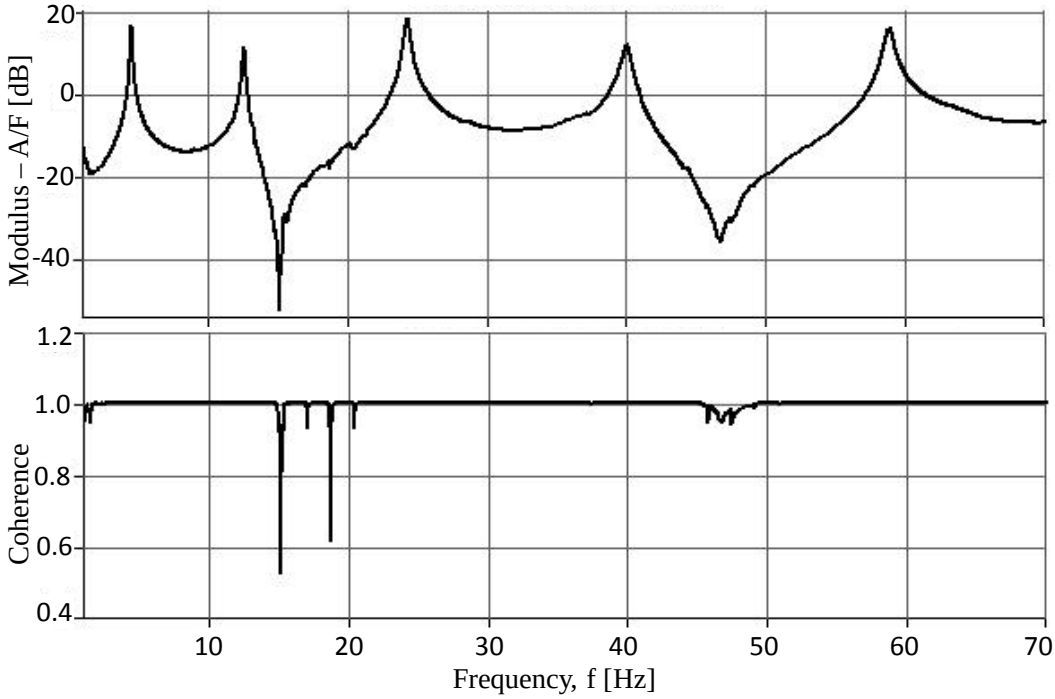

Figure 3.15 : A typical FRF and coherence function.

Table 3.6 : Actual modal damping values (obtained without applying windowing).

Mod No	1	2	3	4	5
Frequency, f (Hz)	4.4	12.5	24.2	40.0	58.8
Modal Damping, η (%)	1.15	0.98	1.20	1.38	0.95

As mentioned before, damping uncertainty is also expected to be dependent on the damping identification method. Assessment of the performances of damping identification methods in terms of damping uncertainty is outside the scope of this investigation. However, performances of the two of the frequency domain methods, namely the line-fit and the circle-fit methods are compared here in terms of damping uncertainty obtained by analysing the same data set using the two methods. Generally, it is seen that the line-fit method yields lower damping uncertainty than the circle-fit method when the same data are analysed using both methods. As an example, the uncertainties for both methods for mode 3 (24.2 Hz) are given in Figure 3.16. As can be seen, the uncertainty values are mostly higher in the case of circle-fit method. It is therefore decided to use the line-fit method for determination of the damping levels in the rest of this section.

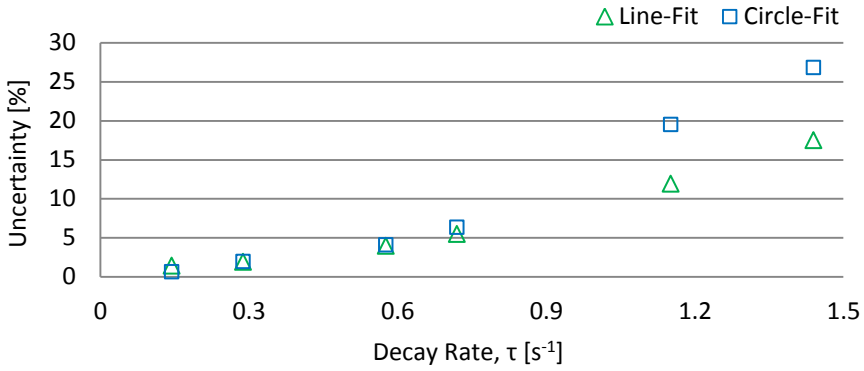

Figure 3.16 : Uncertainty values for two different methods.

Damping uncertainties are presented as a function of decay rate in Figure 3.17 for the first four modes of the test structure. Also, the levels of damping uncertainty for the five first modes are presented in Figure 3.18 as a function of decay rate. For mode 1 (Figure 3.17a), the added numerical damping value is very high. In fact, modal damping for this mode could not be determined for (τ >1.44 s^{-1}). Similar observation can also be made for mode number 2 (Fig. 3.17b), but in this case, the modal damping could not be determined for τ >2.3 s^{-1}. It is clearly seen in Figure 3.17 and Figure 3.18 that the damping uncertainty increases for all the modes as the decay rate (the level of numerical damping) increases.

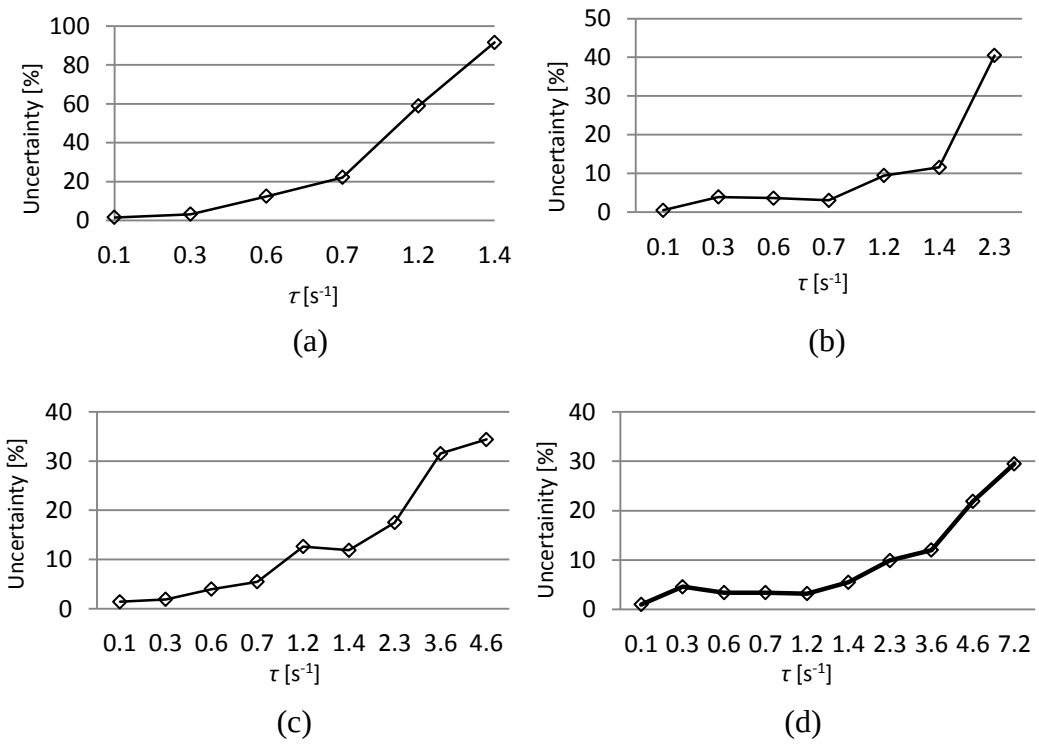

Figure 3.17 : Uncertainties in modal damping values with respect to decay rate: (a) 1st–4.4 Hz, (b) 2nd–12.5 Hz, (c) 3rd–24.2 Hz, (d) 4th–40 Hz modes.

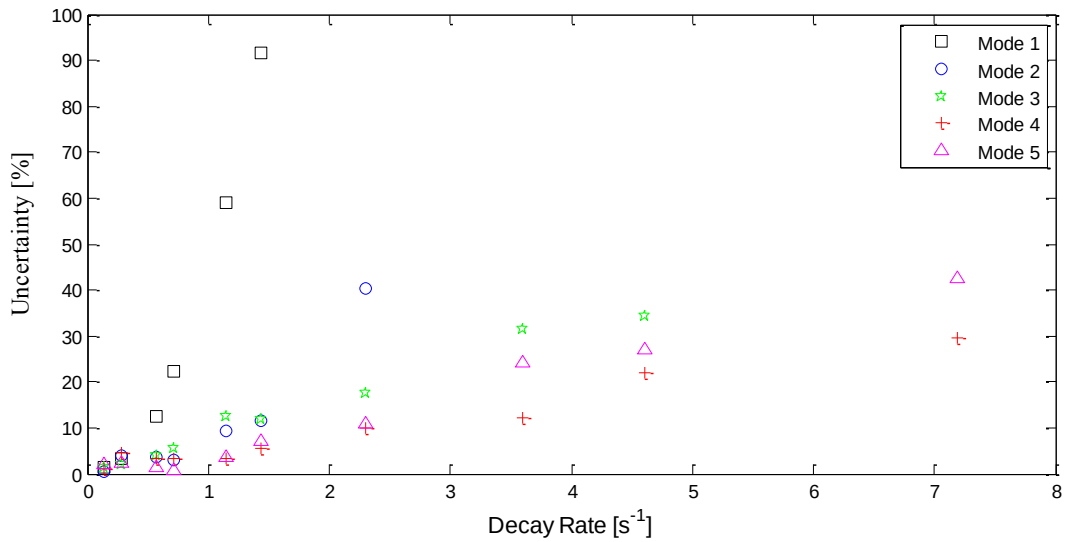

Figure 3.18 : Damping uncertainty versus decay rate.

A normalised parameter is defined here in order to make the results independent of the natural frequencies and actual damping levels. This parameter is the ratio of the added numerical damping to the actual modal damping ($\eta_{numeric}/\eta_{actual}$). When this normalised parameter is used, damping uncertainty values for different modes can be presented on the same plot as shown in Figure 3.19. As seen, there is a gradual increase in uncertainty as the added numerical damping increases for all the modes. It is also seen that damping uncertainty becomes quite significant when the numerical damping added due to exponential windowing is equal or greater than the actual damping in the system. The damping uncertainty can reach to about 40% when the numerical damping is about four times greater than actual damping.

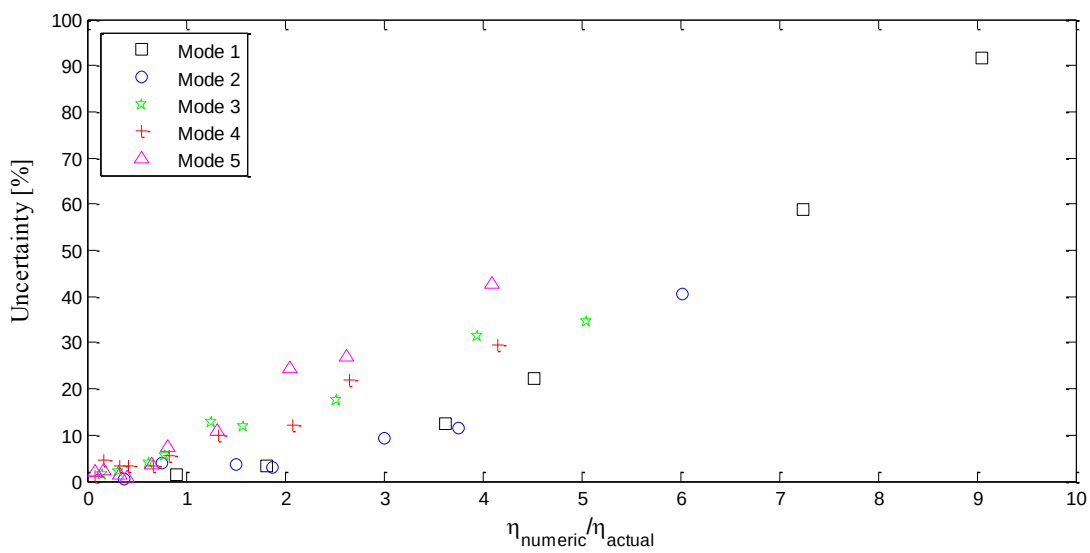

Figure 3.19 : Damping uncertainty versus added numerical damping.

3.5 Concluding Remarks

In this Chapter, damping uncertainty due to both noise and exponential windowing is investigated. In the first part of the study, some numerical simulations are performed in order to assess the damping uncertainty associated with noise level in the data used for damping estimation. For this purpose, a lumped parameter system is modelled and noisy FRFs are regenerated, the level of noise being characterised by SNR. The FRFs with noise are analysed using the line-fit method in order to determine the damping levels and the associated uncertainty. It is shown that damping uncertainty becomes significant when SNR is less than 30 dB and the uncertainty increases gradually as the SNR decreases. It is noted, however that the line-fit method is not very sensitive to noise if SNR is greater than 40 dB. In such cases, the damping uncertainty becomes negligible when the line-fit method is used for damping estimation.

In the second part of the study, the effect of the use of exponential windowing is investigated using experimental data which inevitably contained noise. This is done for various modes by (i) determining the actual damping level without introducing any numerical damping (ii) determining the total damping when numerical damping is introduced, (iii) determining the estimated damping by removing the numerical damping from the total damping and (iv) comparing the actual and the estimated damping levels. It is found that damping uncertainty becomes quite significant when the numerical damping added due to exponential windowing is equal to or greater than the actual damping in the system. Also, the results are presented in normalised format so as to make it independent of the natural frequencies and actual damping levels. It is believed that these results can be used for estimation of possible damping uncertainty due to exponential windowing when the numerical and the estimated damping levels are known. It should be noted however that the results presented here is applicable when line-fit method is used for damping estimation. Furthermore, the use of different damping estimation method may result in somewhat different levels of uncertainty. It is noted, however, that the line-fit method performs better than the circle-fit method in the sense that line-fit method yields lower damping uncertainties.

4. MODELLING DAMPED STRUCTURES

4.1 Introduction

Accurate prediction of the damping levels of structures with passive damping is quite difficult because of the inherent coupling between nonlinear material behaviour and other nonlinear effects [47, 72-75]. Although there are some rheological models such as Maxwell, Kelvin-Voigt and the standard linear solid models for viscoelastic materials where springs and dampers are arranged in series and/or parallel in order to determine their stress or strain interactions [76-78], computational methods [74, 79-81] are widely used for modelling damped structures. Although Statistical Energy Analysis-SEA [80-81] can be used for creating structural models for the purpose of vibration and acoustic analyses of structures, Finite Element (FE) methods [74, 79] are widely used for the prediction of damping levels of structures in practice.

There are basically three approaches for damping modelling in FE applications: the Complex Eigenvalue (CE), the Direct Frequency Response (DFR) and the Modal Strain Energy (MSE) methods [79]. In the DFR method [82], Frequency Response Function (FRF) matrix is obtained by inversion of the dynamic stiffness matrix. Then, damping values can be determined by analysing the FRFs. The DFR method is very costly in terms of computation time as it requires computation of the FRF matrix at individual frequencies. In the MSE method [79], the eigenvalue problem of the actual (damped) system is not solved. Instead, the so-called normal modal analysis of the undamped system is performed to compute the strain energy ratios for individual modes in order to estimate the modal damping levels. During this process, it is assumed that the mode shapes of the damped system are the same as those of the undamped system. Although, the MSE method can be used for modelling complex damped structures, the accuracy of this method should be verified for the specific applications. In the CE method [83-84], on the other hand, the complex eigenvalue problem is needed to be solved without simplifying assumption. Although the CE method is a known approach for the predictions of damping levels of structures, it is computationally more expensive than the MSE method. Overall, the MSE and CE

methods are utilised in this thesis for modelling structures with damping treatments noting once more that the DFR method is very costly for general structures in terms of computation time.

In this chapter, first, the formulation of a FE procedure based on the MSE method is presented for the purpose of modelling damped structures. Then, the theoretical background of a composite finite element with damping capability is presented. After that, some test cases are prepared and FRFs are measured in order to validate the procedure based on the MSE method and the composite FE formulation. It should be noted that the mechanical properties of the damping materials used in the test structures are identified experimentally using the Oberst beam method in Chapter 2 and the experimental identification of structures is investigated in Chapter 3. The results obtained from the MSE method and the composite FE are compared with experimental results and the accuracy of both methods is assessed. Furthermore, the accuracy of the procedure based on the MSE method is examined as a function of damping level and mode shape complexity arising from non-proportional distribution of damping in structures.

4.2 A Damping Prediction Approach Based on The MSE Method

The differential equation for the free vibrations of a damped mechanical system using complex stiffness matrix is expressed as [79]

$$\mathbf{M}\ddot{\mathbf{X}} + \left(\mathbf{K}_S + j\mathbf{K}_L\right)\mathbf{X} = \mathbf{0} \tag{4.1}$$

where $\mathbf{M}$ is the mass matrix of the system; $\mathbf{K}_S$ and $\mathbf{K}_L$ are the storage (or elastic) and loss stiffness matrices of the system, respectively; $\mathbf{X}$ is the displacement vector in the frequency domain, and $j = \sqrt{-1}$. The eigenvalue problem of Equation 4.1 can be written as

$$\left(\mathbf{K}_S + j\mathbf{K}_L\right)\mathbf{\Psi}_r^* = \lambda_r^{*2}\mathbf{M}\mathbf{\Psi}_r^* \tag{4.2}$$

where λ_r^{*2} and $\mathbf{\Psi}_r^*$ are the rth eigenvalue and complex mode shape, respectively. Here the complex eigenvalue can be expressed as

$$\lambda_r^{*2} = \lambda_r^2 \left(1 + j\eta_r\right) \tag{4.3}$$

If $\mathbf{\Psi}_r^*$ is approximated by a real mode shape $\mathbf{\Psi}_r$ [79, 85, 164], which is obtained from the eigenvalue analysis by neglecting the loss stiffness $\mathbf{K}_L$, and Equation 4.2 is pre-multiplied on both sides by $\mathbf{\Psi}_r^T$, Equation 4.4 is obtained

$$\mathbf{\Psi}_r^T \left(\mathbf{K}_S + j\mathbf{K}_L\right)\mathbf{\Psi}_r = \lambda^2 \left(1 + j\eta_r\right)\mathbf{\Psi}_r^T \mathbf{M}\mathbf{\Psi}_r \tag{4.4}$$

Separating this equation into real and imaginary parts yields

$$\lambda_r^2 = \frac{\mathbf{\Psi}_r^T \mathbf{K}_S \mathbf{\Psi}_r}{\mathbf{\Psi}_r^T \mathbf{M}\mathbf{\Psi}_r} \tag{4.5a}$$

$$\eta_r = \frac{\mathbf{\Psi}_r^T \mathbf{K}_L \mathbf{\Psi}_r}{\lambda_r^2 \mathbf{\Psi}_r^T \mathbf{M}\mathbf{\Psi}_r} \tag{4.5b}$$

Equation 4.5b can also be written as

$$\eta_r = \frac{\mathbf{\Psi}_r^T \mathbf{K}_L \mathbf{\Psi}_r}{\mathbf{\Psi}_r^T \mathbf{K}_S \mathbf{\Psi}_r} \tag{4.5c}$$

The value of λ_r obtained from Equation 4.5a is the undamped natural frequency determined based on the real part of the stiffness matrix. If the loss factor of a material, say *x*, is η_x, the loss stiffness matrix of the structure made of the material *x* can be written as $\mathbf{K}_{Lx} = \eta_x \mathbf{K}_{Sx}$ where $\mathbf{K}_{Lx}$ and $\mathbf{K}_{Sx}$ are the loss and storage stiffness matrices, respectively. In practice, $\mathbf{K}_L$ is taken as the loss stiffness matrix contributed to the damping material(s) added to the base structure [85, 164]. The damping of the base structure is also included in the formulation presented in this thesis here. Overall, the natural frequency and the loss factor of the *r*th mode of a structure with passive damping treatments in general can be approximated by

$$\omega_r^2 = \frac{\mathbf{\Psi}_r^T \left(\mathbf{K}_{Sb} + \sum \mathbf{K}_{Sd}\right)\mathbf{\Psi}_r}{\mathbf{\Psi}_r^T \mathbf{M}\mathbf{\Psi}_r} \tag{4.6a}$$

$$\eta_r = \frac{\mathbf{\Psi}_r^T \left[\eta_{rb}\mathbf{K}_{Sb} + \sum\left(\eta_{rd}\mathbf{K}_{Sd}\right)\right]\mathbf{\Psi}_r}{\mathbf{\Psi}_r^T \left(\mathbf{K}_{Sb} + \sum \mathbf{K}_{Sd}\right)\mathbf{\Psi}_r} \tag{4.6b}$$

where the subscripts *b* and *d* denote the base (or untreated) structure and the damping layer; $\mathbf{K}_{Sb}$ is the storage stiffness of the base structure and $\mathbf{K}_{Sd}$ is the storage stiffness of the each damping layer *d*; and η_{rd} and η_{rb} are the loss factors of the damping layer *d* and base material for the *r*th mode, respectively. It is clear that Equation 4.6b can be also written as

$$\eta_r = \frac{\eta_{rb} V_{rb} + \sum \left(\eta_{rd} V_{rd} \right)}{V_{rb} + \sum V_{rd}} \tag{4.7}$$

where V_{rd} and V_{rb} are the strain energies of the individual damping layer *d* and the base structure when structure vibrates at its *r*th mode. It is seen that a damped structure is described using the undamped modal data of the structure in the MSE method. For damping optimisation, the approach based on the MSE method should be formulated in an efficient way in order to minimise the computational cost. In this thesis, the base and the damping layers of damping patches are modelled at their matching surfaces using shell elements. By doing so, it is assured that the strains are continuous across the layers and the structure is modelled using minimum number of elements or DOFs. It should be stated that the composite structures having more than two layers can be modelled at their mid surfaces. Also, as the damping of the base structure can be significant when the base structure is treated relatively with small amount of damping material or when the strain energies of the regions where the damping patches are used are low, the damping of the base structure should be taken into account as in the formulations given in this thesis.

4.3 Formulation of A Composite FE with Damping Capability

Representing multilayer composite structures with an equivalent layer is an effective way of modelling multi-layered composites as this approach does not increase the number of active DOFs in the model. However, the accuracy of the theoretical model depends on how the individual layers are represented and assembled. The formulation of the composite shell element summarised here is based on stacking individual flat homogeneous shell elements on top of each other [165]. It is appropriate here, for completeness, to present a summary of the composite FE developed in [165]. As stated in [165], any shell element can be used to develop the

composite element. However, the specific shell element utilised in [165] has an important feature in the sense that it has physical drilling degrees of freedom θ_z in the element normal direction. This specific homogeneous shell element (Figure 4.1) is a 4-node element which is an assembly of the quadrilateral membrane element with drilling degrees of freedoms [166] and the plate element [167]. The formulations of the finite elements proposed in [166-167] are implemented so as to obtain the element stiffness matrix $\mathbf{k}_s$ in the mentioned formulation. This basic shell element is also extended for dynamic analysis by computing the element mass matrix $\mathbf{m}_s$ and also adding damping capability to the element by considering the complex Young's modulus of the material described in Section 2.2.2.2 and rewritten here as [165]

$$E^* = E(1 + j\eta) \tag{4.8}$$

where E and η are the Young's modulus and the loss factor, respectively, and $j = \sqrt{-1}$. The use of complex Young's modulus results in complex stiffness matrix $\mathbf{k}_s^*$ for individual elements, a feature necessary to develop a composite element with damping capability. It is worth stating here that the composite element summarised here is based on the assumption that the matching surfaces of the individual layers of the composite structure are fully joined together hence there is no rubbing action across the matching surfaces. Therefore, material damping is considered to be the primary source of energy dissipation and the use of the complex Young's modulus approach is appropriate [16, 74, 139-140].

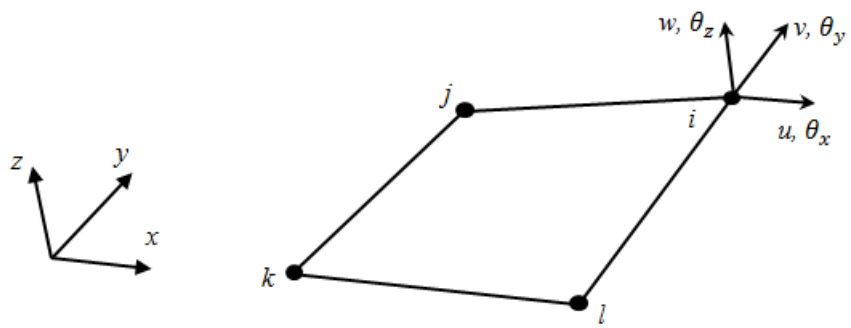

Figure 4.1 : Quadrilateral flat shell element with 6 DOFs per node.

The connectivity definition and the element coordinate system for the composite element are shown in Figure 4.2. As can be seen, the *z*-axis defines the element

normal direction and the neutral plane is on the *x-y* plane. Beside the element coordinate system, the definition of the properties of the individual layers including the stacking order, layer thicknesses and the corresponding material properties are required in composite element formulation. One way of defining the stacking order and the corresponding thicknesses is to define the distance of the top surface of each layer from the bottom surface of the composite element, H_i, as illustrated in Figure 4.3. So, the individual thickness t_i as well as the distance of the mid-surface h_i for individual layers can be determined as

$$t_i = H_i - H_{i-1}; \quad h_i = 0.5\left(H_i + H_{i-1}\right) \qquad i = 1, 2, 3 \ldots, n-2, n-1, n \tag{4.9}$$

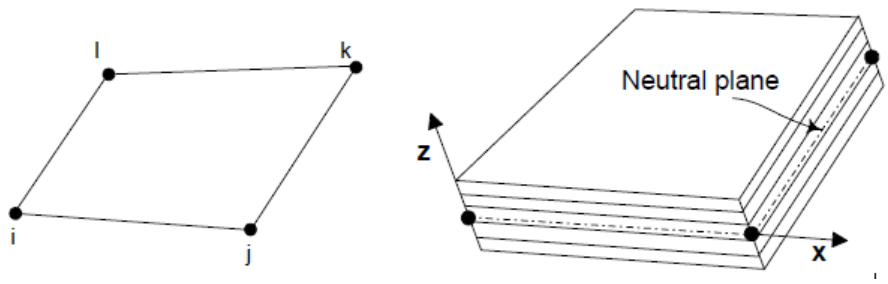

Figure 4.2 : Connectivity and geometry definition of the 4-node composite FE.

In Figure 4.3, each layer is assumed to be made of an isotropic material whose properties can be described by E_i, ν_i and η_i, representing the Young's modulus, Poisson's ratio and loss factor, respectively. The location of the neutral axis depicted in Figures 4.2 and 4.3 are also required to be determined for the formulation of the composite element. Although it is not the case for the formulation of the homogeneous shell element, it is assumed here, only for the purpose of determination of the neutral axis, that the plane sections remain plane which allows the use of the basic bending formulation for the calculation of the distance of the neutral axis from the bottom surface of the composite element. This leads to

$$h = \frac{1}{2} \frac{\sum_{i=1}^{n} E_i \left(H_i^2 - H_{i-1}^2\right)}{\sum_{i=1}^{n} E_i t_i} \tag{4.10}$$

Using h given in Equation 4.10, the offset of the individual layers from the neutral axis can be determined as

$$z_i = h_i - h \tag{4.11}$$

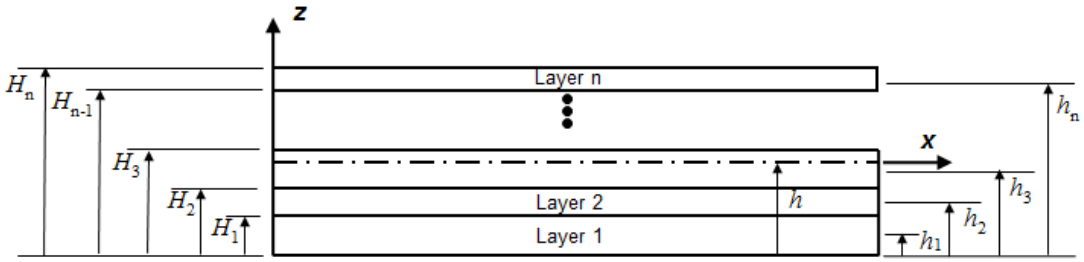

Figure 4.3 : Geometric definition of the layers.

After the geometric parameters are determined, the composite element is formulated as follows. First, the stiffness and mass matrices for each layer ($\mathbf{k}_{si}^{*}, \mathbf{m}_{si}$) are computed as if each layer is oriented on the neutral plane. Then, the stiffness and mass matrices are transformed so as to take into account that each layer is offset from the neutral position by a distance z_i. This is performed by using the relationships between the nodal displacements and forces at the neutral plane and those at the offset location for individual layers. This can be expressed in matrix form as

$$\mathbf{U}_i = \mathbf{T}\mathbf{U}_o \tag{4.12}$$

where

$$\mathbf{U}_i = \left[u_i \; v_i \; w_i \; \theta_{xi} \; \theta_{yi} \; \theta_{zi} \right]^T \tag{4.13a}$$

$$\mathbf{U}_o = \left[u_o \; v_o \; w_o \; \theta_{xo} \; \theta_{yo} \; \theta_{zo} \right]^T \tag{4.13b}$$

$$\mathbf{T} = \begin{bmatrix} 1 & 0 & 0 & 0 & z_i & 0 \\ 0 & 1 & 0 & -z_i & 0 & 0 \\ 0 & 0 & 1 & 0 & 0 & 0 \\ 0 & 0 & 0 & 1 & 0 & 0 \\ 0 & 0 & 0 & 0 & 1 & 0 \\ 0 & 0 & 0 & 0 & 0 & 1 \end{bmatrix} \tag{4.14}$$

Here the subscripts *i* and *o* denote the locations of the *i*th layer and the neutral plane, respectively and **T** is the transformation matrix. It is worth stating that although the transformation matrix for elemental forces is slightly different than that shown in Equation 4.14, it can be shown that the stiffness and mass matrices for individual layers can be expressed with respect to the neutral plane in a conventional manner as

$$\mathbf{K}_{si}^{*} = \begin{bmatrix} \mathbf{T} & \mathbf{0} & \mathbf{0} & \mathbf{0} \\ & \mathbf{T} & \mathbf{0} & \mathbf{0} \\ & & \mathbf{T} & \mathbf{0} \\ & & & \mathbf{T} \end{bmatrix}^{T} \mathbf{k}_{si}^{*} \begin{bmatrix} \mathbf{T} & \mathbf{0} & \mathbf{0} & \mathbf{0} \\ & \mathbf{T} & \mathbf{0} & \mathbf{0} \\ & & \mathbf{T} & \mathbf{0} \\ & & & \mathbf{T} \end{bmatrix} \tag{4.15a}$$

$$\mathbf{M}_{si} = \begin{bmatrix} \mathbf{T} & \mathbf{0} & \mathbf{0} & \mathbf{0} \\ & \mathbf{T} & \mathbf{0} & \mathbf{0} \\ & & \mathbf{T} & \mathbf{0} \\ & & & \mathbf{T} \end{bmatrix}^{T} \mathbf{m}_{si} \begin{bmatrix} \mathbf{T} & \mathbf{0} & \mathbf{0} & \mathbf{0} \\ & \mathbf{T} & \mathbf{0} & \mathbf{0} \\ & & \mathbf{T} & \mathbf{0} \\ & & & \mathbf{T} \end{bmatrix} \tag{4.15b}$$

where **0** is a 6x6 zero matrix. Finally, the element stiffness and mass matrices for the composite element is obtained by adding the contributions of individual layers via a summation process as

$$\mathbf{K}_{c}^{*} = \sum_{i=1}^{n} \mathbf{K}_{si}^{*} \tag{4.16a}$$

$$\mathbf{M}_{c} = \sum_{i=1}^{n} \mathbf{M}_{si} \tag{4.16b}$$

where the subscripts *c* above denotes the composite shell. It should be noted that the summation above represents matrix building rather than simple matrix summation. Once the elemental stiffness and mass matrices are available with respect to the neutral plane, these matrices are transformed to a common global coordinate system and the natural frequencies and modal damping values for a damped system can be obtained by solving the standard eigenvalue problem

$$\left(\mathbf{K}^{*} - \lambda^{2}\mathbf{M}\right)\mathbf{\Psi}^{*} = \mathbf{0} \tag{4.17}$$

where $\mathbf{K}^{*}$ and **M** are the system stiffness and mass matrices, respectively. It is worth noting here that $\mathbf{K}^{*}$ matrix is complex, representing non-proportional damping distribution. The complex eigensolution is obtained here by using Subspace Iteration Method [83] and the solution of the eigenvalue problem above yields complex eigenvalues (λ_{r}^{*2}) and complex eigenvectors or mode shapes ($\mathbf{\Psi}_{r}^{*}$). Overall, the natural frequencies and loss factors are determined as given in Section 3.3. The formulation presented here is already implemented in an FE code FINES [168], designed for modelling and analysing damped and undamped structures. The undamped homogeneous and the damped composite shell elements are named

3SHL04 and 3MIC04, respectively. Obviously, the use of the shell element having damping capability presented here requires the complex Young's moduli of materials.

4.4 Comparisons and Experimental Validation

4.4.1 Test case I: Undamped shell

In this section, the performance of the undamped homogeneous shell element presented in Section 4.3 is evaluated before experimental validation of the composite element. The structure used for this purpose and its material properties are given in Figure 4.4 and Table 4.1, respectively. First, using a very fine mesh, i.e., 1 mm element mesh size, the FE models of the plate given in Figure 4.4 are prepared using the undamped shell element (3SHL04) in FINES [168] and the 4-node (S4R) shell element in ABAQUS program [169]. Each FE model of the structure has 8241 nodes, 8000 elements and 49446 DOFs. It is noted that there are three main differences between the shell element 3SHL04 and the widely used element S4R: i) Unlike the most shell elements available in most commercial software, 3SHL04 element used here has physical rotational degrees of freedom (drilling degrees of freedom) in the direction normal to the surface of the element [166]. ii) Elemental properties of S4R element [169] are obtained using reduced integration but 3SHL04 is not using reduced integration. iii) 3SHL04 element is valid for both thick and thin plates [167]. Natural frequencies, mode shapes and the difference between the results of the two programs are listed in Table 4.2. As seen, almost identical results are obtained using both programs when a very fine mesh is used. Considering these results as the correct or reference values, further analyses and comparisons are performed to evaluate the performance of the undamped shell element.

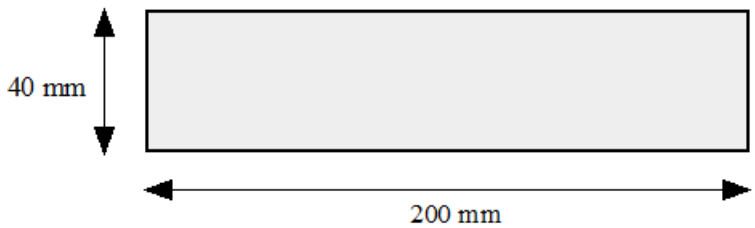

Figure 4.4 : Undamped plate structure (thickness = 1 mm) used in the analyses.

Table 4.1 : Material properties of the plate structure.

Material	Young's modulus (N/m^2)	Density (kg/m^3)	Poisson's ratio
Steel	$204x10^9$	7867	0.3

Table 4.2 : Predicted natural frequencies of the plate for very fine mesh.

Mode			Natural Frequency, *f* (Hz)		
No	Shape	Type	FINES	ABAQUS	Difference (%)
1	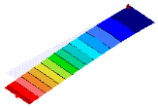	1st Bending	20.8	20.8	0.0
2	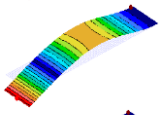	2nd Bending	130.3	130.3	0.0
3	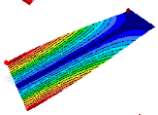	1st Torsional	206.5	206.4	0.1
4	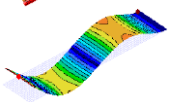	3rd Bending	365.6	365.7	0.0
5	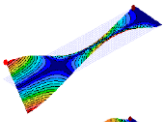	2nd Torsional	631.8	631.4	0.1
6	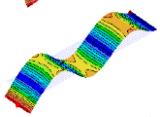	4th Bending	718.7	718.9	0.0
7	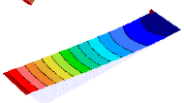	1st inplane Bending	798.8	799.5	-0.1
8	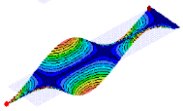	3rd Torsional	1092.3	1091.6	0.1
9	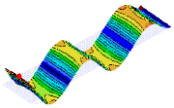	5th Bending	1191.7	1192.1	0.0
10	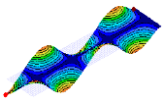	4th Torsional	1607.9	1607.1	0.0

The FE models of the structure for fine (5 mm), medium (10 mm) and coarse (20 mm) element mesh sizes are developed again using both FINES [168] and ABAQUS [169] programs and results are presented in Table 4.3. Using the correct/reference values of the natural frequencies in Table 4.2, the absolute errors in natural frequencies corresponding to different mesh sizes are plotted in Figure 4.5. Also, for the 2nd, 4th and 7th modes, the predicted natural frequencies from FINES and

ABAQUS results as well as the actual (reference) natural frequencies are plotted in Figure 4.6.

Table 4.3 : Predicted natural frequencies of the plate for various mesh sizes.

Mode No	Mesh Size=5 mm, DOF= 2214				Mesh Size=10 mm, DOF= 630				Mesh Size=20 mm, DOF= 198			
	FINES		ABAQUS		FINES		ABAQUS		FINES		ABAQUS	
	f (Hz)	Error (%)	*f* (Hz)	Error (%)	*f* (Hz)	Error (%)	*f* (Hz)	Error (%)	*f* (Hz)	Error (%)	*f* (Hz)	Error (%)
1	20.8	0.0	20.8	0.0	20.8	0.0	20.8	0.0	20.8	0.0	20.8	0.0
2	130.4	0.0	130.6	0.2	130.5	0.1	131.2	0.6	131.0	0.5	133.6	2.5
3	206.1	-0.2	207.2	0.3	204.7	-0.9	207.3	0.4	201.8	-2.3	206.4	-0.1
4	365.9	0.1	367.3	0.5	366.8	0.3	372.2	1.8	370.6	1.4	392.7	7.4
5	630.4	-0.2	634.0	0.3	626.1	-0.9	635.5	0.6	617.1	-2.3	635.2	0.5
6	719.8	0.1	725.2	0.9	723.0	0.6	745.0	3.7	738.1	2.7	<u>832.0</u>	15.8
7	801.2	0.3	794.2	-0.6	804.1	0.7	776.9	-2.7	813.4	1.8	<u>700.8</u>	-12.3
8	1089.9	-0.2	1097.3	0.5	1082.5	-0.9	1103.9	1.1	1067.9	-2.2	1115.2	2.1
9	1194.5	0.2	1209.7	1.5	1203.3	1.0	1265.9	6.2	1246.5	4.6	1531.7	28.5
10	1604.4	-0.2	1618.6	0.7	1594.2	-0.9	1638.9	1.9	1578.5	-1.8	1692.2	5.2

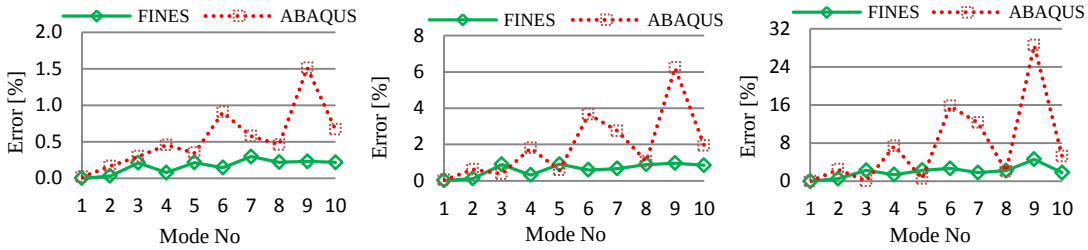

Figure 4.5 : Errors in natural frequencies of the plate for fine-5 mm (left), medium-10 mm (centre) and coarse-20 mm (right) mesh sizes.

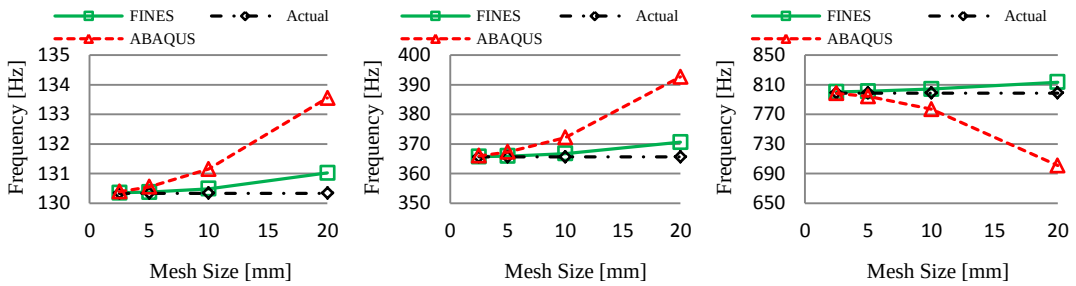

Figure 4.6 : Comparisons of the actual natural frequencies of the plate with the predicted results for 2nd (left), 4th (centre) and 7th (right) modes.

The results show that the errors in natural frequencies of all the modes are smaller when the finite element presented above is used in models with various mesh sizes (Figure 4.5). FINES predicts the sequence of the modes correctly even when a coarse mesh is used while the 6th and 7th modes (frequencies of which are underlined in Table 4.3) are interchanged when ABAQUS program is used. It is clearly seen in

Figure 4.6 that natural frequencies converge to actual values using less number of elements when the shell element in FINES is used. By means of drilling degrees of freedom used in the formulation of the element, FINES model appears to be capable of more accurate natural frequency predictions especially for those modes comprising rotations in the normal direction of the individual elements. This is clearly seen in the results for the 7th mode (an in-plane bending mode). For this mode, the errors are 0.3% and 1.8% for the cases of fine and coarse meshes, respectively, when FINES is used. The corresponding errors in ABAQUS predictions are -0.6% and -12.3%, respectively. Although the results are not presented here for brevity, further analyses are also performed for some other structures and similar results are obtained. All these results show that the undamped shell element presented here has superior performance in predicting modal parameters.

4.4.2 Test case II: Completely damped beams

In this section, a few fully damped beams (used in the Oberst beam measurements in Section 2.6) are modelled using the approach based on the MSE method and composite element presented in Section 4.2 and 4.3, respectively, predictions are made and models are validated using measured data. The so-called fully damped Oberst beam (Figure 4.7) is made by coating a layer of damping material to one side of a bare beam. The dimensions (length and width) of these beams are L=L_1=220 mm and w=10 mm, respectively.

The identified mechanical properties (E, η) of the damping materials are already given in Table 2.14 in Chapter 2. Poisson's ratios (ν values) are taken as 0.3 and 0.45 for steel and damping materials, respectively. Here, using these material properties, damped beams are modelled using both (i) the proposed FE approach based on the MSE method in Section 4.2 and (ii) the composite element presented in Section 4.3. Mesh convergence check is made and an appropriate mesh size is used for both programs (5 mm mesh size for FINES and 2.5 mm mesh size for ABAQUS). The FE model of the damped beam is created using 2x44 composite finite elements (3MIC04) in FINES and each layer of the beam is modelled using 4x88 elements (S4R) in ABAQUS. As each layer of the composite structure needs to be modelled separately in ABAQUS in order to get results via the MSE method, even for the same mesh size, the number of element required by FINES will be half of that

required by ABAQUS. It should also be noted that only bending modes of cantilever beams are measured in the Oberst beam method, hence, in this section, predicted and measured natural frequencies and loss factors are compared for bending modes only.

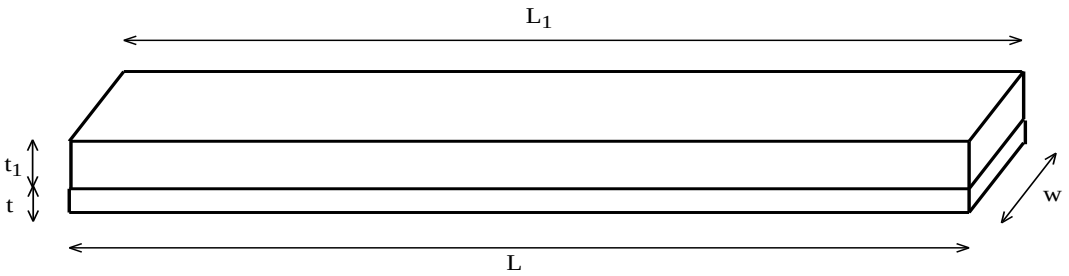

Figure 4.7 : Completely damped (Oberst) beam.

First, the measured and predicted natural frequencies (f_{EXP}, f_{FINES} and f_{ABQ}) of a steel beam that is used as the base of the damped beams using FINES and ABAQUS programs are compared in Table 4.4. As can be seen, the predicted results using both methods are very close to the measured values.

Table 4.4 : Measured and predicted natural frequencies of a steel beam (220 mm).

Bending Mode No	f_{EXP} (Hz)	f_{FINES} (Hz)	f_{ABQ} (Hz)	η_{EXP} (%)
2	107.0	106.8	106.8	0.16
3	299.0	299.3	299.3	0.14
4	584.5	586.9	587.1	0.12
5	966.6	971.2	972.0	0.11

It is known that the material properties of the damping (viscoelastic) materials depend on frequency. Therefore, it is not possible to correctly predict more than one natural frequency of the composite structures using a single eigenvalue (modal) analysis. Therefore, it is necessary to specify the material properties for a specific frequency range and then perform the modal analysis applicable to that frequency range only. The frequency range and the corresponding material properties are changed accordingly and the modal analyses of the damped composite beams are repeated until the whole frequency range of interest are analysed.

Experimentally determined and predicted natural frequencies and loss factors using the FE-based MSE method and the composite element for three different damped beams are given in Tables 4.5 to 4.7. It is worth stating that the damping levels are calculated using Equation 4.6b or 4.7 after normal modal analysis of the structure is performed. It is seen in Table 4.5 to 4.7 that the predicted loss factors and natural

frequencies via new composite element are very close to the experimentally identified values and also to the results of the FE-based MSE method. The results obviously confirm the high accuracy that can be achieved by using the composite FE formulation presented above. It should be noted that the analysis method based on the MSE method is capable of predicting the damping levels for individual modes of such a structure with high accuracy even the damping level of the structure is high (e.g., η=%20).

Table 4.5 : Measured and predicted results of a fully damped beam with DM-1.

Bending Mode No	f_{EXP} (Hz)	f_{FINES} (Hz)	f_{MSE} (Hz)	η_{EXP} (%)	η_{FINES} (%)	η_{MSE} (%)
2	97.9	98.3	98.3	9.22	9.41	9.43
3	274.6	275.9	276.0	12.13	12.34	12.39
4	537.7	540.7	541.0	14.51	14.61	14.70

Table 4.6 : Measured and predicted results of a fully damped beam with DM-2.

Bending Mode No	f_{EXP} (Hz)	f_{FINES} (Hz)	f_{MSE} (Hz)	η_{EXP} (%)	η_{FINES} (%)	η_{MSE} (%)
2	102.4	102.8	102.8	11.99	12.18	12.20
3	286.7	288.1	287.8	15.37	15.55	15.62
4	548.8	552.4	552.5	18.96	19.10	19.24

Table 4.7 : Measured and predicted results of a fully damped beam with DM-3.

Bending Mode No	f_{EXP} (Hz)	f_{FINES} (Hz)	f_{MSE} (Hz)	η_{EXP} (%)	η_{FINES} (%)	η_{MSE} (%)
2	103.9	104.8	104.9	9.93	10.47	10.50
3	307.7	311.6	311.4	10.20	10.61	10.63
4	617.6	626.7	627.6	10.31	10.62	10.69

4.4.3 Test case III: Partially damped beam

A partially damped beam measured again using the Oberst test rig is modelled and the results are evaluated. Configuration of this beam is given in Figure 4.8 where L_1=220 mm, L=250 mm, w=10 mm, t=1 mm and t_1=2.2 mm. This beam is prepared using DM-3 material. As before, the damped regions of the beam are modelled using the composite finite elements (3MIC04) while other regions are modelled by using the undamped shell elements (3SHL04) developed. The measured and the predicted results of this partially damped beam are listed in Table 4.8. As seen, the predicted results are very close to the measured ones, demonstrating once again that the procedure based on the MSE method and the composite FE formulation yield high accuracy if the actual (measured) values of the elastic and damping properties of the individual materials forming the composite structure are provided.

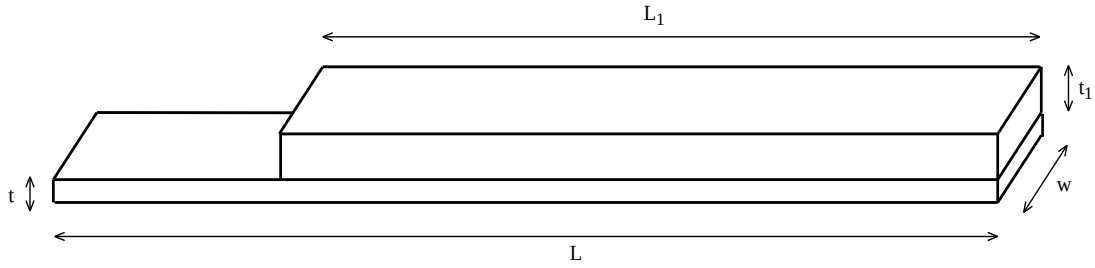

Figure 4.8 : Partially damped beam.

Table 4.8 : Measured and predicted results of a partially damped beam.

Bending Mode No	f_{EXP} (Hz)	f_{FINES} (Hz)	f_{MSE} (Hz)	η_{EXP} (%)	η_{FINES} (%)	η_{MSE} (%)
2	78.3	76.6	76.6	7.89	7.92	7.87
3	233.8	231.2	231.2	9.11	9.14	9.10
4	471.7	470.9	471.1	9.47	9.46	9.43

4.4.4 Test case IV: Damped U-plate

The so-called U-plate made of bare steel is treated using a few different damping materials whose mechanical properties are given in Table 2.14 in Chapter 2. This is done by coating some damping materials at some locations of the plate shown in Figure 4.9 where two different damping materials are used in three different regions of the U-plate (the same type of damping material is used for damping patches labelled 1 and 3). Damping materials and dimensions of the damping patches are given in Table 4.9. FRF measurements are performed [163] on the damped U-plate in free-free conditions using a modal hammer and an accelerometer. The experimental set-up is given in Figure 4.10. By analysing measured FRFs, modal parameters of the U-plate are determined using the line-fit method [37-39].

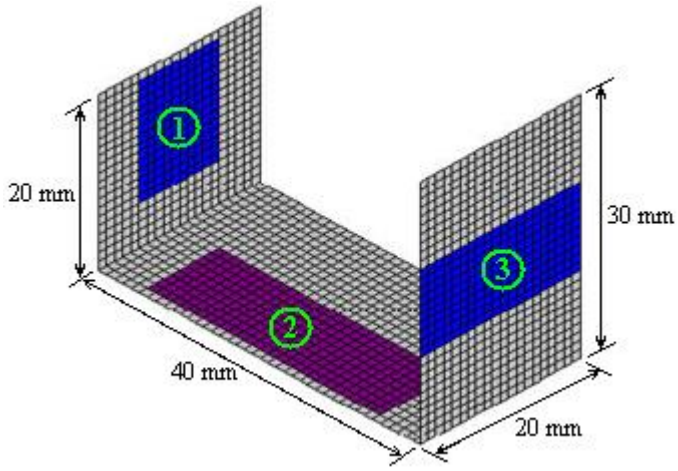

Figure 4.9 : FE model of the damped U-plate prepared using FINES program.

Table 4.9 : Materials and dimensions of the damping patches used in the U-plate.

Damping Patch	Material	Dimensions
1	DM-5	2.2 mm x 100 mm x 140 mm
2	DM-4	2.2 mm x 90 mm x 290 mm
3	DM-5	2.2 mm x 100 mm x 200 mm

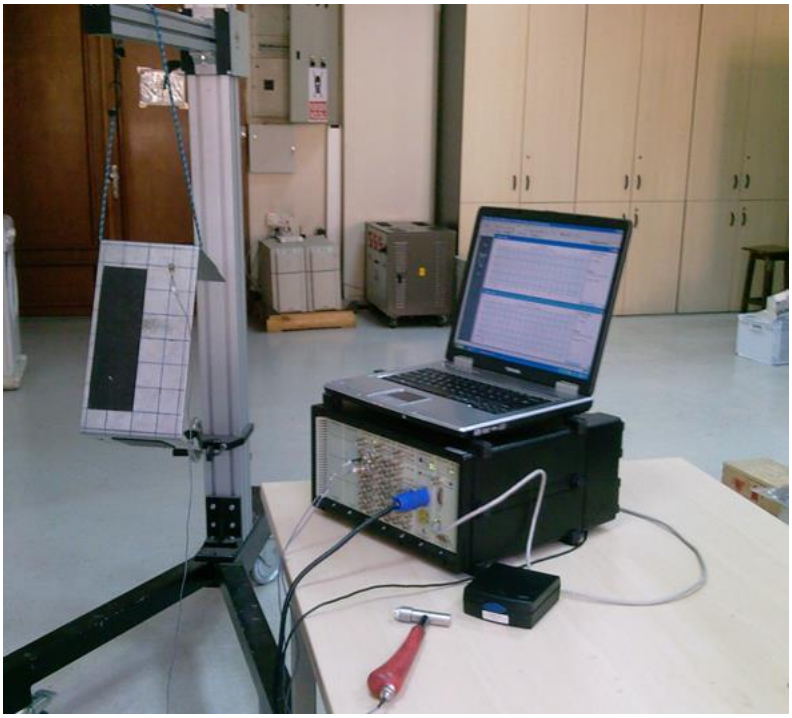

Figure 4.10 : Experimental set-up for measurement of FRFs on the damped U-plate.

As in the beam cases, damped regions of the U-plate are modelled using the composite finite elements (3MIC04) while other regions are modelled with homogeneous undamped shell elements (3SHL04). Here, the analyses are performed twice, each analysis corresponding to a particular frequency range. This required specifying two different sets of material properties applicable within these frequency ranges. Using the identified mechanical properties of the damping materials given in Section 2.6 (Table 2.14), the material properties used in the analyses are given in Table 4.10 for two frequency ranges defined as 0-150 Hz and 150-300 Hz while again Poisson's ratios are taken as 0.3 and 0.45 for steel and damping materials, respectively. The damped U-plate is also modelled using the proposed FE approach based on the MSE method. The predicted and experimentally identified natural frequencies and modal loss factors of the damped U-plate are given in Table 4.11, and also presented graphically in Figure 4.11. It is seen that, the natural frequencies

predicted by using the composite element and the FE approach based on the MSE method are very close to the experimental natural frequencies. It is also seen that both qualitatively and quantitatively, the predicted loss factors are very close to the experimentally identified values. Therefore, it can be safely stated that the procedure based on the MSE method and the composite element are capable of predicting the damping levels for individual modes with high accuracy.

As stated before, although the CE method [168] is the direct method for computing damping levels, it is still difficult to solve complex eigenvalue problem for large scale complicated structures. Overall, the procedure based on the MSE method appears to be the most effective approach for modelling general structures with damping treatments for the purpose of damping optimisation. However, the approach based on the MSE method to be used in damping optimisation should be formulated in an effective way and the accuracy of this approach should be verified before utilised in damping optimisation.

Table 4.10 : Material properties used in the FE models of the damped U-plate.

Damping Material	DM-4		DM-5	
f (Hz)	0-150	150-300	0-150	150-300
E (GPa)	0.45	0.47	0.55	0.62
η	0.43	0.50	0.46	0.47

Table 4.11 : Measured and predicted natural frequencies and loss factors of the damped U-plate.

	Frequency, f (Hz)			Loss Factor, η (%)		
Mode No	EXP	FINES	MSE	EXP	FINES	MSE
1	14.6	14.6	14.7	0.49	0.49	0.49
2	28.9	29.1	29.3	0.52	0.48	0.48
3	34.0	33.9	34.1	0.42	0.44	0.44
4	70.2	72.3	72.6	0.60	0.60	0.60
5	73.6	73.4	73.8	0.48	0.52	0.52
6	106.8	108.9	110.0	0.46	0.51	0.52
7	120.4	121.7	122.2	0.91	0.87	0.87
8	130.5	132.0	132.5	0.45	0.48	0.47
9	189.1	188.7	190.0	0.71	0.71	0.71
10	223.3	232.7	234.0	0.57	0.61	0.62
11	273.3	272.6	274.2	0.74	0.72	0.72
12	278.8	282.0	283.6	0.49	0.52	0.51

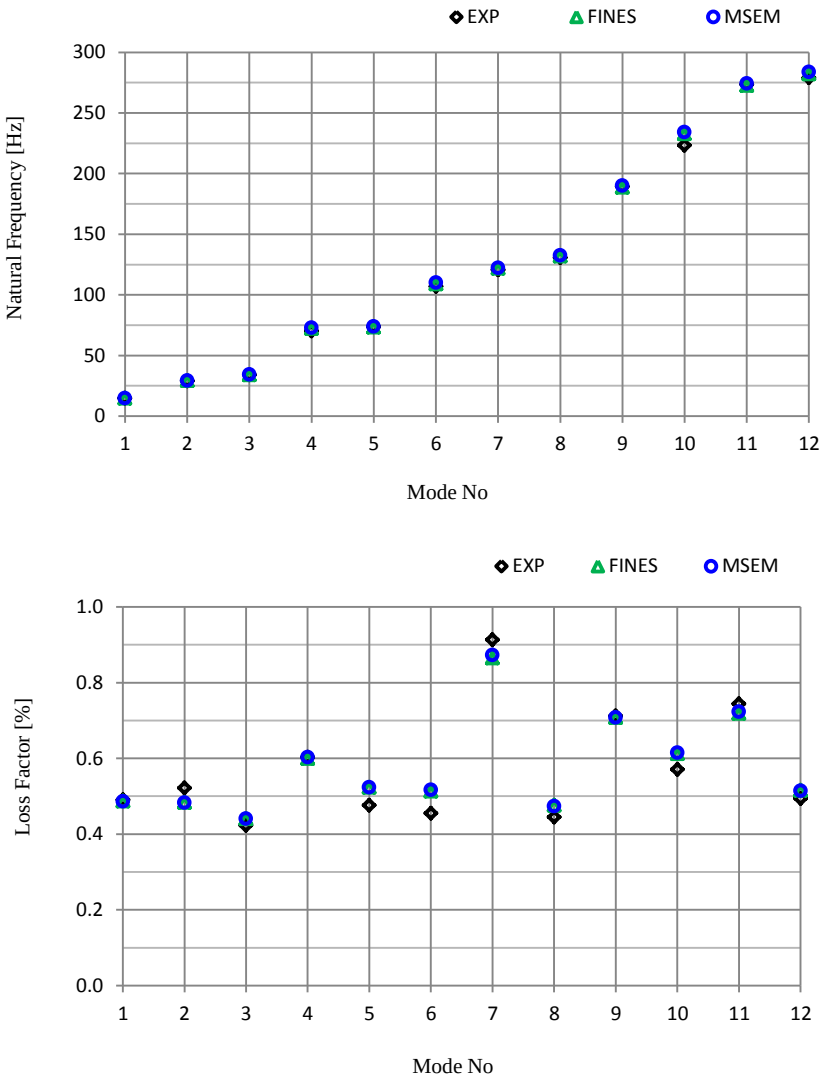

Figure 4.11 : Measured and predicted natural frequencies (up) and loss factors (below) of the damped U-plate.

4.5 Assessment of The Damping Prediction Procedure Based on MSE Method

A simple structure shown in Figure 4.12 is chosen to assess the performance of the damping prediction procedure based on the MSE method presented in Section 4.2. In this structure, two different damping (viscoelastic) materials are used to form a non-proportionally damped composite structure. The material and geometric properties of each layer of the structure are given in Table 4.12. It is worth remembering that when the MSE approach is utilised in this thesis, the sample structures are modelled using 4-node S4R shell elements in ABAQUS program [169] in order to predict the natural frequencies and mode shapes of the undamped structure and modal loss factors are calculated using Equation 4.6b or 4.7. The results of the MSE method are compared

with those obtained using the composite FE formulation presented in Section 4.3. Here, in order to evaluate the performance of the procedure based on the MSE method, complex modal analyses of the test structure are performed for various values of the loss factor of the damping material η_m, ranging from η_m= 0% to 60%.

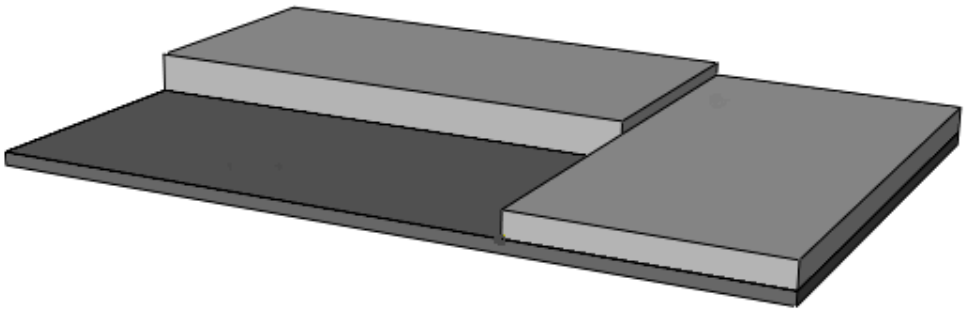

Figure 4.12 : Non-proportionally damped structure.

Table 4.12 : Geometric and material properties of the each layer of the non-proportionally damped structure.

	Width (mm)	Length (mm)	Thickness (mm)	E (GPa)	ρ (kg/m^3)	ν
Base structure	200	300	1.0	205.0	7800	0.30
Thin layer	100	200	2.0	2.5	2500	0.45
Thick layer	100	200	3.0	2.5	2500	0.45

The natural frequencies (ω) predicted using the MSE method and the corresponding errors calculated based on the reference formulation are listed in Table 4.13. Also, the predicted modal loss factors of the non-proportionally damped structure, η_s for various values of the loss factor of damping material ranging from η_m= %5 to %60 using the MSE method, and the corresponding errors in the predicted damping levels are given in Table 4.14. The average error in predicted natural frequencies, even for the case of maximum value of material damping (η_m=60%), is less than 1% while the errors are much lower for lower damping values as seen in Table 4.13. On the other hand, the average error in the predicted damping levels via the MSE method is about 4% when η_m=60%. Also, it is obvious that the level of error increases as the modal damping of the structure increases. It should be noted however that the maximum error is still less than 6% even for η_m=60%, a situation corresponding to a very highly damped system, i.e., modal damping of the structure, η_s, is greater than 20%.

Table 4.13 : Natural frequencies (ω) of the non-proportionally damped structure predicted via the MSE method and the corresponding errors in natural frequencies for various damping levels of damping material (η_m).

Material Damping, η_m		0	10	20	30	40	50	60
Mode	ω (Hz)	Error in natural frequency, ω (%)						
1	58.68	0.16	0.15	0.08	0.01	0.14	0.30	0.65
2	66.61	0.07	0.05	0.01	0.11	0.25	0.43	0.71
3	136.43	0.13	0.10	0.00	0.17	0.39	0.68	1.16
4	146.75	0.04	0.01	0.09	0.24	0.46	0.72	1.07
5	170.33	0.10	0.07	0.01	0.14	0.32	0.54	0.91
6	199.06	0.09	0.07	0.02	0.17	0.36	0.60	0.98
7	252.79	0.16	0.14	0.08	0.00	0.13	0.28	0.62
8	292.15	0.21	0.19	0.12	0.02	0.13	0.31	0.73
Average Error in ω		0.12	0.10	0.05	0.11	0.27	0.48	0.85

Table 4.14 : Loss factors of the non-proportionally damped structure (η_s) predicted via the MSE method and the corresponding errors (ε) in damping levels for various damping levels of damping material (η_m).

η_m (%)	5		10		20		30		40		50		60	
Mode No	η_s (%)	ε (%)	η_s (%)	ε (%)	η_s (%)	ε (%)	η_s (%)	ε (%)	η_s (%)	ε (%)	η_s (%)	ε (%)	η_s (%)	ε (%)
1	1.93	0.54	3.80	0.60	7.55	0.80	11.29	1.11	15.03	1.55	18.77	2.09	22.51	2.74
2	2.14	0.44	4.22	0.51	8.39	0.71	12.55	1.04	16.71	1.50	20.88	2.08	25.04	2.77
3	1.67	0.10	3.27	0.17	6.48	0.44	9.68	0.88	12.89	1.49	16.09	2.26	19.30	3.18
4	1.65	0.39	3.24	0.51	6.41	0.97	9.58	1.74	12.75	2.81	15.92	4.19	19.09	5.87
5	1.81	0.44	3.55	0.54	7.03	0.90	10.51	1.49	13.99	2.29	17.47	3.31	20.95	4.50
6	1.78	0.36	3.50	0.46	6.93	0.83	10.36	1.43	13.79	2.26	17.22	3.29	20.65	4.51
7	1.79	0.33	3.52	0.40	6.97	0.63	10.41	1.02	13.86	1.54	17.31	2.21	20.76	3.01
8	1.83	0.51	3.60	0.59	7.13	0.88	10.66	1.34	14.19	1.97	17.72	2.75	21.25	3.67
Average ε (%)		0.39		0.47		0.77		1.26		1.93		2.77		3.78

The performance of the MSE method is investigated further using a slightly different test case. This time, the base structure in Figure 4.12 is completely coated by a damping layer with a constant thickness of 2 mm. The material and other geometric properties of this so-called proportionally damped structure are the same as those given in Table 4.12. Modal analyses of this proportionally damped structure are performed for various values of the loss factor of the damping material, ranging from η_m= 0 to 60%. Although the results are not tabulated here for brevity, it is noted that the error in the predicted natural frequencies via the MSE method for this proportionally damped structure is less than 0.3% this time, even for η_m=60%. The predicted modal loss factors of the proportionally damped structure for various

values of η_m (η_m= %5 to %60) using the MSE method, and the corresponding errors in the predicted damping levels are given in Table 4.15. It is immediately seen that the average error is quite small and the maximum error is about 1% for η_m=60%. It is worth restating here that the average error was about 4% for the non-proportionally damped structure when η_m=60% as given in Table 4.14. Although the damping levels of the two test structures are close to each other, the errors in the case of the non-proportionally damped structure are significantly higher.

Table 4.15 : Loss factors of the proportionally damped structure (η_s) predicted via the MSE method and the corresponding errors (ε) for various values of η_m.

η_m (%)	5		10		20		30		40		50		60	
Mode No	η_s (%)	ε (%)	η_s (%)	ε (%)	η_s (%)	ε (%)	η_s (%)	ε (%)	η_s (%)	ε (%)	η_s (%)	ε (%)	η_s (%)	ε (%)
1	2.03	0.54	4.00	0.56	7.95	0.59	11.89	0.64	15.83	0.71	19.78	0.80	23.72	0.90
2	2.15	0.11	4.24	0.12	8.43	0.16	12.61	0.22	16.80	0.31	20.99	0.43	25.17	0.56
3	2.08	0.70	4.09	0.72	8.13	0.77	12.16	0.83	16.20	0.91	20.23	1.01	24.26	1.13
4	2.26	0.25	4.46	0.26	8.86	0.30	13.26	0.37	17.66	0.45	22.06	0.57	26.46	0.70
5	2.10	0.50	4.14	0.53	8.21	0.57	12.29	0.63	16.36	0.72	20.44	0.83	24.51	0.96
6	2.27	0.49	4.48	0.51	8.91	0.56	13.34	0.62	17.77	0.72	22.20	0.83	26.62	0.98
7	2.12	0.87	4.18	0.91	8.30	0.96	12.42	1.03	16.55	1.12	20.67	1.24	24.79	1.38
8	2.12	1.00	4.18	1.04	8.30	1.09	12.41	1.15	16.53	1.24	20.65	1.35	24.77	1.48
Average ε (%)		0.56		0.58		0.62		0.69		0.77		0.88		1.01

Some mode shapes of both the proportionally and the non-proportionally damped structures for the case of η_m=50% are plotted in Re-Im plane in Figure 4.13 so as to determine if there is any relationship between the accuracy of the MSE method and the level of mode shape complexity. In contrast to the mode shapes of the proportionally damped structure, it is seen that the mode shapes for the non-proportionally damped structure are quite complex. Not surprisingly, it is also seen that some modes are more complex than the others. In order to demonstrate the situation more clearly, the complexities of mode shapes are quantified using the so-called mean phase deviation (MPD) - being a statistical measure of mode shape complexity - given by [105]

$$\mathrm{MPD}_r = \sqrt{\frac{\sum_{k=1}^{N} |\Psi_{kr}| \cdot \left(\theta_{kr} - \mathrm{MP}_r\right)^2}{\sum_{k=1}^{N} |\Psi_{kr}|}} \qquad \textbf{(4.18)}$$

where θ_{kr} is the phase angle between the element of the eigenvector Ψ_{kr} and the real axis and N is the number of elements of a mode or DOF. MP_r in Equation 4.18 is the weighted mean phase given by

$$\mathrm{MP}_r = \frac{\sum_{k=1}^{N} |\Psi_{kr}| \cdot \theta_{kr}}{\sum_{k=1}^{N} |\Psi_{kr}|} \tag{4.19}$$

The calculated MPD values using Equation 4.18 for both the proportionally and the non-proportionally damped structures are given in Table 4.16. As expected, it is seen that the MPD values for the non-proportionally damped structure are quite high.

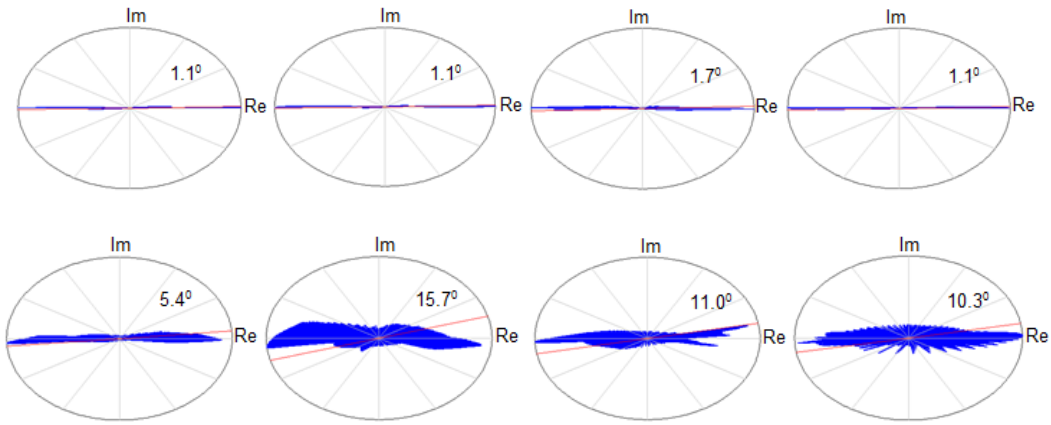

(a) (b) (c) (d)

Figure 4.13 : 2nd (a), 4th (b), 6th (c) and 8th (d) mode shapes of proportionally (up) and non-proportionally (bottom) damped structures (Re-Im plane).

Table 4.16 : The MPDs for various damping levels of damping material (η_m) for both the proportionally and non-proportionally damped structures.

	Proportionally damped structure							Non-proportionally damped structure						
Mode No	MPD (Degree)													
η_m (%)	5	10	20	30	40	50	60	5	10	20	30	40	50	60
1	0.00	0.00	0.10	0.10	0.10	0.20	0.20	0.60	1.10	2.00	2.90	3.70	4.40	5.10
2	0.10	0.20	0.50	0.70	0.90	1.10	1.30	0.70	1.30	2.40	3.50	4.50	5.40	6.30
3	0.00	0.10	0.20	0.30	0.50	0.60	0.70	2.70	5.00	8.90	12.50	15.60	18.60	21.30
4	0.10	0.20	0.40	0.70	0.90	1.10	1.20	1.90	3.70	6.90	10.00	12.90	15.70	18.30
5	0.10	0.20	0.50	0.70	0.90	1.10	1.30	1.20	2.30	4.30	6.20	8.00	9.70	11.40
6	0.20	0.40	0.70	1.10	1.40	1.70	1.90	1.40	2.60	4.90	7.10	9.10	11.00	12.80
7	0.20	0.40	0.60	0.80	1.00	1.10	1.30	2.00	3.70	6.70	9.30	11.70	14.00	16.00
8	0.10	0.20	0.50	0.70	0.90	1.10	1.30	1.50	2.70	4.90	6.90	8.70	10.30	11.80
Average	0.10	0.21	0.44	0.64	0.83	1.00	1.15	1.50	2.80	5.13	7.30	9.28	11.14	12.88

The average values of MPD are plotted as a function of the average damping level for the proportionally and non-proportionally damped structures in Figure 4.14a. It is seen that the value of MPD increases substantially as the damping level of the non-proportionally damped structure increases. On the other hand, there is a slight increase in the value of MPD for the proportional damped case. The average values of the errors in the predicted damping levels are plotted as a function of the average damping level for the proportionally and non-proportionally damped structures in Figure 4.14b. The variation of the error in predicted damping as a function of the damping level presented in Figure 4.14b reveals that there is a similar trend in the sense that the error in predicted damping is small for the proportionally damped case and it is relatively larger for the non-proportionally damped case.

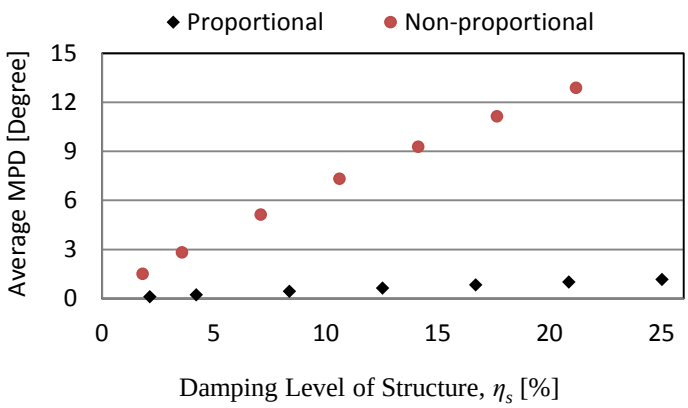

a)

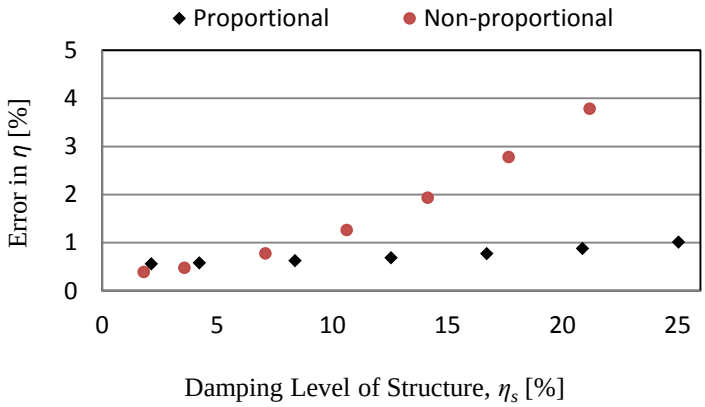

b)

Figure 4.14 : The average values of MPD (a) and the errors in the predicted damping levels (b) as a function of the average damping levels of structures.

Also, the errors in the predicted loss factors are plotted as a function of MPD for both the proportionally and non-proportionally damped structures in Figure 4.15 which shows that the error increases as MPD increases. Even the damping levels of both

structures are close, mode shapes of the non-proportional structure are more complex (MPD values are higher) and the errors in the predicted damping levels of the modes of this structure are higher. For example, the values of average MPD and the average error in the predicted damping level of the proportionally damped structure are about 1.2 degrees and 1.0%, respectively when the average damping of structures (η_s) is about 25% or η_m=60%. On the other hand, these values are about 12.9 degrees and 3.8%, respectively for the non-proportionally damped structure when η_s is about 21% or η_m=60%. The results show that the accuracy of the procedure based on the MSE method depends on the level of mode shape complexity instead of damping level. In the literature, the accuracy of the MSE method is assessed as a function of damping level [for example, 170-172] without stating or quantifying mode shape complexity and non-proportionality of damping treatment.

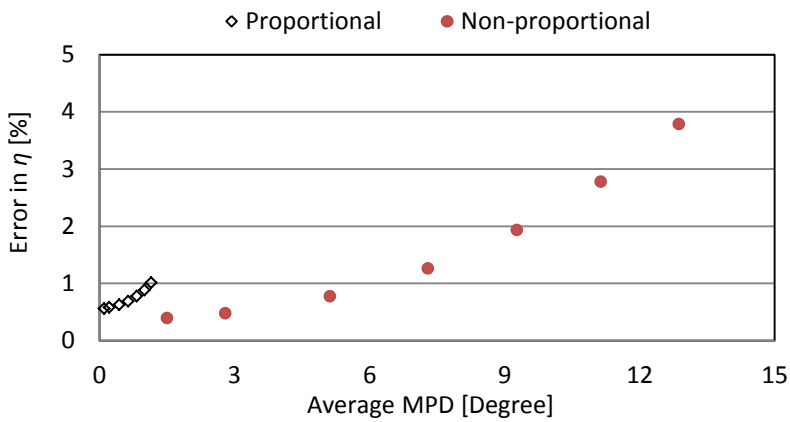

Figure 4.15 : The average values of the errors in the predicted damping levels as a function of the average MPD values.

In order to validate the results given above some other test cases (the plates given in Figure 4.16) are examined here. The dimensions of the plates are 200 mm and 300 mm while the dimensions of the damping patches are 100 mm and 200 mm. The thicknesses of both the base and damping patches are 2 mm. The Young's modulus, Poisson's ratio and density of the base material are 205 GPa, 0.3 and 7800 kg/m^3, respectively, while the corresponding properties for the damping material are 2.5 GPa, 0.45 and 2500 kg/m^3, respectively. The natural frequencies and the modal loss factors of the plates predicted via FE-based MSE method and the composite FE based CE method are given in Table 4.17. The MPDs for individual modes are also given in Table 4.17. The results show that MPD is quite small (smaller than 5^0), indicating that the mode shapes are almost real. Therefore, FE-based MSE method is

expected to predict the natural frequencies and damping levels of the structure with high accuracy. The natural frequencies and the modal loss factors of both plates, predicted via the composite FE-based CE method and the FE-based MSE method, are compared in Figures 4.17 and 4.18, respectively. As seen, the results are nearly the same and match successfully. These results confirm that the MSE method predicts the modal parameters of structures with high level of accuracy as long as the mode shape is real or very close to being real.

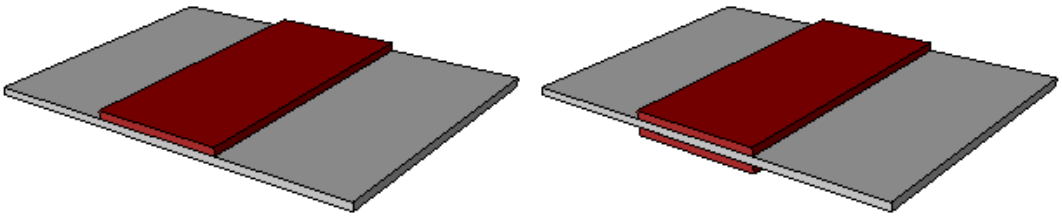

Figure 4.16 : Plates damped one side (left) and both sides (right).

Table 4.17 : Predicted natural frequencies and loss factors of the plates damped one side and both sides using the composite FE-based CE method (FINES) and the FE-based MSE method and the MPDs.

	Damped One Side					Damped Both Sides				
	f (Hz)		η (%)		MPD	f (Hz)		η (%)		MPD
Mode No	FINES	MSE	FINES	MSE	(Degree)	FINES	MSE	FINES	MSE	(Degree)
1	112.5	112.8	3.02	3.04	0.5	115.0	115.3	5.50	5.55	1.0
2	117.6	117.6	4.74	4.75	1.1	118.4	118.3	8.07	8.11	1.8
3	245.2	246.0	2.20	2.21	1.4	240.3	240.9	3.91	3.93	2.1
4	269.0	269.6	3.07	3.10	2.8	265.0	265.4	5.83	5.86	4.2
5	314.1	315.2	2.01	2.03	1.5	311.7	312.6	3.49	3.53	2.1
6	367.8	369.3	1.76	1.78	1.6	368.8	370.1	3.04	3.09	2.4
7	461.7	464.2	2.12	2.12	1.4	455.3	457.5	3.73	3.76	2.5
8	519.0	521.7	2.19	2.21	1.9	506.3	508.9	3.70	3.73	3.9

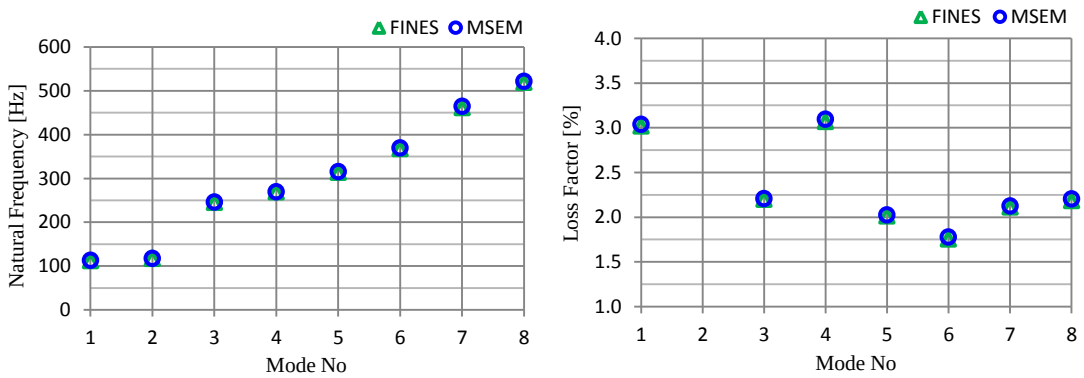

Figure 4.17 : Natural frequencies (left) and modal loss factors (right) of the plate damped one side.

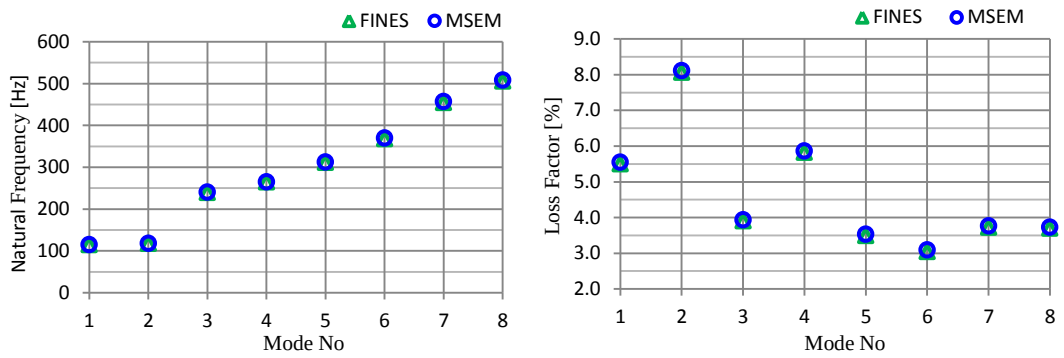

Figure 4.18 : Natural frequencies (left) and modal loss factors (right) of the plate damped both sides.

Also, the MPDs for individual modes of the fully damped beams presented in Section 4.4.2 are given in Table 4.18. The results show that MPD is quite small (smaller than 1^0), indicating that the mode shapes are almost real. It should be remembered that theoretical and experimental natural frequencies and loss factors were very close to each other as presented in Section 4.4.2.

Table 4.18 : The MPDs of the damped beams.

Beam with	*f* (Hz)	MPD (Degree)
DM-1	98.3	0.3
	275.9	0.5
	540.7	0.6
DM-2	102.8	0.4
	288.1	0.5
	552.4	0.8
DM-3	104.8	0.3
	311.6	0.3
	626.7	0.3

In summary, it can be said that although the accuracy of the MSE method decreases as the mode shape complexity increases, the MSE method predicts damping levels with acceptable accuracy even when the damping level of a structure is quite high. It is also worth stating here that there is always an inevitable amount of uncertainty even during experimental determination of damping using measured data. Considering all the results presented so far about the procedure based on the MSE method, it can be said that the MSE method can be conveniently used to predict damping levels for most engineering structures and it can be utilised for damping optimisation purposes during the design stage. It should also be stated that although MPD is used to quantify mode shape complexity here, there is no universally accepted parameter for quantification of mode shape complexity in the literature. A

novel parameter is introduced to overcome the void about quantification of mode shape complexity in the literature in the next chapter.

4.6 Concluding Remarks

In this section, an effective procedure based on the MSE method and a composite FE formulation with damping capability to model structures with damping treatments are presented and validated. The formulation of the FE procedure based on the MSE method is presented first. This approach is applied in an efficient way, i.e., the base and the damping layers of damping patches are modelled at their matching surfaces using shell elements using a minimum number of elements or DOFs and the damping of the base structure is included in the formulation. Then, the formulation of a composite FE with damping capability is summarised. The formulation of the composite element is based on stacking individual 4-node shell elements on top of each other where individual homogeneous layers have different material properties. The damping capability is included in the formulation by means of complex elemental stiffness matrix representing both the elastic and the non-proportional damping properties of the individual layers of the composite element. After all, the performances of the procedure based on the MSE method and the composite FE formulation are assessed and validated experimentally. It is worth noting that the elastic and damping properties of damping materials are determined using the Oberst beam method in Chapter 2 while experimental damping identification of structures is discussed in Chapter 3. The performance of the MSE method as a function of damping level and mode shape complexity is also evaluated in this chapter.

The predicted modal parameters of the procedure based on the MSE method and the composite FE formulation based on complex eigenvalue method presented in this chapter are very close to the experimental results. Although the accuracy of the MSE method decreases with the level of mode shape complexity, the MSE method predicts damping levels with acceptable accuracy even when the damping level of a structure is quite high. It is concluded that the MSE method can be conveniently used to predict damping levels for most engineering structures and it can be utilised for damping optimisation purposes during the design stage.

5. QUANTIFICATION OF MODE SHAPE COMPLEXITY

5.1 Introduction

The performance of the MSE method as a function of damping level and mode shape complexity is evaluated in Chapter 4. Although Mean Phase Deviation-MPD [105] is used to quantify mode shape complexity, it is noted that there is no universally accepted parameter for quantification of mode shape complexity in the literature. Therefore, a novel parameter is introduced in this chapter to overcome the void about quantification of mode shape complexity in the literature. The literature review on the quantification of mode shape complexity is given in Section 1.2.4. It is noted that several parameters have been proposed in the literature to quantify the level of mode shape complexity although they are not derived from fundamental definition of a mode shape being complex. The main parameters utilised to measure the mode shape complexity in the literature are: Mean Phase Deviation (MPD), Modal Correlation Coefficient (MCC), Modal Phase Collinearity (MPC), Mode Complexity Factor 1, 2 and 3 (MCF1, MCF2 and MCF3). MPD [105, 106, 109] is actually an indicator of phase scatter of a mode shape rather than being a direct parameter to quantify the level of complexity of a mode shape. Similarly, MCC [99] is only a correlation function between two vectors (the real and imaginary parts of the eigenvector) while MPC [49, 98, 105, 109-112] is associated with the correlation of phase angles. Also, as stated by Ewins [35], MCF1, MCF2 and MCF3 [35, 38, 101] are not established as the universally-accepted indicators.

Although the mode shapes of most structures in reality exhibit some degree of mode shape complexity, it is noted that the parameters outlined above do not appear to be adequate for the quantification of mode shape complexity as they lack the physical reasoning and/or theoretical foundation and none of these has yet been established as the universally-accepted indicator. A novel approach for quantification of mode shape complexity is proposed in this thesis and the new parameter introduced here can be used by those studies dealing with assessment of the validity of various

methods as a function of mode shape complexity. Also, the new parameter may be utilised by any method dealing with complex mode shapes.

The outline of this chapter is as follows. First, the theories behind the main parameters aiming to quantify mode shape complexity in the literature are presented and discussed. After that, a new parameter, based on conservation of energy principle, i.e., based on the change of strain energy of a structure vibrating at a specific mode, is introduced. In order to demonstrate the performance of the new parameter for quantification of mode shape complexity, a sample structure (a damped beam) is modelled using Finite Element (FE) method and the complex mode shapes are obtained via solving the resulting complex eigenvalue problem. Then, using the complex mode shapes obtained, mode shape complexity is quantified using the parameter proposed in this thesis as well as using some existing parameters in the literature. Finally, the performance of the new parameter introduced in this thesis is compared with those obtained using the other parameters available in the literature.

5.2 Existing Parameters: State-of-The-Art

The formulation of MPD - being a measure of mode shape complexity [105] - is not repeated here as its formulation is readily was given in Section 4.5. Although MPD is utilised to measure the modal complexity of a structure in some applications in the literature, it should be noted that this parameter is a statistical variance of the phase angles for each mode shape coefficient for a specific modal vector from the mean value of the phase angle. In other words, the MPD is an indicator of phase scatter of a mode shape rather than being a direct parameter to quantify the level of complexity of a mode shape.

A correlation coefficient, also called MCC [99] between the real ($\boldsymbol{\Psi}'_r$) and imaginary ($\boldsymbol{\Psi}''_r$) parts of a mode shape vector given below is also used in the literature for the purpose of measuring the modal complexity.

$$\mathrm{MCC}_r = \frac{\left|\boldsymbol{\Psi}'^T_r \boldsymbol{\Psi}''_r\right|^2}{\left|\boldsymbol{\Psi}'^T_r \boldsymbol{\Psi}'_r\right|\left|\boldsymbol{\Psi}''^T_r \boldsymbol{\Psi}'_r\right|} \tag{5.1}$$

It is noted that MCC_r is only a correlation function between two vectors (the real and imaginary parts of the eigenvector).

For lightly damped structures, normal mode behaviour is expected and an indicator referred to as MPC is developed to measure the strength of the linear functional relationship between the real and imaginary parts of the sensor modal displacement for each mode [112] although MPC is also used to measure the complexity of mode shapes in the literature in some applications. MPC of a mode is calculated as [49, 98, 105, 109-112]

$$\mathrm{MPC}_r = \frac{\left|\tilde{\boldsymbol{\Psi}}'_r\right|^2 + \left(\tilde{\boldsymbol{\Psi}}'^T_r \cdot \tilde{\boldsymbol{\Psi}}''_r\right)\left(2\cdot\left(\boldsymbol{\varepsilon}^2+1\right)\cdot\sin^2\boldsymbol{\beta}-1\right)/\boldsymbol{\varepsilon}}{\left|\tilde{\boldsymbol{\Psi}}'_r\right|^2 + \left|\tilde{\boldsymbol{\Psi}}''_r\right|^2} \tag{5.2}$$

where

$$\tilde{\boldsymbol{\Psi}}_r = \boldsymbol{\Psi}_r - \frac{\sum_{k=1}^{N}\boldsymbol{\Psi}_{kr}}{N} \tag{5.3}$$

$$\boldsymbol{\varepsilon} = \frac{\left|\tilde{\boldsymbol{\Psi}}''_r\right|^2 - \left|\tilde{\boldsymbol{\Psi}}'_r\right|^2}{2\cdot\left(\tilde{\boldsymbol{\Psi}}'^T_r \cdot \tilde{\boldsymbol{\Psi}}''_r\right)}; \qquad \boldsymbol{\beta} = \arctan\left(\boldsymbol{\varepsilon} + \mathrm{sgn}\left(\boldsymbol{\varepsilon}\right)\sqrt{\boldsymbol{\varepsilon}^2+1}\right) \tag{5.4}$$

Here, $\tilde{\boldsymbol{\Psi}}_r$ is a vector calculated by subtracting the mean complex value of all elements from each element and $\tilde{\boldsymbol{\Psi}}'_r$ and $\tilde{\boldsymbol{\Psi}}''_r$ are the real and imaginary parts of $\tilde{\boldsymbol{\Psi}}_r$. MPC is associated with the correlation of phase angles. MPC values range from zero for a mode with completely unrelated phase angles to unity for a monophase result. On the other hand, in the case of a noisy mode shape data, the index may be away from unity although the mode is not actually complex.

Three other modal complexity factors called MCF1, MCF2 and MCF3 [35, 38, 101] based on the phase and the amplitude of the elements of a complex modal vector have been proposed for measuring modal complexity. MCF1 simply measures the phase differences between all pairs of mode shape vector elements, regardless of the magnitude of those elements as given by [35]

$$\mathrm{MCF1} = \sum_{j=1}^{N}\sum_{k=1;\neq j}^{N}\left(\theta_{rj} - \theta_{rk}\right) \tag{5.5}$$

In MCF1, all the differences between every combination of two eigenvector elements are summed. MCF2 is defined to be the ratio of the area of the polygon drawn around the extremities of the individual vectors without permitting re-entrant parts to the

area of the circle which is based on the length of the largest vector element. MCF2 [38] reflects the magnitude as well as the phase of each of the elements. MCF3 is identical to MCF1 except that the phase angle is weighted by the amplitudes of the two vectors that define it [38]. As stated by Ewins [35], none of these parameters are established as the universally-accepted indicator.

It is noted that some of the parameters for measuring the complexity of a mode shape mentioned above do not have adequate physical reasoning or theoretical foundation and they may not produce acceptable answers for quantifying mode shape complexity. For example, although a mode shape is actually real, some parameters suggested in the literature may indicate that the mode shape is quite complex or vice versa. Furthermore, none of the parameters in the literature seem to provide acceptable answers in all situations and there is still no globally accepted parameter for defining and quantifying mode shape complexity. In the next section, a novel parameter based on the basic definition of complex modes or travelling waves is introduced.

5.3 A Novel Parameter for Quantification of Mode Shape Complexity

Here, a new and an effective parameter is proposed to measure mode shape complexity. The main idea behind this novel definition is that the complexity of a mode shape can be quantified based on the change of strain energy of a structure vibrating at a specific mode taking into account both the phase and amplitude information of all DOFs of the structure. The idea here can also be explained using the conservation of energy principle. When a structure is vibrating at a specific mode, there is a continuous exchange of kinetic energy (V) and strain energy (U) of the system, the sum of V and U being constant. If the mode shape is a normal one, it is known that V is maximum when U is zero and vice-versa. However, if the mode shape is complex, all the points of the structure do not pass through their undeflected position at the same instant in time, hence U of the structure never becomes zero during a period of vibration although the sum of V and U is still constant. This is a fundamental property of a mode shape being complex and this property is utilised here to define a new parameter for quantification of mode shape complexity. In what follows, the change of strain energy in mechanical systems with different damping properties is discussed. i) For an undamped or proportionally damped system, all the

points of a structure pass through their minima and maxima at the same instant in time, i.e., all the points pass through zero deflection, or zero strain energy level, at the same instant in time. Instantaneous deflections during a half cycle for a completely real mode shape of a hollow disc are illustrated in Figure 5.1 where + and – signs indicate whether the instantaneous deflections are in the direction normal to the page or in opposite direction, respectively. Actually, Figure 5.1 can be considered as some instantaneous animation frames for a particular real mode shape. Referring to Figure 5.1, the deflections of the disc are larger at time $t=t_0$ and $t=t_4$ compared to the deflections at $t=t_1$ and $t=t_3$ while deflections of the disk are zero at $t=t_2$. It is obvious that the strain energy of the system will be zero when all the points pass through undeflected position ($t=t_2$) and the strain energy will be maximum at $t=t_0$ or $t=t_4$ as illustrated in Figure 5.3a which depicts the strain energy as a function of time.

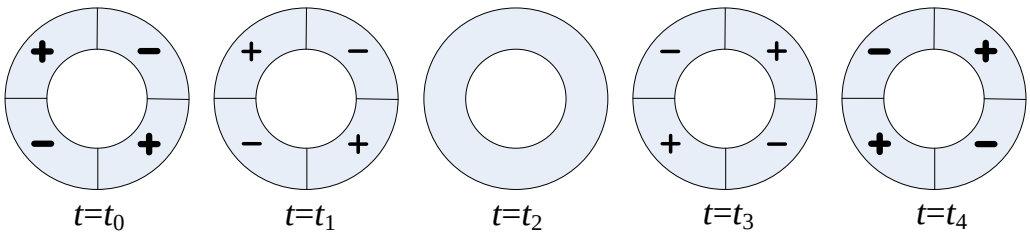

Figure 5.1 : A completely real mode shape: standing wave.

ii) For a completely complex mode, all the points do not pass through their maxima or minima at the same instant in time - points lag behind other points and the mode shape can be adequately described as a travelling wave. In Figure 5.2, instantaneous deflections during a half cycle for a completely complex mode of a hollow disc is depicted, where + and – signs indicate whether the instantaneous deflections are in the direction normal to the page or in opposite direction, respectively. It is seen in this case that the maximum and the minimum deflections are the same at all times causing the strain energy of the system being independent of time as illustrated in Figure 5.3b. However, in general cases other than pure travelling wave situation, mode shapes are not completely complex; hence the strain energy of the system will not be constant.

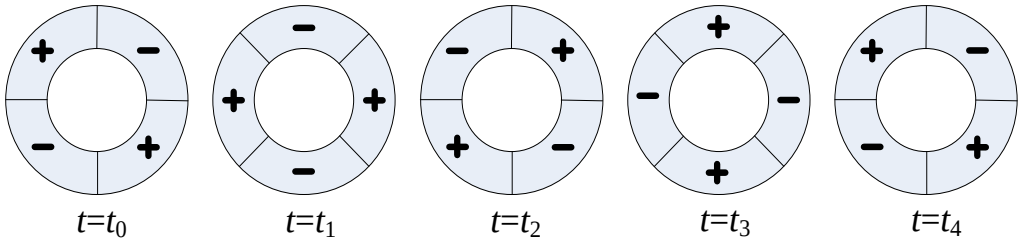

Figure 5.2 : A completely complex mode shape: travelling wave.

iii) For a typical complex mode, the situation is somewhere between the completely complex and the real modes. In this case, as all the points of the structure do not pass through their minima at the same instant in time, the minimum strain energy would be greater than zero as illustrated in Figure 5.3c. As the mode shape complexity increases, the minimum strain energy level also increases.

Based on the energy principle summarised above, Mode Shape Complexity (MSC) of a mode *r* is defined in this thesis as

$$\mathrm{MSC}_r = \frac{\min\left(\mathbf{U}_r\right)}{\max\left(\mathbf{U}_r\right)} \tag{5.6}$$

where $\mathbf{U}_r$ is the strain energy of a structure vibrating at mode *r*. If a structure is vibrating at its *r*th mode, the strain energy of the structure for this mode can be determined as a function of time as

$$U_r\left(t\right) = \frac{1}{2}\mathbf{x}_r\left(t\right)^{\mathrm{T}} \cdot \mathbf{K} \cdot \mathbf{x}_r\left(t\right) \tag{5.7}$$

where $\mathbf{x}_r\left(t\right)$ is the displacement vector due to vibration at mode *r* and **K** is the stiffness matrix of the system. The individual elements of the displacement vector $\mathbf{x}_r\left(t\right)$ can be expressed as

$$x_{rk}\left(t\right) = \Psi_{rk} \cdot \cos\left(2 \cdot \pi \cdot t / T_r + \varphi_{rk}\right) \tag{5.8}$$

where φ_{rk} is the phase angle of the *k*th component of the mode shape $\mathbf{\Psi}_r$ and T_r is the period of the *r*th mode.

As stated before, for an undamped or proportionally damped system, all the points pass through zero deflection at the same instant in time, i.e, $\mathbf{x}\left(t_2\right) = \mathbf{0}$. Therefore the

minimum strain energy of the system is zero, hence MSC_r=0. For a completely complex mode, the strain energy of the system is constant and it is independent of time hence, Equation 5.6 yields unity, i.e., MSC_r=1.0. For a mode shape that is in between being real and completely complex mode, the minimum strain energy will be greater than zero, i.e., MSC value is between zero and unity, and MSC increases as mode shape complexity increases. It is worth stating that the parameter introduced here uses the mode shape data at all DOFs of the system and system dynamic properties. Also, there is no assumption made about the type and level of damping in the structure.

When dealing with experimental mode shapes, spatial parameters or system matrices including the stiffness matrix may not be readily available. In such cases, the stiffness matrix required in Equation 5.7 can be estimated from measured modal data or directly from frequency response function data. It should be noted that there are a variety of methods for the estimation of system matrices from measured data in the literature [173-180]. For example, stiffness matrix can be derived utilising the pseudo-inverse of the mode shape matrix [176] using Equation 5.9 noting that the modal parameters are obtained by analysing a set of FRF measurements.

$$\mathbf{K}=\left[\mathbf{\Phi}^{T}\right]^{+}\mathbf{k}\left[\mathbf{\Phi}\right]^{+} \qquad \textbf{(5.9)}$$

Here **K** is the stiffness matrix (*n* by *n*), $\left[\mathbf{\Phi}\right]^{+}$ is the pseudo-inverse of the mode shape matrix, **k** is the diagonal modal stiffness matrix (*m* by *m*) and *T* and + denote the transpose and the pseudo-inverse, respectively, and *n* and *m* are the number of DOFs and the number of modes, respectively.

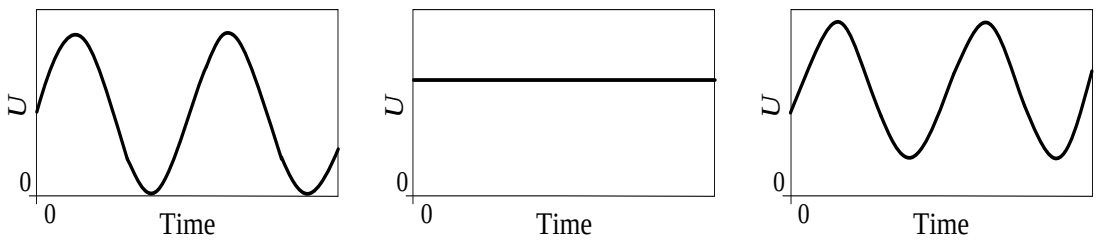

Figure 5.3 : Strain energy as a function of time: completely real (left), completely complex (middle) and typical complex (right) modes.

5.4 Comparisons and Validation

In order to evaluate the performance of the new parameter introduced here and the other parameters in the literature for measuring mode shape complexity, a cantilever beam (Figure 5.4) is modelled using FE method and complex modal analysis of the beam is performed. The stiffness and the consistent mass matrices of the beam element based on the Bernoulli-Euler theory [181] are given in Equations 5.10 and 5.11

$$\mathbf{k}_i^* = \frac{2E^*I}{L^3}\begin{bmatrix} 6 & 3L & -6 & 3L \\ & 2L^2 & -3L & L^2 \\ & sym & 6 & -3L \\ & & & 2L^2 \end{bmatrix} \tag{5.10}$$

$$\mathbf{m}_i = \frac{\rho AL}{420}\begin{bmatrix} 156 & 22L & 54 & -13L \\ & 4L^2 & 13L & -3L^2 \\ & sym & 156 & -22L \\ & & & 4L^2 \end{bmatrix} \tag{5.11}$$

where L, A, I, ρ and E^* are length, area, area moment of inertia, density and complex Young's modulus of the element, respectively. The complex Young's modulus makes the individual elements of the stiffness matrices complex. The stiffness and mass matrices for the beam structure are obtained by adding the contributions of individual elements via a summation process as

$$\mathbf{K}^* = \sum_{i=1}^{n} \mathbf{k}_i^* \; ; \quad \mathbf{M} = \sum_{i=1}^{n} \mathbf{m}_i \tag{5.12}$$

where $\mathbf{K}^*$ and $\mathbf{M}$ are the system stiffness and mass matrices, respectively, and n is the number of elements. It should be stated that the summations in Equation 5.12 represent matrix building rather than simple matrix summation of the matrices in Equations 5.10 and 5.11. Once the stiffness and mass matrices are available, the natural frequencies, mode shapes and modal damping values for a system can be obtained by solving the standard eigenvalue problem as described in Section 3.3. It should be noted that if the damping properties of individual elements are different from each other, the complex stiffness matrix $\mathbf{K}^*$ will represent non-proportional damping distribution. The complex eigensolution of the eigenvalue problem yields

complex eigenvalues (λ_r^2) and complex mode shapes ($\mathbf{\Psi}_r$). Natural frequencies (ω_r) and loss factors (η_r) are determined using Equations 3.42 and 3.43.

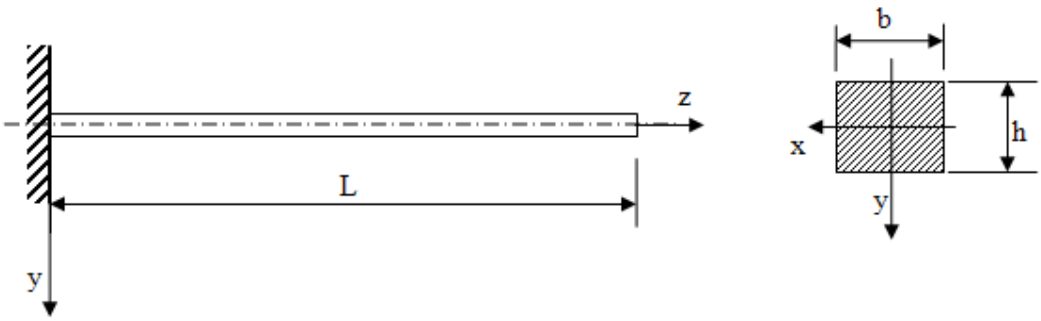

Figure 5.4 : Damped structure used in simulations (*L*=2.0 m, *b*=5 mm, *h*=4 mm).

The damped beam described in Figure 5.4 is divided into six different regions as illustrated in Figure 5.5. The properties of the regions are listed in Table 5.1. The beam is divided into 120 elements. Analyses are performed for four cases, labelled here as Undamped, Proportionally damped, Non-proportionally lightly damped and Non-proportionally highly damped. The predicted natural frequencies and associated modal damping levels are given in Table 5.2 for various damping cases. As modal damping levels are either zero or constant for the undamped and the proportionally damped systems, respectively, they are not listed in Table 5.2.

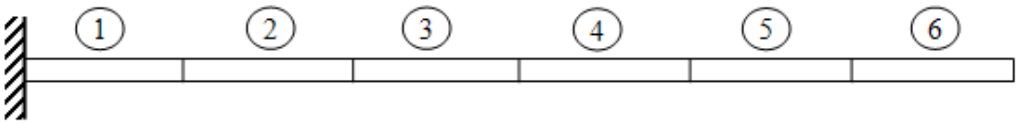

Figure 5.5 : Non-proportionally damped beam.

Table 5.1 : Material properties of the regions of the beam analysed for various damping cases.

Region	ρ (kg/m^3)	E (N/m^2)	η			
			Undamped	Proportional	Lightly D.	Highly D.
1	2500	80	0	0.4	0.02	0.8
2	2500	80	0	0.4	0.00	0.0
3	2500	80	0	0.4	0.03	0.9
4	2500	80	0	0.4	0.03	0.9
5	2500	80	0	0.4	0.00	0.0
6	2500	80	0	0.4	0.01	0.2

Table 5.2 : Predicted natural frequencies and associated modal damping levels for various damping cases.

	Undamped	Proportional	Lightly Damped		Highly Damped	
Mode	f (Hz)	f (Hz)	f (Hz)	η	f (Hz)	η
1	0.9	0.9	0.9	0.02	1.0	0.48
2	5.7	5.9	5.7	0.02	6.6	0.65
3	16.0	16.6	16.0	0.01	17.3	0.29
4	31.4	32.6	31.4	0.01	33.1	0.36
5	51.9	53.9	51.9	0.02	57.4	0.46
6	77.6	80.5	77.6	0.01	84.5	0.37
7	108.4	112.5	108.4	0.01	115.4	0.43
8	144.3	149.7	144.3	0.02	158.0	0.45
9	185.3	192.3	185.4	0.01	198.8	0.33
10	231.5	240.3	231.5	0.01	245.3	0.39
11	282.8	293.5	282.8	0.02	312.7	0.42
12	339.2	352.1	339.3	0.01	366.8	0.36
13	400.8	416.0	400.8	0.01	427.9	0.45
14	467.5	485.2	467.5	0.02	515.8	0.43
15	539.3	559.7	539.4	0.01	572.7	0.33
16	616.3	639.6	616.3	0.01	653.6	0.42
17	698.4	724.8	698.4	0.02	783.9	0.40
18	785.6	815.3	785.7	0.01	832.8	0.35
19	877.9	911.1	878.0	0.01	942.0	0.47
20	975.4	1012.3	975.5	0.02	1094.1	0.44

Using the results of the eigenvalue problem of the damped beam for various damping cases, mode shape complexity is predicted using the proposed parameter (MSC) in this thesis and some other parameters (MPC, MCC and MPD) used in the literature. In what follows, results are evaluated separately for proportionally damped (and also undamped), non-proportionally lightly damped and non-proportionally highly damped cases. It should be remembered that MSC values range from zero for a completely real mode to unity for a completely complex mode while MPC and MCC values range from zero for a mode with completely uncorrelated phase angles to unity or 100 percent for a mode with completely correlated phase angles. Also, MPD yields zero for a completely real mode and its maximum normalised value can become $\pi/4$ (or 45 degrees) for complex modes.

5.4.1 Proportionally damped system

For proportionally damped case, normalised (divided by the maximum value) strain energies of three specific modes are plotted in Figure 5.6. As seen, the minimum strain energy is zero for these three (and all other) modes as expected. When the

parameter MSC introduced in this thesis as well as MPC, MCC and MPD defined in the literature are calculated, it is seen that MSC and MPD are zero while MCC and MPC are unity for all modes. As expected, the same results are obtained for the undamped case and they are not included here for brevity. Also, plotting some mode shapes on Re-Im plane (Figure 5.7) for proportionally damped case, it is seen that the component of the modes are on a straight line indicating normal modes. Therefore, it can be stated that for a proportionally damped (also undamped) system, the parameter introduced here and the other parameters proposed in the literature yield zero complexity values for all the modes.

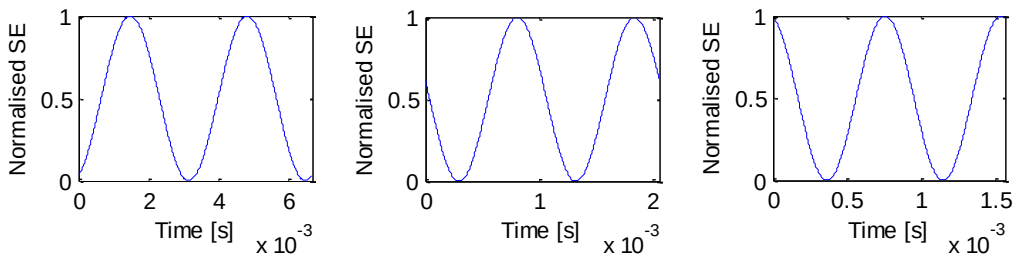

Figure 5.6 : Normalised strain energy (SE) of 8th (left), 14th (middle) and 16th (right) modes for the proportionally damped case (η_{beam} =0.4).

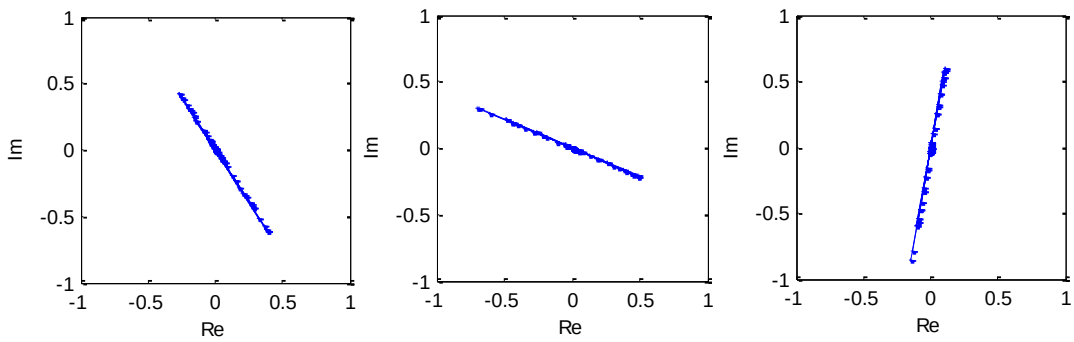

Figure 5.7 : 4th (left), 7th (middle) and 11th (right) modes for the proportionally damped case (η_{beam}=0.4).

5.4.2 Non-proportionally lightly damped system

For a structure similar to the beam studied here, nearly real modes are expected for lower modes as long as the structure is lightly damped, even the damping distribution in the system is non-proportional. Therefore, first, the damping levels of the regions of the beam studied here are set to quite a low level such that non-proportional lightly damping case is obtained. This allowed assessing the performance of the parameter introduced in this thesis and other parameters in the literature for measuring complexity of nearly-real mode shapes. The predicted MSC as well as

MP, MPD, MCC and MPC values for the non-proportionally lightly damped beam are listed in Table 5.3 for the first 20 modes. It should be noted that for this case, the minimum normalised strain energies for all the modes are very close to zero (they are not exactly zero anymore) and they are not plotted here for brevity. As seen in Table 5.3, MSC values are nearly identical to zero while MPC values are very close to unity for all the modes as small damping levels are not expected to cause the mode shapes to be quite complex for this system. These results indicate that MSC and also MPC are effective to quantify the complexity of a mode of a lightly damped system. It should be noted that MPD values are also low although they are not very close to zero as MSC and other parameters. Some mode shapes are plotted on Re-Im plane in Figure 5.8, clearly indicating that mode shapes are very close to being normal modes also. On the other hand, although MCC values are very close to unity for most of the modes, it is about 0.98, 0.49 and 0.96 for the 10th, 11th and 12th modes, respectively. It should be noted that such a high complexity value (e.g., MCC=0.49) is not expected for such a lightly damped system as mentioned before. However, as stated before, MCC is only a correlation function between two vectors and MCC and such similar correlation functions are not expected to be good indicators of mode shape complexity.

Table 5.3 : Calculated MSC, MP, MPD, MPC and MCC values for non-proportionally lightly damped system.

Mode	MSC	MP (Degree)	MPD (Degree)	MPC	MCC
1	0.0001	61.9	0.1	1.0000	1.0000
2	0.0001	35.2	0.2	1.0000	0.9999
3	0.0002	80.8	0.7	0.9999	0.9989
4	0.0001	10.4	0.4	0.9999	0.9995
5	0.0001	14.0	0.6	0.9999	0.9993
6	0.0002	36.2	0.9	0.9998	0.9998
7	0.0001	35.1	0.7	0.9998	0.9998
8	0.0002	51.5	0.8	0.9997	0.9997
9	0.0002	66.9	1.0	0.9996	0.9992
10	0.0002	86.1	1.2	0.9996	0.9783
11	0.0002	0.9	1.5	0.9994	0.4927
12	0.0003	86.2	1.5	0.9993	0.9599
13	0.0002	75.6	1.7	0.9993	0.9971
14	0.0003	38.2	1.6	0.9991	0.9990
15	0.0004	17.3	1.6	0.9989	0.9966
16	0.0003	27.6	1.6	0.9989	0.9984
17	0.0004	62.4	2.0	0.9986	0.9980
18	0.0005	40.0	1.9	0.9985	0.9985
19	0.0004	29.9	2.0	0.9985	0.9980
20	0.0006	47.0	2.1	0.9981	0.9981

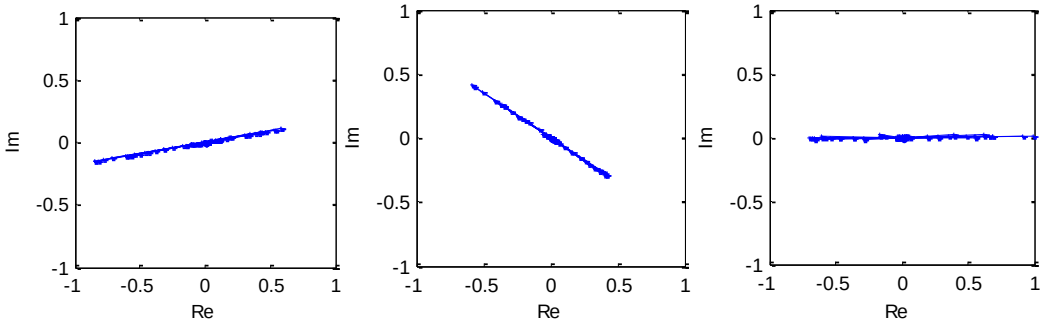

Figure 5.8 : 4th (left), 7th (middle) and 11th (right) modes for the non-proportionally lightly damped system.

5.4.3 Non-proportionally highly damped system

For non-proportionally highly damped system, the normalised strain energies of the three specific modes are plotted in Figure 5.9. As can be seen, the minimum normalised strain energies are quite large and not close to zero anymore, depending on individual modes. Again, MSC introduced in this thesis and the other parameters MP, MPD, MCC and MPC are calculated and the results are listed in Table 5.4 for the first 20 modes. It is seen that the levels of mode shape complexity predicted by all the parameters are much greater than those for non-proportionally lightly damped system. Also, the mode shape plots on Re-Im plane in Figure 5.10 show that modes are actually quite complex. It is seen in Table 5.4 that, MSC value is low (0.04 or 4%) for the 4th mode while it is quite high (0.63 or 63%) for the 17th mode. Also, it is seen in Figure 5.10 that the 4th mode shows small phase angle scatter while the 17th mode shows much larger scatter when these modes are plotted on Re-Im plane as illustrated. This visual observation also confirms the ability of the MSC for quantifying the level of mode shape complexity.

Although not included for brevity here, various analyses are performed for some other non-proportionally damped beams with different dimensions and damping distributions and very similar results are obtained each time. It is also seen that MCC is not capable of quantifying the mode shape complexity adequately, which was also the case for the non-proportionally lightly damped beam case. For example, although all the parameters MSC, MPC and MPD indicate that mode shape complexity for the second mode is less than 10% or 6 degrees, MCC parameter indicates that the complexity is greater than 90% for this mode. As stated before, it can be said that MCC is only a correlation function between two vectors and as such it does not seem to be a good indicator of mode shape complexity. Therefore, MCC is not included in

the rest of the comparisons.

MSC values are plotted with respect to MPD and MPC values in Figure 5.11 for the first 20 modes of the beam. As can be seen, as a trend, MSC value appears to increase as MPD value increases. Also, MSC value decreases as MPC parameter increases. It should also be noted that the relationships between the MSC and the other two parameters in Figure 5.11 are not linear.

It is worth restating that MSC values range from zero for a completely real mode to unity for a completely complex mode while MPC values range from zero for a mode with completely uncorrelated phase angles to unity or 100 percent for a mode with completely correlated phase angles. On the other hand, MPD yields zero for a completely real mode and its maximum normalised value can become $\pi/4$ (or 45 degrees) for complex modes. MPC and MPD parameters are normalised so that they give zero for a completely real mode and unity for a completely complex mode and MSC is compared to the normalised parameters. MSC and normalised MPC and MPD values are plotted with respect to mode number for both non-proportionally lightly and highly damped systems in Figure 5.12. It is seen that MSC values are very close to MPC values for lightly damped system. Although all three parameters indicate that mode shape complexity is low (smaller than 5%) for lightly damped system studied here, MPD values are greater than the values of other parameters. For the highly damped system with non-proportional damping distribution, all the mode shape complexity parameters yield very high values relative to the lightly damped case. As before, there is no linear relation between the parameters and the numerical differences between these parameters depend on individual mode shapes. Although these three parameters appear to exhibit somewhat similar trends, the differences between quantitative results for individual modes can be significant and large. For example, it is seen that the results of all three parameters indicate that 17th mode is the most complex one with numerical values, MPD=0.57, MSC=0.63 and MPC=0.90. It is believed and argued here that MSC parameter introduced in this thesis is providing the most meaningful and adequate quantification of mode shape complexity as it is based on energy principle and the value of MSC increases as the level of mode shape complexity increases as explained in Section 5.3. As stated before, the other parameter MPD is just a statistical variance of the phase angles from the mean value and MPC is associated with the correlation of phase angles.

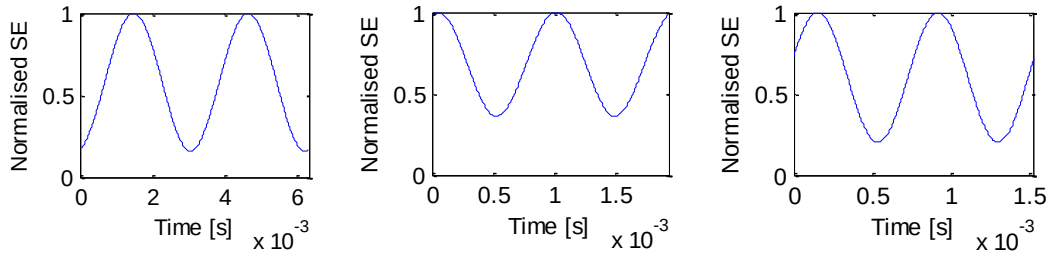

Figure 5.9 : Normalised strain energy (SE) of 8th (left), 14th (middle) and 16th (right) modes for the non-proportionally highly damped system.

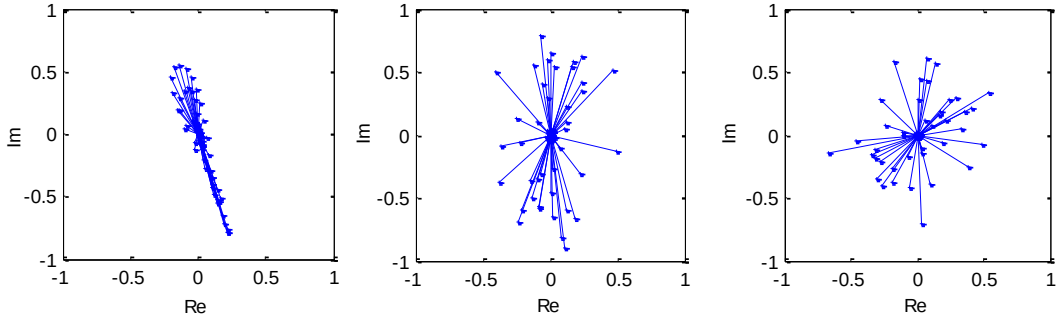

Figure 5.10 : 4th (left), 11th (middle) and 17th (right) modes of the non-proportionally highly damped system.

Table 5.4 : Calculated MSC, MP, MPD, MPC and MCC values for the non-proportional highly damped system.

Mode	MSC	MP (Degree)	MPD (Degree)	MPC	MCC
1	0.12	8.6	3.0	1.00	0.95
2	0.08	83.7	5.5	0.95	0.07
3	0.10	7.4	9.1	0.94	0.20
4	0.04	73.8	8.9	0.96	0.85
5	0.12	12.2	12.8	0.85	0.26
6	0.13	77.1	14.2	0.82	0.17
7	0.07	73.5	14.0	0.84	0.45
8	0.16	19.4	17.4	0.69	0.27
9	0.14	57.9	16.0	0.73	0.67
10	0.10	13.5	16.9	0.75	0.00
11	0.26	69.1	19.5	0.50	0.03
12	0.23	68.5	20.3	0.53	0.07
13	0.18	59.5	19.0	0.55	0.42
14	0.36	44.6	22.2	0.30	0.30
15	0.28	67.0	22.7	0.40	0.00
16	0.20	46.1	18.9	0.48	0.48
17	0.63	47.6	25.6	0.10	0.09
18	0.42	32.3	25.2	0.19	0.03
19	0.27	35.2	20.7	0.36	0.30
20	0.51	34.8	24.4	0.11	0.02

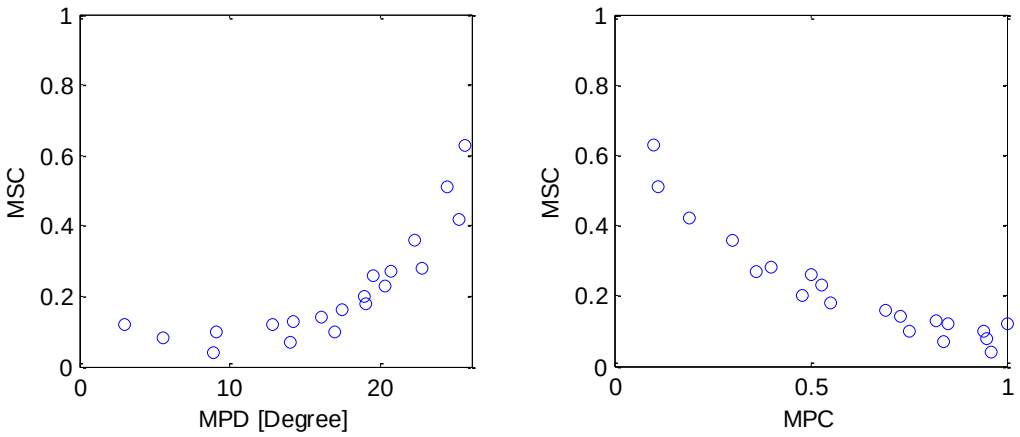

Figure 5.11 : MSC with respect to MPD and MPC for non-proportionally highly damped structure.

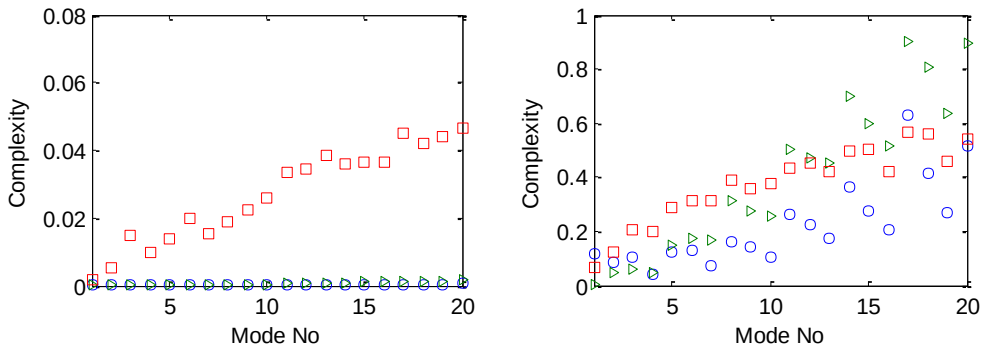

Figure 5.12 : Comparison of MSC and normalised MPC and MPD for non-proportionally lightly (left) and highly (right) damped structures (○ MSC, ▷ MPC and □ MPD).

Overall, the existing parameters in the literature aiming to quantify mode shape complexity are based on either purely geometrical considerations or on statistical variance and correlation of phase angles. However, the new approach for the quantification of mode shape complexity presented here is based on conservation of energy principle, i.e., if a mode shape is complex, strain energy of a structure never becomes zero during a period of vibration at its mode although the total energy (sum of strain and kinetic energies) is conserved. Therefore, the mode shape complexity quantified by the proposed MSC parameter has a physical meaning in terms of energy exchange in the system and this property is the main advantage of MSC parameter over the other existing parameters.

5.5 Concluding Remarks

Although MPD is used to quantify mode shape complexity in Chapter 4, it is noted that there is no universally accepted parameter for quantification of mode shape complexity in the literature. Therefore, a novel parameter is introduced in this chapter to overcome the void about quantification of mode shape complexity in the literature. The mode shape complexity quantified by the proposed MSC parameter in this thesis has a physical meaning in terms of energy exchange in the system and this property is the main advantage of MSC parameter over the other existing parameters. Furthermore, the theoretical foundation of the MSC parameter indicates that the MSC value increases as the level of mode shape complexity increases while the other parameters in the literature do not guarantee this. It is believed that MSC parameter introduced in this thesis is providing the most meaningful and adequate quantification of mode shape complexity compared to other parameters in the literature. As the MSC parameter defined here is based on the energy principle for quantifying the mode shape complexity, it is believed that it is a very good candidate for a universal indicator for mode shape complexity.

6. PASSIVE DAMPING OPTIMISATION

6.1 Introduction

As stated at the beginning of the thesis, vibro-acoustic behaviour of machines is becoming increasingly more important as these properties are usually related to the quality and customer satisfaction of many products including domestic appliances and automobiles. Passive damping materials are widely used in practice as a tool for improving the vibro-acoustic behaviour of many types of machines. However, as the use of damping materials brings additional cost and additional weight to a structure, there is a need for optimising those treatments for maximum benefit with minimum cost.

Design parameters such as the locations, the amount of damping treatments and material type determine the effectiveness of damping application. Trial-and-error approaches are widely used as a traditional way of optimising such design parameters, usually using experimental prototypes during this process. However, optimisation via trial-and-error fashion can easily become cumbersome, very time consuming and prohibitively expensive as this approach requires building many prototypes due to there being so many alternative combinations of damping materials, damping treatment locations and the amount of material that can be used. Furthermore, the structure needs to be excited for a wide range of frequency in order to identify all noise and vibration transfer paths. As an alternative to trial-and-error approaches, engineering structures are sometimes treated with damping materials using the information obtained from modal properties of the untreated or undamped structures in practice. However, this does not usually provide the optimised condition since the dynamic properties of the damped structure usually differ from those of undamped structure. Therefore, a cost-effective theoretical or numerical methodology is required in order to be able to optimise damping treatments of structures in an efficient way. Although some methods appear to be applicable for structures with relatively simple geometries, it is still difficult to utilise them for

general structures. In practice, the emphasis is usually on optimising the locations and sizes of damping treatments.

An efficient approach for optimisation of passive damping treatments that can be applied to general structures is proposed in this chapter. First, an optimisation procedure based on the Big Bang-Big Crunch optimisation method coupled with the modal strain energy method is introduced and its effectiveness for damping optimisation is evaluated. Then, for validation purposes, the proposed optimisation methodology is used to maximise modal damping for a single mode of a structure whose optimised configurations are known for the individual modes. After that, the performance of the proposed optimisation procedure is demonstrated for the maximisation of damping levels for multiple modes at the same time and the applicability of the approach for general structures with passive damping treatments is demonstrated.

6.2 Optimisation Procedure

6.2.1 Statement of the optimisation problem

General optimisation problem can be stated as follows

$$\begin{aligned} &\text{find} && \mathbf{x} = \left(x_1, x_2, x_3 ..., x_n\right), \quad \text{which} \\ &\text{minimise} && f\left(\mathbf{x}\right) \\ &\text{subject to} && g_i\left(\mathbf{x}\right) = 0\,, \quad i = 1, 2, ..., I \\ & && h_j\left(\mathbf{x}\right) \le 0\,, \quad j = 1, 2, ..., J \\ & && \mathbf{x} \in S \end{aligned} \tag{6.1}$$

where $\mathbf{x}$ is an n dimensional design vector, f is the objective or fitness function of the problem, g_i and h_j are known as equality and inequality constraints, respectively, n is the number of design parameters, I and J are the number of equality and inequality constraints, respectively, and the set S is a subset of n dimensional space. In damping optimisation problem, the strategy aims at maximising the modal damping levels using a certain amount of damping material. The maximisation of modal loss factors can also be achieved through minimisation of the objective function given in Equation 6.2.

$$f = \sum_{r=1}^{R} \frac{1}{w_r \eta_r} \tag{6.2}$$

where η_r is rth modal loss factor, w_r is the weighting value for the rth mode and R is the number of modes taken into account during damping optimisation. The thicknesses of the damping layers (t_d), modal loss factors (η_d) and the Young's moduli (E_d) of damping materials as well as the thickness of the base structure (t_b) can be considered as design parameters (**x** vector**)**. There are both space and weight limitations (g and h functions) when treating structures with damping patches. Space limitation can be taken into account by considering only the specific locations as candidates for damping patches while maximum allowable mass or volume of the damping treatment ($m_{d,\max}$ or $V_{d,\max}$) can be specified as a constraint in the algorithm.

6.2.2 Selection of the optimisation method

Although mass and stiffness optimisations of structures are quite common, damping optimisation studies in the literature are relatively rare. Furthermore, the studies on optimisation of damping treatments in the literature are mainly related to systems with special geometries. One of the reasons for this is due to difficulties in modelling highly nonlinear damping materials in damping predictions and optimisations studies. One other difficulty in using known global optimisation methods is related to unacceptable computational cost required to optimise damping treatments applied to structures with large number of Degrees of Freedom (DOFs).

Global optimisation aims to reach to the best possible solution under given set of circumstances. Nature is usually the main source of ideas for proposing optimisation methods such as genetic algorithms and simulated annealing [126-127]. Although Genetic Algorithms (GAs) appear to be one of the widely used global optimisation approaches [127] to solve various optimisation problems, they may suffer from premature convergence, convergence speed and execution time problems. On the other hand, a new competitive global optimisation method called the Big Bang-Big Crunch (BB-BC) method [126] is introduced in 2006. This method also relies on one of the theories of the evolution of the universe: "Big Bang and Big Crunch" theory. It has been demonstrated elsewhere that the BB-BC method has superiority over other heuristic population-based search techniques when employed to perform structural

optimisation tasks [136-138] in a short time after it was introduced in 2006. For example, it has been successfully used for the optimal design of space trusses [136-137], retaining walls [138], skeletal structures [182] and domes [183]. The BB-BC method has also been efficiently used for other purposes such as automatic target tracking [184], inverse fuzzy model control [185] and so on. In this study, an optimisation procedure based on the BB-BC method is proposed to optimise damping treatments applied to any kind of structures.

6.2.3 The Big Bang-Big Crunch (BB-BC) method

As stated, the BB-BC method is a heuristic population-based evolutionary optimisation method [126]. As genetic algorithm [127], this method is a random search method and consists of "bang" and "crunch" phases. According to the BB-BC method, random points are generated in the big bang phase and those points are shrunk to a single representative point via minimal cost approach in the big crunch phase. The steps of the BB-BC method are summarised as follows.

i) The initial population or candidate solution is randomly generated and spread over the entire search space in a uniform manner in the big bang phase.

$$\text{Generate } \mathbf{x}^k = \left[x_1, x_2, ..., x_n\right]^k; \qquad k = 1, 2, ..., N \tag{6.3}$$

where n is the number of design parameters, k is the population index and N is the population size.

ii) In the big crunch phase, the points generated in the big bang phase are shrunk to a single representative point via minimal cost or the so-called centre of mass approach. Here, the term 'mass' refers to the inverse of the fitness or the value of the objective function. The point representing the position of the centre of mass denoted by $\mathbf{x}^c$ is calculated as

$$\mathbf{x}^c = \frac{\sum_{k=1}^{N} \frac{1}{f^k} \mathbf{x}^k}{\sum_{k=1}^{N} \frac{1}{f^k}} \tag{6.4}$$

where f^k is the value of the fitness function at $\mathbf{x}^k$. This centre of mass is used to generate new solutions in the next step as described in (iii).

iii) New solutions or population to be used in the next big bang phase are generated in a random manner based on normal distribution by spreading new off-springs around the centre of mass in every direction in the search space. The problem is formulated in such a way that the standard deviation of this normal distribution function decreases as the number of iterations of the algorithm increases as given below

$$\mathbf{x}_{\text{new}}^{k} = \mathbf{x}^{c} + \frac{1}{2}\boldsymbol{\sigma}^{k}\,\frac{\mathbf{x}_{\max} - \mathbf{x}_{\min}}{1 + g/\lambda} \tag{6.5}$$

where $\mathbf{x}_{\text{new}}^{k}$ is the new solution to be used in the next step, $\boldsymbol{\sigma}^{k}$ is a vector that contains random numbers from a standard normal distribution which changes for each candidate, g is the generation or iteration number and λ denotes after how many iterations search space will be restricted to half, and $x_{i,\min}$ and $x_{i,\max}$ are the minimum and maximum values of the *i*th design parameter, respectively. Since the standard normal distribution can yield numbers greater than unity $(|\sigma| > 1)$, it is necessary to limit the values of the new design parameters in order to keep them in the search space as given in Equation 6.6 below. So, the points which fall outside of the limits are placed at the boundaries ant it is guaranteed that the optimum solution point will not fall outside of the domain. The formulation given here provides different points to be selected in the search space (global optimisation). Also, as the large amounts of solutions generated by the algorithm are around the so-called optimal point, the convergence speed is fast in this method.

$$x_i^k = x_{i,\min} \quad \text{if} \quad x_i^k \le x_{i,\min} \qquad \text{and} \qquad x_i^k = x_{i,\max} \quad \text{if} \quad x_i^k \ge x_{i,\max} \tag{6.6}$$

In the BB-BC method, the successive explosion (big bang) and contraction (big crunch) steps are carried out repeatedly until the stopping criterion is met. It should be noted that the number of individuals in the population must be large enough in order not to miss the optimum point. However, the population size can be significantly reduced as the search domain shrinks. The flowchart of the damping optimisation algorithm based on the BB-BC method is presented in Figure 6.1.

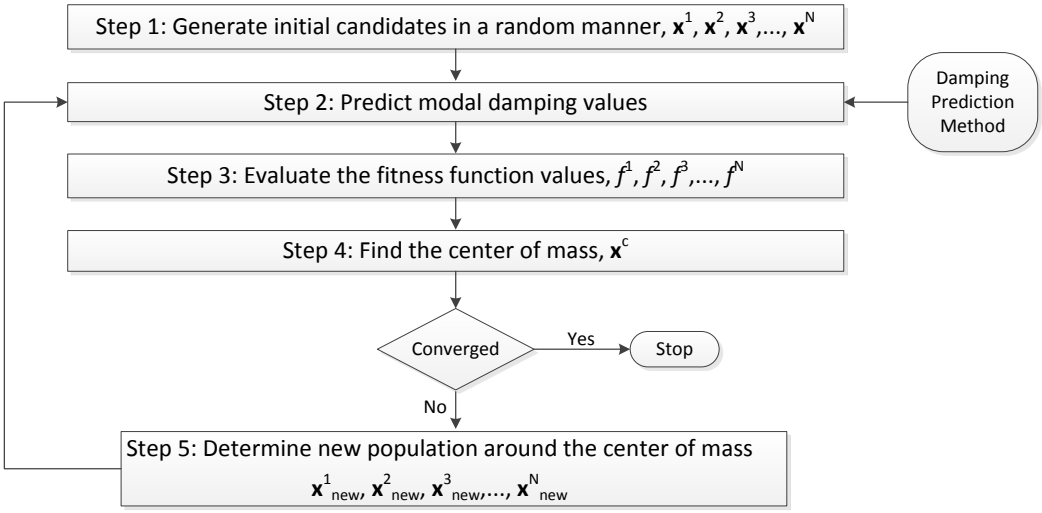

Figure 6.1 : Flowchart of damping optimisation algorithm based on BB-BC.

The performance of the optimisation process outlined in Figure 6.1 strongly depends on the damping prediction method used during the iterations. Therefore, an effective, yet accurate damping prediction method should be adopted in this process. Although the composite FE formulation and the procedure based on the MSE method that are already validated experimentally can be used for damping prediction, it was noted in Section 4 that the MSE method appears to be the most effective approach for modelling general structures with damping treatments for the purpose of damping optimisation. Also, the procedure based on MSE method was assessed in detail in Section 4.5. Therefore, the procedure based on the MSE method is used for damping prediction in this section.

The optimisation procedure based on the BB-BC and MSE methods presented here begins by solving the normal eigenvalue problem of the structure where the damping levels of damping patches are set to zero in order to determine normal modes of the structure and the successive explosion and contraction steps are carried out repeatedly until the stopping criterion is met.

6.3 Results

A beam-like long plate is studied as a test case here. The length, width and thickness of the base structure are L_b=200, w_b=15 and t_b=2 mm. Quadrilateral shell elements with edge length of 5 mm are used to model the base and the damping layers as described in Sections 4.2 and 4.4. The Young's modulus, Poisson's ratio and mass

density of the base structure are E_b=70 GPa, ν_b=0.33 and ρ_b=2800 kg/m^3, respectively, and the corresponding values are E_d=0.5 GPa, ν_d=0.40 and ρ_d=1000 kg/m^3 for the damping material. The loss factor of the damping material is η_d=10%. The beam is divided into ten damping regions or patches. The thickness of each damping layer of the patches is defined to be variable, i.e., the design vector is $\mathbf{x} = [t_{d1}, t_{d2}, ..., t_{d10}]$ where the number of design parameters n=10 in the test case here. The maximum thickness of the damping layer is defined to be $t_{d,\max}$=3 mm and the constraint about the amount of the damping treatments is defined to be $V_{d,\max}$=3600 mm^3 (for example, maximum 4 damping layers with dimensions 3 mm x 15 mm x 20 mm can be allowed). The population number is N=12 and the search space is restricted to half after λ=50 iterations. The proposed optimisation methodology is used to maximise modal damping for single and multiple modes below.

6.3.1 Damping optimisation for a single mode

The optimum (highest) loss factor for the first mode of the beam is searched in an iterative way and the distribution of the damping material (t_d) between damping patches are shown in Figure 6.2 at some iterations steps. It is seen that the optimisation procedure converged successfully after 22 iterations to the expected optimum region where the damping material is placed to the patches near to the clamped end of the beam. According to the optimum solution for this case, the thicknesses of the damping layers for the first four damping patches are 3 mm and the thicknesses of other damping patches are zero. This is an expected result since the strain energy of the beam is highest at the clamped end and the strain energy decreases gradually from the clamped end to the free end as shown in Figure 6.3 for the first bending mode. The loss factor of the first mode is also plotted as a function of iteration number in Figure 6.4. The loss factor of the first mode of the structure in the case of uniformly distributed damping material is determined to be 0.33% and the loss factor determined by the proposed optimisation is 4.61 times higher than that which can be achieved by uniform damping treatment all over the beam. Similarly, the optimisation procedure is employed for the maximisation of the loss factor for the second mode of the beam and the distribution of the damping material between the damping patches at some iteration steps are illustrated in Figure 6.5. It is seen that

the damping material is placed to those damping patches where the strain energy is the highest for the second mode of the cantilever beam as shown in Figure 6.6. In this case, the thicknesses of the damping layers of the patches where the strain energy is the highest are 3 mm while the thicknesses of the other damping patches are zero at 14th iteration step. Also, the loss factor of the second mode is plotted as a function of iteration number in Figure 6.7. The loss factor of the second mode of the structure in the case of uniformly distributed damping material is determined to be again 0.33% and the loss factor determined by the proposed optimisation is 3.90 times higher than that which can be achieved by uniform damping treatment all over the beam.

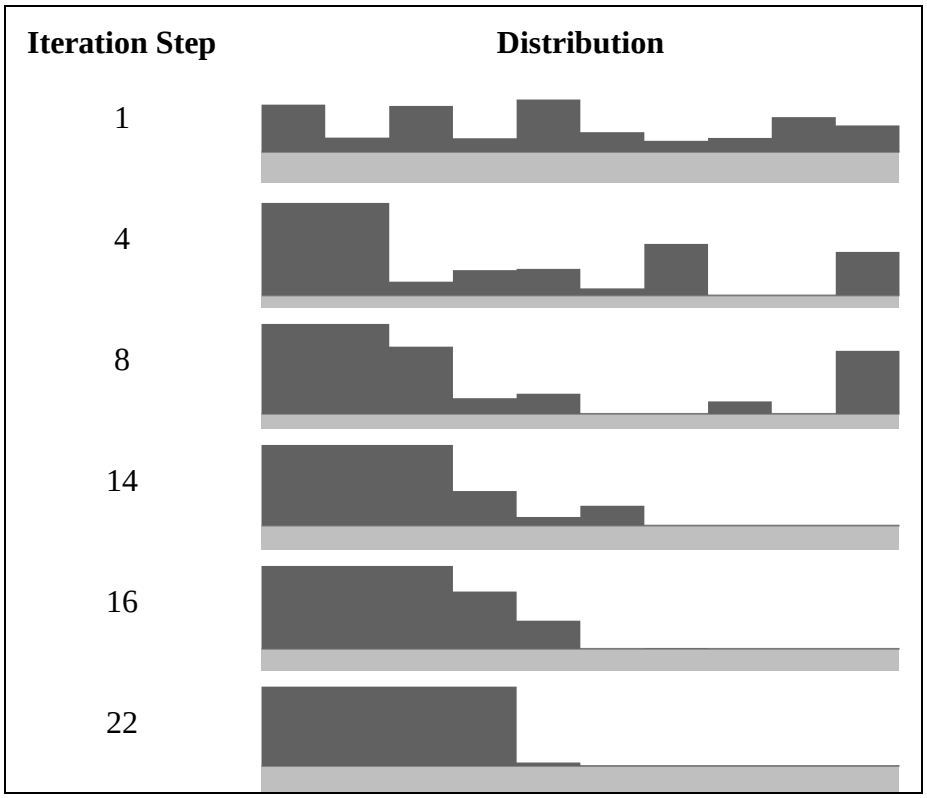

Figure 6.2 : Damping optimisation for the first mode of the beam: distribution of the damping material between damping patches at some iteration steps.

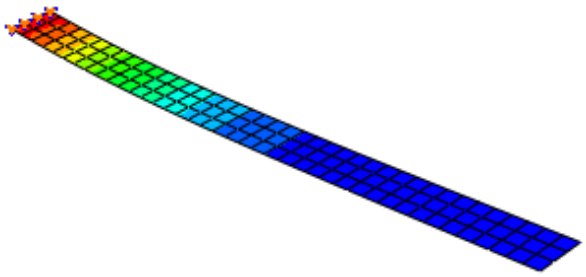

Figure 6.3 : Strain energy distributions of the structure for the first mode.

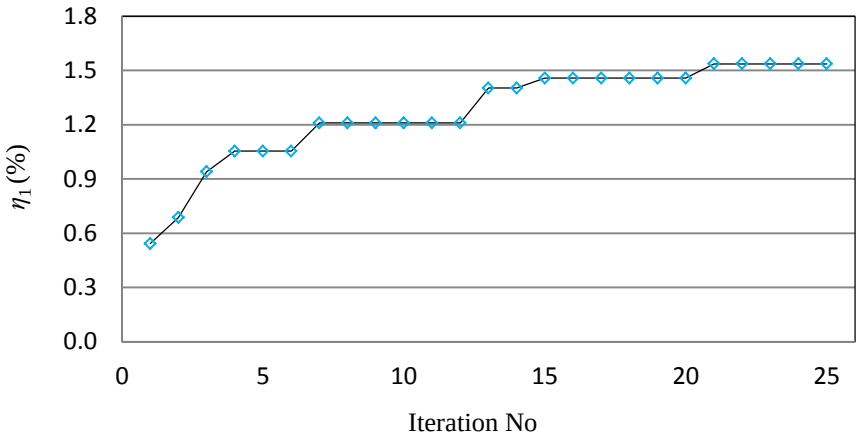

Figure 6.4 : The results for maximisation of the loss factors of the 1st mode.

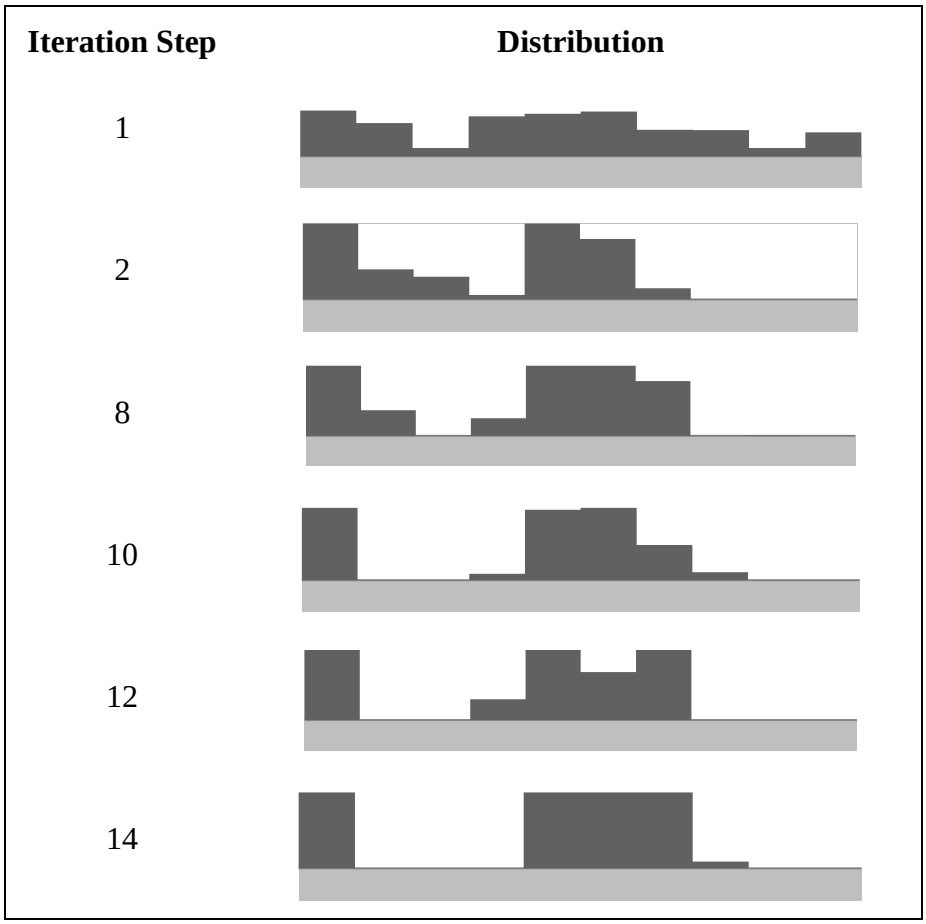

Figure 6.5 : Damping optimisation for the 2nd mode of the beam: distribution of the damping material between damping patches at some iteration steps.

The results presented so far confirms that the proposed optimisation procedure can successfully maximise modal damping for an individual mode. However, more often than not, it is necessary to optimise damping for more than one mode in practice. The next case considered here is to assess the performance of the proposed optimisation

procedure when the modal damping levels are to be optimised for multiple modes as given below.

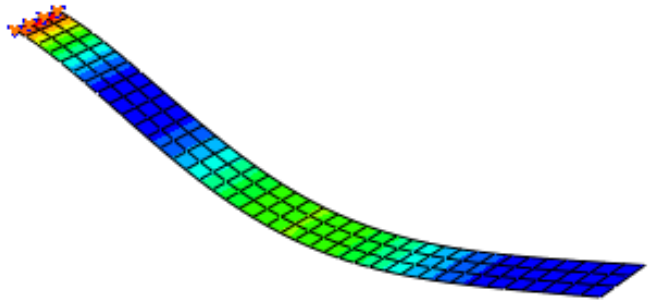

Figure 6.6 : Strain energy distributions of the structure for the second mode.

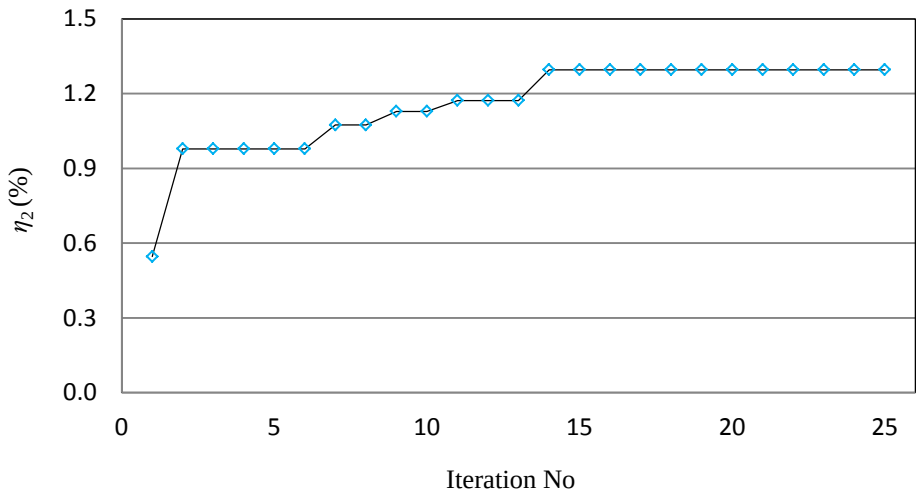

Figure 6.7 : The results for maximisation of the loss factors of the 2nd mode.

6.3.2 Damping optimisation for multiple modes

The optimisation of passive damping treatments is performed here by considering the first two modes of the beam simultaneously and the algorithm aims to optimise the modal damping levels for both modes at the same time. It is worth stating here that each mode can be assigned a weighting factor during the optimisation process. Without any loss of generality, the weighting factors for individual modes are taken as unity here. The distribution of the damping material for this case at some iteration steps are depicted in Figure 6.8. As expected, the optimised configuration (last distribution) in Figure 6.8 is a combination of the damping material distributions (last configurations) in Figures 6.2 and 6.5. Also, the loss factors for the first two modes and the average loss factor are plotted as a function of iteration number in Figure 6.9. It is seen that the modal loss factors reach quite high values after a few number of

iterations. When the optimisation process converges, the average loss factor finally reaches to 1.03% from 0.55% level at the beginning. The average loss factor is determined to be 0.33% in the case of uniform distribution of damping material over the base structure and the loss factor determined by the optimisation is 3.12 times higher than which can be achieved by uniform damping treatment all over the beam. It should be noted that the analyses are performed for some other cases of the single and multiple modes and similar results are obtained although they are not presented here for brevity.

The optimisation results for single and multiple mode cases presented here suggest that damping optimisation using the BB-BC method combined with the MSE method is very effective. There is no need to make any assumptions during the application of the given optimisation scheme. The optimisation methodology given here is a heuristic population-based evolutionary (global) optimisation method and the convergence speed of this method is quite high. Overall, this efficient approach appears to be suitable for optimisation of damping treatments for general structures.

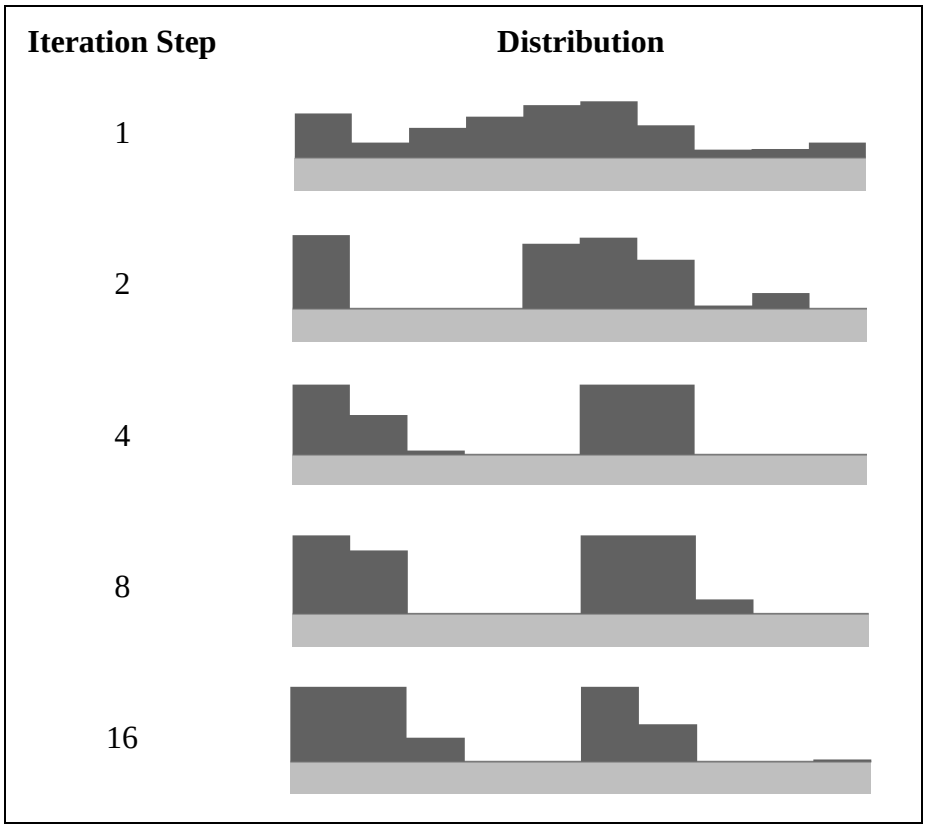

Figure 6.8 : Damping optimisation for the average loss factor of the first two modes of the beam: distribution of the damping material between damping patches at some iteration steps.

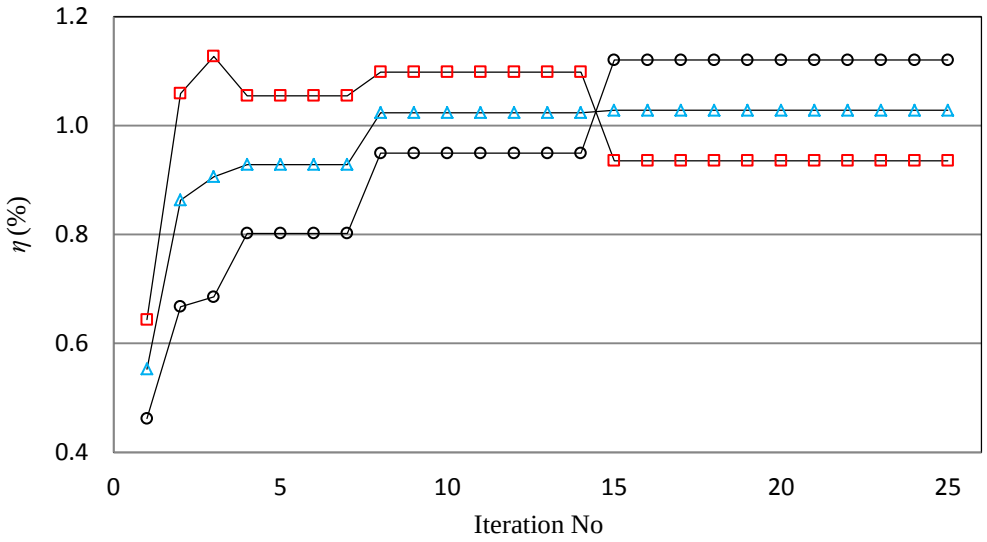

Figure 6.9 : Results for maximisation of the average loss factors of the first two modes of the structure (Key: ○ Mode 1, □ Mode 2 and Δ Average).

6.4 Concluding Remarks

In this chapter, an effective approach for the optimisation of passive damping treatments that can be applied to general structures is introduced. The optimisation procedure is based on the BB-BC global optimisation algorithm and the MSE damping prediction method. This study is the first study presenting a damping optimisation procedure based on the BB-BC method coupled with the MSE method that makes optimisation of passive damping treatments possible for general structures.

After the description of the optimisation methodology based on the BB-BC technique coupled with the damping prediction approach using the MSE method, some validation studies are performed. The application of the methodology for single and multiple modes damping optimisation yields very good results. Overall, it is shown that the BB-BC technique coupled with the damping prediction approach based on the MSE method can be used effectively for the optimisation of passive damping treatments applied to general structures in practice.

7. CONCLUSIONS AND SUGGESTIONS FOR FUTURE WORK

7.1 Conclusions

This thesis aims to improve the modelling and optimisation of structures with passive damping treatments. To this end, various methods are proposed for the identification, modelling and optimisation of such structures and new analytical, numerical and experimental studies are presented on these topics. The main achievements of the thesis are:

- The available methods for the identification of damping materials are assessed and an existing method is improved so as to obtain dynamic properties of materials with better accuracy,
- The levels of uncertainty due to noise and signal processing parameters in measured damping levels of structures are identified and quantified,
- Different damping prediction methods for modelling structures with passive damping treatments are presented and validated using experimental data,
- A novel approach for quantification of mode shape complexity due to non-proportional damping of passive damping treatments is proposed, and
- An effective methodology to optimise passive damping treatments for general structures is proposed.

In what follows, the main tasks performed in this thesis and the associated conclusions are summarised.

i) Although the Oberst beam method is widely used in practice, it is seen that detailed information about how to perform a successful Oberst beam experiment is quite limited in the literature. Therefore, first, the effects of various parameters in an Oberst test rig are examined in an attempt to improve the accuracy of the estimated material properties. Overall, the critical assessment of the Oberst test rig parameters revealed that: A sufficient number of averages should be used in Oberst beam tests in order to minimise the noise levels in measured FRFs; Appropriate forcing level

should be determined before making the final measurements; The length of the beam should be chosen such that the natural frequencies of the beam should not coincide with the frequency of the main electric power; The use of a kind of gauge is very useful for assuring that the beam will have almost the same free length every time it is installed.

As it is observed that the electromagnetic effect created by a non-contact exciter can be the most significant source of error in estimated material properties, a systematic study is performed to quantify and model the adverse effects of non-contact electromagnetic excitation. This work presented in this thesis is the first of its kind in the literature, which led to the following conclusions: The electromagnetic field created by a non-contact exciter around the free end of the Oberst beam introduces additional constraints on the system and this adverse effect can be modelled as a spring between the tip of the beam and the ground; The stiffening behaviour of the non-contact electromagnetic exciter can significantly reduce the accuracy of the estimated material properties and the errors in identified natural frequencies and, thus, estimated Young's modulus increase as the length of the segment of the beam exposed to the electromagnetic field (the gap parameter) increases; The first mode is the worst affected by the adverse effect of electromagnetic excitation and the use of the data associated with the first mode does not result in any consistent material properties unless the results are corrected and the errors in estimated material properties due to the stiffening effect of electromagnetic field decreases as the mode number increases; If relatively longer beams are used in Oberst beam tests, the stiffening effect of electromagnetic field causes higher levels of errors in natural frequencies and estimated material properties; One way of reducing the stiffening effect of electromagnetic excitation, hence the error in estimated material properties, is to minimise the length of the segment of the beam exposed to the magnetic field (gap parameter) as much as possible; When the measurements need to be performed using big gap parameter, the adverse effects of electromagnetic excitation should be removed from test results; A method is proposed to remove the adverse effects of electromagnetic excitation from test results in order to determine the material properties with better accuracy.

ii) In addition to the identification of the properties of damping materials, experimental identification of damping levels of structures is also required to validate

the theoretical models of damped structures. However, experimental approach may not be able to provide definite answers either in the sense that the identified damping level may exhibit high level of uncertainty. This thesis addresses damping uncertainty in frequency domain estimation when the data are contaminated by noise and numerical damping via exponential windowing is used during the signal processing phase of the spectrum estimation to overcome the void about damping uncertainty in the literature. Some numerical simulations are performed in order to assess the adverse effects of noise on damping estimations and resulting damping uncertainty is examined as a function of noise level in the FRF data. Noisy FRFs are analysed using the line-fit method in order to determine the damping levels and the associated uncertainty. It is shown that damping uncertainty becomes significant when SNR is less than 30 dB and the uncertainty increases gradually as the SNR decreases. However, the damping uncertainty becomes negligible when the line-fit method is used for damping estimation when SNR is greater than 40 dB.

Damping uncertainty due to the use of exponential windowing is investigated using experimental data which inevitably contains noise. It is found that the damping uncertainty becomes quite significant when the numerical damping added due to exponential windowing is equal to or greater than the actual damping in the system. It is believed that the results presented in this thesis can be used for the estimation of possible damping uncertainty due to exponential windowing when the numerical and the estimated damping levels are known. Comparison of the results of the line-fit and the circle-fit methods reveals that the line-fit method performs better than the circle-fit method in the sense that line-fit method yields lower damping uncertainties.

iii) An effective procedure based on the MSE method and a composite FE formulation with damping capability to model structures with damping treatments are presented and validated in this thesis. The approach based on the MSE method is formulated in an efficient way, i.e., the base and the damping layers of damping patches are modelled at their matching surfaces using shell elements using a minimum number of elements or DOFs and the damping of the base structure is included in the formulation. The composite FE with damping capability used in this thesis is based on stacking individual four-node shell elements on top of each other where individual homogeneous layers have different material properties. The damping capability is included in the formulation by means of complex elemental

stiffness matrix representing both the elastic and the non-proportional damping properties of the individual layers of the composite element. Also, the performance of the MSE method is evaluated as a function of mode shape complexity first time in this thesis.

The predicted modal parameters using the procedure based on the MSE method and the composite FE formulation based on complex eigenvalue method are very close to the experimental results; Although the accuracy of the MSE method decreases with mode shape complexity (based on Mean Phase Deviation), the MSE method predicts damping levels with acceptable accuracy even when the damping level of a structure is moderately high; The MSE method can be conveniently used to predict damping levels for most engineering structures and it can be utilised for damping optimisation purposes during the design stage.

iv) Although Mean Phase Deviation is used to quantify mode shape complexity during the assessment of the damping prediction procedure based on the MSE method, it is noted that there is no universally accepted parameter for quantification of mode shape complexity in the literature. Therefore, a novel parameter (MSC) is introduced in this thesis to overcome the void about quantification of mode shape complexity in the literature. MSC parameter proposed here has a physical meaning in terms of energy exchange in the system and this property is the main advantage of MSC parameter over the other existing parameters.

v) An effective procedure is proposed for the optimisation of passive damping treatments applied to general structures. The optimisation procedure is based on the BB-BC global optimisation algorithm and the MSE damping prediction method. For validation purposes, the proposed optimisation methodology is used to maximise modal damping of a single mode of a structure whose optimised configurations are known prior to the optimisation. Then, the performance of the proposed optimisation procedure is demonstrated for the maximisation of damping levels for multiple modes. The results suggest that the BB-BC technique coupled with the damping prediction approach based on the MSE method can be used for the optimisation of passive damping treatments applied to general structures in practice. To the best of the Author's knowledge, this is the first damping optimisation study utilising the BB-BC method coupled with the MSE method that makes optimisation of passive damping treatments possible for general structures.

7.2 Suggestions for Future Work

Although very significant contributions are made in this thesis in the areas of identification, modelling and optimisation of structures with passive damping treatments, there is still work to do on these topics as summarised here:

- The adverse effect of the non-contact electromagnetic exciter in the Oberst beam method can be eliminated by designing a new excitation system,
- A theoretical formulation can be derived for the quantification of damping uncertainty due to a windowing function,
- The composite FE can be extended/validated for modelling constrained layer treatments,
- The performance of the MSE method can be evaluated as a function of mode shape complexity using the novel mode shape complexity parameter proposed in this thesis, and
- The optimisation procedure based on the BB-BC method coupled with the MSE method can be assessed using more test cases including its application to industrial products.

REFERENCES

[1] **ASTM E 756** (2005). Standard test method for measuring vibration-damping properties of materials. American Society for Testing and Materials.

[2] **SAE J 1637** (1993). Laboratory measurement of the composite vibration damping properties of materials on a supporting steel bar. Society of Automotive Engineers.

[3] **SAE J 671** (1997). Vibration damping materials and underbody Coatings. Society of Automotive Engineers.

[4] **ISO 10846-2** (1998). Acoustics and vibration - Laboratory measurement of vibro-acoustic transfer properties of resilient elements - Part 2: Direct method for determination of the dynamic stiffness of resilient supports for translatory motion. International Organization for Standardization.

[5] **ISO 10846-3** (1998). Acoustics and vibration - Laboratory measurement of vibro-acoustic transfer properties of resilient elements - Part 3: Indirect method for determination of the dynamic stiffness of resilient supports for translatory motion. International Organization for Standardization.

[6] **ISO 10846-5** (1998). Acoustics and vibration - Laboratory measurement of vibro-acoustic transfer properties of resilient elements - Part 5: Driving point method for determination of the low-frequency transfer stiffness of resilient supports for translatory motion. International Organization for Standardization.

[7] **ISO 4664-2** (2006). Rubber, vulcanized or thermoplastic - Determination of dynamic properties - Part 2: Torsion pendulum methods at low frequencies. International Organization for Standardization.

[8] **ASTM D 945-06** (2006). Standard test methods for rubber properties in compression or shear (mechanical oscillograph). American Society for Testing and Materials.

[9] **Oberst, H.** (1952). Über die dämpfung der biegeschwingungen dünner bleche durch fest haftende belage. *Acustica*. *2*(4), 181-194.

[10] **Gross, B.** (1953). *Mathematical Structure of the Theories of Viscoelasticity*. Herman, Paris.

[11] **Ross, D., Ungar, E. E., and Kerwin, E. M.** (1959). Damping of plate flexural vibrations by means of viscoelastic laminate. *Structural Damping*, (pp. 49-88). ASME, New York.

[12] **Kerwin, E. M.** (1959). Damping of flexural waves by constrained viscoelastic layer. *The Journal of The Acoustical Society of America*. *31*(7), 952-962.

[13] **DiTaranto, R. A.** (1965). Theory of vibratory bending for elastic and viscoelastic layered finite-length beams. *Journal of Applied Mechanics*. *32*, 881-886.

[14] **Wojtowicki, J. L., Jaouen, L., and Panneton, R.** (2004). New approach for the measurement of damping properties of materials using the Oberst beam. *Review of Scientific Instruments*. *75*(8), 2569-2574.

[15] **Read, B. E., and Dean, G. D.** (1978). *The Determination of Dynamic Properties of Polymers and Composites*. Wiley, New York.

[16] **Nashif, A. D., Jones, D. I. G, and Henderson, J. P.** (1985). *Vibration Damping*. Wiley, New York.

[17] **Jones, D. I. G.** (2001). *Handbook of Viscoelastic Vibration Damping*. Wiley, New York.

[18] **Morlier, J., and Michon, G.** (2010). Virtual vibration measurement using KLT motion tracking algorithm. *Journal of Dynamic Systems, Measurement and Control*. *132*(1), 11003-11011.

[19] **Rak, M., Ichchou, M., and Holnicki-Szulc, J.** (2008). Identification of structural loss factor from spatially distributed measurements on beams with viscoelastic layer. *Journal of Sound and Vibration*. *310*(4-5), 801-811.

[20] **Munjal, B. S., Trivedi, H. V., and Sarma, P. V. B. A. S.** (2008). Passive damping characterization of parabolic composite reflectors with hybrid PZT-coated layers. *Journal of Intelligent Material Systems and Structures*. *19*(11), 1281-1294.

[21] **Serabatir, D. A., Bayraktar, F., and Sanliturk, K. Y.** (2007). Structural damping optimization using viscoelastic materials. *Proceedings of The 36th International Congress and Exhibition on Noise Control Engineering*. Istanbul, Turkey August 28-31.

[22] **Torvik, P. J.** (2007). Analysis of free-layer damping coatings. *Key Engineering Materials*. *333*, 195-214.

[23] **Ricci, F., Monaco, E., Polito, T., and Marulo, F.** (2004). Influence of experimental testing set-up and geometric parameters on damping measurements. *Proceedings of SPIE Smart Structures and Materials*. San Diego, CA.

[24] **Black, M. D., and Rao, M. D.** (2001). Material damping properties - Lab tests vs. in-vehicle performance. *Sound and Vibration*. *35*(8), 24-28.

[25] **Renault, A., Jaouen, L., and Sgard, F.** (2011). Characterization of elastic parameters of acoustical porous materials from beam bending vibrations. *Journal of Sound and Vibration*. *330*, 1950-1963.

[26] **Carfagni, M., Lenzi, E., and Pierini, M.** (1998). The loss factor as a measure of mechanical damping. *Proceedings of The 16th International Modal Analysis Conference*, (Paper no. 3243, pp. 580-584). Santa Barbara, CA.

[27] **Fasana, A., Garibaldi, L., Giorceli, E., and Ruzzene, M.** (1998). Notes on the Oberst beam test technique. *Proceedings of SPIE Smart Structures and Materials Conference*. San Diego, CA.

[28] **Saha, P., and Cahine, J.** (1995). The testing of vibration damping materials (reprinted). *Sound and Vibration*. *29*(5), 38-42.

[29] **Lilley, K. M., Fasse, M. J., and Weber, P. E.** (2001). A comparison of NVH treatments for vehicle floorpan applications. *Proceeding of Noise and Vibration Conference and Exposition*, (Paper no. 2001-01-1464). SAE International, Grand Traverse, MI.

[30] **Chen, A., and Qian, Y.** (1999). Simulating low frequency NVH of damped automotive body panels using frequency dependent properties. *Proceedings of Noise and Vibration Conference and Exposition*, (Paper no. 1999-01-1836). SAE International, Traverse City, MI.

[31] **Lewis, T., Jackson, P., and Nwankwo, O.** (1999). Design and implementation of a damping material measurement/design system. *Proceedings of Noise and Vibration Conference and Exposition*, (Paper no. 1999-01-1675). SAE International, Traverse City, MI.

[32] **Singh, R. V., and Pellny, M.** (1998). Lightweight, high-performance, constrained-layer sound dampers. *Proceedings of International Congress and Exposition*, (Paper no. 980466). SAE International, Detroit, MI.

[33] **Hirabayashi, T., Rusch, P., McCaa, D., Saha, P., Rebandt, R., et al.** (1995). Application of noise control and heat insulation materials and devices in the automotive industry. *Proceedings of Noise and Vibration Conference and Exposition*, (Paper no. 951375). SAE International, Traverse City, MI.

[34] **Liao, Y., and Wells, V.** (2008). Estimation of complex Young's modulus of non-stiff materials using a modified Oberst beam technique. *Journal of Sound and Vibration*. *316*(1-5), 87-100.

[35] **Ewins, D. J.** (2000). *Modal Testing: Theory, Practice and Application*. Research Studies Press, Second Edition, England.

[36] **Kennedy, C. C., and Pancu, C. D. P.** (1947). Use of vectors in vibration measurement and analysis. *Journal of The Aeronautical Sciences*. *14*(11), 603-625.

[37] **Dobson, B. J.** (1987). A straight-line technique for extracting modal properties from FRF data. *Mechanical Systems and Signal Processing*. *1*(1), 29-40.

[38] **ICATS** (2009). Imperial College Testing Analysis and Software, Imperial Collage, Dynamic Section, London.

[39] **DTA** (1995). The Dynamic Testing Agency: Handbook on Guidelines to Best Practice, Volume - Modal Testing.

[40] **De Silva, C. W.** (1999). *Vibration: Fundamentals and Practice*. CRC Press, New York.

[41] **De Silva, C. W.** (2007). *Vibration Damping, Control, and Design*. CRC Press, New York.

[42] **Bloss, B., and Rao, M. D.** (2002). Measurement of damping in structures by the power input method. *Experimental Techniques*. *26*(3), 30-32.

[43] **Huang, F. -L., Wang, X. -M., Chen, Z. -Q., He, X. -H., and Ni., Y. -Q.** (2007). A new approach to identification of structural damping ratios. *Journal of Sound and Vibration*. *303*(1-2), 144-153.

[44] **Maia, N. M. M., Silva, J. M. M., He, N., Lieven, N. A., Lin, R. M., Skingle, G. W., To, W. -M., and Urgueira, A. P. V.** (1998). *Theoretical and Experimental Modal Analysis*. Research Studies Press, Hertfordshire.

[45] **Ewins, D. J., and Gleeson, P. T.** (1982). A method for the identification of lightly damped structures. *Journal of Sound and Vibration*. *84*(1), 57-79.

[46] **Gaukroger, D. R., Skingle, C. W., and Heron, K. H.** (1973). Numerical analysis of vector response loci. *Journal of Sound and Vibration*. *29*(3), 341-353.

[47] **Beards, C. F.** (1996). *Structural Vibration: Analysis and Damping*. Arnold, London, England.

[48] **Yan, B. F., Miyamoto, A., and Bruhwiler, E.** (2006). Wavelet transform-based modal parameter identification considering uncertainty. *Journal of Sound and Vibration*. *291*(1-2), 285-301.

[49] **Alvin, K. F., Robertson, A. N., Reich, G. W., and Park, K. C.** (2003). Structural system identification: from reality to models. *Computers and Structures*. *81*, 1149-1176.

[50] **Cohen, L.** (1995). *Time-Frequency Analysis*. Prentice-Hall, New York.

[51] **Qian, S., and Chen, D.** (1996). *Joint Time-Frequency Analysis: Methods and Applications*. Prentice-Hall.

[52] **Newland, D. E.** (1993). *An Introduction to Random Vibrations, Spectral and Wavelet Analysis*. Third Edition, Wiley, New York.

[53] **Almeida, L. B.** (1994). The fractional Fourier transform and time-frequency representations. *IEEE Transactions on Signal Processing*. *42*(11), 3084-3091.

[54] **Partington, J. R., and Ünalmış, B.** (2001). On the windowed Fourier transform and wavelet transform of almost periodic functions. *Applied and Computational Harmonic Analysis*. *10*(1), 45-60.

[55] **Boltezar, M., and Slavic, J.** (2004). Enhancements to the continuous wavelet transform for damping identifications on short signals. *Mechanical Systems and Signal Processing*. *18*(5), 1065-1076.

[56] **Shen, J. H., Li, C. X., and Li, J. H.** (2009). Structural damping identification using analytic wavelet transformation. *Proceedings of World Summit on Genetic and Evolutionary Computation*. Shanghai, China.

[57] **Lamarque, C. -H., Pernot, S., and Cuer, A.** (2000). Damping identification in multi-degree of freedom systems via a wavelet-logarithmic decrement - Part 1: Theory. *Journal of Sound and Vibration*. *235*(3), 361-374.

[58] **Neild, S. A., McFadden, P. D., and Williams, M. S.** (2003). A review of time-frequency methods for structural vibration analysis. *Engineering Structures*. *25*(6), 713-728.

[59] **Rodrigues, J., and Brincker, R.** (2005). Application of the random decrement technique in operational modal analysis. *Proceedings of The 1st International Operational Modal Analysis Conference*. Copenhagen, Denmark.

[60] **Tan, J. -B., Liu, Y., Wang, L., and Yang, W. -G.** (2008). Identification of modal parameters of a system with high damping and closely spaced modes by combining continuous wavelet transform with pattern search. *Mechanical Systems and Signal Processing*. *22*(5), 1055-1060.

[61] **Kijewski, T., and Kareem, A.** (2002). On the presence of end effects and their melioration in wavelet based analysis. *Journal of Sound and Vibration*. *256*(5), 980-988.

[62] **Staszewski, W. J.** (1997). Identification of damping in MDOF systems using time-scale decomposition. *Journal of Sound and Vibration*. *203*(2), 283-305.

[63] **Slavic, J., Simonovski, I., and Boltemar, M.** (2003). Damping identification using a continuous wavelet transform: application to real data. *Journal of Sound and Vibration*. *262*(2), 291-307.

[64] **Fladung, W., and Rost, R.** (1997). Application and correction of the exponential window for frequency response functions. *Mechanical Systems and Signal Processing*. *11*(1), 23-36.

[65] **Kareem, A., and Gurley, K.** (1996). Damping in structures: Its evaluation and treatment of uncertainty. *Journal of Wind Engineering and Industrial Aerodynamics*. *59*(2-3), 131-157.

[66] **Hart, G. C.** (1996). Random damping in buildings. *Journal of Wind Engineering and Industrial Aerodynamics*. *59*(2-3), 233-246.

[67] **Schiller, N., Cabell, R., and Grosveld, F.** (2010). Impact of damping uncertainty on sea model response variance. *The Journal of The Acoustical Society of America*. *127*(3), 1873-1873.

[68] **Kareem, A., and Sun, W. -J.** (1990). Dynamic response of structures with uncertain damping. *Engineering Structures*. *12*(1), 2-8.

[69] **Jokinen, H., Ollila, J., and Aumala, O.** (2000). On windowing effects in estimating averaged periodograms of noisy signals. *Measurement*. *28*(3), 197-207.

[70] **De Troyer, T., Guillaume, P., and Steenackers, G.** (2009). Fast variance calculation of polyreference least-squares frequency-domain estimates. *Mechanical Systems and Signal Processing*. *23*(5), 1423-1433.

[71] **Pintelon, R., Guillaume, P., and Schoukens, J.** (2007). Uncertainty calculation in (operational) modal analysis. *Mechanical Systems and Signal Processing*. *21*(6), 2359-2373.

[72] **Nakra, B. C.** (1998). Vibration control in machines and structures using viscoelastic damping. *Journal of Sound and Vibration*. *211*(3), 449-466.

[73] **Woodhouse, J.** (1998). Linear damping models for structural vibration. *Journal of Sound and Vibration*. *215*(3), 547-569.

[74] **Gounaris, G. D., and Anifantis N. K.** (1999). Structural damping determination by finite element approach. *Computers&Structures*. *73*(1-5), 445-452.

[75] **Rao, M. D.** (2003). Recent applications of viscoelastic damping for noise control in automobiles and commercial airplanes. *Journal of Sound and Vibration*. *262*(3), 457-474.

[76] **Ward, I. M., and Sweeney, J.** (2004). *An Introduction to The Mechanical Properties of Solid Polymers*. Second Edition, Wiley, England.

[77] **Brinson, H. F., and Brinson, L. C.** (2008). *Polymer Engineering Science and Viscoelasticity: An Introduction*. Springer, New York.

[78] **Flügge, W.** (1967). *Viscoelasticity*. Blaisdell Publishing Company, USA.

[79] **Johnson, C. D., and Kienholz, D. A.** (1982). Finite element prediction of damping in structures with constrained viscoelastic layers. *AIAA Journal*. *20*(9), 1284-1290.

[80] **Shorter, P. J., and Langley, R. S.** (2005). Vibro-acoustic analysis of complex systems. *Journal of Sound and Vibration*. *288*(3), 669-699.

[81] **Charpentier, A., Sreedhar, P., and Fukui, K.** (2007). Using the hybrid FE-SEA method to predict structure-borne noise transmission in a trimmed automotive vehicle. *Proceedings of Noise and Vibration Conference and Exhibition*, (Paper no. 2007-01-2181). SAE International, St. Charles, Illinois, May 15-17.

[82] **Rastogi, N.** (2005). Forced frequency response analysis of multimaterial systems. *Proceedings of Noise and Vibration Conference and Exhibition*, (Paper no. 2005-01-2374). Grand Traverse, MI.

[83] **Bathe, K. -J.** (1996). *Finite Element Procedures*. Prentice-Hall.

[84] **Cortés, F., and Elejabarrieta, M. J.** (2006). An approximate numerical method for the complex eigenproblem in systems characterised by a structural damping matrix. *Journal of Sound and Vibration*. *296*(1-2), 166-182.

[85] **Rao, M. D., Echempati R., and Nadella S.** (1997). Dynamic analysis and damping of composite structures embedded with viscoelastic layers. *Composites Part B: Engineering*. *28*(5-6), 547-554.

[86] **Zhang, S. H., and Chen, H. L.** (2006). A study on the damping characteristics of laminated composites with integral viscoelastic layers. *Composite Structures*. *74*(1), 63-69.

[87] **Cortés, F., and Elejabarrieta, M. J.** (2008). Structural vibration of flexural beams with thick unconstrained layer damping. *International Journal of Solids and Structures*. *45*(22-23), 5805-5813.

[88] **Moreira, R. A. S., and Rodrigues, J. D.** (2006). A layerwise model for thin soft core sandwich plates. *Computers&Structures*. *84*(19-20), 1256-1263.

[89] **Plagianakos, T. S., and Saravanos, D. A.** (2003). Mechanics and finite elements for the damped dynamic characteristics of curvilinear laminates and composite shell structures. *Journal of Sound and Vibration*. *263*, 399-414.

[90] **Adhikari, S**. (2000). *Damping models for structural vibration* (PhD Thesis). Cambridge University, Engineering Department, Cambridge.

[91] **He, J., and Fu, Z. -F.** (2001). *Modal Analysis*. Butterworth-Heinemann, Oxford.

[92] **Mitchell, L. D.** (1990). Complex modes: A review. *Proceedings of The 8th International Modal Analysis Conference*, (pp. 891-899). Kissimmee, Florida, January 29-February 1.

[93] **Lallement, G., and Inman, D. J.** (1995). A tutorial on complex eigenvalues. *Proceedings of The 13th International Modal Analysis Conference*, (pp. 490-495). Nashville, Tennessee, February 13-16.

[94] **Garvey, S. D., Penny, J. E. T., and Friswell, M. I.** (1998). The relationship between the real and imaginary parts of complex modes. *Journal of Sound and Vibration*. *212*(1), 75-83.

[95] **Hoen, C.** (2005). An engineering interpretation of the complex eigensolution of linear dynamic systems. *Proceedings of The 23rd International Modal Analysis Conference*, (pp. 527-535), Orlando, Florida, January 31-February 3.

[96] **Prells, U., and Friswell, M. I.** (2000). A measure of non-proportional damping. *Mechanical Systems and Signal Processing*. *14*(2), 125-137.

[97] **Prater, G., and Singh, R.** (2000). Quantification of the extent of non-proportional viscous damping in discrete vibratory systems. *Journal of Sound and Vibration*. *104*(1), 109-125.

[98] **Pappa, R. S., Elliott, K. B., and Schenk, A.** (1992). A consistent-mode indicator for the eigensystem realization algorithm (Report No. NASA TM-107607). National Aeronautics and Space Administration, April.

[99] **Ahmida, K. M., and Arruda, J. R. F.** (2002). On the relation between complex modes and wave propagation phenomena. *Journal of Sound and Vibration*. *255*(4), 663-684.

[100] **Ibrahim, S. R., and Sestieri, A.** (1995). Existence and normalization of complex modes in post-experimental use in modal analysis. *Proceedings of The 13th International Modal Analysis Conference*, (pp. 483-489). Nashville, Tennessee, February 13-16.

[101] **Imregun, M., and Ewins, D. J.** (1995). Complex modes: Origins and limits. *Proceedings of The 13th International Modal Analysis Conference*, (pp. 496-506), Nashville, Tennessee, February 13-16.

[102] **Adhikari, S.** (2004). Optimal complex modes and an index of damping non-proportionality. *Mechanical Systems and Signal Processing*. *18*(1), 1-27.

[103] **Wei, M. L., Allemang, R. J., and Brown, D. L.** (1987). Real normalization of measured complex modes. *Proceedings of The 5th International Modal Analysis Conference*, (pp. 708-712). London, England, April 6-9.

[104] **Purekar, D. M.** (2005). A study of modal testing measurement errors, sensor placement and modal complexity on the process of finite element correlation (MSC Thesis). University of Cincinnati, Mechanical Engineering Department, Cincinnati, Ohio.

[105] **Heylen, W., Lammens, S., and Sas, P.** (1997). *Modal Analysis Theory and Testing*. Katholieke Universiteit Leuven, Leuven, Belgium.

[106] **Fuellekrug, U.** (2008). Computation of real normal modes from complex eigenvectors. *Mechanical Systems and Signal Processing*. *22*(1), 57-65.

[107] **Sestieri, A., and Ibrahim, S. R.** (1994). Analysis of errors and approximations in the use of modal co-ordinates. *Journal of Sound and Vibration*. *177*(2), 145-157.

[108] **Bilbao, A., Avilés, R., Agirrebeitia, J., and Ajuria, G.** (2006). Proportional damping approximation for structures with added viscoelastic dampers. *Finite Elements in Analysis and Design*. *42*(6), 492-502.

[109] **Phillips, A. W., and Allemang, R. J.** (2010). Application of modal scaling to the pole selection phase of parameter estimation. *Proceedings of The 28th International Modal Analysis Conference*, (pp. 499-518). Jacksonville, Florida, February 1-4.

[110] **Bakir, P. G.** (2011). Automation of the stabilization diagrams for subspace based system identification. *Expert Systems with Applications*. *38*(12), 14390-14397.

[111] **Reynders, E., Houbrechts, J., and De Roeck, G.** (2011). Automated interpretation of stabilization diagrams. *Proceedings of The 29th International Modal Analysis Conference*, (pp. 189-201). Jacksonville, Florida, 31 January-3 February.

[112] **Juang, J. -N., and Pappa, R. S.** (1985). An eigensystem realization algorithm for modal parameter identification and model reduction. *Journal of Guidance, Control and Dynamics*. *8*(5), 620-627.

[113] **Tong, M., Liang, Z., and Lee, G. C.** (1994). An index of damping non-proportionality for discrete vibrating systems. *Journal of Sound and Vibration*. *174*(1), 37-55.

[114] **Bellos, J., and Inman, D. J.** (1990). Frequency response of nonproportionally damped, lumped parameter, linear dynamic systems. *Journal of Vibration and Acoustics*. *112*(2), 194-201.

[115] **Park, I. W., Kim, J. S., and Ma, F.** (1994). Characteristics of modal coupling in nonclassically damped systems under harmonic excitation. *Journal of Applied Mechanics*. *61*(1), 77-83.

[116] **Bhaskar, A.** (1995). Estimates of errors in the frequency response of non-classically damped system. *Journal of Sound and Vibration*. *184*(1), 59-72.

[117] **Bhaskar, A.** (1999). Mode shapes during asynchronous motion and non-proportionality indices. *Journal of Sound and Vibration*. *224*(1), 1-16.

[118] **Liu, K., Kujath, M. R., and Zheng, W.** (2000). Quantification of non-proportionality of damping in discrete vibratory systems. *Computers&Structures*. *77*(5), 557-570.

[119] **Liu, K., Kujath, M. R., and Zheng, W.** (2001). Evaluation of damping non-proportionality using identified modal information. *Mechanical Systems and Signal Processing*. *15*(1), 227-242.

[120] **Morzfeld, M., Ajavakom, N., and Ma, F.** (2009). Diagonal dominance of damping and the decoupling approximation in linear vibratory systems. *Journal of Sound and Vibration*. *320*(1-2), 406-420.

[121] **Luenberger, D. G., and Ye, Y.** (2008). *Linear and Nonlinear Programming*. Third Edition, Springer, New York.

[122] **Rao, S. S.** (1996). *Engineering Optimisation: Theory and Practice*. Third Edition, Wiley, USA.

[123] **Bazaraa, M., Sherali, H., Shetty, C. M.** (1993). *Nonlinear Programming Theory and Algorithms*. 2nd Edition, Wiley.

[124] **Boyd, S., and Vandenberghe, L.** (2004). *Convex Optimization*. Cambridge University Press, Cambridge.

[125] **Weise, T.** (2009). *Global Optimization Algorithms - Theory and Application*, online available at http://www.it-weise.de/.

[126] **Erol, O. K., and Eksin, I.** (2006). A new optimization method: Big Bang-Big Crunch. *Advances in Engineering Software*. *37*(2), 106-111.

[127] **Goldberg, D. E.** (1989). *Genetic Algorithms in Search, Optimization and Machine Learning*. Addison-Wesley, New York.

[128] **Kang, Y. K., and Kim, C. M.** (2003). Hybrid control of sound fields from vibrating laminated plate using piezoelectric and viscoelastic material. *Proceedings of International Noise and Vibration Conference and Exhibition*, (Paper no. 2003-01-1416). Grand Traverse, MI, May 5-8.

[129] **Wyerman, B., Baker, B., Dinsmore, M., Carey, A., Saha, P., and Hadi, R.** (2003). Automotive noise and vibration control practices in the new millennium. *Proceedings of International Noise and Vibration Conference and Exhibition*, (Paper no. 2003-01-1589). Traverse City, MI, May 5-8.

[130] **Deng, J., and Liu, X.** (2007). Acoustic-structural sensitivity analysis and optimism of car body multilayer panels. *Proceedings of International Asia Pacific Automotive Engineering Conference*, (Paper no. 2007-01-3711). SAE International, California, August 5-8.

[131] **Hajela, P., and Lin, C. -Y.** (1991). Optimal design of viscoelastically damped beam structures. *Applied Mechanics Review*. *44*(11), 96-106.

[132] **Trindade, M. A.** (2007). Optimization of passive constrained layer damping treatments applied to composite beams. *Latin American Journal of Solids and Structures*. *4*, 19-38.

[133] **Ro, J., and Baz, A.** (2002). Optimum placement and control of active constrained layer damping using modal strain energy approach. *Journal of Vibration and Control*. *8*, 861-876.

[134] **Subramanian, S., Surampudi, R., Thomson, K. R., and Vallurupalli, S.** (2003). Optimization of damping treatment for structure borne noise reduction. *Proceedings of International Noise and Vibration Conference and Exhibition*, (Paper no. 2003-01-1592). SAE International, Grand Traverse, MI, May 5-8.

[135] **Chia, C. M., Rongong, J. A., and Worden, K.** (2009). Strategies for using cellular automata to locate constrained layer damping on vibrating structures. *Journal of Sound and Vibration*. *319*(1-2), 119-139.

[136] **Camp, C. V.** (2007). Design of space trusses using Big Bang-Big Crunch optimization. *Journal of Structural Engineering*. *133*(7), 999-1008.

[137] **Kaveh, A., and Talatahari, S.** (2009). Size optimization of space trusses using Big Bang-Big Crunch algorithm. *Computers&Structures*. *87*(17-18), 1129-1140.

[138] **Camp, C. V., and Akin, A.** (2012). Design of retaining walls using Big Bang-Big Crunch optimization. *Journal of Structural Engineering-ASCE*. *138*(3), 438-448.

[139] **Macioce, P.** (2013). *Viscoelastic Damping 101-Insight* (Article). Retrieved from http://www.roush.com/downloads/published-articles.aspx

[140] **Macioce, P.** (2013). *Viscoelastic Damping 101-Sound and Vibration* (Article). Retrieved from http://www.roush.com/downloads/published-articles.aspx

[141] **Lakes, R. S.** (1999). *Viscoelastic Solids*. CRC Press, New York.

[142] **Tomlinson, G. R**. (1995). Using viscoelastic materials for practical damping applications (Course Notes). University of Sheffield, December 1.

[143] **Inman, D. J.** (1994). *Engineering Vibration*. Prentice-Hall, New Jersey.

[144] **Chen, C. -C., and Yeh, M. -K.** (2001). Parametric instability of a beam under electromagnetic excitation. *Journal of Sound and Vibration*. *240*(4), 747-764.

[145] **Schmidt, E., Paradeiser, W., Dohnal, F., and Ecker, H.** (2007). Design of an electromagnetic actuator for parametric stiffness excitation. COMPEL: *The International Journal for Computation and Mathematics in Electrical and Electronic Engineering. 26*(3), 800-813.

[146] **Fan, C. -C., and Pan, M. -C.** (2010). Fluid-induced instability elimination of rotor-bearing system with an electromagnetic exciter. *International Journal of Mechanical Sciences*. *52*(4), 581-589.

[147] **Nagaya, K., and Sugiura, M.** (1995). A method for obtaining a linear spring for a permanent-magnet levitation-system using electromagnetic control. *IEEE Transactions on Magnetics, Part 2. 31*(3), 2332-2338.

[148] **Takagi, T., and Tani, J.** (1994). Dynamic behavior analysis of a plate in magnetic field by full coupling and MMD methods. *IEEE Transactions on Magnetics. 30*(5), 3296-3299.

[149] **Takagi, T., Tani, J., Matsubara, Y., and Mogi, I.** (1995). Dynamic behavior of fusion structural components under strong magnetic fields. *Fusion Engineering and Design. 27*, 481-489.

[150] **Takagi, T., Tani, J., Ruatto, P., Krevet, B., and Boccaccini, L. V.** (1996). Numerical evaluation of natural frequency change of a ferromagnetic plate due to magnetic stiffness effect. *IEEE Transactions on Magnetics. 32*(3), 1054-1057.

[151] **Zhou, Y. -H., and Miya, K.** (1999). A theoretical prediction of increase of natural frequency to ferromagnetic plates under in-plane magnetic fields. *Journal of Sound and Vibration. 222*(1), 49-64.

[152] **Tanaka, Y., Horie, T., and Niho, T.** (2000). Simplified analysis method for vibration of fusion reactor components with magnetic damping. *Fusion Engineering and Design. 51-52*, 263-271.

[153] **Zheng, X. J., Zhou, Y. -H., and Miya, K.** (2001). An analysis of variable magnetic damping of a cantilever beam-plate with end coils in transverse magnetic fields. *Fusion Engineering and Design. 55*(4), 457-465.

[154] **Bonisoli, E., and Vigliani, A.** (2006). Passive effects of rare-earth permanent magnets on flexible conductive structures. *Mechanics Research Communications. 33*(3), 302-319.

[155] **Sodano, H. A., Bae, J. -S., Inman, D. J., and Belvin, W. K.** (2006). Improved concept and model of eddy current damper. *Journal of Vibration and Acoustics. 128*, 294-302.

[156] **Tanaka, Y., Okamoto, K., and Fujimoto, Y.** (2009). Coupled vibration analysis of magnetizable plate in steady magnetic field with considering geometric nonlinearity. *IEEE Transactions on Magnetics. 45*(3), 1254-1257.

[157] **Lee, J. -L., and Lin, C. -B.** (2010). The magnetic viscous damping effect on the natural frequency of a beam plate subject to an in-plane magnetic field. *Journal of Applied Mechanics. 77*(1), 1-10.

[158] **Jung, S. S., Kim, Y. T., and Lee, Y. B., Shin, S. H., Kim, D., and Kim, H. C.** (2006). Measurement of the resonance frequency, the loss factor, and the dynamic Young's modulus in structural steel and polycarbonate by using an acoustic velocity sensor. *Journal of the Korean Physical Society. 49*(5), 1961-1966.

[159] **Kelly, S. G.** (1993). *Fundamentals of Mechanical Vibrations*. McGRAW-HILL.

[160] **Bendat, J. S., and Piersol, A. G.** (2010). *Random Data Analysis and Measurement Procedures*. 4th Edition, John Wiley.

[161] **Randall, R. B.** (1987). *Frequency Analysis*. Brüel & Kjær, Nærum.

[162] **Körük, H.** (2008). Measurement, modelling and modal analyses of helicopter structures (MSC Thesis). Istanbul Technical University, Mechanical Engineering Department, Istanbul.

[163] **PULSE Labshop** (2006). Sound and Vibration Measurement Software. Version 7.0, Bruel and Kjaer, Copenhagen, Denmark.

[164] **Ungar, E. E., and Kerwin, E. M.** (1962). Loss factors of viscoelastic systems in terms of energy concepts. *Journal of the Acoustical Society of America. 34*(7), 954-957.

[165] **Sanliturk, K. Y.** (2004). Modelling and validation of a multilayered composite finite element with damping capability. *Proceedings of The 11th International Congress on Sound and Vibration*. St. Petersburg, Russia.

[166] **Ibrahimbegovic, A., and Frey, F.** (1992). Membrane quadrilateral finite elements with rotational degrees of freedom. *Engineering Fracture Mechanics. 43*(1), 13-24.

[167] **Ibrahimbegovic, A.** (1993). Quadrilateral finite elements for analysis of thick and thin plates. *Computer Methods in Applied Mechanics and Engineering. 110*(3-4), 195-209.

[168**]** **FINES** (2010). Finite Element for Structures. Istanbul Technical University, Mechanical Engineering Department, Istanbul.

[169] **ABAQUS** (2010). Finite Element Software. Version 6.9.1.

[170] **Lin, R. M., and Lim, M. K.** (1996). Complex eigensensitivity-based characterization of structures with viscoelastic damping. *Journal of The Acoustical Society of America. 100*(5), 3182-3191.

[171] **Xu, Y.** (2001). Finite element formulation for vibration analysis of multi-layer laminated beam. *Proceedings of The 19th International Modal Analysis Conference*. Orlando, FL, February 5-9.

[172] **Torvik, P. J., and Runyon, B.** (2007). Modifications to the method of modal strain energy for improved estimates of loss factors for damped structures. *Shock and Vibration. 14*, 339-353.

[173] **Potter, R., and Richardson, M.** (1974). Mass, stiffness and damping matrices from measured modal parameters. *Proceedings of International Instrumentation-Automation Conference* & Exhibit. New York, October 28-31.

[174] **Shye, K., and Richardson, M.** (1987). Mass, stiffness, and damping matrix estimates from structural measurements. *Proceedings of The 5th International Modal Analysis Conference*, (pp. 756-761). London, England, April 6-9.

[175] **Luk, Y. W.** (1987). Identification of physical mass, stiffness and damping matrices using pseudo-inverse. *Proceedings of The 5th International Modal Analysis Conference*, (pp. 679-685). London, England, April 6-9.

[176] **Mannan, M. A., and Richardson, M. H.** (1990). Detection and location of structural cracks using FRF measurements. *Proceedings of The 8th International Modal Analysis Conference*, (pp. 652-657). Kissimmee, Florida, January 29-February 1.

[177] **Minas, C., and Inman, D. J.** (1991). Identification of a nonproportional damping matrix from incomplete modal information. *Journal of Vibration and Acoustics. 113*(2), 219-221.

[178] **Mottershead, J. E., and Friswell, M. I.** (1993). Model updating in structural dynamics-A survey. *Journal of Sound and Vibration. 167*(2), 347-375.

[179] **Chen, S. Y., Ju, M. S, and Tsuei, Y. G.** (1996). Estimation of mass, stiffness and damping matrices from frequency response functions. *Journal of Vibration and Acoustics. 118*(1), 78-82.

[180] **Sivasundaram, S.** (2004). *Advances in Dynamics and Control*. CRC Press, New York.

[181] **Hughes, T. J. R.** (1987). *The Finite Element Method: Linear Static and Dynamic Finite Element Analysis*. Prentice-Hall, New Jersey.

[182] **Kaveh, A., and Talatahari, S.** (2010). A discrete Big Bang–Big Crunch algorithm for optimal design of skeletal structures. *Asian Journal of Civil Engineering* (*Building and Housing*). *11*(1), 103-122.

[183] **Kaveh, A., and Talatahari, S.** (2010). Optimal design of Schwedler and ribbed domes via hybrid Big Bang Big Crunch algorithm. *Journal of Constructional Steel Research. 66*(3), 412-419.

[184] **Genc, H. M., and Hocaoglu, A. K.** (2008). Bearing-only tracking based on Big Bang-Big Crunch algorithm. *Proceedings of The Third International Multi-Conference on Computing in The Global Information Technology*. Athens, Greece, July 27-August 1.

[185] **Kumbasar, T., Yesil, E., Eksin, I., and Guzelkaya, M.** (2008). Inverse fuzzy model control with online adaptation via Big Bang-Big Crunch optimization. *Proceedings of The 3rd International Symposium on Communications, Control and Signal Processing*. Malta, March 12-14.

CURRICULUM VITAE

Name Surname: Hasan Körük

Place and Date of Birth: K.Maraş/Turkey, 28 Feb 1981

Address: ITU, Mechanical Engineering Department, 34437, Istanbul, Turkey

E-Mail: koruk@itu.edu.tr

B.Sc.: ITU, Mechanical Engineering Department, June 2005

M.Sc.: ITU, Machine Dynamics, Vibration and Acoustics Programme, June 2008

Professional Experience and Rewards:

Project Engineer Arçelik A.Ş., R&D Center, Dryer Group (Nov 2004-June 2005)

Project Engineer ITU, Rotorcraft Center of Excellence (Aug 2005-Dec 2005)

Visiting Scholar The Ohio State University, The Department of Mechanical and Aerospace Engineering (July 2012-Jan 2013)

Research Assistant ITU, Mechanical Engineering Department (Dec 2005–Present)

Arçelik Invention (Patent) Award, Arçelik VIII. Invention Day, Arçelik A.Ş., 2006

Derbentli Publication Award, Mechanical Engineering Department, ITU, 2012

Publication Award, ITU, Mechanical Engineering Department, 2012

Inter-Noise 2013 Young Professionals Grant, I-INCE, 2013

List of Publications and Patents:

Koruk, H., Ersever, E., and Sarioglu, K., 2007. A dryer. *International Patent*. Publication Number: WO 2007/049191 A1, Filling Date: 18.10.2006, Publication Date: 03.05.2007.

Körük, H., Gürses, K., and Şanlıtürk, K. Y., 2007. Experimental modal analysis of a helicopter tail boom section and comparison of experimental results with results of a numerical model (in Turkish). In *UMTS 2007. Proceedings of The 13. National Machine Theory Symposium*, (page 453-464). Cumhuriyet University, Sivas, 7-9 June.

Koruk, H., and Sanliturk, K. Y., 2007. Validation of finite element models of structures with riveted joints using vibration data. In *Inter-Noise 2007. Proceedings of The 36th International Congress and Exhibition on Noise Control Engineering*. Istanbul, Turkey, 28-31 August.

Körük, H., and Şanlıtürk, K. Y., 2007. Modelling riveted structures (in Turkish). In *TAKT 2007. Proceedings of The V. Turkey Abaqus Users' Meeting*, (page 261-278). Istanbul, 8-9 November.

Kay, M. S., İbaçoğlu, H., and **Körük, H.,** 2008. Updating the finite element model of the blade of an unmanned helicopter using experimental modal analysis results (in Turkish). In *UHUK 2008. Proceedings of The II. National Aeronautics and Aerospace Conference*, (Paper no. UHUK-2008-093). ITU, Istanbul, 15-17 October.

Körük, H., Öğe, A., Gürses, K., and Şanlıtürk, K. Y., 2008. Structural analysis of the airframe-tail connection of a helicopter (in Turkish). In *TAKT 2008. Proceedings of The VI. Turkey Abaqus Users' Meeting*. Istanbul, 6-7 November.

Öğe, A., **Körük, H.**, and Şanlıtürk, K. Y., 2008. Detailed structural analysis of the airfarme-tail connection of a helicopter (in Turkish). In *TAKT 2008. Proceedings of The VI. Turkey Abaqus Users' Meeting*. Istanbul, 6-7 November.

Körük, H., and Şanlıtürk, K. Y., 2008. Evaluation of the performances of lead-lag elastomeric damper designs of the blades of a helicopter (in Turkish). In *UAK 2008. Proceedings of The 8. National Acoustics Congress*. Kemer, Antalya, 27-28 November.

Körük, H., and Şanlıtürk, K. Y., 2009. Dynamic modelling and validation of a helicopter tail boom (in Turkish). In *UMTS 2009. Proceedings of The 14. National Machine Theory Symposium*, (page 37-45). Middle East Technical University, Turkish Republic of Northern Cyprus Campus, Turkish Republic of Northern Cyprus, 2-4 July.

Cakir, C., **Koruk, H.,** and Ulas, B., 2010. A low cost velocity measurement system design for rotary machinery. In *ESDA 2010. Proceedings of The ASME 2010 10th Biennial Conference on Engineering Systems Design and Analysis*. Istanbul, Turkey, 12-14 July.

Özbakış, F., **Körük, H.,** Yazgaç, D., Şanlıtürk, K. Y., and Belek, H. T., 2010. Investigation of the dymanic behaviours of the lead-lag damper designs of the blades of a helicopter (in Turkish). In *UHUK 2010. Proceedings of The III. National Aeronautics and Aerospace Conference*, (Paper no. UHUK-2010-020). Anadolu University, Eskişehir, 16-18 September.

Koruk, H., and Sanliturk, K. Y., 2012. Modeling, analyses and validation of riveted helicopter structures. In *Inter-Noise 2012. Proceedings of The 41st International Congress and Exposition on Noise Control Engineering*. New York City, USA, 19-22 August.

Koruk, H., Belek, H. T., Alparslan, M., Bilgin, N., Akaydin, O., and Akgul, A., 2012. Investigation of refrigerator noise on the prototype designs. In *Inter-Noise 2012. Proceedings of The 41st International Congress and Exposition on Noise Control Engineering*. New York City, USA, 19-22 August.

PUBLICATIONS/PRESENTATIONS ON THE THESIS

Koruk, H., and Sanliturk, K. Y., 2009. Assessment of the accuracy of damping estimation for lightly damped structures. In *ICSV16. Proceedings of The Sixteenth International Congress on Sound and Vibration*. Krakow, Poland, 5-9 July.

Koruk, H., and Sanliturk, K. Y., 2010. On measuring dynamic properties of damping materials using Oberst beam method. In *ESDA 2010. Proceedings of The ASME 2010 10th Biennial Conference on Engineering Systems Design and Analysis*. Istanbul, Turkey, 12-14 July.

Koruk, H., and Sanliturk, K. Y., 2011. Assessment of the complex eigenvalue and the modal strain energy methods for damping predictions. In *ICSV18. Proceedings of The 18th International Congress on Sound and Vibration*. Rio De Janeiro, Brazil, 10-14 July.

Koruk, H., and Sanliturk, K. Y., 2011. Damping uncertainty due to noise and exponential windowing. *Journal of Sound and Vibration*. *330*(23), 5690–5706.

Koruk, H., and Sanliturk, K. Y., 2012. Identification and removal of adverse effects of non-contact electromagnetic excitation in Oberst beam test method. *Journal of Mechanical Systems and Signal Processing*. *30*, 274-295.

Koruk, H., and Sanliturk, K. Y., 2012. Assessment of modal strain energy method: Advantages and limitations. In *ESDA 2012. Proceedings of The ASME 2012 11th Biennial Conference On Engineering Systems Design And Analysis*. Nantes, France, 2-4 July.

Sanliturk, K. Y., and **Koruk, H.,** 2013. Development and validation of a composite finite element with damping capability. *Composite Structures. 97*, 136-146.

Koruk, H., and Sanliturk, K. Y., 2013. A novel definition for quantification of mode shape complexity. *Journal of Sound and Vibration*. *332*(14), 3390-3403.